



UNIVERSITÀ DEGLI STUDI DI TRIESTE
XXV CICLO DEL DOTTORATO DI RICERCA IN FISICA

Galaxy Populations in Clusters and Proto-Clusters

Settore scientifico-disciplinare: FIS/05

Dottorando

EMANUELE CONTINI

Coordinatore

PROF. PAOLO CAMERINI

Supervisori di tesi

PROF. STEFANO BORGANI

DR. GABRIELLA DE LUCIA

ANNO ACCADEMICO 2012/2013

Alla mia Famiglia

Contents

1	Introduction	1
2	Galaxy Clusters	7
2.1	What is a Galaxy Cluster?	7
2.2	Detection of Galaxy Clusters	9
2.3	Galaxy Population in Clusters: Optical and Near Infra-Red Properties	10
2.3.1	Colour-Magnitude Relation	12
2.3.2	Morphology-Density Relation	13
2.3.3	Luminosity Function	13
2.3.4	Number of Galaxies-Cluster Mass Relation	16
2.4	Evolution of Galaxies in Clusters	18
2.5	Intra-Cluster Light	22
3	Theoretical Models of Galaxy Formation	25
3.1	N-Body Simulations	25
3.2	Identification of Dark Matter Haloes	27
3.2.1	Subhalo Finders	28
3.2.2	Merger-Trees	30
3.3	Halo Occupation Distribution	32
3.4	A Semi-Analytic Model of Galaxy Formation	33
3.4.1	Reionization	39
3.4.2	Cooling	40
3.4.3	Star Formation	41
3.4.4	Supernova Feedback	42
3.4.5	AGN Feedback	43
3.4.6	Galaxy Mergers	44
3.4.7	Metal Enrichment	45
3.4.8	Stellar Population Synthesis	45
3.5	Hydrodynamical Simulations	45

4	Statistics of Substructures in Cold Dark Matter Haloes	49
4.1	Introduction	49
4.2	Cluster simulations	51
4.3	Amount and distributions of dark matter substructures	53
4.3.1	Mass Fraction in Subhaloes	53
4.3.2	Subhalo Mass Function	55
4.3.3	Radial Distribution of Subhaloes	59
4.4	Evolution of Substructures	63
4.4.1	Mass Accretion History	63
4.4.2	Merging Rate	68
4.5	Discussion and conclusions	71
5	ICL Formation in a Hierarchical Galaxy Formation Model	75
5.1	Introduction	75
5.2	Semi-analytic models for the formation of the ICL	76
5.2.1	Disruption Model	76
5.2.2	Tidal Radius Model	77
5.2.3	Continuous Stripping Model	78
5.2.4	Merger channel for the formation of the ICL	80
5.2.5	Modelling the bulge and disk sizes	81
5.3	The Galaxy Stellar Mass Function	81
5.4	ICL fraction and dependency on halo properties	84
5.5	Formation of the ICL	89
5.6	ICL and BCG properties	95
5.7	ICL metallicity	100
5.8	Numerical Convergence	103
5.9	Discussion and conclusions	104
6	Galaxy Population in Proto-Clusters	107
6.1	Introduction	107
6.2	The Set of Simulated Proto-Clusters	109
6.3	A Case Study	109
6.4	Statistical Analysis of Proto-Cluster Regions	113
6.5	Interlopers in Observed-like Proto-Cluster Regions	116
6.6	Galaxy Population in Proto-Clusters	118
6.7	Star Formation Rate in Proto-Clusters	125
6.8	Conclusions	128
7	Conclusions and Future Prospects	131
A	Basics of Cosmology	135

Bibliography

Chapter 1

Introduction

Our Universe was born about 14 Gyr ago from a singularity in the space-time. At that time, it was extremely dense and hot, and began expanding very rapidly (Peebles 1993; Padmanabhan 1996; Peacock 1999; Coles & Lucchin 2002). The initial expansion brought the Universe to cool and about three minutes after the *Big Bang*, the primordial nucleosynthesis was complete (Weinberg 1993). Hydrogen, helium and some traces of lithium were the atoms produced by the Big Bang. Prediction of the abundance of such primordial cosmic elements have been possible by studying what we call *the wail of the Universe*, also known as the Cosmic Microwave Background (CMB, Penzias & Wilson 1965), thanks to the signature left by the recombination of free electrons and nuclei to the CMB photons (Komatsu et al. 2009).

The CMB is considered one important confirmation of the so-called ΛCDM *Concordance Model*, which is consistent with a flat geometry of the Universe and implies a total energy density very close to the critical one. The baryonic matter accounts for only $\sim 5\%$ of the total matter-energy content (Mo et al. 2010). In fact, the bulk of the matter-energy present in the Universe is in a non-baryonic and poorly known form of dark matter, $\sim 23\%$, and in an even more poorly known form of energy called dark energy, $\sim 72\%$. Dark matter with its gravity is responsible for the formation of the observed structures, while dark energy is responsible for the accelerating expansion of the Universe (see, e.g. Kowalski et al. 2008).

In addition to the study of the *relic radiation*, other important observations confirm the ΛCDM model, including Baryonic acoustic oscillations, Supernovae Ia and the large scale structure (LSS) of the Universe. Baryonic acoustic oscillations are regular and periodic fluctuations in the density of baryonic matter of the Universe, caused by acoustic waves generated by the competition between gravity and gas pressure in the primordial plasma. They leave their imprint on very large scales ($\sim 100h^{-1}\text{Mpc}$), thus providing a robust standard ruler from which the expansion history of the Universe can be inferred (Eisenstein et al. 2005; Percival et al. 2007). Type Ia supernovae explosions occur in binary systems where one of the two stars is a carbon/oxygen white dwarf that accretes material from the

other star, which can be either a giant star or another white dwarf. This kind of supernovae is characterized by a high peak luminosity, and the stability in the value of the peak makes these supernovae useful as standard candles to measure the distance of their host galaxies. Their importance in cosmology is testified by the Nobel Prize in Physics given to Saul Perlmutter, Brian P. Schmidt, and Adam G. Riess in 2011 for the 1998 discovery of the accelerating expansion of the Universe through observations of distant type Ia supernovae (Perlmutter et al. 1999). The structure or inhomogeneity of the Universe on scales larger than that of a galaxy is usually referred to as Large Scale Structure (LSS). It is characterised by the presence of voids, filaments and agglomerates of tens to hundreds of galaxies. The clustering properties of these structures are strongly dependent on cosmology which makes LSS useful for constraining cosmological parameters (see discussion in Chapter 2).

Right after recombination baryons do no longer feel the radiation pressure of photons with which they were coupled. Since then, baryons feel only the potential well due to dark matter that started to collapse, originating *halo*-like structures. Baryons collapse in these dark matter haloes and give rise to the formation of the observed structures in the Universe. In the *CDM* scenario, during the inflation, small density fluctuations originate from the homogeneous mean density field and then grow with time in a Bottom-Up fashion, with the smallest structures forming first then merging to form the larger ones. The collapse of matter can be followed with the linear perturbation theory until fluctuations are small, which means until the contrast with respect to the mean density field is close to unity. Once the collapse enters the non-linear regime, more sophisticated models/techniques such as the *spherical collapse model* or N-body simulations are needed.

At the top of the hierarchy of the non-linear structures we find Galaxy Clusters, the largest gravitationally bound and relaxed structures in the Universe, that arise from the collapse of initial density fluctuations having a comoving scale of about $10 Mpc$. They originate from the highest peaks of primordial density fluctuations, and their evolution is sensitive to the details of the cosmological model, which makes clusters a powerful cosmological probe. Moreover, most of the baryons in galaxy clusters are in the form of a hot and ionized gas, called Intra-Cluster Medium (ICM), that emits via thermal bremsstrahlung in the X-ray band. Clusters can be detected also at high redshifts and then used to probe the large scale structure, and as tracers for the history of baryons in the Universe. Thanks to modern telescopes (e.g. the Hubble Space Telescope (HST), the Very Large Telescope (VLT), Chandra, XMM-Newton and Spitzer) in various bands, our knowledge of the inner properties of clusters considerably improved during the last years. Their luminosity and temperature functions are not trivially related to their mass function, that is what one would expect for virialised gravitation-driven objects. Observations have also shown that the thermodynamical processes acting in galaxy clusters are more complex than we thought, thus severely testing our skills in modelling the physics of the gas, and generally speaking, the physics of their galaxy population. A large number of physical processes play an important role in the formation and evolution of galaxies: cooling, that allows the condensation of gas at

the centre of dark matter haloes; star formation, that converts cold gas in stars; feedback from Active Galactic Nuclei (AGN), that prevents the gas in the central regions of haloes from "over-cooling"; feedback from Supernovae, which liberates energy in the surrounding, mixing the gas and enriching it with heavy metals. Moreover, galaxy clusters are special environments in which additional important processes take place, and play an important role in the evolution of the cluster galaxy population. Galaxy merging, harassments, tidal interactions, ram pressure stripping and strangulation are all processes acting in dense environments such as clusters of galaxies. The study of galaxy formation requires detailed understanding of all the above mentioned processes, and of their evolution as a function of cosmic time. This means that we need strong constraints from observations of both nearby galaxies, and very distant galaxies. For a full understanding of the physics behind galaxy formation, we need to look also at the extreme environments given by galaxy clusters, by studying the population of galaxies they contain. To understand what drives the evolution in time of the properties of cluster galaxies, we also need to look at those objects thought to be progenitors of clusters, i.e. proto-clusters of galaxies. They are found at high redshifts, $z \gtrsim 2$, which are interesting, for example, because: see the birth of the first giant galaxies; the process of star formation, as well as the chemical enrichment of the ICM, are in the middle of their activity; clusters are forming and mergers are contributing to the assembly of galaxies; the intra-cluster light (ICL) begins to originate through tidal interactions and mergers, and galaxies in dense regions start to experience morphological transformations.

It is possible to describe the physics of baryons in a cosmological framework by adopting different theoretical/numerical approaches: two of these are provided by high-resolution numerical simulations and semi-analytic models. Both take advantage of efficient and detailed codes that consider different physical processes and their complex interplay, allowing us to predict and describe, in a reasonable way, cluster galaxy populations. Hydrodynamical simulations are expensive in terms of computational cost, and make use of parametric descriptions of the sub-grid physics, i.e. the description of the physics under the scale imposed by the numerical resolution. Semi-analytic models, instead, require negligible computational time compared to simulations. These models assume baryons to follow the dynamics of the dark matter, which can be computed either via merger-trees extracted from numerical simulations or analytically. The physics of baryons is implemented through physically motivated and observationally constrained prescriptions. Semi-analytic models can access large dynamic ranges in mass and spatial resolution and offer the possibility to quickly explore the parameter space, giving the opportunity to easily switch on and off one or more prescriptions to isolate their relative influence (see, e.g., Baugh 2006; De Lucia 2009). Since our knowledge lacks a full understanding of the physical processes at play during galaxy formation, these models contain free parameters which are usually chosen to provide a reasonable good agreement with observational data in the local Universe.

The aim of my Thesis is to explore the physical properties of the galaxy population in clusters and proto-clusters of galaxies. I will take advantage of a *state of the art*-semi-analytic

model of galaxy formation and a set of high-resolution dark matter only simulations, that provide the merger-trees needed to generate mock catalogues of galaxies. The “reference” model does not include any prescription for important processes that take place in galaxy clusters, i.e. tidal interactions between satellite galaxies and the potential of the cluster. I will address this point by updating the model with specific prescriptions for tidal stripping, and use the model to study the formation of the Intra-Cluster Light (ICL). The updated model will be then used to investigate the galaxy population in proto-clusters and study their link to the galaxy populations in local clusters.

This Thesis is structured as follows.

Chapter 2 provides an overview of galaxy clusters. I introduce them from a historical point of view and discuss the reasons for which they are important in the context of galaxy formation and evolution.

In *Chapter 3*, I describe the main tools of this Thesis, i.e. numerical simulations and semi-analytic models. I first describe the main numerical methods used in N-body simulations and the halo finders and algorithms that I used to identify haloes and construct the merger-trees that represent the input of the semi-analytic model used in this Thesis. I also describe the most important theoretical methods used to study galaxy formation, i.e. the halo occupation distribution approach and hydrodynamical simulations, besides the semi-analytic modelling that is the main tool. This will be described in details to give the reader the full description of the physics implemented in the model.

In *Chapter 4*, I make use of a set of high resolution dark matter simulations to carry out a statistical study of dark matter substructures. In the framework of modern theories of galaxy formation, dark matter substructures can be considered as the birth-sites of luminous galaxies. Therefore, the analysis of subhaloes, and in particular of their mass and spatial distributions, merger and mass accretion histories, provides important information on the expected properties of galaxies in the framework of hierarchical galaxy formation models. I have studied the amount and distribution of dark matter substructures within dark matter haloes, focusing mainly on the measured properties of subhaloes as a function of the mass and physical properties of their parent haloes, and redshift. I show that the fraction of halo mass in substructures increases with increasing mass, reaching 10% for haloes with mass of the order of $10^{15} h^{-1} M_{\odot}$. The scatter in the relation is driven by halo concentration, with less concentrated haloes having larger fractions of mass in substructures. Most of this mass is located in the external regions of haloes, in relatively few, but massive subhaloes, thus giving rise to a mass segregation which appears to be stronger at increasing redshift. Tidal stripping is found to be the process responsible for that. In fact, haloes that are more massive at the time of accretion, and that are supposed to host more luminous galaxies, are brought closer to the centre on shorter time-scales by dynamical

friction, and therefore suffer a more significant stripping. Results confirm that the main properties of galaxies, such as luminosity or stellar mass, are related to the mass of sub-halos at infall, as found in previous studies. The main results discussed in this part of the Thesis have been published in Contini et al. (2012).

In *Chapter 5*, I describe the implementation of physical processes responsible for the generation of the Intra-Cluster Light (ICL) in the available semi-analytic model, that, in its original form, does not account for them. The inclusion of these physical processes is, thus, an important improvement of the model. I use this implementation to investigate the origin of the ICL and to discuss how galaxy properties change with respect to a model that does not include these additional prescriptions. I find the fraction of ICL in groups and clusters predicted by the model to range between 10% and 40%, with a large scatter and no halo mass dependence. Large part of the scatter on cluster scales is due to a range of dynamical histories, while on smaller scales it is mainly driven by individual accretion events and stripping of relatively massive satellites, with mass of the order of $10^{10.5} M_{\odot} h^{-1}$, found to be the major contributors to the ICL. The ICL is predicted to form late, below $z \sim 1$ and a non negligible fraction (between 5% and 25%) of it has been accreted during the hierarchical growth of haloes. Moreover, the ICL is made of stars which cover a relatively large range of metallicity, with the bulk of them being sub-solar, in agreement with recent observational data. The main results of this analysis have been published in Contini et al. (2014).

Chapter 6 discusses the properties of the galaxy population found in proto-cluster regions selected from the set of simulations presented in Chapter 4, as predicted by the semi-analytic model constructed in Chapter 5. The aim is to test the predictions of the semi-analytic model and compare them with the observed properties of proto-cluster galaxies such as galaxy colours, star formation and stellar mass. The analysis shows that the galaxy population gets red and tend to cluster around the most massive galaxy as time goes by. There are, in literature, only a few attempts to characterise such peculiar regions of the Universe from a theoretical point of view. The novelty of this work lies in the attempt to connect massive clusters observed in the local Universe and the proto-cluster regions from which they have formed. I will investigate the spatial and velocity distributions of galaxies in simulated proto-clusters, and probe the red and blue galaxy populations. The main results of this work will be the subject of a paper in preparation.

In *Chapter 7* I summarize the main conclusions of my Thesis and outline future directions of investigation opened by the results presented in this work.

Finally, *Appendix A* contains the basic concepts of cosmology that have been used throughout the Thesis.

Chapter 2

Galaxy Clusters

A significant fraction of galaxies in our Universe are part of larger systems called groups and clusters of galaxies (Mo et al. 2010), systems that may contain ten to thousands of galaxies. Galaxy clusters are the largest known gravitationally bound objects that originate from the process of cosmic structure formation, forming the densest part of the large-scale structure of the Universe (Kravtsov & Borgani 2012, and references therein). In the standard scenario of structure formation with cold dark matter, the smallest structures collapse first and eventually build larger structures merging to each other. This means that clusters formed relatively recently, below redshift $z \sim 1$.

This chapter is aimed to introduce galaxy clusters, focusing mainly on their role in galaxy formation. In Section 2.1 I will give a historical overview of the most important studies on galaxy clusters, and their importance in cosmology. In Section 2.2 I will focus on the main techniques to identify clusters, by discussing both theoretical and observational results, while in Sections 2.3 and 2.4 I discuss their role in the context of galaxy formation and evolution. Section 2.5 provides an introduction to the Intra-Clusters Light, an important component of galaxy clusters that will be studied in more detail, in the framework of a theoretical model, in Chapter 5.

2.1 What is a Galaxy Cluster?

The scientific study of galaxy clusters starts more than 200 years ago, when two astronomers, Charles Messier and F. Wilhelm Herschel, produced the first two catalogues of *nabulae* (see Biviano, 2000 for a historical introduction). Years later, many others studied the distribution of these objects, with the aim to understand whether they were part of the Galaxy or external systems. The first written reference to a galaxy cluster is probably due to the French astronomer Charles Messier in 1784 (Messier, 1784), who catalogued 103 nebulae, 30 of which are now known to be galaxies. One year later, F. Wilhelm Herschel published *On the Construction of the Heavens* (Herschel, 1785), where he suggested that our Galaxy

is a nebula very similar to many other nebulae, then concluding that these systems must be external to our own Galaxy. In the course of his life, Herschel classified more than 2000 nebulae and recognized several other nearby clusters and groups of galaxies, such as Leo, Ursa Major, Hydra, NGC4169. His son, John F.W. Herschel, continued his work by cataloguing over 6000 nebulae reported in his *General Catalogue of Nebulae and Clusters of Stars*.

In the early years of the last century, intensive photographic observations of nebulae have been done mainly with the aim of establishing whether they were external to our own galaxy or not. On this topic, on April 26th 1920, the *Great Debate* between Shapley and Curtis took place, but with no clear winner. It was mainly through the works of V.M. Slipher and E. Hubble, that the extragalactic nature of nebulae was confirmed. After this finding, many clusters of galaxies were discovered and astronomers started to consider them as physical systems.

Soon, astronomers understood the important role of clusters as laboratories for studying the evolution of galaxies, and the number of discovered objects increased rapidly, from a few tens during the Hubble's time, to thousands at the beginning of the second half of the last century. *The distribution of rich clusters of galaxies* published by Abell in 1958 (Abell 1958) became a reference work in studying clusters. Since then, galaxy clusters have been considered one of the main research topics in astrophysics. Many studies have focused on this subject, covering a wide range of theoretical and observational aspects and making the knowledge in the field progress rapidly.

Galaxy clusters have had, and still have, a remarkable importance also in cosmology. The first cluster mass estimates by means of the virial theorem and using the velocity distribution of cluster galaxies, pointed out the need of dark matter (Zwicky 1933). Soon, it became clear that clusters are dominated by dark matter, with galaxies being able to explain no more than 5 per cent of the total mass. Luminous galaxies have been used as standard candles to study the expansion of the Universe (Hoessel et al. 1980), and in 1983 Bahcall & Soneira (1983) found that the spatial correlation function of rich clusters has the same shape as the galaxy correlation function, supporting the model of random Gaussian initial conditions expected from inflationary theories. The role of galaxy clusters in cosmology became more clear at the end of the last century. Measurements of the mass to light ratio in clusters suggested a sub-critical matter density in the Universe (Gott et al. 1974), subsequently confirmed by baryon fraction measurements (Fabian 1991; White et al. 1993; Evrard 1997). Cluster counts became important for measuring the amplitude of the matter power spectrum (e.g. Borgani et al. 1997 and references therein), and X-ray studies showed an amplitude lower than expected (Borgani et al. 2001; Schuecker et al. 2003). Also clusters abundances have been used to argue against models with critical matter density, since cluster abundance is sensitive to both the amplitude of the matter power spectrum σ_8 , and the matter density Ω_m . As clusters form from the gravitational collapse of fluctuations on scales close to 8 Mpc, their abundance tracks σ_8 , and since the mass in the collapsed

volume scales linearly with Ω_m , the number of haloes is sensitive to the combination of the two quantities, usually constrained in the functional form $\sigma_8\Omega_m^q$. This degeneracy can be broken by measuring abundances at different halo masses and redshifts. Nowadays, studies of galaxy clusters in a cosmological context are limited by the uncertainties in measuring the cluster mass (Allen et al. 2011 for a recent review). For this reason, precise determination of cluster mass and knowledge of cluster structure are needed (Böhinger & Werner 2010, and references therein).

2.2 Detection of Galaxy Clusters

There are several methods to detect galaxy clusters, based on their galaxy population and gas. The diffuse gas accounts for most of the baryons in the Universe (Mo et al. 2010; Allen et al. 2011) and it is usually difficult to observe. In cluster environments, gravity can be so strong to heat the gas up to very high temperatures by means of adiabatic compression and shock waves, that its light is then detected in X-ray band. The main mechanism responsible for this emission is free-free (an additional minor contribution is given by free-bound and bound-bound) emission, while the primary observables are flux, spectral hardness and spatial extent. Modern X-ray techniques provide measurements of the density, temperature and metallicity profiles of the Intra-Cluster Medium (ICM). One of the most important pro in using X-ray based techniques to search for clusters lies in the fact that they are almost free of projection effects, since the X-ray emission scales as density-squared amplifying the contrast with the sky (see Weinberg et al. 2012 for further details). Assuming the ICM to be in hydrostatic equilibrium, and the cluster to be spherically symmetric, X-ray data can also be used to estimate the cluster mass.

The hot gas in clusters can also be detected through its effects on the Cosmic Microwave Background (CMB, Penzias & Wilson 1965). When CMB photons pass through a cluster they gain energy through collisions with the high energy cluster electrons (inverse Compton scattering). This scatter produces small but measurable distortions in the CMB spectrum, an effect that is known as thermal Sunyaev-Zel'dovich (SZ) effect (Sunyaev & Zeldovich 1972). The relative motion of a cluster with respect to the CMB produces an additional distortion that is instead known as the kinetic S-Z effect. The SZ effect is a powerful tool for mapping the LSS of the Universe traced by galaxies clusters. One major advantage of this method lies in the fact that it is not sensitive to redshift, allowing the detection of clusters at high redshift where their abundance is significantly dependent on cosmology (Carlstrom et al. 2002).

Galaxy clusters can be detected also through the optical and near infra-red (NIR) emission of their galaxy population, that is dominated by early-type galaxies (e.g. ellipticals and lenticulars). Richness, luminosity and colours are the main observable of optical surveys of cluster. The first optical catalogue was constructed by Abell (Abell 1958) based

on visual inspection of photographic plates from the Palomar Observatory Sky Survey, by identifying clusters with 50 or more members with magnitude smaller than $m_3 + 2$ (being m_3 the magnitude of the third brightest member), and within $1.5 h^{-1} Mpc$ from the centre. In 1989, Abell et al. (1989) extended the original catalogue, reaching a final sample of more than 4000 clusters.

The centres of clusters are dominated by the red population of galaxies. One particular cluster identification technique, based on this population, has been used to construct the Red Sequence Cluster Survey (Gladders & Yee 2005). The method consists in selecting galaxies around the red-sequence, where it is possible to exclude most of background and foreground galaxies, which are redder and bluer respectively. The Red-Sequence Cluster Survey comprises a sample of 956 clusters identified with a single $R_c - z'$ colour.

Koester et al. (2007) use the maxBCG technique (Bahcall et al. 2003) to construct a catalogue of 13,823 clusters with optical richness $N_{gal} \geq 10$, spanning the redshift range $0.1 < z < 0.3$. The maxBCG technique is based on the fact that the BCG generally lies in a narrow region of the colour-magnitude space. A BCG likelihood is calculated based on the galaxy colours ($g - r$) and ($r - i$) and magnitude in i -band. The BCG likelihood is then weighted by the number of close galaxies located within the colour-magnitude region of the appropriate E/S0 ridgeline. The combined likelihood is then used for cluster identification. Recently, extensions of the maxBCG method (Hao et al. 2010) have been used to make large Sloan Digital Sky Survey (SDSS) clusters samples up to redshift $z \sim 0.6$. E.g., the adaptive matched filtering approach (Szabo et al. 2011), that is a likelihood method which identifies clusters by convolving the optical galaxy survey with a set of filters based on a modelling of the cluster and field galaxy distributions, or the algorithm presented in Takey et al. (2013), where the main idea is to identify the likely BCG among the galaxies with similar redshift within one arcmin from the X-ray centroid position and then search for an overdensity of surrounding member candidates. Other important past and future surveys are listed in Table 2.1.

2.3 Galaxy Population in Clusters: Optical and Near Infra-Red Properties

It is undeniable that clusters of galaxies are “peculiar” environments where many physical processes act together to shape the observed properties of the galaxy population (see discussion in Section 2.4). In this section I review the observed optical and NIR properties of the galaxy population within nearby clusters. In Chapter 5, I will present a comparison of some of these observed properties with those predicted by the semi-analytic model used in this Thesis (presented in Section 3.4).

The dynamical state of clusters and the morphology/colour of galaxies they host are usually linked together: more relaxed cluster contain a larger fraction of passive-ellipticals.

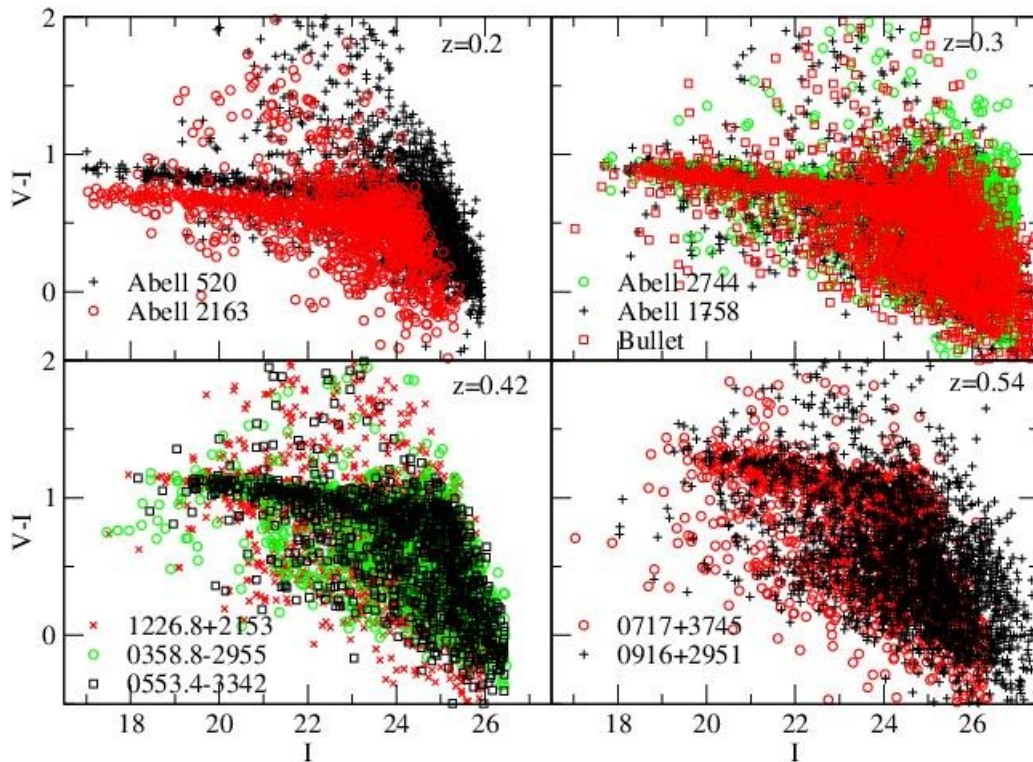


Figure 2.1: Colour-magnitude diagrams for galaxies in clusters at different redshift. With the exception of Abell 2163, where the extinction coefficients are uncertain, the authors find that all clusters are consistent with a single colour-magnitude relation. The slope and intercept of the relation are consistent with passively evolving stellar populations formed at high redshift. Figure taken from De Propris et al. (2013).

Table 2.1: List of the most important recent galaxy cluster surveys at different redshifts. Name (first column), reference (second column), detection band (third column), number of clusters (fourth column) and redshift range (fifth column) are reported.

Name	Reference	Band	Clusters	z-range
ICBS	Oemler et al. (2013)	IR	5	0.3-0.5
CLASH	Postman et al. (2012)	UV/OPT/IR	25	0.2-0.9
MaDCowS	Gettings et al. (2012)	IR	n.r.	~ 1
IDCS	Brodwin et al. (2012)	IR	n.r.	0-2
DAFT/FADA	Guennou et al. (2010)	OPT/IR	91	0.4-0.9
SpARCS	Wilson et al. (2009)	IR	hundreds	≥ 1
RCS2	Yee et al. (2007)	OPTICAL	$\sim 20,000$	0.15-1
WINGS	Fasano et al. (2006)	X	77	≤ 0.07
EDisCS	White et al. (2005)	X/OPT	20	0.4-1
XCS	Romer et al. (2001)	X	~ 8000	0-1.5
REFLEX	Böhringer et al. (2001)	X	447	~ 0.01
CNOC	Yee et al. (1996)	X	16	0.2-0.6

There are a number of properties/relations that can provide important information of the galaxy population in clusters. In what follows, I briefly introduce some of them.

2.3.1 Colour-Magnitude Relation

Galaxies follow a bimodal distribution in the colour-magnitude plane, separated into *red sequence* galaxies, that consists mainly of gas-poor and passive galaxies, and *blue cloud* galaxies, typically gas-rich and star forming galaxies. The location of a given galaxy in the colour-magnitude diagram (CMD, see Figure 2.1) can provide important information on their formation mechanisms and time-scales.

The CMD was first observed by Baum (1959) and a preliminary description of the two populations can be found in Bell et al. (2004), who confirmed the bimodal distribution of red and blue galaxies seen by Strateva et al. (2001) using Sloan Digital Sky Survey data. The CMD of early-type galaxies can be interpreted as a mass-metallicity relation (Kodama & Arimoto 1997; Stanford et al. 1998; Gladders et al. 1998; De Lucia et al. 2004c). In fact, more massive galaxies have deeper potential wells, and are then able to retain the metals released by supernovae explosions and stellar winds in the surrounding medium (see, e.g., Kodama et al. 1998). There are different viewpoints about the mechanisms that are responsible for the evolution of galaxies on the red-sequence. The most important (and invoked) physical processes are: a) passive stellar evolution; b) galaxy mergers and galaxy-galaxy interactions (such as galaxy harassments, frequent high speed galaxy encounters (Moore et al. 1999));

c) environmental effects (that I will discuss in Section 2.4), such as strangulation (Larson et al. 1980) and ram pressure stripping of gas (Gunn & Gott 1972). Observations of the CMD in galaxy clusters (see, e.g., Mei et al. 2009), show no evolution of the intercept, slope and scatter of the relation up to redshift $z \simeq 1.3$, and no significant dependence on cluster mass. Stott et al. (2009), instead (but see also e.g., De Lucia et al. 2004c; Kodama et al. 2004), find an evolution of the slope between $z \simeq 0.5$ and the present-day, that they attribute to the build up of the red-sequence over time.

2.3.2 Morphology-Density Relation

Early-type galaxies are preferentially located in high density environments, while late-type galaxies are preferentially located in low density environments (Dressler 1980). The morphology-density relation (MDR), therefore, suggests that star formation is suppressed when galaxies enter higher density environments such as clusters. The physical processes responsible for shaping the MDR involve the partial or even total removal of the gas from satellite galaxies that enter the cluster, via interactions with its intergalactic medium. Ram-pressure stripping (Gunn & Gott 1972, see Section 2.4) is usually considered a valid option (see van der Wel et al. 2010), but also stripping of the hot gas known as starvation or strangulation (Larson et al. 1980, see discussion in Section 2.4) is believed to play a role.

The interpretation of the MDR, however, is not trivial because many galaxy properties such as morphology, stellar mass, colour and star formation, all environment-dependent properties, are correlated to each other (Lewis et al. 2002; Kauffmann et al. 2003; Hogg et al. 2003; Blanton et al. 2005; Poggianti et al. 2006; Baldry et al. 2006; Poggianti et al. 2008; Skibba & Sheth 2009). Moreover, as recently pointed out by van der Wel et al. (2010), morphology is a parameter given by the combination of several physical quantities such as structure (e.g. bulge-to-disk ratio or concentration) and star formation activity. These two quantities are correlated (Kauffmann et al. 2003; Hogg et al. 2004), but also behave quite differently as a function of environment. The structure seems to weakly depend on environment (Kauffmann et al. 2004; Blanton et al. 2005), while the star formation activity decreases from low to high-density environments (Lewis et al. 2002; Hogg et al. 2003; Skibba & Sheth 2009). Moreover, as shown by Balogh et al. (1998), galaxies that have similar structures have lower star formation rates if they reside in high-density environments. This highlights a non-trivial link between the morphological mix and the environment (van der Wel 2008; Bamford et al. 2009; Poggianti et al. 2009).

2.3.3 Luminosity Function

The luminosity distribution of galaxies in clusters is described by the luminosity function (LF, see Figure 2.2). The LF in low and high-density environments probes the relevance of the environmental effects on the galaxy populations and given the large number of galaxies

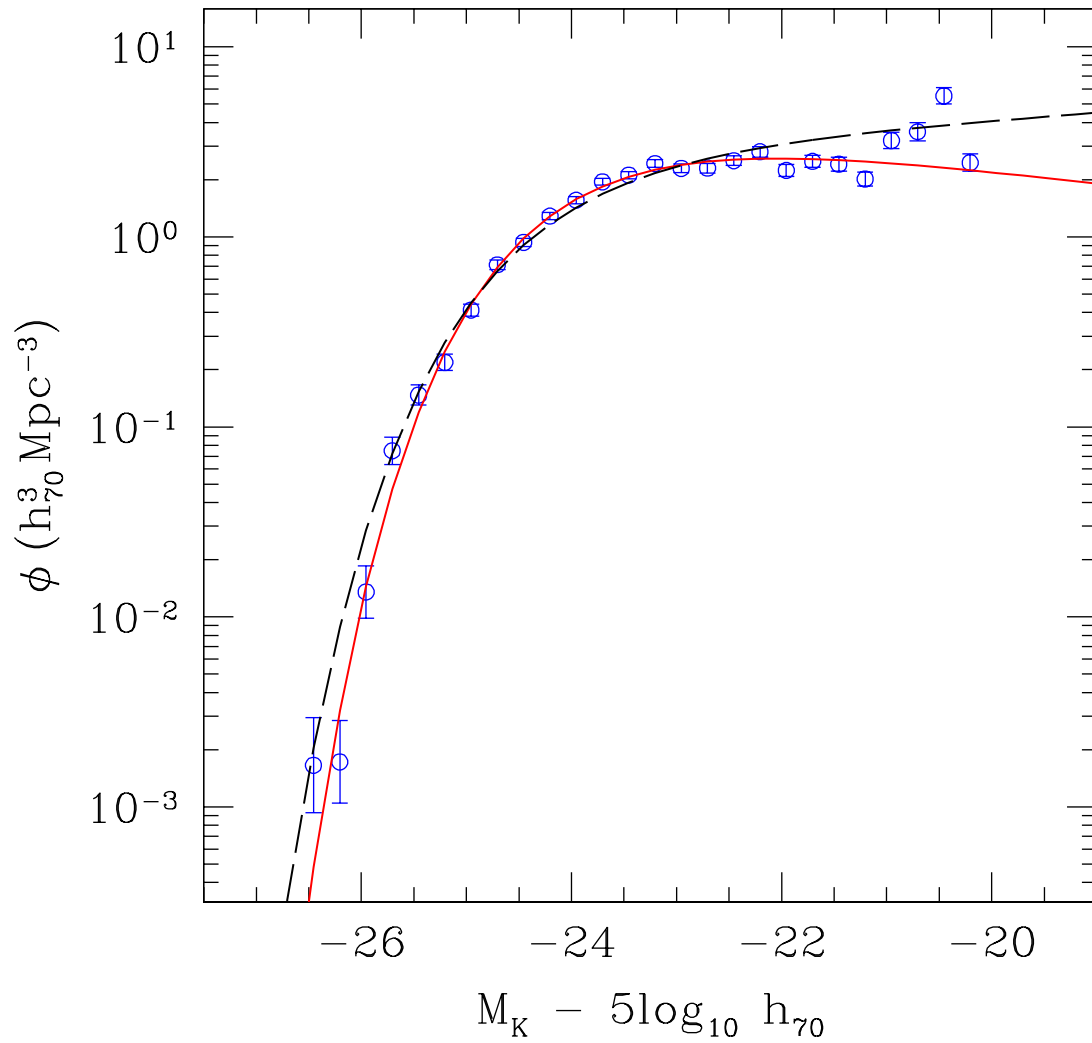


Figure 2.2: K-band composite cluster luminosity function of 5932 galaxies in 93 groups and clusters. Symbols refer to observed data, while lines represent Schechter functions with different values for the free parameters. Figure taken from Lin et al. (2004).

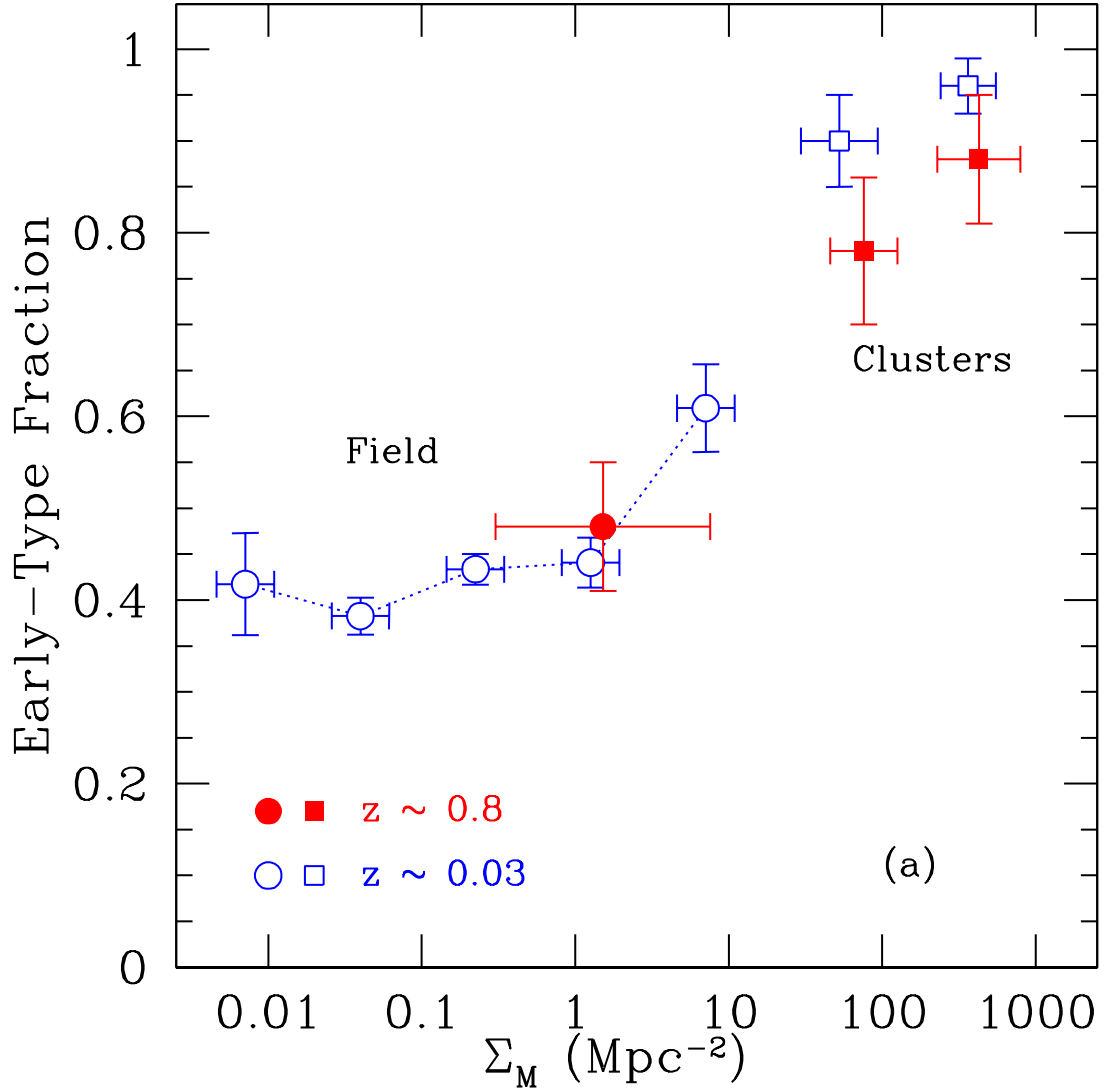


Figure 2.3: Morphology-density relation for mass-selected galaxies ($M > 4 \cdot 10^{10} M_{\odot}$) at $z \sim 0$ and $z \sim 0.8$. The circles indicate a sample of field galaxies ($\Sigma \lesssim 50 Mpc^{-2}$) at $z \sim 0.03$ (open blue circles) and $z \sim 0.8$ (filled red circle). The squares indicate a sample of cluster galaxies ($\Sigma \gtrsim 50 Mpc^{-2}$) at $z \sim 0.02$ (open blue squares) and $z \sim 0.8$ (filled red squares). Figure taken from van der Wel et al. (2007).

they provide, clusters are ideal places where to study the LF (Lin et al. 2004, but see also Mancone et al. 2012 and references therein).

The near-infrared luminosity function (NIR LF) can be used to study the stellar mass growth of a galaxy population, since the rest-frame NIR is a good proxy for stellar mass (see, e.g., Into & Portinari 2013). The NIR LF has been used to study also the assembly of the most massive galaxies in clusters. These studies (see Mancone et al. 2010 and reference therein) show that the massive end of the NIR LF evolves passively out to redshift $z \sim 1.3$, thus suggesting that the bulk of the stellar mass of these galaxies forms early, at high redshift. Other studies have tried to probe the faint end of the cluster LF at high redshift. Recently, Mancone et al. (2012) use seven high-redshift spectroscopically confirmed galaxy clusters drawn from the IRAC Shallow Cluster Survey (Eisenhardt et al. 2008 and references therein) to measure the cluster galaxy LF down to $M^* + 3$ ($3.6\mu m$) and $M^* + 2.5$ ($4.5\mu m$). Comparing their results with the LF in low-redshift clusters, they conclude that there is no significant evidence of evolution. Moreover, by combining these results with those showing that M^* is passively evolving out to $z \sim 1.3$, they conclude that the shape of the cluster LF is largely in place by that redshift, suggesting that the processes that govern the build up of the mass of low-mass cluster galaxies have no effect on the faint end slope of the cluster LF at $z \lesssim 1.3$.

2.3.4 Number of Galaxies-Cluster Mass Relation

The number of galaxies N_g as a function of the cluster mass M gives important information on the physics of galaxy formation and on the merging rate of galaxies. Lin et al. (2004) studied a sample of 93 galaxy clusters and groups using data from the Two Micron All Sky Survey (Jarrett et al. 2000) and found that the slope of the $N_g - M$ relation is the same as the slope of the luminosity-mass relation (BCG excluded), in the K-band (see Figure 2.4). This implies that the sum of the galaxy luminosity scales linearly with the total galaxy number in clusters, implying a constant shape parameter L_* of the luminosity function with cluster mass. Moreover, they found a value of the slope smaller than one, 0.84 ± 0.04 (found to be slightly larger in r-band by Popesso et al. 2007a), which indicates that more massive clusters have fewer galaxies per unit mass than low-mass clusters, in contrast with results by Poggianti et al. (2010) who show that it is just an apparent result due to the way of computing the mass observationally. In a hierarchical scenario, massive clusters form via mergers/accretions of smaller objects. Assuming that galaxies survive during these processes, we should expect their number to remain the same. Lin et al. 2004 claimed that the transformation of the galaxy population from low-mass to high-mass clusters consists in a building up of a few extremely luminous galaxies and in the destruction (or fainting) of galaxies fainter than M_* . None of the mechanisms they considered can by itself offer a sufficient explanation of the galaxy population differences among clusters of different mass.

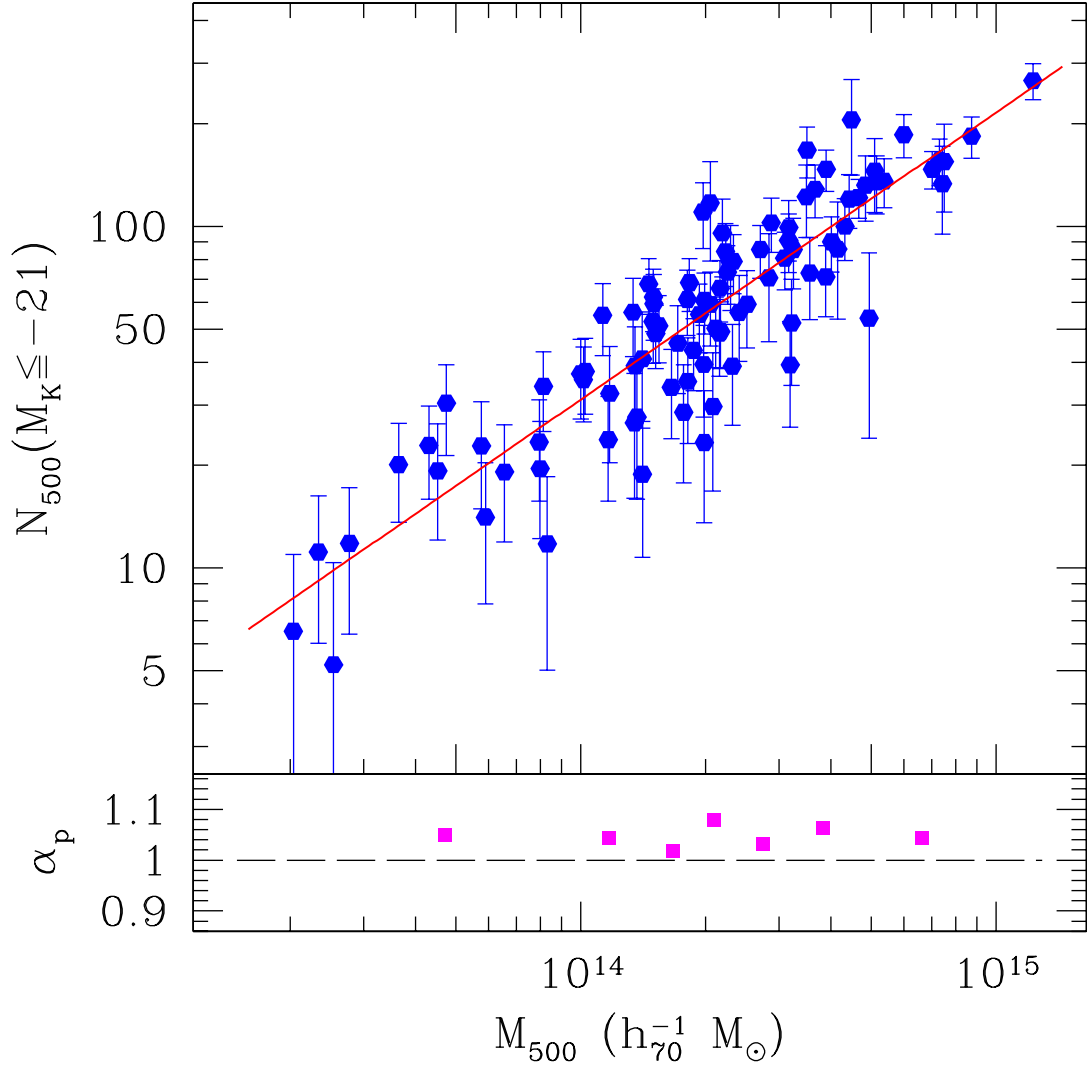


Figure 2.4: Top: Number of galaxies as a function of cluster mass, with the best-fit relation that gives $N \propto M^{0.84 \pm 0.04}$. Bottom: deviation of the halo occupation number $P(N|M)$, the probability distribution that a halo of mass M contains N galaxies, from a Poisson distribution. Figure taken from Lin et al. (2004).

2.4 Evolution of Galaxies in Clusters

The standard scenario of galaxy formation finds its seeds in the pioneering work of White & Rees (1978), who proposed a two-stage model for the formation of galaxies: gas cools and condenses at the centres of dark matter haloes which form in a dissipationless gravitational collapse and grow hierarchically through accretion and merging.

Galaxy clusters are high density environments and many galaxy properties such as star formation rate, gas content and morphology can be affected by physical processes that take place within them. These processes can be collected in two different groups: processes acting among galaxies, such as galaxy-galaxy collisions, mergers and harassment, and processes among galaxies and the cluster potential, such as strangulation, and with the intra-cluster gas, such as ram pressure stripping.

Galaxy-galaxy interactions within clusters, such as collisions and mergers, play an important role in galaxy evolution, and this was understood much before the first theories of galaxy formation. Shapley (Shapley 1936) was the first author to highlight the importance of collisions in dense environments as galaxy clusters (even if they are rare in clusters since the relative velocity among galaxies is high), and two years later Zwicky (Zwicky 1937) suggested that such collisions might explain the different morphological mix of cluster galaxies from the field. Since the pioneering work of (Toomre & Toomre, 1972), which pointed out the importance of mergers of spiral galaxies, a large effort has been spent in numerical simulations to understand the role of these processes in galaxy evolution (Hernquist 1989; Mihos & Hernquist 1994; Springel & Hernquist 2005; Cox et al. 2006). Numerical simulations allowed us to understand that galaxy-galaxy interactions are important not only in driving the morphological transformations of galaxies (Roos & Norman 1979; Barnes 1992), but for driving also bursts of star formation (Young et al. 1986; Barnes & Hernquist 1992; Saitoh et al. 2009). Nowadays we know that the gas content in the galaxies involved in the process plays a crucial role. Depending on the amount of new stars produced during such processes, galaxies can change their luminosity, colour and morphology. Dry-mergers (e.g. van Dokkum et al. 1999 for an observational example), that take place between gas-poor galaxies, or red galaxies, are events that may not affect the star formation rate but that can play an important role in the stellar mass growth. On the other hand, wet mergers between gas-rich galaxies produce bursts of star formation, thus increasing the luminosity of the galaxies which become bluer due to the stars newly formed. The end product of these mergers is usually an elliptical galaxy. For further details of the importance of dry and wet mergers in the context of galaxy evolution, I refer to the recent review by Shlosman (2012).

Ram pressure stripping (Gunn & Gott 1972) is another important process for the evolution of galaxies in clusters. As said before, galaxy clusters are pervaded by a hot and X-ray emitting gas known as intra-cluster medium. Galaxies that travel through the ICM experience it as a wind, and, if the wind is strong enough to overcome the galaxy gravitational potential well, it sweeps the cold gas out of the stellar disk. Many galaxies in clusters show

evidence of ram pressure stripping at work. A clear example is NGC 4402, that is falling into the Virgo cluster (Crowl et al. 2005). The disk of dust of this galaxy is curved, which may be due to the fact that the galaxy is experiencing some pressure in the outer regions of the disk (which are less bound) and starting to lose gas. Moreover, the stellar disk of NCG 4402 extends well beyond the star forming disk of dust and gas, which indicates that the gas in the outer regions of the disk has been stripped from the galaxy after the formation of these stars.

The effect of ram pressure stripping is that of halting star formation in galaxies, which supports the idea that ram pressure stripping may be one of the process at work in shaping the morphology-density relation (see Section 2.3.2), as well as strangulation. As a galaxy falls into the cluster environment for the first time, the gravitational potential of the cluster creates tidal effects that allow the hot gas contained within the galaxy to escape. This entails a continuous decreasing of star formation that carries on until some cold gas is available. Once the galaxy uses up all the cold gas supply, which cannot be replenished by cooling that is suppressed, star formation within the galaxy ceases, and the galaxy is strangled because of the lack of gas.

The discovery of the Butcher-Oemler effect (Butcher & Oemler 1978) was the first clear observational evidence of galaxy evolution in clusters, then confirmed some years later by the work of Butcher & Oemler (1984) who showed that rich galaxy clusters have an excess of galaxies with blue colours when compared to similar nearby clusters (see Figure 2.5). More recent studies (e.g. Duc et al. 2002; Tran et al. 2005; Haines et al. 2009; Urquhart et al. 2010; Lerchster et al. 2011) have refined the measurements of Butcher and Oemler. The fraction of blue galaxies in massive clusters ranges from approximately 3 per cent for $z < 0.1$ clusters, to 25 per cent at $z \sim 0.5$ and about 70 per cent at $z \sim 1$. Moreover, some of these studies have also pointed out that the fraction of blue galaxies depends on cluster richness, mass or velocity dispersion (Margoniner et al. 2001; Poggianti et al. 2006), X-ray luminosity (Holden et al. 2002; Aguerri et al. 2007; Popesso et al. 2007b), the cluster-centric radius (Ellingson et al. 2001; Goto et al. 2003; Loh et al. 2008; Mahajan & Raychaudhury 2009) and the presence of substructure (Metevier et al. 2000; Hou et al. 2012). Nevertheless, the existence itself of the Butcher-Oemler effect has been criticised by several authors (Smail et al. 1998; Andreon & Etori 1999; De Propris et al. 2003; Andreon et al. 2004, 2006) and for different reasons. The main criticism comes from the fact that the Butcher-Oemler sample is not homogeneous, being composed by optically selected clusters that favours the inclusion of objects with a significant fraction of blue galaxies at high redshift, and being, indeed, selection biased.

In light of this, it appears of crucial importance to investigate the galaxy population in clusters at high redshift and in the so-called proto-clusters. Most of the studies of high-redshift clusters agree on the early formation of the population of massive cluster early-type galaxies, with their stars formed at high redshift ($z \gtrsim 2$) and their mass mainly assembled before $z \sim 1$ (De Propris et al. 2007; Lidman et al. 2008; Mancone et al. 2010;

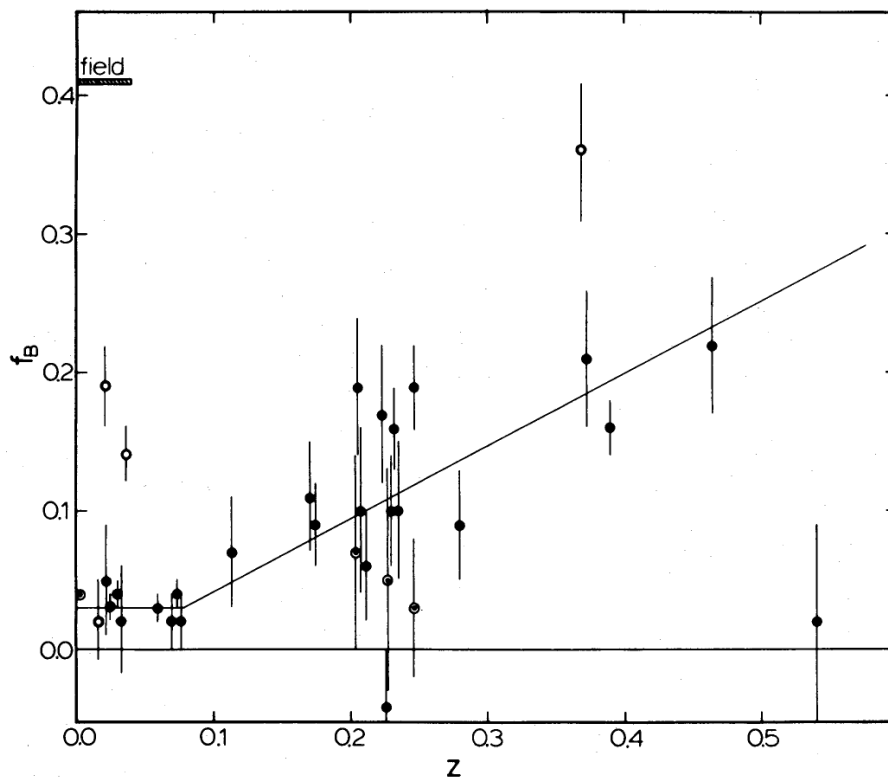


Figure 2.5: Fraction of blue galaxies as a function of redshift. Filled circles represent compact clusters ($C \geq 0.4$); open circles represent irregular clusters ($C < 0.35$); dotted circles represent intermediate clusters ($0.35 \leq C < 0.4$). The concentration index C is defined as $C = \log(R_{60}/R_{20})$, where R_n is the radius of the circle containing n per cent of the cluster's projected galaxy distribution. Figure taken from Butcher & Oemler (1984).



Figure 2.6: Combined $I_{814} - J_{110} - K_s$ image of MRC 1138-262 (centre) and its neighbouring satellites galaxies within 150 kpc, at $z = 2.2$. The total extent of the image is 300 kpc on each side. Figure taken from Hatch et al. (2009).

Strazzullo et al. 2010; Mancone et al. 2012; Strazzullo et al. 2013). $z > 1.5$ appears to be a crucial epoch to study massive cluster galaxies, since it is close to their formation epoch. Recent observations in this redshift range are starting to show that the population of massive galaxies is still in an active formation stage, even in the cluster core (see Strazzullo et al. 2013 and references therein).

Proto-clusters are high density environments in the early Universe that evolve with time originating the observed clusters in the local Universe. Putative proto-cluster regions (see example shown in Figure 2.6) are often localized around high- z radio galaxies (HzRGs, e.g., Pentericci et al. 1997; Miley et al. 2004; Kurk et al. 2004; Venemans et al. 2007; Kuiper et al. 2011), that are among the most massive galaxies at high redshift and likely the progenitors of massive elliptical galaxies that sit at the centre of local massive clusters (e.g., McLure et al. 1999; Zirm et al. 2005; Cooke et al. 2008; Miley & De Breuck 2008; Hatch et al. 2011a). Proto-cluster galaxies are usually selected by looking for strong emission lines such as Ly α or H α . The latter is the favourite tracer, since it is less affected by dust extinction than other strong lines emitted in the rest-frame optical or ultra-violet (Koyama et al. 2013).

Observationally, there are no simple criteria to define a proto-cluster, simply because it is not trivial to characterize the typical region in the sky that encloses all progenitors of galaxies in local clusters, or most of them. The reason lies in the fact that it is not possible, observationally, to know a priori which are actual progenitors, and which are not. A common technique is to take relatively small areas around HzRGs (e.g., Hatch et al. 2009; Kuiper et al. 2011) and study the properties of galaxies in their inner vicinity, such as galaxy velocity dispersion or total star formation rate. However, proto-clusters seem to be very extended objects (Kurk et al. 2004; Venemans et al. 2007; Tanaka et al. 2011; Hatch et al. 2011a; Toshikawa et al. 2012), up to 20 Mpc at redshift $z \sim 2$. They host mainly star forming galaxies with little evidence of a passive evolving populations (Hatch et al. 2011b). Only very recently Gobat et al. (2011) have found a red galaxy population in a $z \sim 2$ cluster. The need to investigate larger regions appears clear if the goal is to probe a more complete sample of proto-cluster galaxy population, and not only galaxies very close to HzRGs.

2.5 Intra-Cluster Light

Not all stars in clusters are bound to galaxies. The presence of a diffuse population of intergalactic stars in galaxy clusters was first proposed by Zwicky (1937), and later confirmed by the same author using observations of the Coma cluster with a 48-inch schmidt telescope (Zwicky, 1952). More recent observational studies have confirmed that a substantial fraction of stars in clusters are not bound to galaxies. This diffuse component is generally referred to as Intra-Cluster Light (hereafter ICL).

Both from the observational and the theoretical point of view, it is not trivial to define the ICL component. A fraction of central cluster galaxies are characterized by a faint

and extended stellar halo. These galaxies are classified as *cD galaxies*, where ‘c’ refers to the fact that these galaxies are very large and stands for supergiant and ‘D’ for diffuse (Matthews et al. 1964), to highlight the presence of a diffuse stellar envelope made of stars that are not bound to the galaxy itself. Separating these two components is not an easy task. On the observational side, some authors use an isophotal limit to cut off the light from satellite galaxies, while the distinction between the brightest cluster galaxy (hereafter BCG) and ICL is based on profile decomposition (e.g. Zibetti et al., 2005). Others (e.g. Gonzalez et al., 2005) rely on two-dimensional profile fittings to model the surface brightness profile of brightest cluster galaxies. In the framework of numerical simulations, additional information is available, and the ICL component has been defined using either a binding energy definition (i.e. all stars that are not bound to identified galaxies, e.g. Murante et al., 2007), or variations of this technique that take advantage of the dynamical information provided by the simulations (e.g. Dolag et al., 2010). In a recent work, Rudick et al. (2011) discuss different methods that have been employed both for observational and for theoretical data, and apply them to a suite of N-body simulations of galaxy clusters. They find that different methods can change the measured fraction of ICL by up to a factor of about four (from ~ 9 to ~ 36 per cent). In contrast, Puchwein et al. (2010) apply four different methods to identify the ICL in hydrodynamical SPH simulations of cluster galaxies, and consistently find a significant ICL stellar fraction (~ 45 per cent).

There is no general agreement in the literature about how the ICL fraction varies as a function of cluster mass. Zibetti et al. (2005) find that richer clusters (the richness being determined by the number of red-sequence galaxies), and those with a more luminous BCG have brighter ICL than their counterparts. However, they find roughly constant ICL fractions as a function of halo mass, within the uncertainties and sample variance. In contrast, Lin & Mohr (2004) empirically infer an increasing fraction of ICL with increasing cluster mass. To estimate the amount of ICL, they use the observed correlation between the cluster luminosity and mass and a simple merger tree model for cluster formation. Results are inconclusive also on the theoretical side, with claims of increasing ICL fractions for more massive haloes (e.g. Murante et al. 2004; Purcell et al. 2007; Murante et al. 2007; Purcell et al. 2008), as well as findings of no significant increase of the ICL fraction with cluster mass (e.g. Monaco et al. 2006; Henriques & Thomas 2010; Puchwein et al. 2010), at least for systems more massive than $10^{13} M_{\odot}/h$.

Different physical mechanisms may be at play in the formation of the ICL, and their relative importance can vary during the dynamical history of the cluster. Stars can be stripped away from satellite galaxies orbiting within the cluster, by tidal forces exerted either during interactions with other cluster galaxies, or by the cluster potential. This is supported by observations of arclets and similar tidal features that have been identified in the Coma, Centaurus and Hydra I clusters (Gregg & West, 1998; Trentham & Mobasher, 1998; Calcáneo-Roldán et al., 2000; Arnaboldi et al., 2012). As pointed out by several authors, in a scenario where galaxy stripping and disruption are the main mechanisms for the

production of the ICL, the major contribution comes from galaxies falling onto the cluster along almost radial orbits, since tidal interactions by the cluster potential are strongest for these galaxies. Numerical simulations have also shown that large amounts of ICL can come from 'pre-processing' in galaxy groups that are later accreted onto massive clusters (Mihos, 2004; Willman et al., 2004; Rudick et al., 2006; Sommer-Larsen, 2006). In addition, Murante et al. (2007) found that the formation of the ICL is tightly linked to the build-up of the BCG and of the other massive cluster galaxies, a scenario supported by other theoretical studies (e.g. Diemand et al. 2005; Abadi et al. 2006; Font et al. 2006; Read et al. 2006). It is important, however, to consider that results from numerical simulations might be affected by numerical problems. Murante et al. (2007) find an increasing fraction of ICL when increasing the numerical resolution of their simulations. In addition, Puchwein et al. (2010) show that a significant fraction (~ 30 per cent) of the ICL identified in their simulations forms in gas clouds that were stripped from the dark matter haloes of galaxies infalling onto the cluster. Fluid instabilities, that are not well treated within the numerical techniques used in this study, might be able to disrupt these clouds suppressing this mode of ICL formation.

Chapter 3

Theoretical Models of Galaxy Formation

In this Chapter I provide the necessary background for the following chapters, by introducing the tools that I used in order to achieve the aims discussed in Chapter 1. There are different ways to approach galaxy formation from a theoretical point of view. The aim of this Chapter is also that of describing each of them, giving a brief summary of the main developments made in the last years. In particular, I will emphasize the main tool of this work, i.e. the semi-analytic model I used, discussing the most important details of the modelling.

3.1 N-Body Simulations

Large scale structures such as clusters of galaxies form by the amplification of small perturbations. As long as these perturbations in the gravitational potential are small, the density fluctuations can be treated as perturbations about a Friedmann Universe. Since it appears that these perturbations are in non-relativistic matter and involve scales much smaller than the horizon size, we can work in the Newtonian limit for studying their evolution. Gravity is the dominant force at large scales and it is believed to drive the growth of these perturbations. Numerical simulations are a powerful tool for evolving density perturbations in the non-linear regime. Generally speaking, numerical simulations can be split into two vast categories: N-body simulations, that take into account only gravitational interactions, and hydrodynamical simulations (they will be discussed in Section 3.5), that also treat the gas dynamics.

N-body simulations are numerical solutions of the equations of motions for N particles that interact gravitationally. A set of particles represent the density field, and the state of the system can be described by the positions and velocities of all these particles, (\vec{r}_i, \vec{u}_i) . If we assume to have a system of N collisionless particles with equal mass, the motion of each

of these particles is given by

$$\frac{d\vec{u}_i}{dt} = \vec{a}_i = -\nabla\phi_i \quad (3.1)$$

where \vec{a}_i is the acceleration at the position of the particle and ϕ is the gravitational potential determined by the mass density $\rho(r, t)$ by means of the the Poisson equation

$$\nabla^2\phi = 4\pi G\rho(r, t). \quad (3.2)$$

The set-up of the initial conditions, the evaluation of forces and the algorithm for solving the equation of motion are key elements of N-body simulations. There are different approaches for calculating the force:

- **PP (Particle-Particle) Algorithm:** This is the most straightforward and intuitive method to calculate the gravitational force on a particle due to all the other particles. The force that acts on the i -th particle due to the j -th is:

$$\vec{F}_{ij} = G \frac{m_i m_j (\vec{x}_i - \vec{x}_j)}{(|\vec{x}_i - \vec{x}_j|^2 + \epsilon^2)^{3/2}} \quad (3.3)$$

where G is the gravitational constant, m_i and m_j are the masses, x_i and x_j are the positions and ϵ is the *softening parameter*. It has been introduced to avoid divergences in the forces when two particle are very close to each other and therefore represent the spatial resolution of the simulation. The problem of this method is the computational time it requires. At each time-step, the total time required to calculate all the forces scales as N^2 , which necessarily limits the number of particles in the simulation.

- **PM (Particle-Mesh) Algorithm:** This method was the first to be used for large cosmological simulation, with a number of particles of the order of $N \sim 10^5$ (Klypin & Shandarin 1983). This takes advantage of the fact that the Poisson equation is a simple algebraic equation in the Fourier space. In this approach, the gravitational potential of the system is constructed over a grid from the density field solving the Poisson equation. Particles do not interact among each others but through a mean field. This method has an important advantage: since the computational cost for the evaluation of the forces scales with N , a large number of particles can be used, but the size of the mesh limits the force resolution. A large number of resolution levels are usually required, that translates in using more memory with respect to other methods.
- **P³M (Particle-Particle-Particle-Mesh) Algorithm:** The basic idea of this method is that of adding a correction to the force computed using the particle-mesh method. In the P^3M scheme, forces between distant particles are calculated using the PM method, while the force between particles with distance less than about two times the size of the meshes is derived by means of the PP method. An advantage lies in an improvement of the resolution with respect to the PM method.

- **Tree Algorithm:** The tree algorithm is one of the methods that allow simulations with a large number of particles to be carried out (Barnes & Hut 1986). In this approach, particles are grouped together according to their distance to the particle on which one wants to compute the force. The idea is that of treating many distant particles as one more massive particle. The space is partitioned in sub-unit, or cubes, in order to find these groups of particles. Each cube is then partitioned again in sub-unit until it contains either exactly one particle or it does not contain any particle. The following step is that of calculating the force by walking the tree, summing up the force contribution of each node. The most important advantage of this method is that of reducing the computational time for the evaluation of the force, that is proportional to $N \log N$. It is cheaper in terms of computational time with respect to the P^3M method, but more expensive in terms of memory requirements.

3.2 Identification of Dark Matter Haloes

The identification of groups of particles constitutes the very first step in the analysis of simulations. One way to address this point, but also the most used in literature, is given by the friends-of-friends (FOF) algorithm. This identifies objects at different overdensities depending on the chosen linking length, by linking together all the particles distant to each other less than a factor b times the mean interparticle separation. The linking length f is usually set to return objects of a particular overdensity. It has been shown that values of about 0.2 allow groups of particles close to the virial overdensity predicted by the spherical collapse model to be identified (see Appendix A). The halo mass function computed using this approach is in agreement with theoretical predictions (Press & Schechter 1974). The FOF algorithm has also an undesirable disadvantage: sometimes it links together different structures with a bridge of particles.

The FOF algorithm is not able to find sub-haloes in haloes. To this aim, I used an algorithm called SUBFIND (Springel et al. 2001a), that identifies gravitationally bound and locally overdense regions within dark matter haloes previously provided by a FOF algorithm. SUBFIND computes a local estimate of the density at the positions of all particles in the input group. This is done in the usual SPH-fashion, i.e., the local smoothing scale is set to the distance of the N_{dens} nearest neighbour, and the density is estimated by kernel interpolation over these neighbours. In the resulting density field, locally overdense regions which are enclosed by isodensity contours that traverse a saddle point are taken as substructure candidates. In practice: the algorithm reconstructs the density field by sorting particles in order of decreasing density. It gradually lowers a global threshold in the density field sampled by the distribution of particles. Isolated overdense regions grow slowly in size during this process. When two of them coalesce to form a single region, their density contours join at a saddle point. Each time such an event occurs, the algorithm finds two

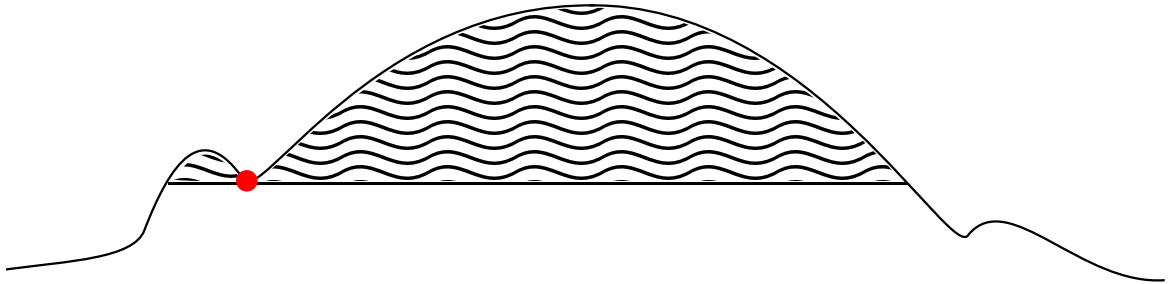


Figure 3.1: Schematic representation (2-dimensional) of the density field within a FOF group. SUBFIND identifies a maximum and then lowers the density threshold until it finds a saddle point (red point). When this happens, it identifies two substructures, that are represented by the shaded regions. The largest one corresponds to the 'main halo', i.e. the bound part of the FOF.

substructure candidates (see the schematic representation shown in Figure 3.1). Since the entire procedure leads to a hierarchy of substructures which are processed from inside out, SUBFIND is also able to find substructures within substructures. To summarize, SUBFIND decomposes a given particle group into a set of disjoint self-bound subhaloes, each identified as a locally overdense region within the density field of the background halo. Those particles not bound to any subhalo that has been considered as a genuine substructure are assigned to the main halo.

3.2.1 Subhalo Finders

Since the first generation of simulations, dated already to more than 30 years ago, the identification of dark matter haloes has been a key element for the analysis of the simulations. For this reason, much effort has been spent during in developing different algorithms able to identify bound structures (and substructures) in simulations (see Figure 3.2). The number of different halo finders developed highlights the importance of such procedure. For a long time the spherical overdensity method (Press & Schechter 1974; Lacey & Cole 1994) and the FOF algorithm remained the standard techniques, but since the early 90's the situation started to change.

The first generation of codes focused mainly on the identification of isolated haloes. Once the problem of the premature disruption of subhaloes in larger haloes has been solved (also known as overmerging problem, Klypin et al. 1999) increasing the resolution of simulations, later codes addressed a new challenge, that of finding both haloes and subhaloes. Despite that, every new code finds its seeds in one of the two halo finders above mentioned, i.e the spherical overdensity method and the friends-of-friends algorithm, since either it links particles in a FOF fashion or it collects particles within spherical shells (Knebe

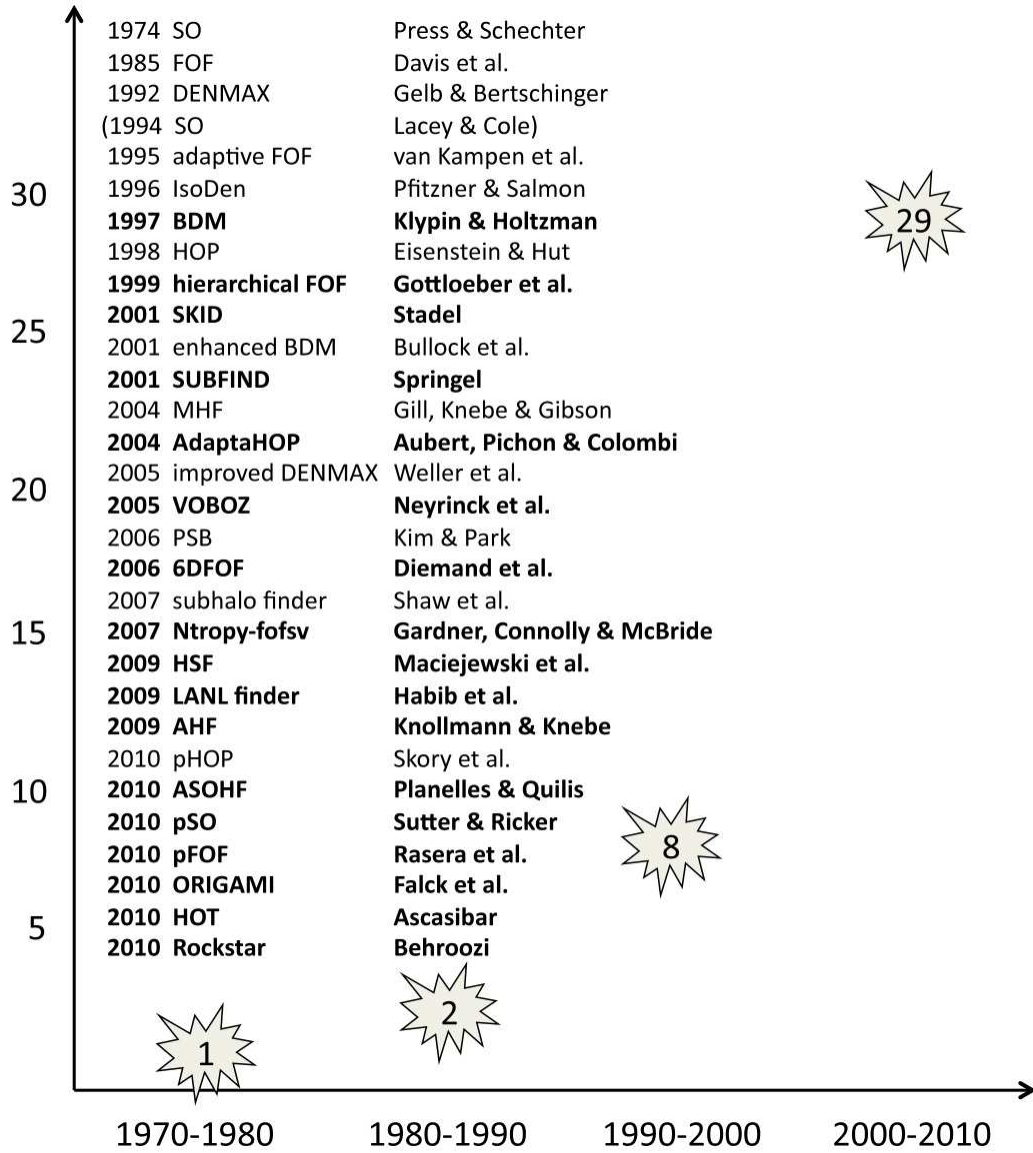


Figure 3.2: Schematic presentation of the (cumulative) number of halo finders as a function of time, binned in ten year intervals since 1970. Figure taken from Knebe et al. (2011).

et al. 2011).

SUBFIND is one of the most used algorithms, but there exist many others. They work in different ways, and each of them has its own advantages and weaknesses. Knebe et al. (2011) presented a detailed comparison of dark matter halo properties recovered by a large set of different halo finders, spanning a wide range of techniques such as the FOF algorithm, the spherical-overdensity method and phase-space based algorithms. They find that the halo finders codes they tested could successfully recover the spatial location of their mock haloes, and comparing them using a high-resolution cosmological volume, they find that the halo finders agree remarkably well on fundamental properties of astrophysical importance (e.g. mass, position, velocity and peak of the rotation curve). Pujol et al. (2013) present a study of the substructure finder dependence of subhalo clustering in the Aquarius Simulation by running 11 different subhalo finders on the haloes of the Aquarius Simulation. They study the differences in the density profile, mass fraction and 2-point correlation function of subhaloes in haloes predicted by the different subhalo finders. They find a good agreement at around 10 per cent level inside the virial radius R_{200} and at intermediate resolutions for subhaloes above a certain threshold (better than 5 per cent when the mass is replaced with the maximum circular velocity).

3.2.2 Merger-Trees

In this Thesis, a merger tree (a schematic representation is shown in Figure 3.3) is constructed by identifying a unique *descendant* for each substructure. For each subhalo, the algorithm finds all haloes that contain all its particles in the following snapshot, and then counts the particles by giving higher weight to those that are more tightly bound to the halo under consideration. The halo that contains the largest (weighted) number of its particles is selected as descendant. Next, all the pointers to the progenitors are constructed. The most massive progenitor at each node of the tree is selected as the *main progenitor*. De Lucia & Blaizot (2007) noted that this can lead to ambiguous selections when, for example, there are two progenitors of similar mass. In order to avoid occasional failures in the merger tree construction algorithm, they modified the definition of the main progenitor by selecting, as main progenitor, the one on the branch that accounts for most of the mass of the final system, for the longest time. I have applied this modification to merger trees used here. As will be more clear in Section 3.4, merger trees are the input for the semi-analytic model I used in this work. They provide the necessary information about dark matter haloes that the model needs in order to generate mock catalogues of galaxies, based on the physics implemented in the code.

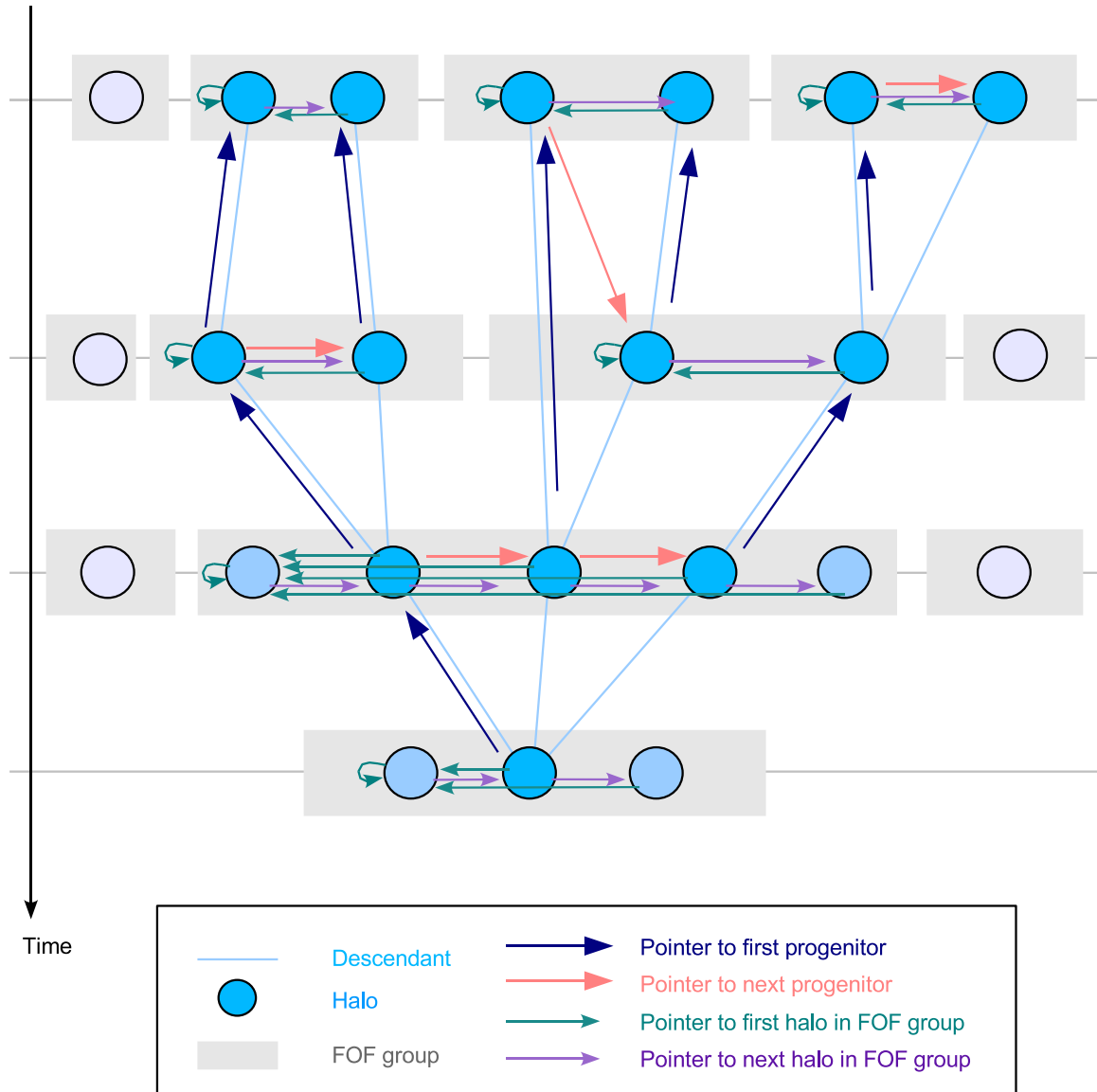


Figure 3.3: Schematic representation of the merger tree structure used in this work. At each output time, FOF groups are identified which contain one or several (sub)halos. The merger tree connects these halos, and each of them knows its descendant and its most massive progenitor. Possible further progenitors can be retrieved by following the chain of next progenitors. In a similar fashion, all halos in a given FOF group are linked together. Figure taken from Springel et al. (2005).

3.3 Halo Occupation Distribution

The halo occupation distribution (hereafter HOD) is a method that allows us to link the observed properties of luminous galaxies to dark matter haloes (Berlind et al. 2003; Lin et al. 2004; Kravtsov et al. 2004a). The evolution and clustering of haloes depend on the background cosmology, while the physics responsible for galaxy formation specifies how galaxies populate dark matter haloes. This formalism describes the bias between galaxies and mass¹ using the probability $P(N|M)$ that a halo with mass M contains a number N of galaxies, and additional prescriptions that specify the relative distribution of galaxies and dark matter within haloes, such as spatial and velocity distributions.

For more details on the HOD modelling, I refer the reader to van den Bosch et al. (2007). The authors highlight the main concepts behind this approach and quote the most important studies that made use of this approach. These have shown that the observed two-point correlation function of galaxies tightly constrains the first and second moments of $P(N|M)$ (see, e.g., Jing et al. 1998 or Collister & Lahav 2005 for a more recent reference), and that these constraints are in good agreement with occupation statistics of dark matter subhaloes (see, e.g. Kravtsov et al. 2004a; van den Bosch et al. 2005). The HOD approach has also been tested on galaxy populations at intermediate and high redshifts (e.g., Bullock et al. 2002; Zheng 2004; Phleps et al. 2006; Lee et al. 2006). Moreover, (Zheng et al. 2005) have shown that cosmology and galaxy bias are not degenerate, that makes possible to use the HOD technique to simultaneously constrain both the galaxy bias and cosmology.

Berlind et al. (2003) compared in details the HOD predicted by semi-analytic models and that of simulations. The modelling of the most important physical processes such as cooling, star formation and feedback between the two approaches were rather different. Nevertheless, these authors found that the HODs predicted by the two approaches are very similar, thus supporting the idea that galaxy clustering is mainly driven by gravitational dynamics rather than by the physics of baryons. Studies of the HOD predicted by dark matter only simulations and comparisons with that of galaxies, observationally constrained, can then be important in order to understand what is the relative contribution of gravity in galaxy clustering (see also Kravtsov et al. 2004a).

The HOD method is conceptually very simple and easy to implement. It remains, however, difficult to move from a purely statistical characterization of the link between dark matter haloes and galaxies to a more physical understanding of the galaxy formation process itself.

Another commonly used approach for connecting dark matter halos to galaxies is the subhalo abundance matching technique (Vale & Ostriker 2006; Conroy et al. 2007; Behroozi et al. 2010; Moster et al. 2010). The fundamental assumption is that of a monotonic mapping

¹There is not a perfect connection between the galaxy field and the overall matter distribution. Different types of galaxies have different clustering properties due to baryonic physics and environmental effects (Marín et al. 2013 and references therein).

between a given galaxy property (typically luminosity or stellar mass) and a given property of halos (such as mass or circular velocity). One pro of these methods is that they are easy to use, because they require very few assumptions and avoid the explicit modelling of the physics of galaxy formation. Unfortunately, this entails to lose a large amount of information, that is, indeed, the main handicap of the modelling.

Haloes that enter denser system and become subhaloes are subjected to tidal interactions with the potential of the host halo. Several authors have then argued that properties of satellite galaxies should be better correlated with the properties of subhalos at the time of their accretion onto a more massive halo rather than their present day properties (Gao et al. 2004a; Vale & Ostriker 2006; Conroy et al. 2006). Taking advantage of the subhalo abundance matching technique, Conroy et al. (2006) match the observed luminosity dependence of galaxy clustering at a wide range of epochs, ranging from $z = 0$ to $z = 5$. Guo et al. (2010), instead, reproduce the observationally inferred relation between stellar mass and halo virial mass, while Trujillo-Gomez et al. (2011) use this technique to match the observed relations between stellar mass and circular velocity and between luminosity and circular velocity, and to match the estimated galaxy velocity function (see Simha et al. (2012) for further details).

3.4 A Semi-Analytic Model of Galaxy Formation

Semi-analytic models (SAMs) are theoretical tools that can be used to predict a large number of galaxy properties. The semi-analytic approach consists in modelling galaxy formation on the basis of our knowledge of the physics involved, and compare model predictions with the observed properties of galaxies.

Originally, SAMs made use of a Monte-Carlo approach ² for sampling the distribution of progenitor masses predicted by the extended Press-Schechter theory (Bond et al. 1991; Lacey & Cole 1993) and connect dark matter haloes with galaxies. Modern semi-analytic models use all the information stored in the merger-trees of numerical simulations to construct galaxies within dark matter haloes and let them evolve in time. They contain realistic prescriptions for the most important mechanisms taking place during galaxy formation, such as cooling, star formation and feedback. Owing to our rather poor knowledge of these processes, and especially their mutual interplays, semi-analytics include a number of free parameters that are usually tuned to match some important features of the galaxy population, such as the luminosity function or some well known relations among two observables. The parametrizations adopted to describe a process are usually motivated by results from simulations or observations.

²Monte Carlo methods are a wide class of computational algorithms that are based on repeated random sampling to obtain numerical results, i.e. by running simulations many times in order to compute probabilities heuristically.

SAMs offer the opportunity to test prescriptions used to model physical processes rapidly, since they require negligible computational time with respect to other tools such as numerical simulations. They also allow one or more processes to be switched on or off to test their efficiency in the formation/evolution of galaxies. They also have some disadvantages. Our lack of understanding of the physics behind galaxy formation translates in the use of free parameters that, as explained above, are tuned on the basis of observational data, but always physically motivated. In addition, this approach does not include an explicit treatment of the gas dynamics.

In this work I use a semi-analytic model that is based on a modified version of that used in Springel et al. (2005); Croton et al. (2006) and De Lucia et al. (2006), that finds its seeds in Kauffmann & Haehnelt (2000); Springel et al. (2001a) and De Lucia et al. (2004b) and works on the merger-trees described in Section 3.2.2. As other SAMs, it follows the two-stage theory of White & Rees (1978) and assumes that galaxies form within dark matter haloes implementing our current knowledge of the most important physical processes of galaxy formation. The general picture (see Figure 3.4) sees the hot gas surrounding a halo that cools and condenses at the centre of the halo. This gas is then able to form stars that are assumed to form in a disk, according to a simplified version of the empirical Kennicutt relation (Kennicutt 1998) between the star formation rate and the gas density. Stars can eventually explode as Supernovae and reheat the gas bringing it back again to the hot phase, a process usually referred to as Supernova feedback. The other important feedback is driven by Active Galactic Nuclei (AGN). The hot gas is accreted onto the supermassive central black hole and this process liberates an amount of energy that is proportional to the mass growth rate of the black hole. This energy is believed to be able to partially offset cooling in high mass haloes. Once a galaxy is formed, it grows in stellar mass by forming stars, but also via galaxy mergers, that are another important process in the model, fundamental for the evolution of galaxies in a hierarchical picture. In this model, three different types of galaxies are considered:

- Type 0: these are central galaxies, defined as those located at the centre of the main halo³ of each FOF group;
- Type 1: these are satellite galaxies associated with a distinct dark matter substructure. A Type 0 galaxy becomes Type 1 once its parent halo is accreted onto a more massive system;
- Type 2: also called *orphan* galaxies, these are satellites whose parent substructures have been stripped below the resolution limit of the simulation. Our reference model assumes that, when this happens, the baryonic component is unaffected and the corresponding galaxy survives for a residual time before merging with the correspond-

³This is the most massive subhalo of a FOF, and typically contains about 90 per cent of its total mass (see Section 4.3.1).

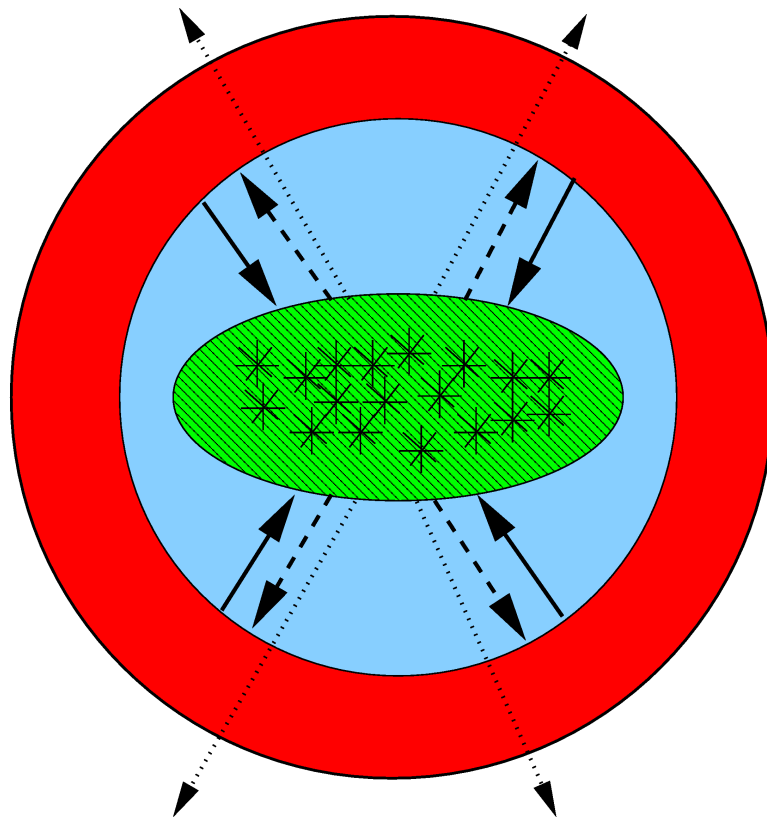


Figure 3.4: A schematic representation that shows the gas cooling from the hot halo (solid lines) and building up the reservoir of cold gas in the galactic disk. Some cooled gas can be reheated by Supernovae explosions and return back to the hot phase (dashed lines). The Supernovae feedback can also be so strong to eject material outside the halo. Figure taken from Baugh (2006).

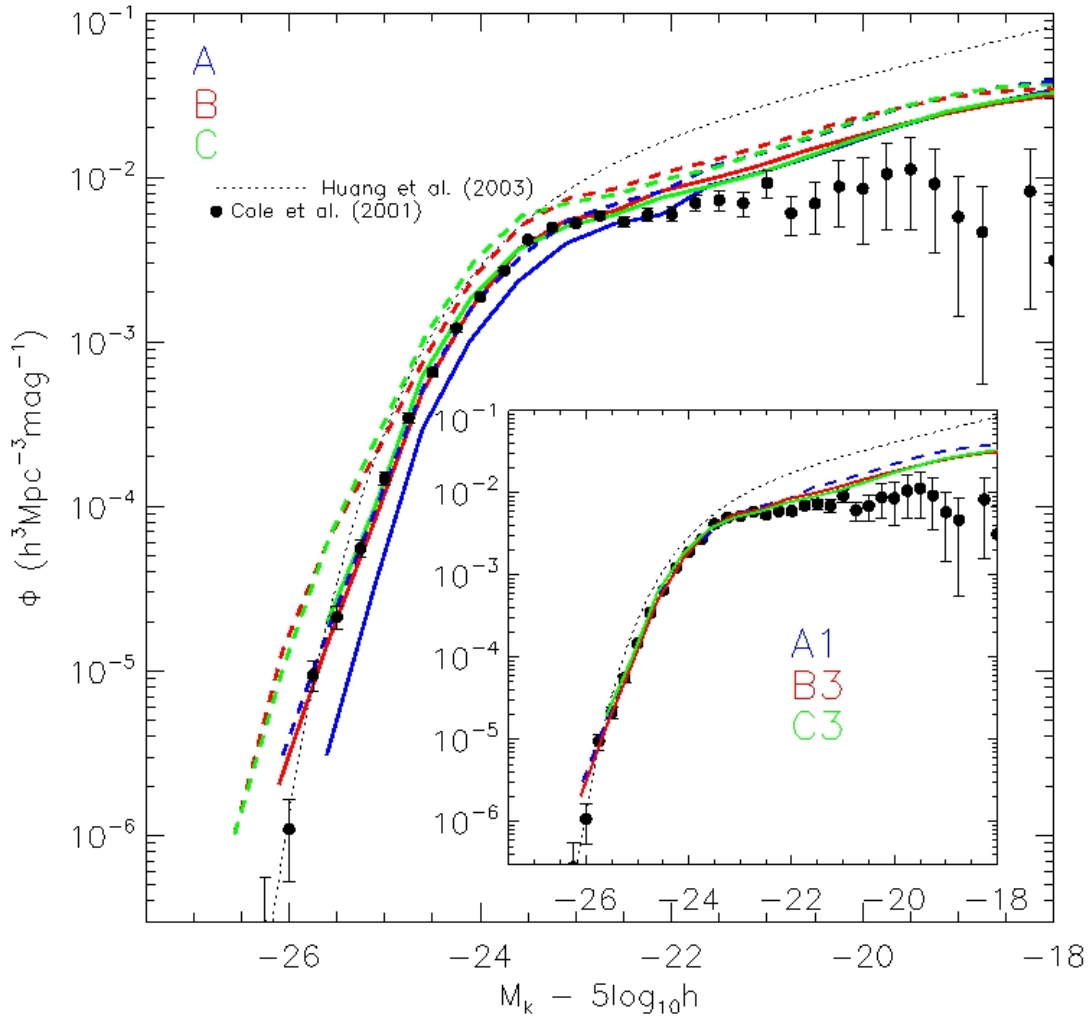


Figure 3.5: K-band luminosity function as predicted by the model with different cosmologies (WMAP1 simulation (dashed lines), derived from a combination of first-year WMAP results (Spergel et al. 2003) with the 2dFGRS galaxy power spectrum (Colless et al. 2001), and WMAP3 simulation (solid lines), that adopts cosmological parameters derived from a combination of third-year WMAP data on large scale, and Cosmic BackgroundImager (CBI) and extended Very Small Array (VSA) data on small scale) and/or values of the set of free-parameters of the model (colour lines), compared with the observed luminosity function by Cole et al. (2001) (black points). At faint magnitudes the model tends to predict higher number of galaxies than observed. Figure taken from Wang et al. (2008).

ing central galaxy. The position of an orphan galaxy is traced by following the position of the particle that was the most bound particle of the parent substructure at the last time it was identified.

This semi-analytic model has been largely improved during the last years. Despite several modifications and additional prescriptions, the model has some unsatisfactory features. The most important is the overprediction of the faint end of the luminosity function, which translates in an excess of faint and red galaxies in clusters with respect to observations (e.g., Weinmann et al. 2011). Many attempts have been made in the past to fix these problems (Font et al. 2008; Weinmann et al. 2010; Guo et al. 2011). A strong supernovae feedback has been proposed in order to suppress the large excess of faint galaxies (see, e.g., Guo et al. 2010). This feedback is supposed to heat up cold gas and remove it from the galactic disk. This reduces the efficiency of star formation in low mass haloes which, as a consequence, flattens the slope of the faint end of the luminosity function (see Figure 3.5). Nevertheless, it seems that even a strong supernovae feedback, already taken to be unrealistically high, is not enough for reproducing the correct slope (see Liu et al. 2010) and some other mechanisms or processes must be invoked. However, Guo et al. (2010), who updated the model of De Lucia & Blaizot (2007) by introducing revised treatments of the transition between the rapid infall and cooling flow regimes of gas accretion (see Section 3.4.2), a more sophisticated modelling of bulge and disk sizes, superovae feedback and gas/star stripping of satellite galaxies, show a good match of the observed luminosity function at redshift $z = 0$, in different bands.

The excess of faint and red galaxies (shown in Figure 3.6) highlights the simplistic treatment of satellite galaxies. Once a galaxy enters the densest cluster regions, many secondary mechanisms act on it, e.g. strangulation and ram-pressure stripping. As discussed in Section 2.4, strangulation stands for the removal of hot gas halo associated with the infalling galaxy. Cooling is suppressed because there is no more gas and combined with the strong efficiency of supernova feedback, this leads to a quick decline of star formation. The ram-pressure stripping due to the intra-cluster medium acts on a short time-scale, $\sim 1\text{Gyr}$, and sweeps cold gas from the galactic disk. In this semi-analytic model, the first process is assumed to be instantaneous. As a consequence, galaxies infalling in larger systems consume very rapidly their cold gas and move to the red sequence rapidly. For this reason, the second process has no time to operate and affect significantly galaxy properties. This simplistic picture may not be the correct one and needs to be revised.

A long standing problem for hierarchical models has been to match the zero-point of the Tully-Fisher relation (Tully & Fisher 1977), i.e. the observed correlation between the rotation speed and the luminosity of spiral disks, and reproducing the observed luminosity function at the same time. So far, no model with a realistic calculation of galaxy sizes has been able to match the zero-point of the Tully-Fisher relation using the circular velocity of the disk measured at the half mass radius, and the nature of this difficulty is still unclear.

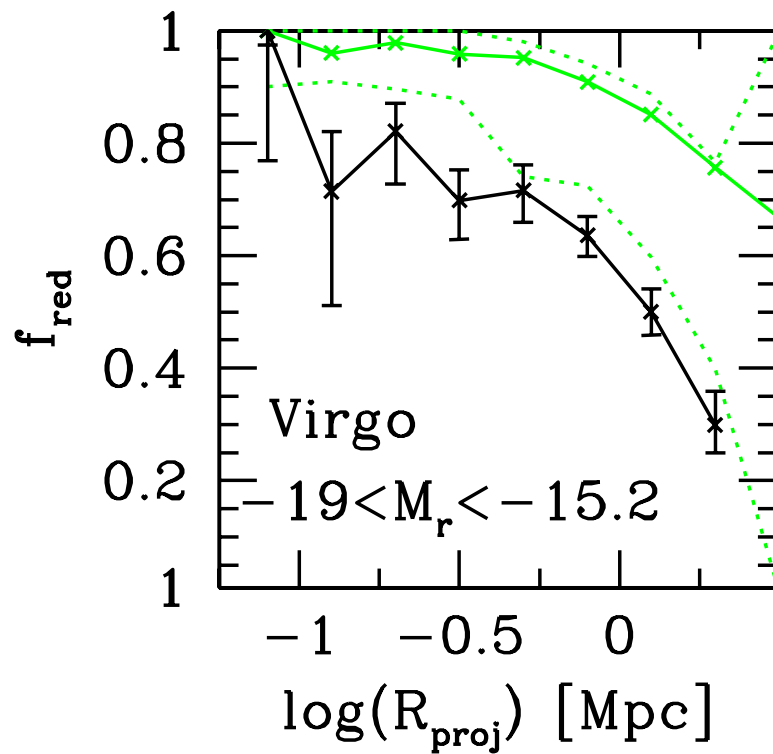


Figure 3.6: Red fraction as a function of projected cluster-centric radius. Observations are shown as black lines with error-bars, results from the model as coloured lines. Dotted lines show the minimum and maximum red fractions for the clusters in the model. Clearly, the model predicts an excess of faint and red galaxies in clusters, irrespective of the distance from the centre. Figure taken from Weinmann et al. (2011).

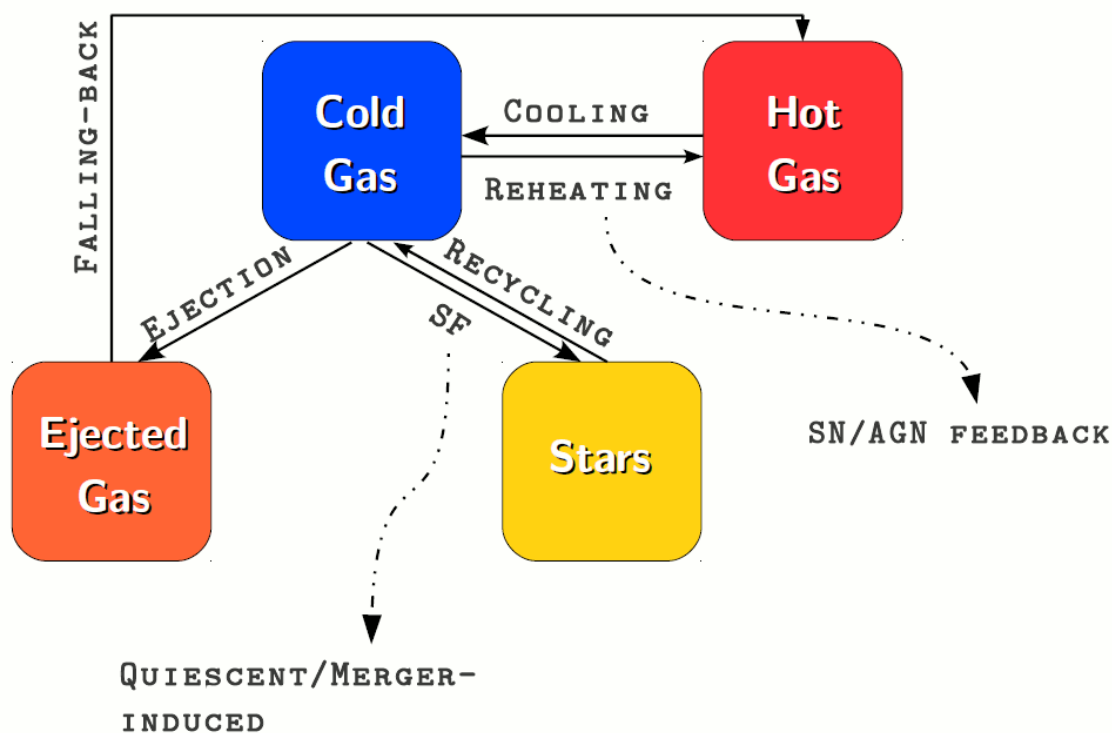


Figure 3.7: A schematic representation of how mass is exchanged between the different phases considered in the model in absence of accretion from outside. Each arrow is accompanied by a name indicating the physical process driving the mass exchange. Metals follow the same routes as the mass. Figure taken from De Lucia et al. (2004b).

For further details of the open problems in semi-analytics, I refer the reader to the review by De Lucia (2009).

In the following, I will describe the most important physical prescriptions implemented in the model of De Lucia & Blaizot (2007), that will be hereafter used as “the reference model”. The schematic representation of the exchange of mass between the different phases shown in Figure 3.7 may help the reader to follow the description of these prescriptions. Modifications of the reference model will be described in Chapter 5.

3.4.1 Reionization

Between redshift 20 and 6 the Universe experienced another phase of ionization (the second after recombination). This second phase occurred right after the formation of the first objects in the early Universe that were able to ionize the neutral hydrogen thanks to their UV radiation. Recent observations show that the Universe reionized at $z_{reion} > 5.5$ (McGreer et al. 2011). In the past, several studies of the Ly_α forest of high-redshift quasar (e.g. Fan

et al. 2006) have confined the redshift interval for the reionization of HI between $z \sim 6$ and $z \sim 12$, and during this epoch, HI and HeI ionizing photons were likely provided by the abundant Population II stars associated to the first stages of galaxy formation (Compostella et al. 2013, and references therein).

The baryon fraction in galaxy clusters is found to be mostly in the form of hot gas and close to 0.17. The observed baryon fraction in small haloes, like those of dwarf galaxies, is smaller than the one detected in larger haloes. The photoionization heating of the intergalactic medium due to this UV background has been invoked as the process able to lower the efficiency of galaxy formation in small haloes, preventing the gas to condense within dark matter haloes if the thermal energy exceeds the halo potential well depth (Doroshkevich et al. 1967; Couchman & Rees 1986; Efstathiou 1992).

The model adopted in this work uses a fitting function proposed by Gnedin (2000), who showed that the effect of photoionization heating on the gas content of a halo can be described by the following relation:

$$f_b(z, M_{vir}) = \frac{f_b^{cosm}}{(1 + 0.26M_f(z) / M_{vir})^3}, \quad (3.4)$$

where $f_b^{cosm} = 0.17$ is the universal baryon fraction (WMAP, Spergel et al. 2003). $M_f(z)$ is the characteristic halo mass used as filter that is a function of redshift and changes mostly around the epoch of reionization, and M_{vir} the mass of the halo. The filtering mass, below which the gas fraction f_b is reduced relative to the universal value, is set to $4 \cdot 10^9 M_\odot$ at the reionization epoch and reaches $3 \cdot 10^{10} M_\odot$ at the present-day. The model adopts the analytic expressions presented in Kravtsov et al. (2004b) to derive $M_f(z)$. It is worth noting that, according to the results of cosmological hydrodynamical simulations (Okamoto et al. 2008), the filtering mass should be significantly lower than that quoted above.

3.4.2 Cooling

The cooling of gas is one of the most important processes in galaxy formation. The hot gas cools and condenses at the centre of dark matter haloes, providing the reservoir of cold gas that is then available for star formation. In massive haloes the gas is completely ionized and bremsstrahlung emission from free electrons is the main responsible for cooling. In haloes with virial temperature in the range $10^4 K < T_{vir} < 10^6 K$ electron-ion recombinations and collisions among atoms can play a role. It is worth noting also that, independently of the mass of haloes, the cooling rate depends strongly on the metallicity of the gas.

Cooling in this semi-analytic model is treated as in Springel et al. (2001a). The hot gas within an halo is assumed to be distributed as an isothermal sphere with density $\rho_{hot}(r)$ and the cooling time at each radius is given by

$$t_{cool} = \frac{3\mu m_H \kappa_b T_{vir}}{2\rho_{hot}(r)\Lambda(T, Z)}, \quad (3.5)$$

i.e. the ratio between the specific thermal energy of the gas and the cooling rate per unit volume. In the definition of the cooling time μm_H is the mean particle mass, κ_b is the Boltzmann's constant, and $\Lambda(T, Z)$ is the cooling function. The cooling function depends on Z , that is the metallicity of the hot halo gas and $T = 35.9(V_{vir}/kms^{-1})^2$ its temperature, assumed to be the virial temperature of the host halo. These dependences are modelled using the collisional ionization cooling curves of Sutherland & Dopita (1993). The gas temperature is updated according to the current circular velocity of the main haloes. The cooling radius is then calculated by means of the following relation:

$$r_{cool} = \left[\frac{t_{dyn} M_{hot} \Lambda(T, Z)}{6\pi \mu m_H \kappa T_{vir} R_{vir}} \right]^{\frac{1}{2}}, \quad (3.6)$$

with $t_{dyn} = R_{vir}/V_{vir}$ the halo dynamical time, R_{vir} the virial radius of the halo, and M_{hot} the hot halo gas mass available to cool. Cooling is assumed to behave differently depending on how the cooling radius compares to the halo virial radius. In the case the cooling radius is smaller than the virial radius, also called "hot phase regime", the gas is assumed to cool quasi-statically and the cooling rate is given by

$$\dot{M}_{cool} = M_{hot} \frac{r_{cool}}{R_{vir} t_{dyn}}. \quad (3.7)$$

In case the cooling radius is instead larger than the virial radius, cooling is assumed to happen instantaneously and all the available hot gas falls onto the central object. Cooling is rapid at early times and in low mass haloes. The accretion is very close to the central object which accretes gas at the free-fall rate. At late times and for massive haloes the picture changes. The infalling gas forms a hot atmosphere from which the gas condenses onto the galaxy through cooling flows.

3.4.3 Star Formation

After cooling, the gas can collapse due to its own gravity. This brings to an increasing of the density and the temperature of the gas which may fragment in many smaller clouds that can eventually form stars. Star formation is still a poorly understood process. We know that it occurs in giant molecular clouds, but only a small fraction of them ends up forming stars (Mo et al. 2010, and references therein). At galactic scale, one way to study star formation is through the well known relation between the star formation rate and the surface density of the gas, also known as Kennicutt-Schmidt law (Schmidt 1959; Kennicutt 1998). Many observational studies in spiral galaxies have shown it to be a good description of the global star formation rates. Semi-analytic models and numerical simulations usually start from the Kennicutt-Schmidt law to model star formation.

The reference model assumes that all star formation occurs in cold disk gas, either quiescently or in a merger induced burst. Based on Kennicutt (1998), the model adopts

a threshold surface density for the cold gas below which no star formation occurs. As suggested by Kauffmann (1996), this critical surface density at a distance R from the galaxy centre can be approximated by

$$\Sigma(R) = 12 \cdot \left(\frac{V_{vir}}{200 \text{ Km/s}} \right) \left(\frac{R}{10 \text{ Kpc}} \right)^{-1} M_{\odot} \text{pc}^{-2}, \quad (3.8)$$

that can be converted in a "critical mass" by assuming the cold gas mass to be distributed over the disk. The integration leads to this critical cold gas mass:

$$M_{crit} = 3.8 \cdot 10^9 \left(\frac{V_{vir}}{200 \text{ Km/s}} \right) \left(\frac{r_{disk}}{10 \text{ Kpc}} \right) M_{\odot}. \quad (3.9)$$

r_{disk} is obtained by following the model of Mo et al. (1998) who assume that the specific angular momentum of the disk is equal to the one of the dark halo in which the disk is embedded. Based on the properties of our Galaxy (see van den Bergh 2000), the radius of the star forming region r_{disk} is taken to be three times the disk scale radius. If the mass in cold gas is larger than the above threshold, the model assumes the star formation rate to be

$$\dot{M}_{star} = \alpha_{SF} \frac{M_{cold} - M_{crit}}{t_{dyn,disk}}, \quad (3.10)$$

where α_{SF} is the star formation efficiency set to 0.03, and $t_{dyn,disk} = r_{disk}/V_{vir}$ is the disk dynamical time.

3.4.4 Supernova Feedback

Supernova feedback plays an important role in shaping the faint-end of the luminosity function. Massive stars die rapidly as supernovae and these events bring a copious amount of radiative and mechanical energy to the surrounding medium (Croton et al. 2006; Monaco et al. 2007; Lagos et al. 2013). This leads to heat up and ionize the gas in the interstellar medium that can affect the evolution of galaxies, especially low-mass galaxies.

The model assumes that the amount of cold gas reheated up and injected into the hot phase is

$$\Delta M_{reheat} = \epsilon_{disk} \Delta M_{star} \quad (3.11)$$

where ΔM_{star} is the mass of newly formed stars and ϵ_{disk} is a parameter set to 3.5 based on observational data (Martin 1999). The energy released and injected by massive stars into the cold gas in the disk is approximated by

$$\Delta E_{SN} = \frac{1}{2} \cdot \epsilon_{halo} \Delta M_{star} V_{SN}^2, \quad (3.12)$$

where $0.5V_{SN}^2$ is the mean energy in supernova ejecta per unit mass of stars formed and ϵ_{halo} , set to 0.35, is the parameter that regulates the efficiency of this energy in reheating

the gas. Based on the standard supernova theory, $V_{SN} = 630 \text{ km/s}$. Part of the gas in the hot phase can be moved in an external reservoir due to the excess of energy present in the hot halo after reheating. The efficiency of this process depends on the potential well of the dark halo:

$$\Delta M_{eject} = \left(\epsilon_{halo} \frac{V_{SN}^2}{V_{vir}^2} - \epsilon_{disk} \right) \Delta M_{star}. \quad (3.13)$$

The model assumes also that part of the gas in the ejected phase is re-incorporated in the cooling cycle per halo dynamical time according to

$$\Delta M_{eject} = -\gamma \frac{M_{eject}}{t_{dyn}} \quad (3.14)$$

with $\gamma = 0.5$ in the reference model.

3.4.5 AGN Feedback

It is well known that the galactic centres are populated by supermassive black holes and there is evidence that these active galactic nuclei (AGN) are important for galaxy formation (Shao et al. 2013 for a recent reference). In particular, they are believed to partially offset cooling in high mass haloes. In this model, a distinction is made between "quasar" and "radio" mode.

Quasar Mode

The quasar mode controls the black growth during mergers. The new black hole mass is given by the sum of the progenitor masses plus an amount of cold gas mass. The latter is proportional to the total cold gas mass present in the merging system, with an efficiency that depends on the mass ratio of the system. Then, the central black hole of the remnant grows as follows:

$$\Delta M_{BH} = M_{BH,min} + f_{BH} \left(\frac{M_{min}}{M_{maj}} \right) \left(\frac{M_{cold}}{1 + (280 \text{ km/s}/V_{vir})^2} \right) \quad (3.15)$$

where $M_{BH,min}$ is the black hole mass of the smallest progenitor, f_{BH} a free parameter set to 0.03 in order to reproduce the observed local $M_{BH} - M_{bulge}$ relation (see Croton et al. 2006 and references therein), M_{min} and M_{maj} are the total masses (cold gas plus stellar) of the minor and major progenitors, and M_{cold} is the total cold gas mass of the system. It is worth noting that the feedback due to this mode is not explicitly implemented in the model used in this work. This mode always coincides with a starburst in the merging galaxies, and any feedback from accretion onto the black holes is thought to be part of the substantial energy input which this starburst is assumed to produce. Moreover, feedback from this channel can be also associated with feedback of supernovae due to the enhanced star formation.

Radio Mode

Radio mode feedback describes the accretion of hot gas onto the central black hole, that attracts the surrounding gas by its gravitational force and liberates gravitational energy as radiation. When gas accretes toward a black hole, the centrifugal force acting upon the gas will increase in importance relative to the gravitational force. The gas is then expected to settle into a rotating disk, known as *accretion disk*. In the model used here, the growing rate is regulated by the following relation (Croton et al. 2006):

$$\dot{M}_{BH,radio} = \kappa_{AGN} \left(\frac{M_{BH}}{10^8 M_{\odot}} \right) \left(\frac{f_{hot}}{0.1} \right) \left(\frac{V_{vir}}{200 \text{ km/s}} \right)^3 M_{\odot}/\text{yr}, \quad (3.16)$$

where κ_{AGN} is a free-parameter equal to $7.5 \cdot 10^{-6}$ that sets the efficiency of the accretion and f_{hot} the ratio between the hot gas and dark matter masses. The model assumes that this hot mode releases energy in jets that is then deposited in the hot gas and that can reduce or also stop cooling flows. The rate of mechanical energy generated by the accretion is given by

$$\dot{E}_{radio} = \eta \dot{M}_{BH} c^2, \quad (3.17)$$

where c is the speed of light and η the efficiency, usually taken the order of 10 per cent. As said above, the injection of this energy partially compensates gas cooling, giving a net mass cooling rate

$$\dot{M}_{cool,new} = \dot{M}_{cool} - 2 \frac{\dot{E}_{radio}}{V_{vir}^2} \quad (3.18)$$

that is never allowed to fall below zero.

3.4.6 Galaxy Mergers

Mergers are important in galaxy formation since they affect galaxy morphology and star formation history. They can occur between a central and satellite galaxies or, less frequently, between two satellites. The model follows each galaxy until the mass of its subhalo falls below the resolution of the simulation. Later on, a satellite is traced by means of the most bound particle of its subhalo at the last time it has been identified. At the same time, the model estimates a merging time for the satellite using the dynamical friction formula of Binney & Tremaine (2008):

$$\tau_{merge} = f_{fudge} \frac{1.17 D^2 M_{par}}{\ln \Lambda R_{vir}^2 M_{sat}} \tau_{dyn} \quad (3.19)$$

where D is the distance between the satellite and the centre of its parent FOF, R_{vir} is the virial radius of the parent halo, M_{sat} the sum of the dark and baryonic mass of the satellite, M_{par} the (dark matter) mass of the accreting halo, $\tau_{dyn} = R_{vir}/V_{vir}$ is the dynamical time of the parent halo, and $\Lambda = 1 + M_{par}/M_{sat}$ is the Coulomb logarithm. As in the reference

model, I assume $f_{fudge} = 2$, which is in better agreement with recent numerical work indicating that the classical dynamical friction formulation tends to under-estimate the merging times measured from simulations (Boylan-Kolchin et al., 2008; Jiang et al., 2008).

Mergers induce a starburst that is implemented in the model following the prescription of Somerville et al. (2001). During the merger, a fraction e_{burst} of the total cold gas in the system is converted into stars, and this fraction is estimated by

$$e_{burst} = 0.56 \left(\frac{M_{min}}{M_{maj}} \right)^{0.7} \quad (3.20)$$

where M_{min} and M_{maj} are the sum of the cold gas and stellar masses of the minor and major progenitors, respectively.

3.4.7 Metal Enrichment

The model adopts an “instantaneous recycling approximation” for chemical enrichment. In particular, it assumes that a constant yield of heavy elements (taken to be 0.03) is produced per solar mass of gas converted into stars, and that all metals are instantaneously returned to the cold phase. Metals are then exchanged between the different phases proportionally to the mass flows among these phases, and assumed to be fully mixed with the pre-existing material.

3.4.8 Stellar Population Synthesis

In the reference model, photometric properties are computed employing the stellar population synthesis model from Bruzual & Charlot (2003) and adopting the initial mass function (IMF) from Chabrier (2003). This has fewer low-mass stars than a Salpeter IMF (Salpeter 1955), and provides a better description of the observational data in our Galaxy and in nearby early-type galaxies (Cappellari et al. 2006). For consistency with the use of a Chabrier IMF, the model adopts an instantaneous recycled fraction $R = 0.43$, which means that 43 per cent of the newly formed stars comes back to the cold phase immediately after star formation.

3.5 Hydrodynamical Simulations

Hydrodynamical simulations describe the physical processes that take place in galaxy formation by following the dynamics of gas explicitly. There are two main techniques for following the dynamics of the gas in a hydrosimulation: Lagrangian schemes (GADGET-3, Springel et al. 2005; Puchwein et al. 2013; GASOLINE, Wadsley et al. 2004; EvoL, Merlin et al. 2010), also known as smoothed particle hydrodynamics techniques (SPH), and grid based Eulerian schemes (ENZO, Bryan & Norman 1997, 1998; RAMSES, Teyssier 2002;

ATHENA, Stone et al. 2008; CASTRO, Almgren et al. 2010; Zhang et al. 2011). The SPH scheme was developed originally by Lucy 1977 and Gingold & Monaghan 1977.

In a cosmological SPH simulation there are two different kinds of particles, of which one traces the dark component and the other traces the baryonic component. Dark matter particles are assumed to be collisionless and follow only the gravity due to the overall distribution of the other particles (see Section 3.1). Gas particles, instead, feel pressure and dissipate energy through cooling. The hydrodynamical equations are written in a Lagrangian formulation, where coordinates are comoving with the fluid element. Grid based codes, instead, use a grid of cells to represent the gas properties, and the hydrodynamical equations are solved by computing the fluxes of mass, momentum and energy across the grid cell boundaries.

Due to its Lagrangian nature, that allows the SPH method to automatically adjust its resolution to the clumping of matter (Springel 2010b), it can reach higher resolution than grid schemes. In particular, SPH codes have the advantage to improve the resolution automatically in dense regions, and lower it in voids. They also have some shortcomings if compared with grid based schemes, e.g. the fact that it is not possible to represent an arbitrarily large density gradient with a finite number of particles. To alleviate this problem and offer a better treatment of shock waves, it is necessary to introduce an artificial viscosity (see, e.g., Springel 2010b). To solve this problem in the SPH framework, Price (2008) propose the introduction of an artificial thermal conductivity that minimises dissipation away from discontinuities. Recently, it has been proposed an improvement of the standard SPH scheme called "Godunov Smoothed Particle Hydrodynamics (GSPH)" (Murante et al. 2011) originally proposed by Inutsuka (2002). The method consists in computing the exchange of hydrodynamic forces and momenta between pairs of particles by using a Riemann solver. Since shocks are described as solutions of the Riemann problem, the introduction of an artificial viscosity is no longer needed.

In Eulerian codes, the mass is carried by volume elements. The Eulerian nature is important for modelling fluid discontinuities, but it is also a disadvantage. In fact, since they are not fully Galilean invariant, it is extremely difficult to conserve the angular momentum on a grid-based code, and this makes them less efficient in modelling disk galaxies.

Springel (2010a) proposed an hybrid code called AREPO, i.e. a code that takes advantage of both schemes. This code is based on a moving-mesh defined by using a Voronoi tessellation of the set of discrete points to be evolved. The moving-mesh approach is able to combine the geometric flexibility and Galilean invariance of SPH codes and, at the same time, the high accuracy treatment of shocks, shear waves and fluid instabilities.

A comparison between SPH and grid-based codes gives the possibility to verify if results converge or are numerical artefacts. An attempt in this direction has been recently done by Scannapieco et al. (2012). The authors perform 13 different gas-dynamical simulations of the formation of a galaxy in a Λ CDM halo with mass very similar to that of our galaxy, using different techniques. They find that, despite the large spread in properties

shown by the simulated galaxies, none of them has properties fully consistent with observational constraints in terms of mass, size, gas content, and morphology. Their results suggest that some differences can be due to the different numerical techniques adopted (e.g., more gas seems able to cool and become available for star formation in grid-based codes than in SPH), but others depend on the description of processes happening on small scales, such as star formation, supernovae and AGN feedback. These processes, which are rather poorly understood, take place on scales well below the spatial resolution of the simulations, and are generally referred to as sub-grid physics. The physics that operates below these scales is described in the simulations by means of prescriptions very similar to those used in semi-analytics. Current hydrodynamical simulations follow well the gravity and they are efficient in following the gas dynamics. The real challenge for the next future is to improve the description of the physics below the sub-grid scale.

Chapter 4

Statistics of Substructures in Cold Dark Matter Haloes

In the framework of modern theories of galaxy formation, dark matter substructures can be considered as the birth-sites of luminous galaxies. Therefore, the analysis of subhaloes, and in particular of their mass and spatial distributions, merger and mass accretion histories, provides important information about the expected properties of galaxies in the framework of hierarchical galaxy formation models. In this chapter to study the amount and distribution of dark matter substructures within dark matter haloes, using a large set of high-resolution simulations ranging from group size to cluster size haloes, and carried out within a cosmological model consistent with WMAP 7-year data. In particular, we study how the measured properties of subhaloes vary as a function of the parent halo mass, the physical properties of the parent halo, and redshift. We find that the fraction of halo mass in substructures increases with increasing mass, being of the order of 5 per cent for haloes with $M_{200} \sim 10^{13} M_{\odot}$ and of the order of 10 per cent for haloes with $M_{200} \sim 10^{15} M_{\odot}$. However, there is a very large halo-to-halo scatter that can be explained only in part by a range of halo physical properties, e.g. concentration. Most of the substructure mass is located at the outskirts of the parent haloes, in relatively few massive subhaloes, and this mass segregation is stronger at increasing redshift. We also find that haloes accreted on to larger structures lose a significant amount of mass due to tidal stripping. Haloes that are more massive at the time of accretion (these should host more luminous galaxies) are brought closer to the centre on shorter time-scales by dynamical friction, and therefore suffer a more significant stripping.

4.1 Introduction

In the currently accepted Λ CDM paradigm for cosmic structure formation, small dark matter haloes form first while more massive haloes form later through accretion of diffuse

matter and mergers between smaller systems. During the last decades, we have witnessed a rapid development of numerical algorithms and a significant increase in numerical resolution, that have allowed us to improve our knowledge of the formation and evolution of dark matter structures. In particular, the increase in numerical resolution has allowed us to overcome the so-called *overmerging problem*, i.e. the rapid disruption of galaxy-size substructures in groups and clusters (Klypin et al., 1999, and references therein). If any, we are now facing the opposite problem, at least on galaxy scales, where many more substructures than visible dwarf galaxies are found (Ishiyama et al., 2009; Tikhonov & Klypin, 2009, and references therein).

According to the two stage theory proposed by White & Rees (1978), the physical properties of galaxies are determined by cooling and condensation of gas within the potential wells of dark matter haloes. Therefore, substructures represent the birth-sites of luminous galaxies, and the analysis of their mass and spatial distribution, as well as of their merger and mass accretion histories provide important information about the expected properties of galaxies in the framework of hierarchical galaxy formation models.

Nowadays, a wealth of substructures are routinely identified in dissipationless simulations, and their statistical properties and evolution have been studied in detail in the past years. The identification of dark matter substructures, or *subhaloes*, remains a difficult technical task that can be achieved using different algorithms (see e.g. Knebe et al., 2011). Each of these has its own advantages and weaknesses, and different criteria for defining the boundaries and membership of substructures are likely leading to systematic differences between the physical properties of subhaloes identified through different algorithms. However, these might be probably corrected using simple scaling factors, as suggested by the fact that different studies find very similar slopes for the subhalo mass function, i.e. the distribution of substructures as a function of their mass. This is one of the most accurately studied properties of dark matter substructures, although it remains unclear if and how it depends on the parent halo mass. Moore et al. (1999) used one high-resolution simulation of a cluster-size halo and one high-resolution simulation of a galaxy-size halo, and found that the latter can be viewed as a scaled version of the former. Later work by De Lucia et al. (2004a) used larger samples of simulated haloes, and found no clear variation of the subhalo mass function as a function of the parent halo mass. Such a dependency was later found by Gao et al. (2004b) and Gao et al. (2011), who showed that the subhalo mass function varies systematically as a function of halo mass and halo physical properties like concentration and formation time.

Typically, only about 10 per cent of the total mass of a dark matter halo is found in substructures. In addition, their spatial distribution is found to be *anti-biased* with respect to that of dark matter (Ghigna et al., 2000; De Lucia et al., 2004a; Nagai & Kravtsov, 2005; Saro et al., 2010). It is unclear if the radial distribution of substructures depends on the parent halo mass. De Lucia et al. (2004a) found hints for a steeper radial number density profiles of substructures in low mass haloes than in high mass haloes. They used, however,

a relatively small sample of simulated haloes, that were run with different codes and numerical parameters. In this chapter, we will re-address this issue by using a much larger sample of simulated haloes, all run with the same code and numerical parameters.

Most previous work focusing on dark matter substructures has studied their properties as a function of their *present day* mass. This quantity cannot be, however, simply related to the luminosity of the galaxies residing in the substructures under consideration. Indeed, dark matter substructures are very fragile systems that are strongly affected by tidal stripping (De Lucia et al., 2004a; Gao et al., 2004b). Since this process affects primarily the outer regions of subhaloes, and galaxies reside in their inner regions, it is to be expected that the galaxy luminosity/stellar mass is more strongly related to the mass of the substructure at the time of *infall* (i.e. before becoming a substructure) than at present (Gao et al., 2004a; Wang et al., 2006; Vale & Ostriker, 2006). Here, we will study the evolution of dark matter substructures splitting our samples according to different values of the mass at infall.

In this chapter, we take advantage of a large set of N-body simulations covering a wide dynamical range in halo mass, and with relatively high-resolution. This will allow us to study how the statistical properties of substructures vary as a function of halo mass, cosmic epoch, and physical properties of the parent halo. The layout of the chapter is as follows: in section 4.2, we introduce the simulation samples used in our study. In section 4.3, we study how the subhalo mass function and subhalo spatial distribution vary as a function of halo mass, redshift and concentration. In the second part (section 4.4), we discuss the mass accretion and merging histories of subhaloes as a function of their mass, accretion time, and environment. Finally, in Section 4.5, we discuss our findings and give our conclusions.

4.2 Cluster simulations

Our set of DM haloes is based on ‘zoom-in’ simulations of 27 Lagrangian regions extracted around massive dark matter haloes, originally identified within a low-resolution N-body cosmological simulation. For a detailed discussion of this simulation set, we refer to Bonafede et al. (2011, see also Fabjan et al. 2011). The parent simulation followed 1024^3 DM particles within of a box of $1 h^{-1}\text{Gpc}$ comoving on a side. The adopted cosmological model assumed $\Omega_m = 0.24$ for the matter density parameter, $\Omega_{\text{bar}} = 0.04$ for the contribution of baryons, $H_0 = 72 \text{ km s}^{-1}\text{Mpc}^{-1}$ for the present-day Hubble constant, $n_s = 0.96$ for the primordial spectral index, and $\sigma_8 = 0.8$ for the normalization of the power spectrum. The latter is expressed as the r.m.s. fluctuation level at $z = 0$ within a top-hat sphere of $8 h^{-1}\text{Mpc}$ radius. With this parameters choice, the assumed cosmogony is consistent with constraints derived from seven-year data from the Wilkinson Microwave Anisotropy Probe (WMAP7, Komatsu et al. 2011).

The selected Lagrangian regions were chosen so that 13 of them are centred around the

Table 4.1: Our simulation set has been split in five subsamples, according to the halo mass. In the first column, we give the name of the subsample, while the second column indicates the range of M_{200} values corresponding to each subsample. The third and fourth columns give the number of haloes and mean number of subhaloes (with mass above $2 \cdot 10^9 h^{-1} M_{\odot}$) within the virial radius (R_{200}), respectively.

Name	Mass range	N_{haloes}	\bar{N}_{subs}
S1	$\geq 10^{15} h^{-1} M_{\odot}$	13	2943
S2	$[5-10] \times 10^{14} h^{-1} M_{\odot}$	15	1693
S3	$[1-5] \times 10^{14} h^{-1} M_{\odot}$	25	358
S4	$[5-10] \times 10^{13} h^{-1} M_{\odot}$	29	146
S5	$[1-5] \times 10^{13} h^{-1} M_{\odot}$	259	40

13 most massive clusters found in the cosmological volume, all having virial¹ mass $M_{200} \simeq 10^{15} h^{-1} M_{\odot}$. Additional regions were chosen around clusters in the mass range $M_{200} \simeq (5 - 10) \times 10^{14} h^{-1} M_{\odot}$. Within each Lagrangian region, we increased mass resolution and added the relevant high-frequency modes of the power spectrum, using the Zoomed Initial Condition (ZIC) technique presented by Tormen, Bouchet, & White (1997). Outside the regions of high-resolution, particles of mass increasing with distance are used, so that the computational effort is concentrated on the cluster of interest, while a correct description of the large-scale tidal field is preserved. For the simulations used in this study, the initial conditions have been generated using $m_{DM} = 10^8 h^{-1} M_{\odot}$ for DM particle mass in the high-resolution regions. This mass resolution is a factor 10 better than the value used by Bonafede et al. (2011) and Fabjan et al. (2011) to carry out hydrodynamic simulations for the same set of haloes.

Using an iterative procedure, we have shaped each high-resolution Lagrangian region so that no low-resolution particle ‘contaminates’ the central ‘zoomed in’ halo, out to 5 virial radii of the main cluster at $z = 0$. In our simulations, each high resolution region is sufficiently large to contain more than one interesting massive halo, with no ‘contaminants’, out to at least one virial radius. Our final sample contains 341 haloes with mass larger than $10^{13} h^{-1} M_{\odot}$. We have split this sample into 5 different subsamples, as indicated in Table 4.1, where we list the number of non-contaminated haloes for each sample and the mean number of substructures within R_{200} per halo in each subsample.

Simulations have been carried out using the Tree-PM GADGET-3 code. We adopted a Plummer-equivalent softening length for the computation of the gravitational force in the high-resolution region. This is fixed to $\epsilon = 2.3 h^{-1}$ kpc in physical units at redshift

¹Here we define the virial mass (M_{200}) as the mass contained within the radius R_{200} , that encloses a mean density of 200 times the critical density of the Universe at the redshift of interest.

$z < 2$, and in comoving units at higher redshift. For each simulation, data have been stored at 93 output times between $z \sim 60$ and $z = 0$. Dark matter haloes have been identified using a standard friends-of-friends (FOF) algorithm, with a linking length of 0.16 in units of the mean inter-particle separation in the high-resolution region. The algorithm SUBFIND (see Section 3.2 for a detailed description) has then been used to decompose each FOF group into a set of disjoint substructures. As in previous work, only substructures which retain at least 20 bound particles after a gravitational unbinding procedure are considered to be genuine substructures. Given our numerical resolution, the smallest structure we can resolve has a mass of $M = 2 \times 10^9 h^{-1} M_{\odot}$. To avoid being too close to the resolution limit of the simulations, we will in some cases consider only substructures that contain at least 100 particles, i.e. we will adopt a mass limit of $1 \times 10^{10} h^{-1} M_{\odot}$.

4.3 Amount and distributions of dark matter substructures

In this section we will consider some basic statistics of the dark matter substructures in our sample. In particular, we will address the following questions: what is the mass fraction in substructures? What is their mass and spatial distribution? And how do these properties vary as a function of the halo mass, or as a function of other physical properties of the parent haloes? As discussed above, if subhaloes are to be considered the places where galaxies are located, these statistics provide important information about the statistical properties of cluster galaxy populations expected in hierarchical cosmologies.

4.3.1 Mass Fraction in Subhaloes

Previous work has found that only 5 to 10 per cent of the halo mass is contained in substructures, with most of it actually contained in relatively few massive subhaloes (Ghigna et al., 1998, 2000; Springel et al., 2001b; Stoehr et al., 2003; Gao et al., 2004b; De Lucia et al., 2004a).

Results for our simulation set are shown in Figure 4.1. The top left panel shows the cumulative mass fraction in subhaloes above the mass indicated on the x-axis, for the five samples considered in our study. There is a clear trend for an increasing mass in substructures for more massive haloes. For our most massive sample (S1), about ten per cent of the halo mass is contained in substructures more massive than $2 \times 10^9 h^{-1} M_{\odot}$, and approximately ten per cent of the mass in substructures is contained in the most massive ones. For less massive haloes, the mass fraction in substructures decreases.

Most of the substructures are located outside the central core of dark matter haloes. In particular, the top right panel of Figure 4.1 shows that the substructure mass fraction is

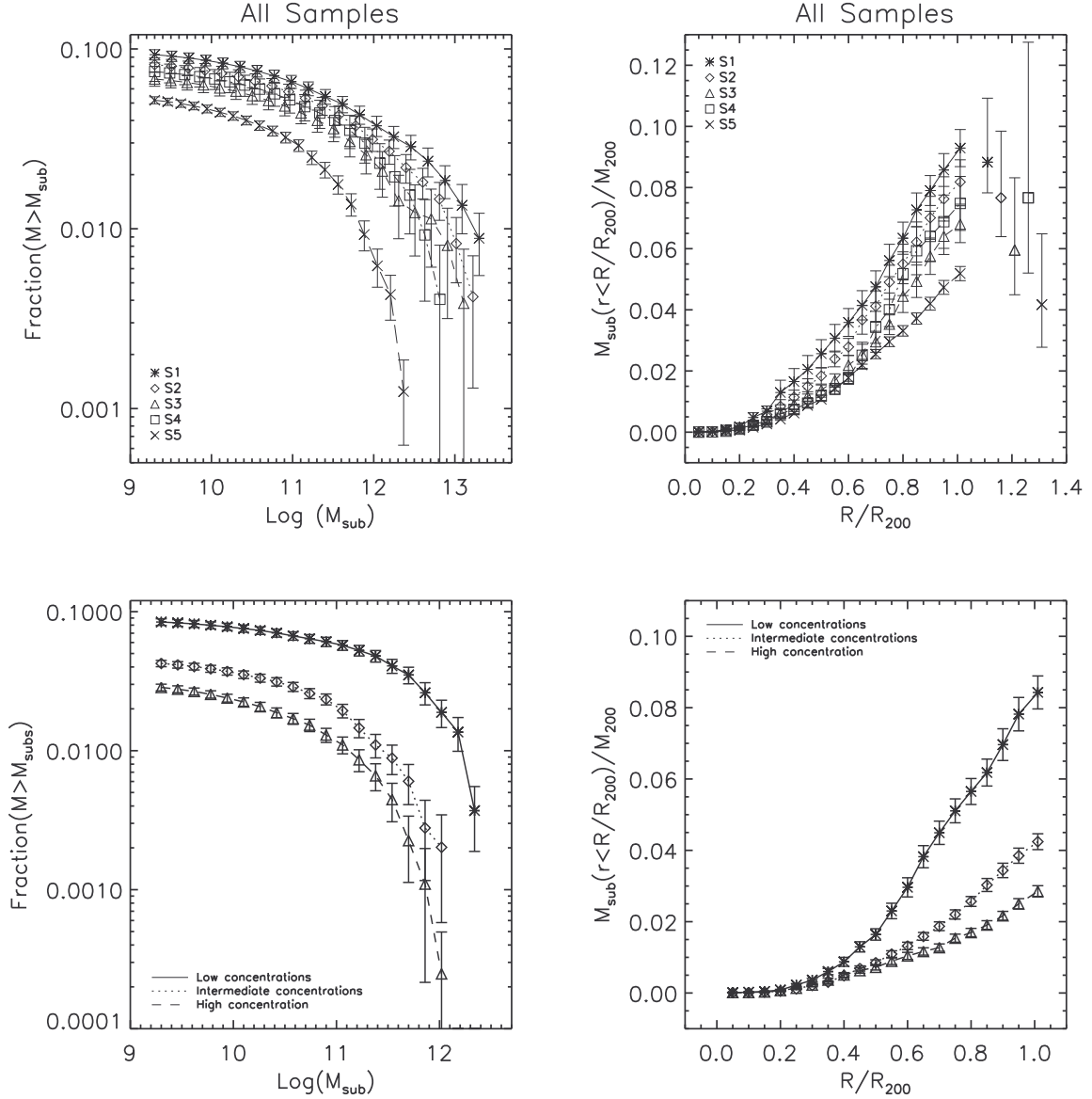


Figure 4.1: Top panels: cumulative mass fraction in substructures as a function of subhalo mass (left) and normalized distance from the halo centre (right), for the five samples used in this study (different symbols, as indicated in the legend). In the right panel the rightmost symbols with error bars show the median, 25th and 75th percentile of the distributions at $R/R_{200} = 1$. Bottom panels: same as in the top panels but using only haloes from our sample S5 (the least massive one), and splitting the sample in three different bins according to the concentration of the parent haloes. In all panels, symbols connected by lines show the mean values, while error bars show the rms scatter around the mean.

smaller than ~ 1 per cent out to $\sim 0.3 \times r_{200}$, and increases to half its total (within r_{200}) value at $\sim 0.8 \times r_{200}$. The results shown can be explained by considering that haloes of larger mass are less concentrated and dynamically younger than their less massive counterparts. As we will show below, and as discussed in previous studies, subhaloes are strongly affected by dynamical friction and tidal stripping. Less massive haloes assemble earlier than their more massive counterparts, i.e. accrete most of the haloes that contribute to their final mass at early times, so that there was enough time to ‘erase’ the structures below the resolution of the simulation in these systems. In addition, haloes that were accreted earlier, and therefore suffered of tidal stripping for longer times, are preferentially located closer to the centre (see Figure 15 in Gao et al., 2004b).

For haloes of the same mass, a relatively large range of concentrations is possible so that a range of mass fractions is expected. This is confirmed in the bottom panels of Figure 4.1 where we have considered only haloes in our least massive sample (S5), and split it into three different bins according to the halo concentration so as to have the same number of haloes for each bin. We approximate the concentration by V_{max}/V_{200} , where V_{max} is the maximum circular velocity, which is computed by considering all particles bound to a given halo, while $V_{200} = \sqrt{GM_{200}/R_{200}}$. Interestingly, the lowest concentration bin contains substructure mass fractions that are, on average, very close to those of our most massive samples (S1 in the top panels). This confirms that the halo to halo scatter is very large, and that it can be explained only in part by haloes in the same mass bin covering a range of physical properties. In order to give an idea of the intrinsic scatter of haloes in the same mass bin, we have repeated the last point in the top right panel of Figure 4.1, showing this time the median and the 25th and 75th percentile of the distributions obtained at $R/R_{200} = 1$.

4.3.2 Subhalo Mass Function

One of the most basic statistics of the subhalo population is provided by the subhalo mass function, i.e. the distribution of dark matter substructures as a function of their mass. This has been analysed in many previous studies with the aim to answer the following questions: does the subhalo mass function vary as a function of the parent halo mass? How does it vary as a function of cosmic time? And as a function of halo properties (e.g. concentration, formation time, etc.)?

First studies were based on very small samples of simulated haloes, and claimed the ‘universality’ of the subhalo mass function. E.g. Moore et al. (1999) compared the substructure mass distribution obtained for one simulated cluster of mass similar to that of the Virgo Cluster, and one simulated galaxy-size halo, and argued that galactic haloes can be considered as ‘scaled versions’ of cluster-size haloes. De Lucia et al. (2004a) used a sample of ~ 11 high resolution resimulations of galaxy clusters together with a simulation of a region with average density. They argued that the subhalo mass function depends *at most*

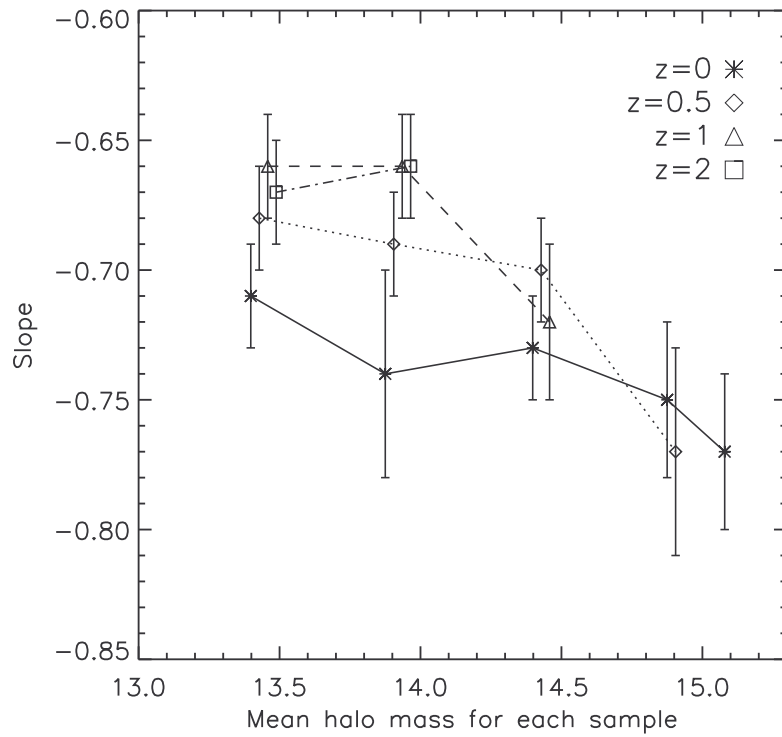


Figure 4.2: Slope of the differential mass function measured for the different samples considered in this study, at different cosmic epochs (solid line for $z = 0$, dotted for $z = 0.5$, dashed line for $z = 1$, and dash-dotted line for $z = 2$). Error bars are computed as the standard deviation of the slopes measured for each halo within the sample. For reasons of clarity, a small shift has been added to the abscissa.

weakly on the parent halo mass and that the (nearly) invariance of the subhalo mass function could lie in the physical nature of the dynamical balance between two opposite effects: the destruction of substructures due to dynamical friction and tidal stripping on the one hand, and the accretion of new substructures on the other hand. Contemporary work by Gao et al. (2004b) and later work (e.g. Gao et al., 2011) has demonstrated that the subhalo mass function does depend on the parent halo mass, as well as on the physical properties of the parent halo, in particular its concentration and formation time. We note that Gao et al. (2004b) used a sample of simulated haloes that was not homogeneous in terms of resolution (typically lower than ours), cosmological parameters, and simulation codes. The sample used in Gao et al. (2011) was instead based on a homogeneous set of cosmological parameters (consistent with WMAP first-year results) and included simulations with resolution higher than that of our sample. Their sample, however, did not include very massive haloes ($\sim 10^{15} h^{-1} M_{\odot}$). It is therefore interesting to re-address the questions listed above using our simulation sample.

In Figure 4.2, we plot the slope of the differential mass function obtained by fitting a power law to the mass functions of each sub-sample considered in our study. Following De Lucia et al. (2004a), we have restricted the fit by discarding the most massive (and rarest) substructures (those with mass above $10^{12} h^{-1} M_{\odot}$ for the samples S1 and S2, and with mass above $10^{11.5} h^{-1} M_{\odot}$ for the samples S3, S4 and S5). We find that, albeit weakly, the slope of the subhalo mass function depends on the parent halo mass, and that there is a weak trend for shallower slopes with increasing lookback times. The best fit values we measure vary in the range between ~ -0.65 and ~ -0.8 , in agreement with results from previous studies (e.g. Ghigna et al., 2000; De Lucia et al., 2004a; Gao et al., 2004b). When including the most massive substructures in the fit, we obtain steeper slopes, ranging from ~ -0.91 and ~ -0.86 at redshift $z = 0$, but the trends shown in Figure 4.2 are not altered significantly.

As explained by Gao et al. (2011), the dependence of the subhalo mass function on halo mass is a consequence of the fact that more massive haloes are on average less concentrated and dynamically younger than their less massive counterparts. Since the strength of tidal disruption depends on halo concentration, and since haloes of a given mass are on average less concentrated at higher redshift, we also expect that the subhalo mass function depends on time. Figure 4.3 shows the cumulative subhalo mass function (normalized as in Gao et al. 2004b) at four different redshifts in the left panels and for different concentrations in the right panels (in these panels, only haloes identified at redshift zero have been considered). Top and bottom panels refer to the haloes in the mass range $[1 - 3] \times 10^{13} h^{-1} M_{\odot}$ and $[1 - 5] \times 10^{14} h^{-1} M_{\odot}$ respectively. We derive the three subsamples by splitting the range of concentration in order to have the same number of haloes in each subsample. Results shown in Figure 4.3 confirms previous findings by Gao et al. (2011), and extend them to

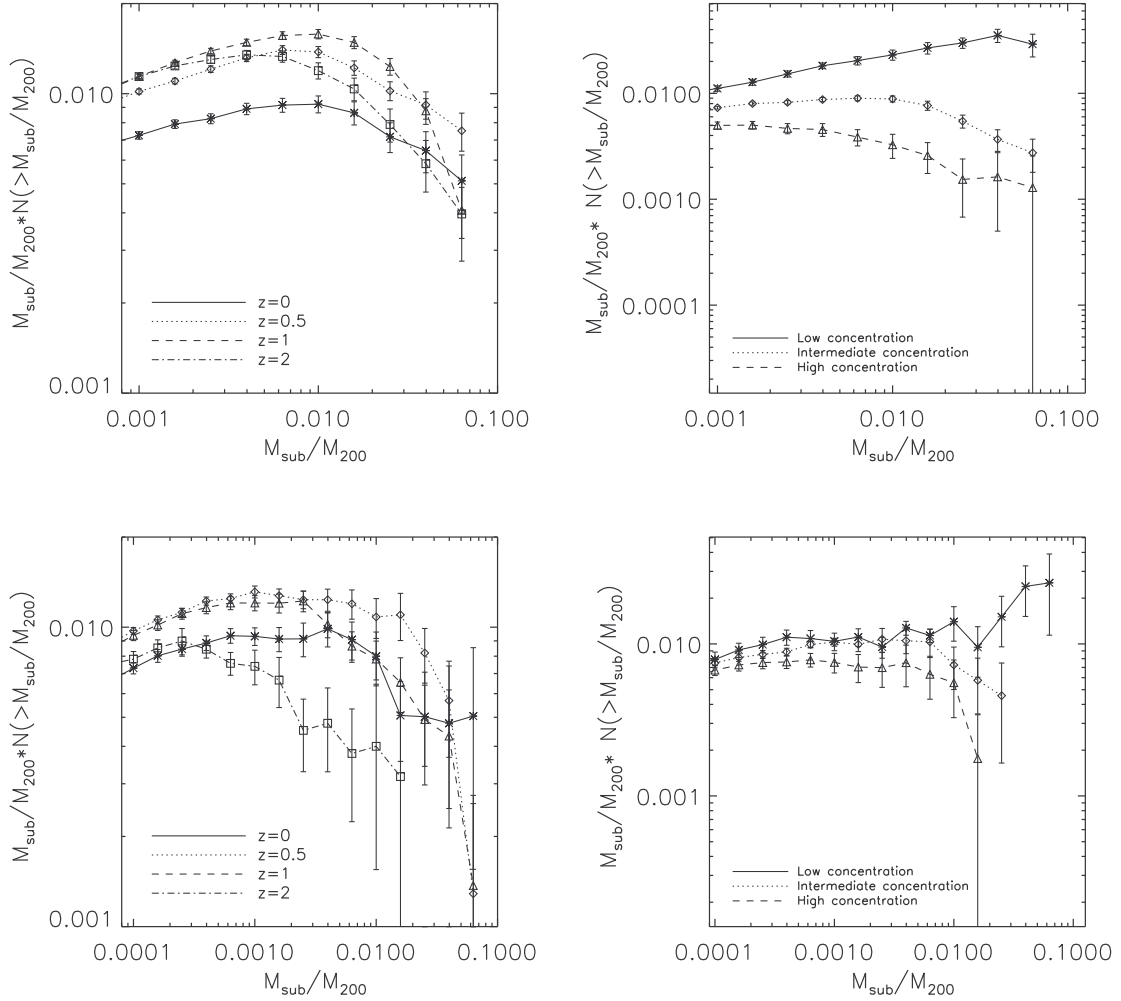


Figure 4.3: Cumulative mass functions (CMF) in units of rescaled subhalo mass, and multiplied by M_{sub}/M_{200} to take out the dominant mass dependence. Top and bottom panels are for haloes in the mass range $[1 - 3] \times 10^{13} h^{-1} M_{\odot}$ and $[1 - 5] \times 10^{14} h^{-1} M_{\odot}$, respectively. In the left panel, results are shown for different redshifts (solid line for $z=0$, dotted line for $z=0.5$, dashed line for $z=1$ and dash-dotted line for $z=2$). In the right panel, only haloes identified at redshift zero have been considered, and they have been split in three bins, according to their concentration. Only subhaloes with more than 100 bound particles have been used to build these functions.

larger parent haloes masses: haloes at higher redshift have significantly more substructures than those of the same mass at later times. The figure suggests that there is a significant evolution between $z = 0$ and $z \sim 0.5$, but it becomes weaker at higher redshifts. We note that for the highest redshift considered, the subhalo mass function does not significantly differ from that found at $z \sim 1$, but we note that this could be due to poor statistics. Gao et al. (2011) find a similar trend for haloes of similar mass. At any given cosmic epoch, there is a large halo-to-halo scatter which is due, at least in part, to internal properties of the parent halo like concentration, as shown in the right panels of Figure 4.3. For the ranges of mass shown in Fig. 4.3, low concentration haloes host up to an order of magnitude more substructures than haloes of the same mass but with higher concentration. The difference between the different concentration bins are larger (and significant) for the most massive substructures.

In order to verify that the results of our analysis are robust against numerical resolution, we have compared the cumulative sub-halo mass function obtained for the set of simulated halos presented here to that obtained for the same halos simulated at a 10 times lower mass resolution. We find that the two distributions agree very well, within the mass range accessible to both resolutions. This confirms that both our simulations and the procedure of halo identification have numerically converged.

4.3.3 Radial Distribution of Subhaloes

Previous studies (Ghigna et al., 2000; De Lucia et al., 2004a; Nagai & Kravtsov, 2005; Saro et al., 2010) have shown that subhaloes are ‘anti-biased’ relative to the dark matter in the inner regions of haloes. No significant trend has been found as a function of the parent halo mass, with only hints for a steeper profiles of subhaloes in low massive haloes (De Lucia et al., 2004a).

The analysis of our sample of simulated halos confirms previous findings that dark matter subhaloes are anti-biased with respect to dark matter, with no dependence on parent halo mass. In fact, there is no physical reason to expect such a trend. We note that De Lucia et al. (2004a), who found hints for such a correlation, used a smaller sample of simulated haloes, that were carried out using different simulation codes and parameters. In contrast, our simulated haloes are all carried out using the same parameters and simulation code.

Nagai & Kravtsov (2005) find that the anti-bias is much weaker if subhaloes are selected on the basis of the mass they had at the time of accretion onto their parent halo. We confirm their results in Figure 4.4, where we show the radial distribution of substructures in our sample S1 (the most massive haloes in our simulation set). The top-left panel of Figure 4.4 shows the radial distribution of substructures selected on the basis of their present day mass, while in the top-right panel the mass of the substructure at the time of accretion

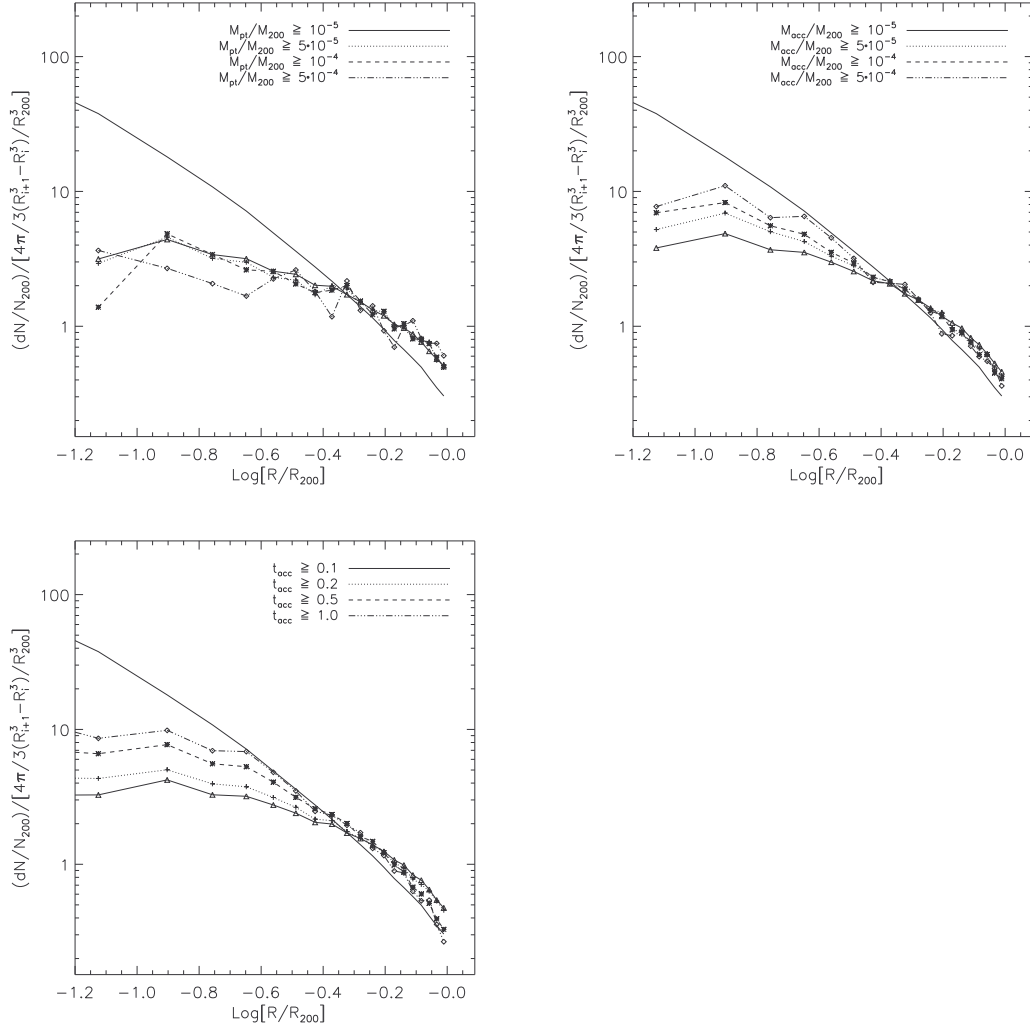


Figure 4.4: Radial distribution of dark matter substructures belonging to haloes of the sample S1. In the top-right panel, different lines correspond to different thresholds in the M_{sub}/M_{200} ratio, based on the present-day subhalo mass. In the top-right panel, the subhalo mass at the time of accretion has been considered, while in the bottom panel different lines correspond to subhaloes accreted at different times.

(defined as the last time the halo was identified as a central halo, see below) has been used. The figure shows that, in this case, selecting progressively more massive substructures reduces the anti-bias between subhaloes and dark matter. The bottom panel of Figure 4.4 shows that the same is obtained by discarding substructures that are accreted recently. The two selections tend to pick up haloes that suffered a stronger dynamical friction (i.e. haloes that were more massive at the time of accretion) or that suffered of dynamical friction for a longer time (haloes that were accreted earlier). As a consequence, both selections tend to preferentially discard subhalos at larger radii, thus bringing the radial distribution of subhaloes closer to that measured for dark matter.

As shown above (see right panels of Figure 4.1), most of the substructure mass is located at the cluster outskirts. De Lucia et al. (2004a) showed that this distribution is dependent on the subhalo mass, with the most massive substructures being located at larger distances from the cluster centre with respect to less massive substructures. In particular, De Lucia et al. (2004a) split their subhalo population in two subsamples by choosing a rather arbitrary mass ratio between the subhalo mass and the parent halo mass (they chose the value 0.01 for this ratio). Our simulations exhibit the same trends, but we find that this can be more or less ‘significant’ depending on the particular threshold adopted to split the sample. In Figure 4.5, we show the radial distribution of substructures with $M_{sub}/M_{200} > 0.01$ (solid lines) and $M_{sub}/M_{200} < 0.001$ (dashed lines). Our trends are weaker than those found by De Lucia et al. (2004a) at redshift zero, when the same division is adopted. We note, however, that these trends are dominated by the most massive substructure and are, therefore, significantly affected by low number statistics. Figure 4.5 also shows that the mass segregation becomes more important at increasing redshift.

Considering that haloes of a given mass are less centrally concentrated and dynamically younger than their counterparts at later redshift, the trend found can be explained as follows: the ‘younger’ haloes have massive subhaloes preferentially in their outer regions because stripping has not had enough time to strip their outer material and eventually disrupt them. In more dynamically evolved clusters (those at present time), stripping has had more time to operate and to wash out any difference between the two distributions. In this picture, the balance between dynamical friction and stripping on one hand, and the accretion of new subhaloes on the other hand is such that the latter effect is dominating over the former. This is in agreement with the results shown above for the evolution of the cumulative mass function of substructures, whose normalization increases with increasing redshift.

We stress that in Figure 4.5 we are considering subhaloes of different mass at the time they are identified. As discussed in Section 4.1, this cannot be simply related to the mass and/or luminosity of the galaxies. So the trend shown in Figure 4.5 cannot simply be related a different spatial distribution for galaxies in different luminosity bins, as done for example in Lin & Mohr (2004, see their figure 8).

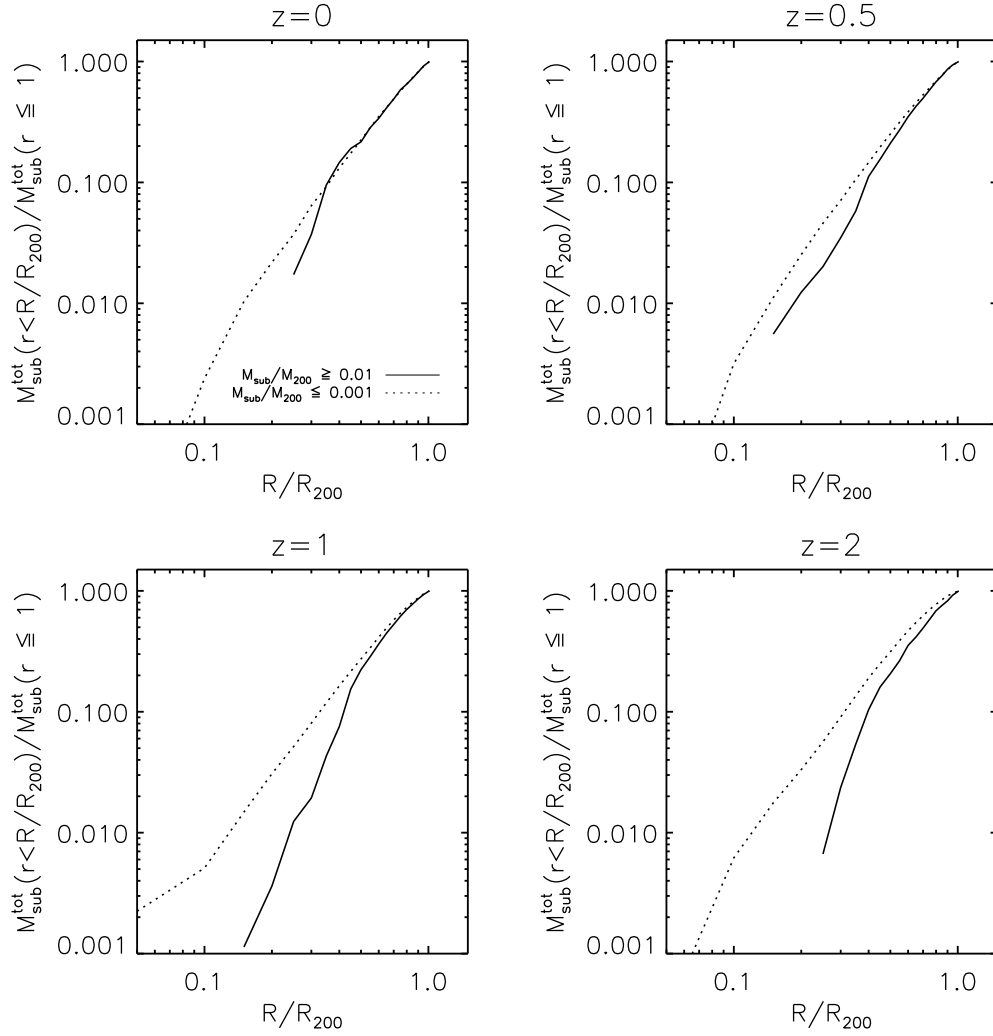


Figure 4.5: Cumulative radial distributions for subhaloes with $M_{sub}/M_{200} > 0.01$ (solid line) and $M_{sub}/M_{200} < 0.001$ (dotted line) from all samples, at different redshifts. On the y-axis, we plot the total mass in subhaloes within a given distance from the centre, normalized to the total mass in subhaloes within R_{200} , for each subhaloes population.

4.4 Evolution of Substructures

In this section, we study the evolution of substructures as a function of time, focusing in particular on their mass accretion histories and merger histories. In order to obtain these information, we have constructed merger histories for all self-bound haloes in our simulations, following the method adopted in Springel et al. (2005) and the improvements introduced in De Lucia & Blaizot (2007), as described in Section 3.2.2. Here, we consider only substructures that contain at least 100 bound particles, and in a few cases, we use particular mass ranges to ease the comparison with the literature.

In this section we will also study if the accretion and merger history of substructures depend on the environment, that we will approximate using the parent halo mass. It is worth stressing, however, that our haloes provide likely a biased sample for this analysis. In fact, excluding the most massive sample and some haloes that belong to the sample S2, all the other haloes reside in the regions surrounding the most massive haloes, which might not represent the ‘typical’ environment for haloes in the same mass range.

4.4.1 Mass Accretion History

In this section, we use the merger trees constructed for our cluster sample to study the mass accretion histories of subhaloes of different mass and residing in different environments. Several previous studies (Gao et al., 2004b; De Lucia et al., 2004a; Warnick et al., 2008) have pointed out that once haloes are accreted onto larger systems (i.e. they become substructures), their mass is significantly reduced by tidal stripping. The longer the substructure spends in a more massive halo, the larger is the destructive effect of tidal stripping. Previous studies have found that the efficiency of tidal stripping is largely independent of the parent halo mass (De Lucia et al., 2004a; Gao et al., 2004b).

We re-address these issues using all substructures residing within the virial radius of our haloes, and with mass larger than $10^{10} h^{-1} M_{\odot}$ at redshift $z = 0$ (in our simulations, these substructures contain at least 100 particles). By walking their merger trees, following the main progenitor branch, we construct the mass accretion history (MAH) for all of these subhaloes, and record the accretion time (z_{accr}) as the last time the halo is a central halo, i.e. before it is accreted onto a larger structure and becomes a proper subhalo. Our final sample includes 39005 haloes, that we split in two bins of different mass by using either their present day mass or their mass at the accretion time. We end up with 33576 haloes with mass larger than $10^{11} h^{-1} M_{\odot}$ at present (25344 when using the mass at the accretion time), and 5429 haloes with mass lower than the adopted threshold (13661 if the accretion mass is used). In order to analyse the environmental dependence of the mass accretion history, we consider separately subhaloes residing in our S5 and S1 samples (these correspond to our lowest and largest parent halo mass, respectively).

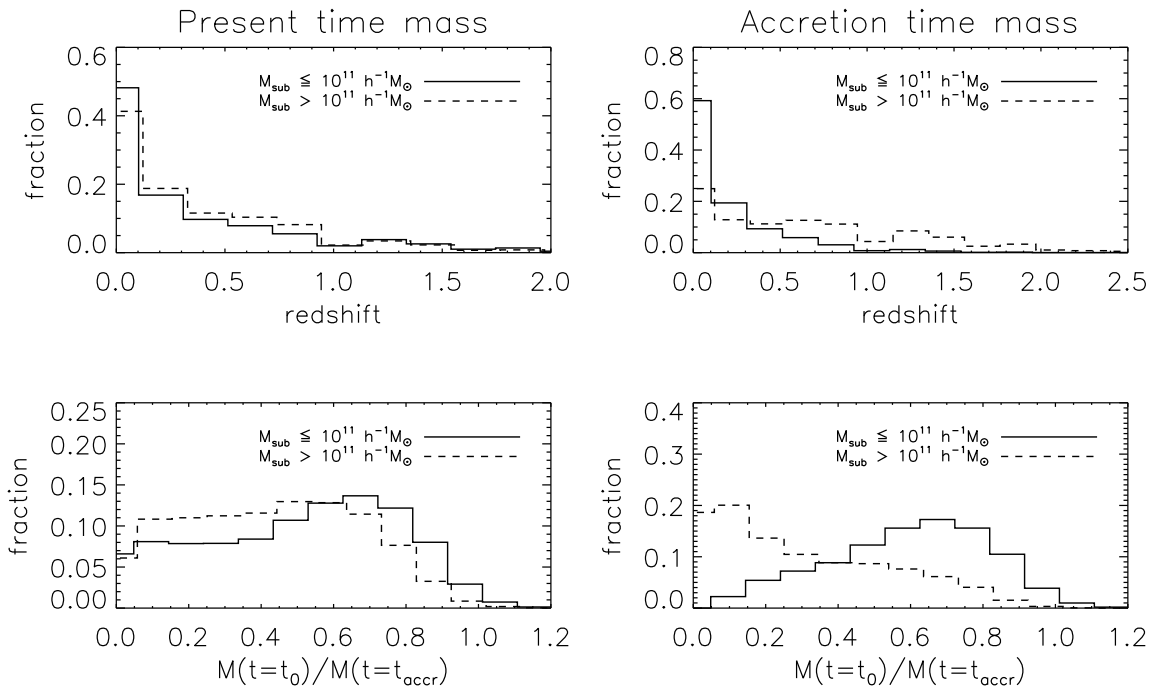


Figure 4.6: Left panels: distribution of the accretion times (top panel) and of the fraction of mass loss since accretion (bottom panel) for subhaloes of different mass at present time (different line styles, as indicated in the legend). Right panels show the same distributions but for subhaloes split according to their mass at the accretion time.

The top panels in Figure 4.6 show the distribution of the accretion times for the two mass bins considered. Left and right panels correspond to a splitting in mass done on the basis of the present day mass and of the mass at accretion, respectively. When considering the present day mass (left panel), the differences between the two distributions are small, with only a slightly lower fraction of more massive substructures being accreted very late, and a slightly larger fraction of substructures in the same mass range being accreted between $z \sim 0.1$ and $z \sim 1$. A larger difference between the two distributions can be seen when considering the mass at the time of accretion (right panel). Substructures that are less massive at the time of accretion have been accreted on average later than their more massive counterparts. In particular, about 90 per cent of the substructures in the least massive bin considered have been accreted below redshift 0.5, while only 50 per cent of the most massive substructures have been accreted over the same redshift range. The distribution obtained for the most massive substructures is broader, extending up to redshift ~ 2 . This is largely a *selection effect*, due to the fact that we are only considering substructures that are still present at $z = 0$. Once accreted onto larger systems, substructures are strongly affected by tidal stripping so that, among those that were accreted at early times, only the most massive ones will still retain enough bound particles at present to enter our samples. The less massive substructures that were accreted at early times, have been stripped below the resolution of our simulations and therefore do not show up in the solid histogram that is shown in the top right panel of Figure 4.6.

The bottom panels of Figure 4.6 show the distribution of the ratios between present day mass and mass at accretion for subhaloes of different present day mass (left panel) and for different mass at accretion (right panel). Less massive subhaloes, which were accreted on average more recently, lose on average smaller fractions of their mass compared to more massive subhaloes for which the distribution is skewed to higher values. The difference between these distributions becomes more evident when one splits the samples according to the mass at the time of accretion, as shown in the right panel. As explained above, however, this is affected by the fact that many of the least massive substructures will be stripped below the resolution of the simulation at $z = 0$. We have repeated the analysis done in Fig. 4.6 for subhaloes in each of the five samples used in our study, and we found there is no significant dependency on the environment.

Fig. 4.7 shows that, as expected, substructures accreted earlier suffered significantly more stripping than substructures that were accreted at later times. In particular, about 90 per cent of subhaloes accreted at redshift larger than 1 have been stripped by more than 80 per cent of their mass at accretion. For haloes that have been accreted at redshift lower than 1, the distribution is much broader, it peaks at ~ 0.6 (i.e. about 40 per cent of the mass has been stripped for about 20 per cent of these haloes) but has a long tail to much lower values. Similarly to Fig. 4.6, we also tried to split this plot for different parent halo masses, finding no significant trend with the environment.

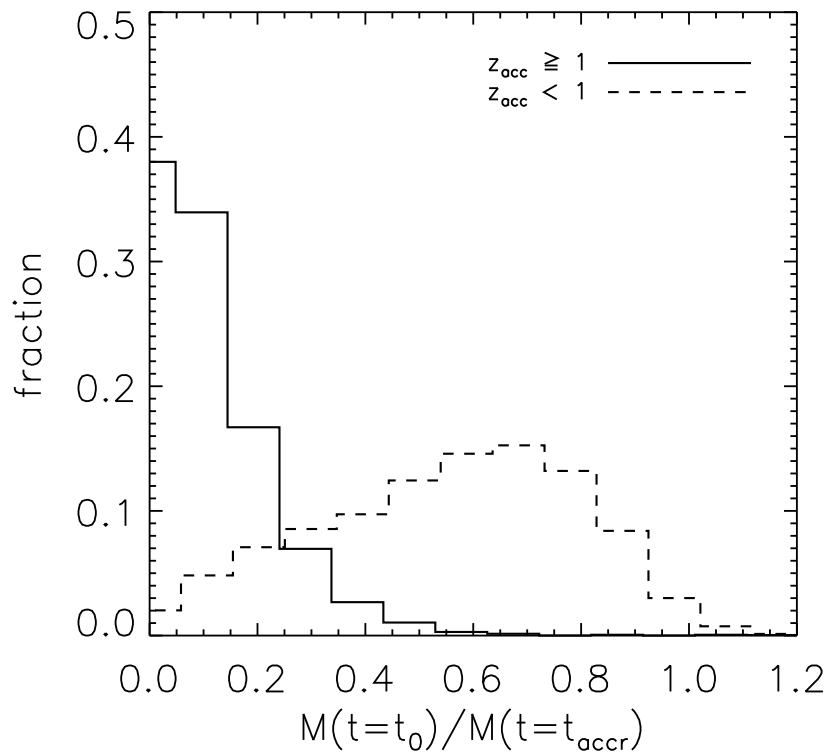


Figure 4.7: Distribution of mass loss (ratio between the present day mass and the mass at accretion) for two different accretion ranges: solid line for $z_{accr} \geq 1$ and dotted line for $z_{accr} < 1$.

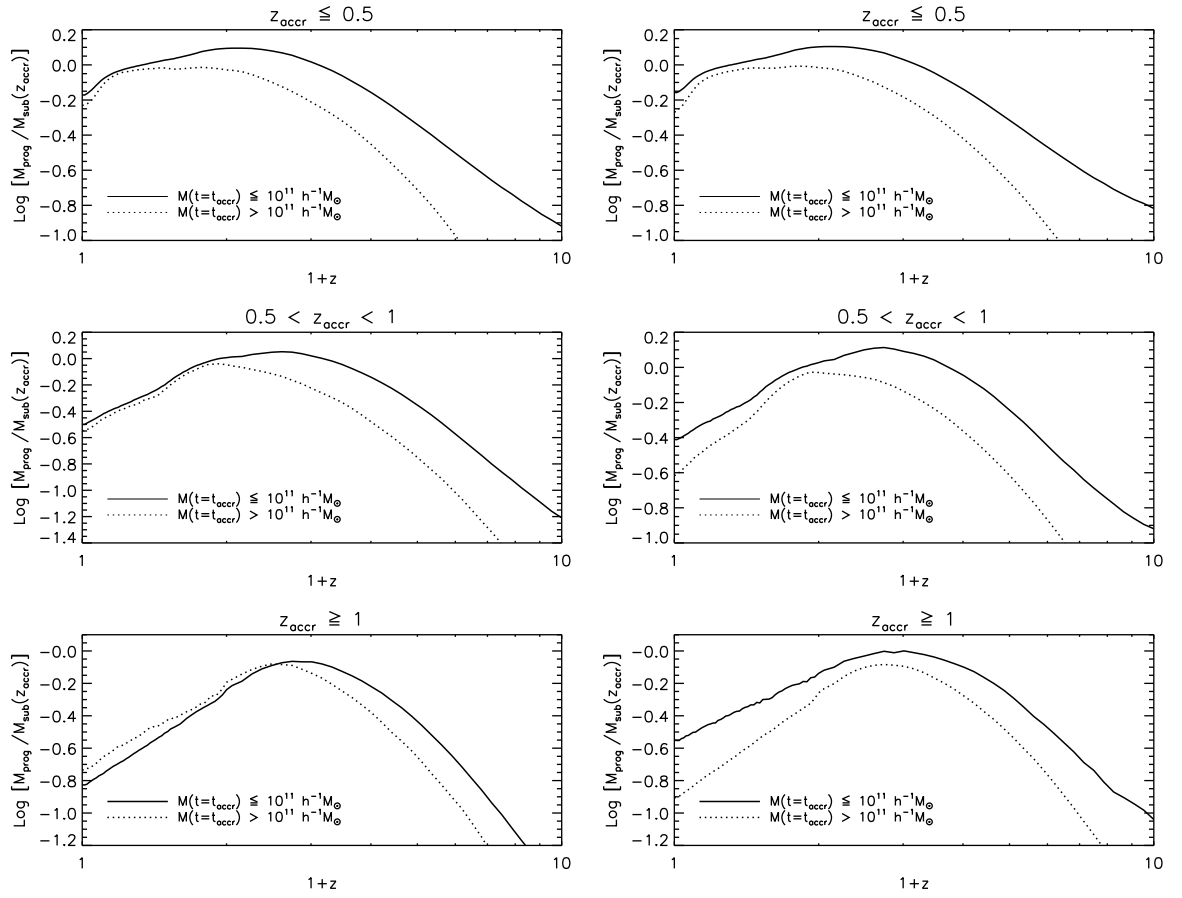


Figure 4.8: Average mass accretion history for three ranges of accretion times. In the left panels, substructures are split according to their present day mass, while in the right panels they are split according to their mass at the time of accretion.

Fig. 4.8 shows the MAHs of subhaloes accreted at different times. It shows results when subhaloes are split according to their present day mass (left panels), and the mass at accretion (right panels). As shown in previous studies, the longer the halo is a substructure, the larger is its stripped mass. When substructures are split according to their present day mass, the influence of tidal stripping does not appear to depend strongly on the substructure mass. In contrast, if the mass at the accretion time is considered, in a given range of accretion times, haloes that are more massive lose a larger fraction of their mass with respect to their less massive counterparts. This is due to the fact that more massive haloes sink more rapidly towards the centre because of dynamical friction, and therefore suffer a more significant stripping due to tidal interactions with the parent halo. Once again, this entails the fact that luminosity must correlate stronger with the subhalo mass computed at the time of accretion, i.e. before stripping had time to operate.

In Fig. 4.9 we plot the mean MAHs for subhaloes in the two mass bins considered and for two different ‘environments’, parametrized as the mass of the parent halo. In particular, we consider the samples S5 and S1 (i.e. the least and the most massive haloes used in our study). Dashed and long-dashed lines show the MAHs for subhaloes in the sample S5 with mass in the range $[10^{10} - 10^{11}] h^{-1} M_{\odot}$ and larger than $10^{11} h^{-1} M_{\odot}$, respectively. Solid and dotted lines show the MAH for subhaloes in the same mass ranges but for the sample S1. Here we consider the present day subhalo mass. Computing the same plot by adopting the subhalo mass at the time of accretion does not alter the results. We find that the environment does not significantly influence the mass accretion history of substructures. In the bottom panel, the long dashed line (corresponding to substructures more massive than $10^{11} h^{-1} M_{\odot}$ in the sample S5) is likely affected by low number statistics. In the same panel a small difference can be seen for the less massive substructures that appear to be less stripped in the sample S5 than in S1 (compare dashed and solid lines). The difference, however, is not large, but this might be affected by the fact that our haloes all reside in the regions surrounding very massive clusters.

4.4.2 Merging Rate

In recent years, a large body of observational evidence has been collected that demonstrates that galaxy interactions and mergers play an important role in galaxy evolution. In particular, numerical simulations have shown that major mergers between two spiral galaxies of comparable mass can completely destroy the stellar disk and leave a kinematically hot remnant with structural and kinematical properties similar to those of elliptical galaxies (Mo, van den Bosch, & White, 2010, and references therein). Minor mergers and rapid repeated encounters with other galaxies residing in the same halo (*harassment*; Moore et al. 1996; Moore et al. 1998) can induce disk instabilities and/or the formation of a stellar bar,

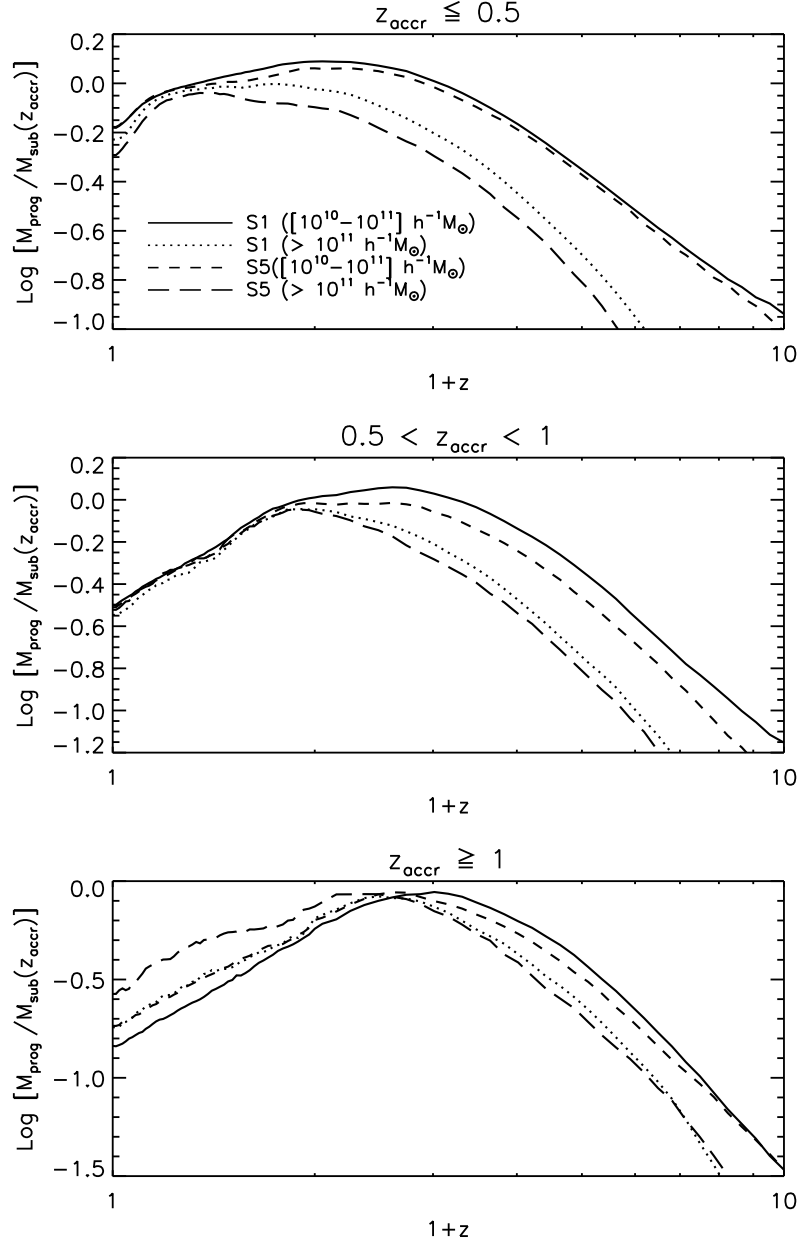


Figure 4.9: Average mass accretion history for subhaloes in three different ranges of accretion time, as a function of environment. Dashed and long-dashed lines show the MAH for subhaloes in the sample S5 with mass in the range $[10^{10} - 10^{11}] h^{-1} M_{\odot}$ and larger than $10^{11} h^{-1} M_{\odot}$, respectively. Solid and dotted lines show the MAH for subhaloes in the same mass ranges but for the sample S1.

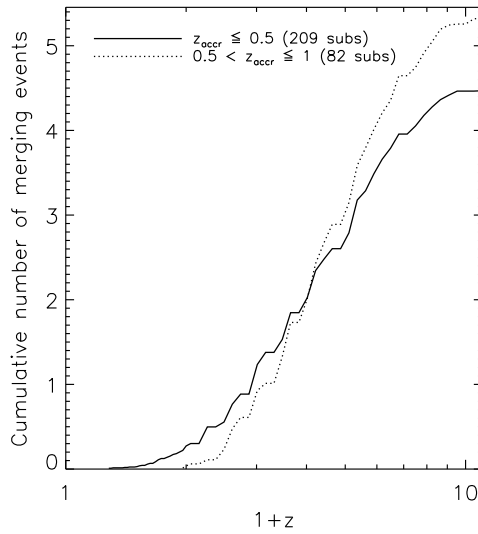


Figure 4.10: Mean number of major mergers as a function of redshift, for subhaloes in two different ranges of accretion time. We take into account only subhaloes with mass $M \geq 10^{12} h^{-1} M_{\odot}$ at redshift $z = 0$ and merger events that include systems with mass $M \geq 10^{10} h^{-1} M_{\odot}$.

each of which affects the morphology of galaxies falling onto clusters (see also discussion in Section 2.4). As galaxy mergers are driven by mergers of the parent dark matter haloes, it is interesting to analyse in more detail the merger statistics of dark matter substructures.

The mass accretion history discussed in the previous section does not distinguish between merger events (of different mass ratios) and accretion of ‘diffuse material’. In order to address this issue, and in particular to study the merger rates of dark matter substructures, we have taken advantage of the merger trees constructed for our samples. We have selected all subhaloes with mass larger than $10^{12} h^{-1} M_{\odot}$ at redshift zero, and have followed them back in time by tracing their main progenitor branch, and recording all merger events with other structures. In particular, we take into account only mergers with objects of mass larger than $10^{10} h^{-1} M_{\odot}$, and mass ratios larger than 5 : 1. We note that both these values are computed at the time the halo is for the last time central (the mass of the main progenitor at the time of accretion is considered to compute the mass ratio).

Fig. 4.10 shows the merging rate for all subhaloes that satisfy the above conditions. We consider in this plot only objects that experienced at least one merger event. The solid line shows the mean number of mergers for subhaloes that were accreted at $z < 0.5$, while the dotted line shows the resulting merger rate for objects accreted between $0.5 < z \leq 1$. The figure shows that in both cases, the slope of the lines become shallower close to the accretion time, i.e. mergers between substructures are suppressed because of the large velocity dispersion of the parent haloes. Interestingly, haloes that were accreted earlier experience, on average, one more major merger than haloes accreted at later times.

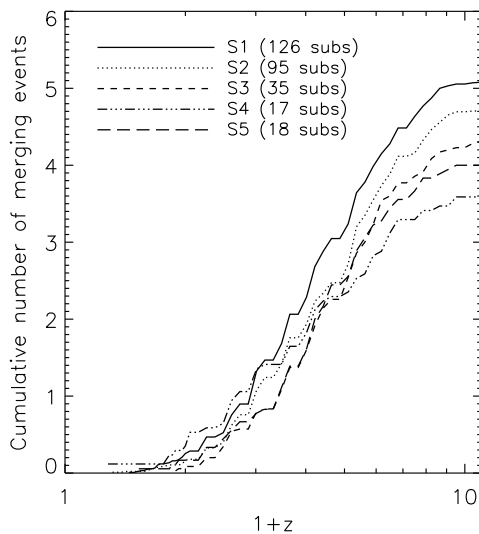


Figure 4.11: Mean number of major mergers as a function of redshift, for subhaloes in different environments, quantified as the mass of their parent halo. As in Fig. 4.10 we take into account only subhaloes with mass $M \geq 10^{12} h^{-1} M_{\odot}$ at redshift $z = 0$ and merger events that include systems with mass $M \geq 10^{10} h^{-1} M_{\odot}$.

We repeat the same analysis looking at the merging rate as a function of environment. Fig. 4.11 shows the cumulative number of mergers for subhaloes in our five samples. The mean number of mergers increases as a function of the parent halo mass, although subhaloes in the sample S4 experience on average fewer mergers than subhaloes in the sample S5. This is not surprising since subhaloes in the surroundings of more massive haloes have a larger probability to merge with other structures.

4.5 Discussion and conclusions

We have used a large set of high-resolution simulated haloes to analyse the statistics of subhaloes in dark matter haloes, and their dependency as a function of the parent halo mass and physical properties of the parent halo. While some of the results discussed in this chapter confirm results from previous studies, it is the first time that a systematic analysis of the properties and evolution of dark matter substructures is carried out using a large simulation set carried out using the same cosmological parameters and simulation code. Our main results can be summarized as follows:

- (i) More massive haloes contain increasing fractions of mass in subhaloes. This does not exceed ~ 10 per cent of the total mass, in agreement with previous studies. There is, however, a very large halo-to-halo scatter that can be partially explained by a range of

halo physical properties, e.g. the concentration. Indeed, in more concentrated haloes substructures suffer of a stronger tidal stripping so that they are characterized by lower fractions of mass in substructures.

- (ii) We find that the subhalo mass function depends weakly on the parent halo mass and on redshift. This can be explained by considering that haloes of larger mass are less concentrated and dynamically younger than their less massive counterparts, and that haloes of a given mass are on average less concentrated at higher redshift. Our findings confirm results from previous studies (Gao et al., 2011), and extend them to larger halo masses.
- (iii) As shown in previous work (e.g. Ghigna et al., 1998; De Lucia et al., 2004a), subhaloes are anti-biased with respect to the dark matter in the inner regions of haloes. The anti-bias is considerably reduced once subhaloes are selected on the basis of their mass at the time of accretion, or neglecting those that were accreted at later times. We also find that the spatial distribution of subhaloes does not depend significantly on halo mass, as suggested in previous work by De Lucia et al. (2004a). The most massive substructures are located at the outskirts of haloes and this mass segregation is more important at higher redshift.
- (iv) Once accreted onto larger systems, haloes are strongly affected by tidal stripping. The strength of this stripping appears to depend on the mass of the accreting substructures: those that are more massive at the time of accretion tend to be stripped by larger fractions of their initial mass.
- (v) Mergers between substructures are rare events. Following the merger trees of substructures, however, we find that they have suffered in the past about 4-5 important (mass ratio 1:5) mergers. As expected, the number of mergers experienced depends on the environment: subhaloes in more massive systems have experienced more mergers than those of similar mass residing in less massive haloes.

Dark matter substructures mark the sites where luminous satellites are expected to be found, so their evolution and properties do provide important information on the galaxy population that forms in hierarchical models. As discussed in previous studies, however, because of the strong tidal stripping suffered by haloes falling onto larger structures, it is not possible to simply correlate the population of subhaloes identified at a given cosmic epoch to that of the corresponding galaxies. The galaxy luminosity/stellar mass is expected to be more strongly related to the mass of the substructure at the time of *infall* and, depending on the resolution of the simulations, there might be a significant fraction of the galaxy population that cannot be traced with dark matter substructures because they have been stripped below the resolution limit of the simulation (the ‘orphan’ galaxies - see for example Wang et al. 2006). This is particularly important in the context of the next chapter,

where we implement stellar stripping in the reference model described in Section 3.4. One particular prescription takes into account the subhalo properties and those of the galaxy it contains, at the time of its accretion onto a larger system. An alternative prescription considers the satellite population originated by the above mentioned ‘orphan’ galaxies as the contributor to the intra-cluster light, via galaxy disruption.

Our results do provide indications about the properties of the galaxy populations predicted by hierarchical models. Tidal stripping is largely independent of the environment (we have parametrized this as the parent halo mass), while the accretion rates of new subhaloes increases at increasing redshift. The nearly invariance of the subhalo mass function results from the balance between these two physical processes. If the amount of dark matter substructures is tracing the fraction of recently infallen galaxies, the fraction of star forming galaxies is expected to increase with increasing redshift (the ‘Butcher-Oemler’ effect, Butcher & Oemler 1978, Kauffmann 1995). In addition, our findings suggest that stronger mass segregation should be found with increasing redshift.

There is a large halo-to-halo scatter that can be only partially explained by a wide range of physical properties. This is expected to translate into a large scatter in e.g. the fraction of passive galaxies for haloes of the same mass, with more concentrated haloes hosting larger fraction of red/passive galaxies. Finally, there is an obvious merger bias that is expected to translate into a different morphological mix for haloes of different mass.

Chapter 5

ICL Formation in a Hierarchical Galaxy Formation Model

In this chapter we study the formation of the Intra-Cluster Light (ICL) using the semi-analytic model presented in Section 3.4, coupled to merger trees extracted from the set of simulations described in Section 4.2. We assume that the ICL forms by (1) stellar stripping of satellite galaxies and (2) relaxation processes that take place during galaxy mergers. The fraction of ICL in groups and clusters predicted by our models ranges between 10 and 40 per cent, with a large halo-to-halo scatter, no halo mass dependence, and a resolution dependence. The ICL forms very late (below $z \sim 1$), and a fraction varying between 5 and 25 per cent of it has been accreted during the hierarchical growth of haloes. In agreement with recent observational measurements, we find the ICL to be made of stars covering a relatively large range of metallicity, with the bulk of them being sub-solar.

5.1 Introduction

In Section 2.5 we have introduced the most relevant observational and theoretical studies focused on the formation and properties of the ICL. In this chapter, we use the semi-analytic model presented in De Lucia & Blaizot (2007, hereafter DLB07) and described in Section 3.4, that we extend by including three different prescriptions for the formation of the ICL. We couple this model to the suite of high-resolution N-body simulations of galaxy clusters presented in Section 4.2 to study the formation and evolution of the ICL component, as well as its physical properties, and the influence of the updated prescriptions on model basic predictions (in particular, the galaxy stellar mass function, and the mass of the BCGs). There are some advantages in using semi-analytic models to describe the ICL formation with respect to hydrodynamical simulations: they do not suffer from numerical effects related to the fragility of poorly resolved galaxies, and allow the relative influence of different channels of ICL generation to be clearly quantified. However, the size and abun-

dance of satellite galaxies (that influence the amount of predicted ICL) might be estimated incorrectly in these models. We will comment on these issues in the following.

The layout of the chapter is as follows. In Section 5.2 we describe the prescriptions we develop to model the formation of the ICL component. In Section 5.3 we discuss how our prescriptions affect the predicted galaxy stellar mass function, and in Section 5.4 we discuss how the predicted fraction of ICL varies as a function of halo properties. In Section 5.5, we analyse when the bulk of the ICL is formed, and which galaxies provide the largest contribution. We then study the correlation between the ICL and the properties of the corresponding BCGs in Section 5.6, and analyse the metal content of the ICL in Section 5.7. Finally, we discuss our results and give our conclusions in Section 5.9.

5.2 Semi-analytic models for the formation of the ICL

In this study, we use the semi-analytic model presented in Section 3.4, but we update it in order to include three different prescriptions for modelling the formation of the ICL component. Below, we describe three different models that we have implemented to account for the ICL component. We assume that it is formed through two different channels: (i) stellar stripping from satellite galaxies and (ii) relaxation processes that take place during mergers and may unbind some fraction of the stellar component of the merging galaxies. In the following, we describe in detail each of our prescriptions.

5.2.1 Disruption Model

This model is equivalent to that proposed by Guo et al. (2011), and assumes that the stellar component of satellite galaxies is affected by tidal forces only after their parent substructures have been stripped below the resolution of the simulation (i.e. the galaxies are Type 2). We assume that each satellite galaxy orbits in a singular isothermal potential,

$$\phi(R) = V_{vir}^2 \ln R, \quad (5.1)$$

and assume the conservation of energy and angular momentum along the orbit to estimate its pericentric distance:

$$\left(\frac{R}{R_{peri}} \right)^2 = \frac{\ln R/R_{peri} + \frac{1}{2}(V/V_{vir})^2}{\frac{1}{2}(V_t/V_{vir})^2}. \quad (5.2)$$

In the equation above, R is the distance of the satellite from the halo centre, and V and V_t are the velocity of the satellite with respect to the halo centre and its tangential part, respectively. Following Guo et al. (2011), we compare the main halo density at pericentre with the average baryon mass density (i.e. the sum of cold gas mass and stellar mass) of the satellite within its half mass radius. Then, if the following condition is verified:

$$\frac{M_{DM,halo}(R_{peri})}{R_{peri}^3} = \rho_{DM,halo} > \rho_{sat} = \frac{M_{sat}}{R_{half}^3}, \quad (5.3)$$

we assume the satellite galaxy to be disrupted and its stars to be assigned to the ICL component of the central galaxy. In the equation above, we approximate R_{half} by the mass weighted average of the half mass radius of the disk and the half mass radius of the bulge, and M_{sat} is the baryonic mass (cold gas plus stellar mass). The cold ¹ gas mass that is associated with the disrupted satellite is added to the hot component of the central galaxy. When a central Type 0 galaxy is accreted onto a larger system and becomes a Type 1 satellite, it carries its ICL component until its parent substructure is stripped below the resolution limit of the simulation. At this point, its ICL is added to that of the new central galaxy.

In a recent paper, Villalobos et al. (2012) discuss the limits of this implementation with respect to results from controlled numerical simulations of the evolution of disk galaxies within a group environment. The model discussed above is applied only after the galaxy's dark matter subhalo has been completely disrupted, but the simulations by Villalobos et al. show that the stellar component of the satellite galaxy can be significantly affected by tidal forces when its parent subhalo is still present. In addition, this model assumes that the galaxy is completely destroyed when equation (5.3) is satisfied, but the simulations mentioned above show that galaxies can survive for a relatively long time (depending on their initial orbit) after they start feeling the tidal forces exerted by the cluster potential.

Predictions from this model are affected by numerical resolution. We carried out a convergence test by using a set of low-resolution simulations with the same initial conditions of the high-resolution set used in this paper, but with the dark matter particle mass one order of magnitude larger than the one adopted in the high resolution set and with gravitational softening increased accordingly by a factor $10^{1/3}$. We find that, on average, the ICL fraction is ~ 30 per cent higher in the low-resolution set (~ 20 per cent in group-like haloes with mass $\sim 10^{13}M_{\odot}h^{-1}$ and ~ 50 in the most massive haloes considered in our study, as shown in the right panel of Figure 5.14 in Section 5.8). This is due to the fact that, decreasing the resolution, a larger fraction of satellite galaxies are classified as Type 2 and are subject to our stripping model. While the lack of numerical convergence does not affect the qualitative conclusions of our analysis, we point out that the amount of ICL measured in our simulations should be regarded as an upper limit.

5.2.2 Tidal Radius Model

In this prescription, we allow each satellite galaxy to lose mass in a continuous fashion, before merging or being totally destroyed. Assuming that the stellar density distribution

¹In our model, no hot component is associated with satellite galaxies.

of each satellite can be approximated by a spherically symmetric isothermal profile, we can estimate the *tidal radius* by means of the equation:

$$R_t = \left(\frac{M_{sat}}{3 \cdot M_{DM,halo}} \right)^{1/3} \cdot D \quad (5.4)$$

(Binney & Tremaine, 2008). In the above equation, M_{sat} is the satellite mass (stellar mass + cold gas mass), $M_{DM,halo}$ is the dark matter mass of the parent halo, and D the satellite distance from the halo centre.

In our model, a galaxy is a two-component system with a spheroidal component (the bulge), and a disk component. If R_t is smaller than the bulge radius, we assume the satellite to be completely disrupted and its stellar and cold mass to be added to the ICL and hot component of the central galaxy, respectively. If R_t is larger than the bulge radius but smaller than the disk radius, we assume that the mass in the shell $R_t - R_{sat}$ is stripped and added to the ICL component of the central galaxy. A proportional fraction of the cold gas in the satellite galaxy is moved to the hot component of the central galaxy. We assume an exponential profile for the disk, and $R_{sat} = 10 \cdot R_{sl}$, where R_{sl} is the disk scale length (R_{sat} thus contains 99.9 per cent of the disk stellar mass). After a stripping episode, the disk scale length is updated to one tenth of the tidal radius.

This prescription is applied to both kinds of satellite galaxies. For Type 1 galaxies, we derive the tidal radius including the dark matter component in M_{sat} , and we impose that stellar stripping can take place only if the following condition is verified:

$$R_{half}^{DM} < R_{half}^{Disk}, \quad (5.5)$$

where R_{half}^{DM} is the half-mass radius of the parent subhalo, and R_{half}^{Disk} the half-mass radius of the galaxy's disk, that is $1.68 \cdot R_{sl}$ for an exponential profile. When a Type 1 satellite is affected by stellar stripping, the associated ICL component is added to that of the corresponding central galaxy.

As for the Disruption model, predictions from the Tidal Radius model are affected by numerical resolution. We carried out the same convergence test used for the Disruption model. Again, we find for the low resolution set a larger amount of ICL (by about 40 per cent, almost independent of halo mass, as shown in the left panel of Figure 5.14 in Section 5.8). In this model, Type 2 galaxies are the dominant contributors to the ICL and, as for the Disruption model, the larger number of these satellites in the low-resolution set translates in a larger number of galaxies eligible for tidal stripping.

5.2.3 Continuous Stripping Model

This model is calibrated on recent numerical simulations by Villalobos et al. (2012). These authors have carried out a suite of numerical simulations aimed to study the evolution of a disk galaxy within the global tidal field of a group environment (halo mass of about

$10^{13} M_{\odot}$). In the simulations, both the disk galaxy and the group are modelled as multi-component systems composed of dark matter and stars. The evolution of the disk galaxy is followed after it crosses the group virial radius, with initial velocity components consistent with infalling substructure from cosmological simulations (see Benson 2005). The simulations cover a broad parameter space and allow the galaxy-group interaction to be studied as a function of orbital eccentricity, disk inclination, and galaxy-to-group mass ratio. We refer to the original paper for a more detailed description of the simulations set-up, and of the results.

Analysing the outputs of these simulations (Villalobos et al, in preparation), we have derived a fitting formula that describes the evolution of the stellar mass lost by a satellite galaxy as a function of quantities estimated at the time of accretion (i.e. at the time the galaxy crosses the virial radius of the group). Our fitting formula reads as follow:

$$M_{lost}^* = M_{accr}^* \exp \left[\left(\frac{-16}{1-\eta} \right) \left(\frac{M_{sub}}{M_{par}} \right)^{\frac{1}{2}} \left(1 - \frac{t}{t_{merg}} \right) \right] \quad (5.6)$$

where M_{accr}^* is the stellar mass at the time of accretion, η is the circularity of the orbit, M_{sub} and M_{par} are the subhalo and parent halo dark matter masses respectively, and t_{merg} is the residual merger time of the satellite galaxies. We approximate the accretion time as the last time the galaxy was a central galaxy (a Type 0), and compute the circularity using the following equation:

$$\eta = V_{\theta} \sqrt{\frac{2f - V_r^2 - V_{\theta}^2}{2f - 1}}, \quad (5.7)$$

where V_r and V_{θ} are the radial and tangential velocities of the accreted subhalo, and $f = 1 + M_{sub}/M_{par}$. For each accreted galaxy, V_r and V_{θ} are extracted randomly from the distributions measured by Benson (2005) from numerical simulations.

Since Eq. 5.6 is estimated at the time of accretion, we cannot use the merger time prescription that is adopted in the reference model, where a residual merger time is assigned only at the time the substructure is stripped below the resolution of the simulation. To estimate merger times at the time of accretion, we use the fitting formula by Boylan-Kolchin et al. (2008) (hereafter BK08), that has been calibrated at the time the satellite galaxy crosses the virial radius of the accreting system, and is therefore consistent with our Eq. 5.6. In a few cases, it happens that the merger time is elapsed when the satellite galaxy is still a Type 1. In this case, we do not allow the galaxy to merge before it becomes a Type 2.

De Lucia et al. (2010) compared the merger times predicted using this formula with no orbital dependency and for circular orbits with those provided by Equation 3.19 used in the reference model, and found a relatively good agreement. We find that, once the orbital dependency is accounted for, the BK08 fitting formula predicts merger times that are on average shorter than those used in our reference model by a factor of ~ 3 for mass-ratios

$M_{sub}/M_{par} > 0.025$. Therefore, in our continuous stripping model, mergers are on average shorter than in the disruption and tidal radius models.

To implement the model described in this section for the formation of the ICL, we use Eq. 5.6 to compute how much stellar mass has to be removed from each satellite galaxy at each time-step. The stripped stars are then added to the ICL component of the corresponding central galaxy, and a proportional fraction of the cold gas in the satellite is moved into the hot component associated with the central galaxy. If the stripped satellite is a Type 1, and it carries an ICL component, this is removed at the first episode of stripping and added to the ICL component of the central galaxy.

It is worth stressing that Eq. 5.6 is valid for disk galaxies that are accreted on a system with velocity dispersion typical of a galaxy group, and that we are extrapolating the validity of this equation to a wider halo mass ranges.

5.2.4 Merger channel for the formation of the ICL

Murante et al. (2007) argue that the bulk of the ICL is not due to tidal stripping of satellite galaxies (that in their simulations accounts for no more than 5-10 per cent of the total diffuse stellar component), but to relaxation processes taking place during the mergers that characterize the build-up of the central dominant galaxy.

In our reference model, if two galaxies merge, the stellar mass of the merging satellite is added to the stellar (bulge) mass of the central galaxy. Based on the findings described above, we add a ‘merger channel’ to the formation of the ICL by simply assuming that, when two galaxies merge, 20 per cent of the satellite stellar mass gets unbound and is added to the ICL of the corresponding central galaxy. We have verified that this simple prescriptions reproduces approximately the results of the numerical simulations by Villalobos et al. (2012), though in reality the fraction of stars that is unbound should depend on the orbital circularity (Villalobos et al., in preparation). We have also verified that assuming that a larger fraction of the satellite stellar mass gets unbound, obviously leads to higher ICL fractions. In particular, assuming that 50 per cent of the stellar mass of the satellite is unbound, almost doubles the ICL fractions predicted. Assuming an even higher fraction does not affect further the ICL fraction because the effect of having more stellar mass unbound is balanced by the fact that merging galaxies get significantly less massive.

A similar prescription was adopted in Monaco et al. (2006) who showed that this has important consequences on the assembly history of the most massive galaxies, and in Somerville et al. (2008) as one possible channel for the formation of the ICL in the context of a hierarchical galaxy formation model. In order to test the influence of this channel on our results, in the following we will present results with this channel both on and off.

5.2.5 Modelling the bulge and disk sizes

Our reference model (DLB07) does not include prescriptions to model the bulge size, that we use in our stellar stripping models. To overcome this limitation, we have updated the reference model including the prescriptions for bulge and disk growth described in Guo et al. (2011).

Both the gaseous and stellar components of the disk are assumed to follow an exponential profile. Assuming a flat circular velocity curve, the scale-lengths of these two components can be written as:

$$R_{sl}^g = \frac{J_{gas}/M_{gas}}{2V_{max}}, \quad R_{sl}^* = \frac{J_*/M_{*,disk}}{2V_{max}}, \quad (5.8)$$

where J_{gas} and J_* are the angular momenta of the gas and stars, M_{gas} and $M_{*,disk}$ are the gas and stellar mass of the disk, and V_{max} is the maximum circular velocity of the dark halo associated with the galaxy. Following Guo et al. (2011), we assume that the change in the angular momentum of the gas disk during a timestep can be expressed as the sum of the angular momentum changes due to addition of gas by cooling, accretion from minor mergers, and gas removal through star formation. The latter causes a change in the angular momentum of the stellar disk. We refer to the original paper by Guo et al. for details. We have verified that switching back to the simple model for disk sizes of Mo et al. (1998) used in our reference model, does not affect significantly the results discussed in the following².

Bulges grow through two different channels: mergers (both major and minor) and disk instability. Following Guo et al. (2011), we estimate the change in size due to a merger using energy conservation and the virial theorem:

$$\frac{GM_{new,b}^2}{R_{new,b}} = \frac{GM_1^2}{R_1} + \frac{GM_2^2}{R_2} + \frac{M_1M_2}{R_1 + R_2} \quad (5.9)$$

The same approach is adopted in case of disk instability, simply replacing R_1 and M_1 with the size and mass of the existing bulge, and R_2 and M_2 with the size and mass of the stars that are transferred from the disk to the bulge so as to keep the disk marginally stable. R_2 is determined assuming that the mass is transferred from the inner part of the disk, with the newly formed bulge occupying this region. Again, we refer to the original paper by Guo et al. (2011) for details on this implementation.

5.3 The Galaxy Stellar Mass Function

²Note that the disk size enters in the calculation of the star formation rate. Therefore, a change in the disk size model could, in principle, affect significantly model results.

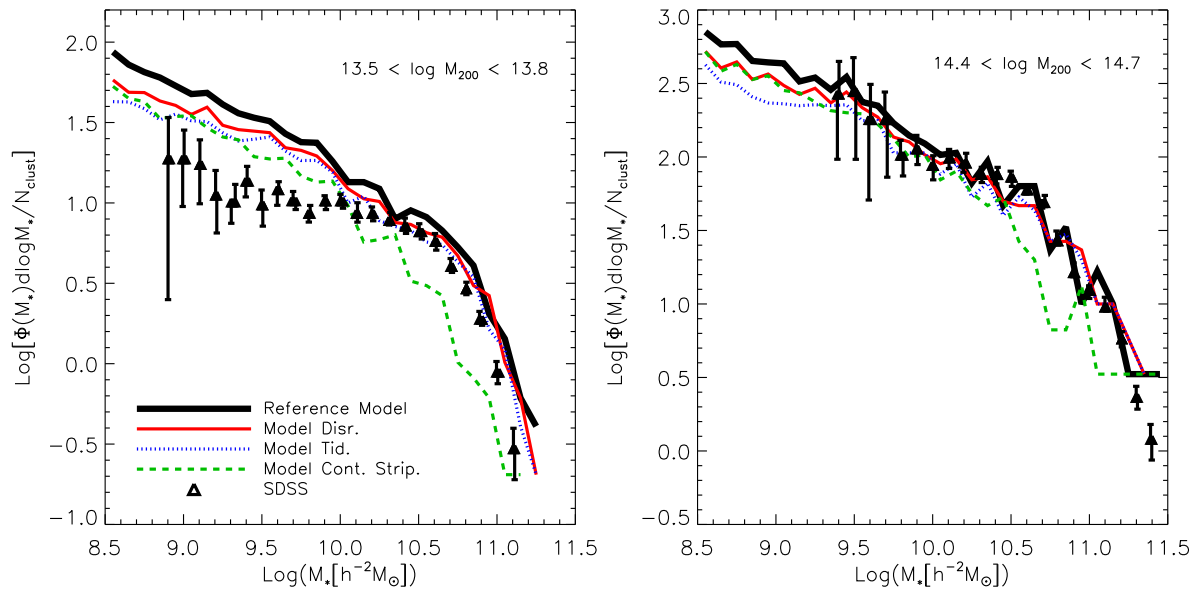


Figure 5.1: Left panel: The conditional stellar mass function of satellite galaxies in haloes in the mass range $13.5 < \log M_{200} [M_{\odot} h^{-1}] < 13.8$. Our simulations provide a total of 49 haloes in this mass range. Predictions from our reference model (DLB07) are shown by a solid black line, while predictions from our three models including disruption or/and stripping of satellite galaxies are shown by thinner lines of different style, as indicated by the legend. Symbols with error bars show observational measurements based on SDSS by Liu et al. (2010). Right panel: as in the left panel, but for the 3 haloes from our simulations with $14.4 < \log M_{200} [M_{\odot} h^{-1}] < 14.7$.

Before focusing our discussion on the ICL component, it is interesting to analyse how the proposed prescriptions affect one basic prediction of our model, that is the galaxy stellar mass function. In Figure 5.1, we show the conditional stellar mass function of satellite galaxies in the 49 haloes from our simulations that fall in the mass range $13.5 < \log M_{200}[M_{\odot}h^{-1}] < 13.8$ in the left panel, and in the 3 haloes from our simulations with $14.4 < \log M_{200}[M_{\odot}h^{-1}] < 14.7$ in the right panel. We show predictions from both our reference model (DLB07, shown as a solid black line), and from the three models including the treatments for the stripping and/or disruption of satellite galaxies discussed in Section 5.2 (lines of different style, see legend). Model predictions are compared with observational measurements by Liu et al. (2010). These are based on group catalogues constructed from the Sloan Digital Sky Survey (SDSS) Data Release 4, using all galaxies with extinction corrected magnitude brighter than $r = 18$ and in the redshift range $0.01 \leq z \leq 0.2$. We do not show here predictions from the models with the merger channel for the formation of the ICL switched on, as these do not deviate significantly from the corresponding models with the merger channel off.

For the lower halo mass range considered, the reference model fails in reproducing the observed stellar mass function, over-predicting the abundance of galaxies with stellar mass below $\sim 10^{10} M_{\odot}$. This problem is somewhat alleviated when including a model for stellar stripping, but not solved. In particular, our ‘disruption model’ (model Disr. in the figure and hereafter) does not significantly affect the abundance of the most massive satellites, while reducing the number of their lower mass counterparts (not by the amount required to bring model predictions in agreement with observational results). This is expected as this model only acts on Type 2 galaxies, that dominate the low-mass end of the galaxy mass function.

Predictions from the ‘tidal radius model’ (model Tid.) are not significantly different from those of model Disr., while the ‘continuous stripping model’ (model Cont. Strip.) significantly under-predicts the abundance of the most massive satellite galaxies. There are two possible explanations for this behaviour: (i) the abundance of massive satellites is reduced because these are significantly affected by our stripping model or (ii) these massive satellites have disappeared because they have merged with the central galaxies of their parent haloes. As discussed in Section 5.2.3, our model Cont. Strip. uses a different prescription for merger times with respect to that employed in the reference model and in models Disr. and Tid. We find that, in this model, merger times are on average shorter than in the other models, which is the reason for the under-prediction of massive satellites shown in Figure 5.1. As we will discuss in the following, this also implies that the stellar mass of the BCGs in model Cont. Strip. are on average larger than those predicted by models Disr. and Tid.

For the higher halo mass range considered, the observed number density of intermediate-to-low mass galaxies is higher, and all our models appear to be in agreement with observational measurements. The agreement remains good also at the massive end, with the

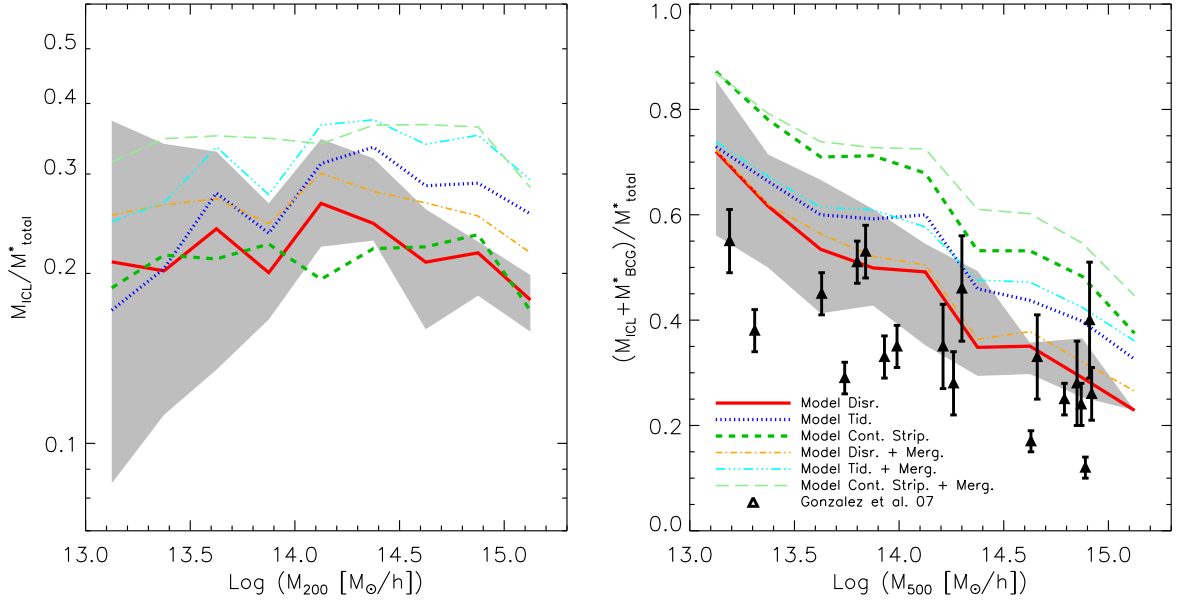


Figure 5.2: Left panel: ICL fraction as a function of halo mass. Lines of different style and colour show median results from different models, as indicated in the legend. Right panel: ratio between the ICL component plus BCG stellar mass and the total stellar mass within R_{500} . Symbols with error bars show observational estimates by Gonzalez et al. 2007. In both panels, the grey shaded region shows the 20th and 80th percentiles of the distribution for model Disr. The other models have comparable scatter.

exception of model Cont. Strip. that significantly under-predicts the number density of massive galaxies. As explained above, this is due to the shorter galaxy merger times used in this model.

We will show below that, in our models, the merger channel does not provide the dominant contribution to the ICL formation so that this is mainly driven by stripping and/or disruption of satellites. Therefore, the excess of intermediate to low-mass galaxies for haloes in the lower mass range might invalidate our predictions. However, as we will show below, the bulk of the ICL originates from relatively massive galaxies so that this particular failure of our models does not significantly affect our results.

5.4 ICL fraction and dependency on halo properties

We now turn our analysis to the ICL component, and start by analysing the overall fraction of ICL predicted by our models, and how it depends on halo properties. The left panel of Figure 5.2 shows the ICL fraction as a function of halo mass. To measure the predicted fractions, we have considered all galaxies within R_{200} and with stellar mass larger than

$M_* = 10^{8.3} M_\odot$, that approximately corresponds to the resolution limit of our simulations. Lines of different style and colour show the median relations predicted by our different prescriptions, as indicated in the legend. The grey region marks the 20th and 80th percentiles of the distribution found for model Disr. (the other models exhibit a similar dispersion).

The predicted fraction of ICL varies between ~ 20 per cent for model Disr. with the merger channel off, and ~ 40 per cent for model Cont. Strip. with the merger channel on. A relatively large halo-to-halo variation is measured for all models. For none of our models, we find a significant increase of the ICL fraction with increasing halo mass (see discussion in Section 5.1), at least over the range of M_{200} shown. In the figure, we have also considered the ICL associated with Type 1 galaxies within R_{200} of each halo. We stress, however, that their contribution is, on average, smaller than 7 per cent of the total ICL associated with the halo.

As expected, when including a merger channel for the formation of the ICL, its fraction increases, by about ~ 25 per cent in models Disr. and Tid., and by about ~ 50 per cent in model Cont. Strip. As mentioned in the previous Section, this difference is due to the different dynamical friction formula used in this model, which makes merger times significantly shorter than in the other two models. The amount of ICL that comes from the merger channel is not negligible in the framework of our models and, as expected, increases in the case of shorter merger times. Overall, predictions from our models agree well with fractions of ICL quoted in the literature, i.e. 10 – 40 per cent going from groups to clusters (e.g. Feldmeier et al. 2004; Zibetti 2008; McGee & Balogh 2010; Toledo et al. 2011).

As discussed in Section 5.1, it is not an easy task to separate the ICL from the stars that are bound to the BCG. To avoid these difficulties, and possible biases introduced by the adoption of different criteria in the models and in the observations, we consider the ratio $(M_{ICL} + M_{BCG}) / M_{total}^*$. The right panel of Figure 5.2 shows how this fraction varies for the different models considered in this study, and compares our model predictions with observational measurements by Gonzalez et al. (2007). To be consistent with these observational measurements, we consider in this case all galaxies within R_{500} and brighter than $m_I = 18$ (i.e. galaxies more massive than $\sim 10^{10} M_\odot$). Considering the scatter in both our model predictions and in the observational data, the Figure shows that model Disr. (as well as its variation with the merger channel on) is in relatively good agreement with observational data, though it tends to predict higher ratios for the lowest halo masses considered. Model Tid. predicts a higher fraction of stars in ICL+BCG than model Disr., and the median relation lies close to the upper envelope of the observational data. Finally, model Cont. Strip. over-predicts the fraction of stars in ICL+BCG over the entire mass range considered.

The merger channel does not affect the predicted trend as a function of halo mass, but this channel increases on average the fraction of stars in ICL+BCG. This is surprising: stars that are contributed to the ICL through the merger channel would contribute to the BCG

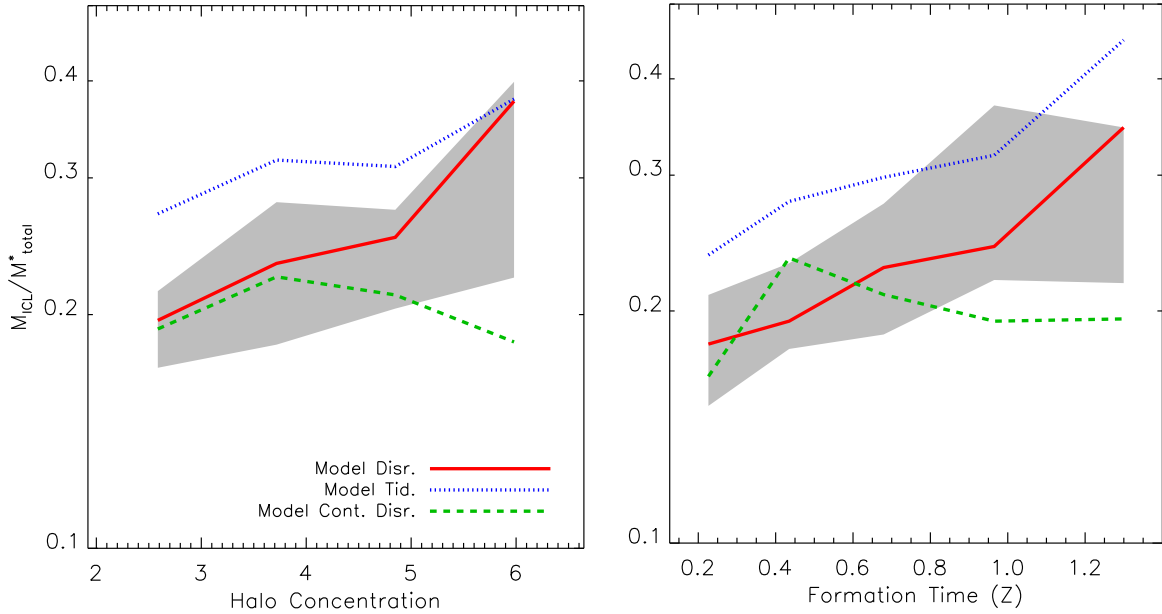


Figure 5.3: Left Panel: Fraction of ICL as a function of halo concentration for the 53 haloes from our simulations with $M_{200}[M_{\odot}/h] > 10^{14}$. Halo concentration is defined as $c_{200} = r_s/r_{200}$, where r_s is the characteristic scale obtained by fitting the halo density profile to a NFW profile. Right Panel: Fraction of ICL as a function of halo formation time, defined as the time when the main progenitor of the halo has acquired 50 per cent of its final mass. Predictions from different models are shown by lines of different colour, as indicated in the legend. The grey shaded region shows the 20th and 80th percentile of the distribution found for model Disr.

mass if the channel is off so that the merger channel should not affect the sum of the ICL and BCG stellar masses. The difference found is due to slight changes in the merger history of the BCGs, due to variations in the merger times of satellite galaxies. In fact, satellite merger times become slightly longer than in a model that does not include stellar stripping because satellite galaxies gain less stellar mass through accretion as central galaxies (also the satellites that were accreted on them were stripped). Because of the shorter merger times mentioned above, model Cont. Strip. is affected more by this change.

As discussed above, the ICL fraction predicted by our models does not vary as a function of the host halo mass but exhibits a relatively large halo-to-halo scatter, particularly at the group mass scale. The natural expectation is that this scatter is largely determined by a variety of mass accretion histories at fixed halo mass. We can address this issue explicitly using our simulations. In Figure 5.3, we show how the ICL fraction correlates with the halo concentration in the left panel, and with the halo formation time in the right panel. We note that these two halo properties are correlated (see e.g. Giocoli et al., 2012).

As usually done in the literature, we have defined the formation time of the halo as the time when its main progenitor has acquired half of its final mass. The concentration has been computed by fitting the density profile of the simulated haloes with a NFW profile (Navarro, Frenk, & White, 1996). To remove the known correlations between halo mass and concentration/formation time (Bullock et al., 2001; Neto et al., 2007; Power et al., 2012), we consider in Figure 5.3 only the 53 haloes from our simulations with $M_{200}[M_{\odot}/h] > 10^{14}$. As in previous figures, we show the dispersion (20th and 80th percentiles of the distribution) only for model Disr. The other two models exhibit a similar scatter.

The figure shows that, for the halo mass range considered, the ICL fraction increases with increasing concentration/formation time for models Disr. and Tid while remaining approximately constant for model Cont. Strip. Therefore, for models Disr. and Tid., large part of the scatter seen in Figure 5.2 for haloes in the mass range considered can be explained by a range of dynamical histories of haloes. Haloes that ‘formed’ earlier (those were also more concentrated) had more time to strip stars from their satellite galaxies or accumulate ICL through accretion of smaller systems, and therefore end up with a larger fraction of ICL. For model Cont. Strip., no clear trend as a function of either halo concentration or halo formation time is found. This happens because, contrary to the other two models, the way we model stellar stripping in the Cont. Strip. model does not introduce any dependence on halo concentration. In this model, the amount of stellar mass stripped from satellite galaxies depends only on properties computed at the time of accretion (i.e. mass ratio, circularity of the orbit). In contrast, in models Disr. and Tid., the stripping efficiency is computed considering the instantaneous position of satellite galaxies. Dynamical friction rapidly drags more massive satellites (those contributing more to the ICL) towards the centre, where stripping becomes more efficient. Our results show that equation 5.6 is not able to capture this variation, although it is by construction included in the simulations used to calibrate our model.

For lower mass haloes, there is no clear correlation between ICL fraction and the two halo properties considered. This is in part due to the fact that, as we will see in the next section, the bulk of the ICL forms very late - later than the typical formation time of low-mass haloes. In this low-mass range, large part of the scatter in the ICL fraction is driven by the fact that these haloes typically contain relatively few massive galaxies, that are those contributing the bulk of the ICL (see next section). So it is the scatter in the accretion of single massive galaxies that drives the relatively large dispersion seen in Figure 5.2 for haloes with mass smaller than $10^{14} M_{\odot}$. We have explicitly verified this by considering the 20 per cent haloes in this mass range with the highest and lowest ICL fractions. We find that for those haloes that have larger ICL components, this has been contributed by a few relatively massive satellite galaxies (stellar mass larger than $10^{10} M_{\odot}$). In contrast, the ICL in haloes with lower ICL fractions was contributed by less massive satellite galaxies.

In a recent work, Purcell et al. (2007) study how the fraction of ICL varies over a wide range of halo masses (from that of spiral galaxies like our Milky Way to that of massive

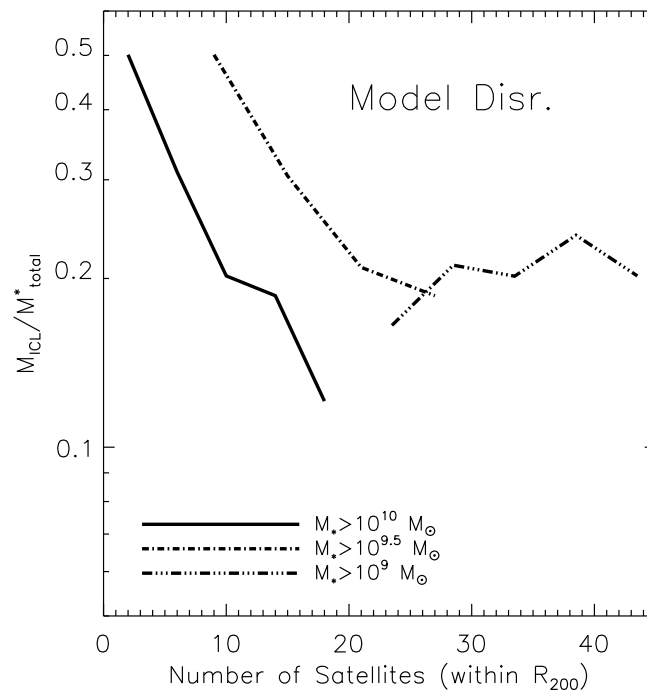


Figure 5.4: Fraction of ICL as a function of the number of satellites within R_{200} , with mass larger than the thresholds indicated in the legend. The figure refers to haloes in the mass range $10^{13.4} < M_{200}[M_{\odot}h^{-1}] < 10^{13.6}$, and to the model Disr.

galaxy clusters) using an analytic model for subhalo infall and evolution, and empirical constraints to assign a stellar mass to each accreted subhalo. In their model, the stellar mass associated with a subhalo is assumed to be added to the diffuse component when a certain fraction of the subhalo dark matter mass has been stripped by tidal interaction with the parent halo. In particular, their fiducial model assumes that disruption of the stellar component starts when 20 per cent of the subhalo mass remains bound. Over the range of halo masses sampled in our study, Purcell et al. (2007) predict a weak increase of the ICL fraction, from ~ 20 per cent for haloes of mass $\sim 10^{13} M_{\odot}$ to about 30 per cent for massive galaxy clusters of mass $\sim 10^{15} M_{\odot}$. One specific prediction of their model is that the fraction of ICL correlates strongly with the number of surviving satellite galaxies. As they explain, this correlation arises from the fact that haloes that acquired their mass more recently had relatively less time to disrupt the subhaloes they host, and therefore have less ICL.

We analyse the same correlation within our models in Figure 5.4. This shows the ICL fraction as a function of the number of satellite galaxies within R_{200} for haloes in the mass range $10^{13.4} < M_{200}[M_{\odot}h^{-1}] < 10^{13.6}$, and for model Disr.. Lines of different style correspond to different mass cuts, as indicated in the legend. The figure shows that, when considering all galaxies with stellar mass larger than $10^9 M_{\odot}$, no significant trend is found between the ICL fraction and the corresponding number of surviving satellite galaxies (this number ranges between ~ 20 and ~ 45 for this stellar mass cut). When increasing the stellar mass cut, the number of surviving satellites decreases (as expected), and a trend appears in the sense that larger ICL fractions are measured for lower numbers of surviving satellites. Similar trends are found for model Tid., while for model Cont. Strip. no trend is found between the number of surviving satellites and the ICL fraction, for any mass cut used.

5.5 Formation of the ICL

In this section, we take advantage of our models to analyse when the bulk of the ICL forms, which galaxies provide the largest contribution to it, what is the fraction of ICL that has been accreted from other haloes during the hierarchical growth of clusters, and what fraction is instead contributed from the merger channel.

In Figure 5.5, we show the contribution to the ICL from galaxies with different stellar mass. For model Disr., the galaxy mass on the x-axis corresponds to that of the satellite right before its disruption, while for model Cont. Strip. it corresponds to the satellite mass before stripping takes place. For model Tid., both cases can occur. The distributions shown in Figure 5.5 represent the average obtained considering all haloes in our simulated sample. When considering haloes in different mass bins, the distributions are similar but, as expected, they shift towards lower stellar masses for lower mass haloes.

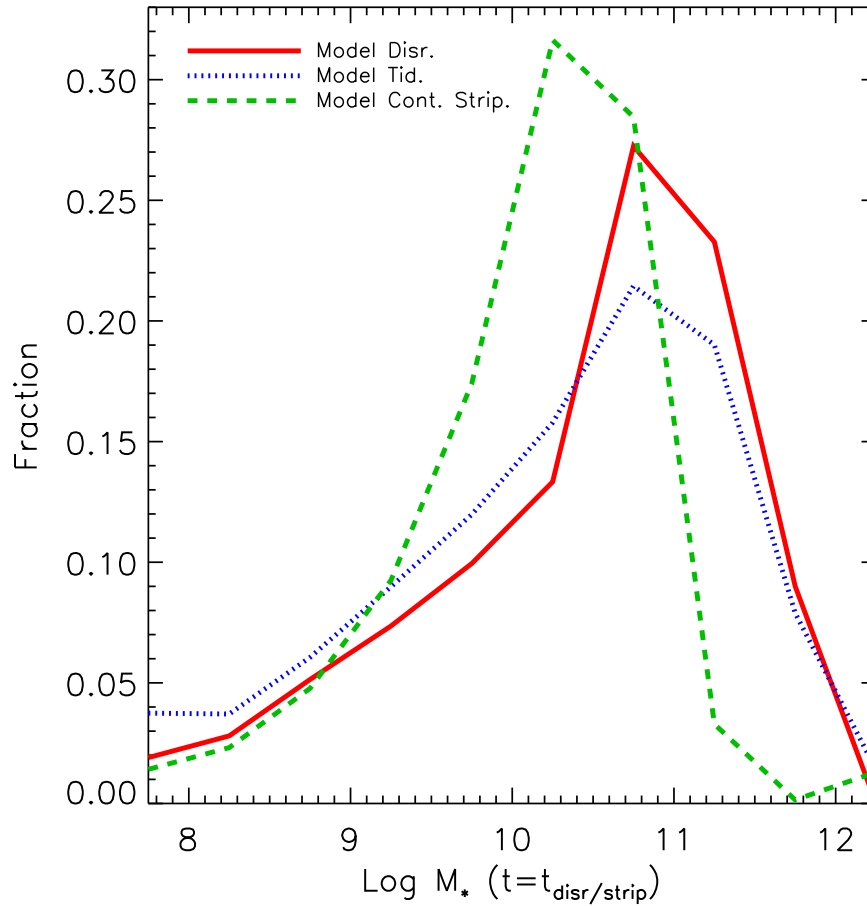


Figure 5.5: Fraction of the ICL component as a function of the galaxy stellar mass that contributed to it. In the case of model Disr., the galaxy stellar mass on the x-axis refers to the mass that the satellite has before its disruption. For model Cont. Strip., it corresponds to the satellite mass before stripping takes place. For model Tid., both cases can occur.

The figure shows that the bulk of the ICL comes from galaxies with stellar masses $\sim 10^{11} M_{\odot}$ for models Disr. and Tid., and $\sim 10^{10.3} M_{\odot}$ for model Cont. Strip. In particular, we find that for models Disr. and Tid., about 26 per cent of the ICL is contributed by galaxies with stellar mass in the range $10^{10.75} - 10^{11.25} M_{\odot}$. About 68 per cent comes from satellites more massive than $10^{10.5} M_{\odot}$, while dwarf galaxies contribute very little. For model Cont. Strip., almost all the ICL mass (~ 90 per cent of it) comes from satellites with mass in the range $10^9 - 10^{11} M_{\odot}$. The merger channel does not affect significantly the distributions shown.

The result discussed above can be easily understood in terms of dynamical friction: the most massive satellites decay through dynamical friction to the inner regions of the halo on shorter time-scales than their lower mass counterparts. Tidal forces are stronger closer to the halo centre, so that the contribution to the ICL from stripping and/or disruption of massive galaxies is more significant than that from low mass satellites. The latter tend to spend larger fractions of their lifetimes at the outskirts of their parent halo, where tidal stripping is weaker.

The differences between predictions from models Disr. and Tid. and those from model Cont. Strip. are due to a combination of different effects. On one side, model Cont. Strip. uses a different merger time prescription that leads to significantly shorter merger times than in models Disr. and Tid. This is particularly important for the most massive satellites that have the shortest merger times. In addition, while in models Disr. and Tid. satellite galaxies can be completely destroyed, stripping takes place in a more continuous and smooth fashion in model Cont. Strip. These two effects combine so that the largest contribution to the ICL in this model comes from ‘intermediate’ mass satellites that orbit long enough in the cluster potential to be affected significantly by stellar stripping.

Similar results have been found in other studies. In the work by Purcell et al. (2007) mentioned above, the ICL on the cluster mass scale is largely produced by the disruption of satellite galaxies with mass $\sim 10^{11} M_{\odot}$. In a more recent work, Martel et al. (2012) combine N-body simulations with a sub-grid treatment of galaxy formation. They find that about 60 per cent of the ICL in haloes more massive than $\sim 10^{14} M_{\odot}$ is due to the disruption of galaxies with stellar mass in the range $6 \times 10^8 - 3 \times 10^{10} M_{\odot}$. Their results are close to predictions from our model Cont. Strip., with an enhanced contribution of intermediate-mass galaxies with respect to the other two models discussed in this study and results from Purcell et al. (2007). However, in agreement with our results and those from Purcell et al. (2007), they also find that the contribution from low-mass galaxies to the ICL is negligible, though they dominate the cluster galaxy population in number.

The analysis discussed above answers the question on ‘which’ galaxies contribute (most) to the ICL component. We can now take advantage of results from our models to ask ‘when’ the ICL is produced. We address this issue in Figure 5.6 that shows the ICL fraction (normalized to the total amount of ICL measured at present) as a function of cosmic time, for all different prescriptions used in this study (thick lines of different colour and style).

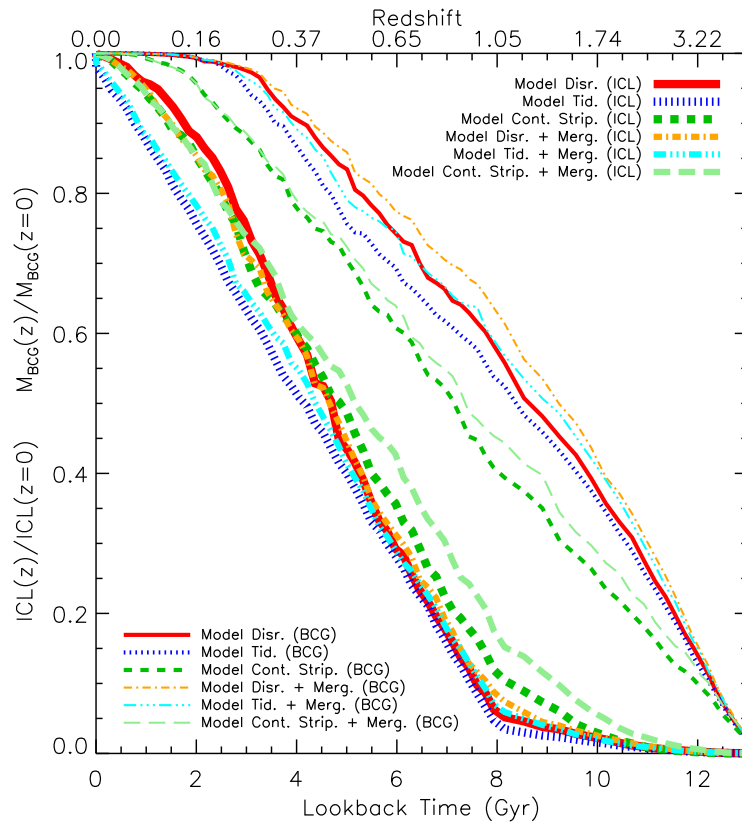


Figure 5.6: Fraction of stellar mass in ICL as a function of the look-back time, normalized to the amount of ICL at present (thick lines of different style and colour). Thinner lines show the evolution in the stellar mass of the main progenitor of BCGs as a function of lookback time.

The cosmic evolution of the ICL component is compared with the evolution of the stellar mass in the main progenitor of the corresponding BCGs, shown as thin lines.

In agreement with previous studies both based on simulations (Willman et al., 2004; Murante et al., 2007) and on analytic or semi-analytic models (Conroy et al., 2007; Monaco et al., 2006), we find that the bulk of the ICL forms relatively late, below $z = 1$. Models Disr. and Tid. predict very similar ICL growth histories, while in model Cont. Strip. the ICL formation appears to be anticipated with respect to the other two models. At redshift ~ 1 , less than 10 per cent of the ICL was already formed in models Disr. and Tid. If the merger channel for the formation of the ICL is switched on in these models, the ICL fraction formed at the same redshift increases to $\sim 15 - 20$ per cent. As explained earlier, the importance of the merger channel is enhanced in model Cont. Strip. The figure also shows that the ICL grows slower than the mass in the main progenitor of the BCG down to $z \sim 1$, i.e. at a lookback time of ~ 8 Gyr. Below this redshift, the ICL component grows much faster than the BCG, with more than 80 per cent of the total ICL mass found at $z=0$ being formed during this redshift interval.

We now want to quantify what is the fraction of ICL that is accreted onto the cluster during its hierarchical growth. As explained in Section 5.2, the amount of ICL associated with a central galaxy can increase through three channels:

- (i) stripping of satellite galaxies orbiting in the same parent halo;
- (ii) mergers, if this particular channel is switched on;
- (iii) accretion of the ICL component that is associated with new galaxies infalling onto the cluster during its assembly history or with satellite galaxies (i.e. when a Type 1 becomes a Type 2 galaxy in model Disr. or when a Type 1 is stripped for the first time in models Tid. and Cont. Strip).

In the following, we define the ‘accreted’ component as the ICL fraction that is coming through the third channel described above. The contribution from this component is shown in the top panel of Figure 5.7 as a function of the stellar mass of the BCG. In models Disr. and Tid., the fraction of the accreted component increases from a few per cent for the least massive BCGs in our sample to $\sim 13 - 25$ per cent for the most massive BCGs, in case the merger channel is off. For model Cont. Strip., the increase as a function of the BCG stellar mass is less pronounced, and the fraction of accreted ICL is always below 10 per cent even in the case the merger channel is on.

The bottom panel of Figure 5.7 quantifies the amount of ICL that comes from the merger channel. If this channel is switched on, as we have seen in the left panel of Figure 5.2, the ICL fraction increases in each model. We note that the amount of ICL that comes from this channel cannot be inferred precisely by comparing each model in Figure 5.2 with its counterpart including the merger channel, because it affects slightly the merger times of galaxies. The contributions to the ICL coming from mergers are shown in the bottom panel

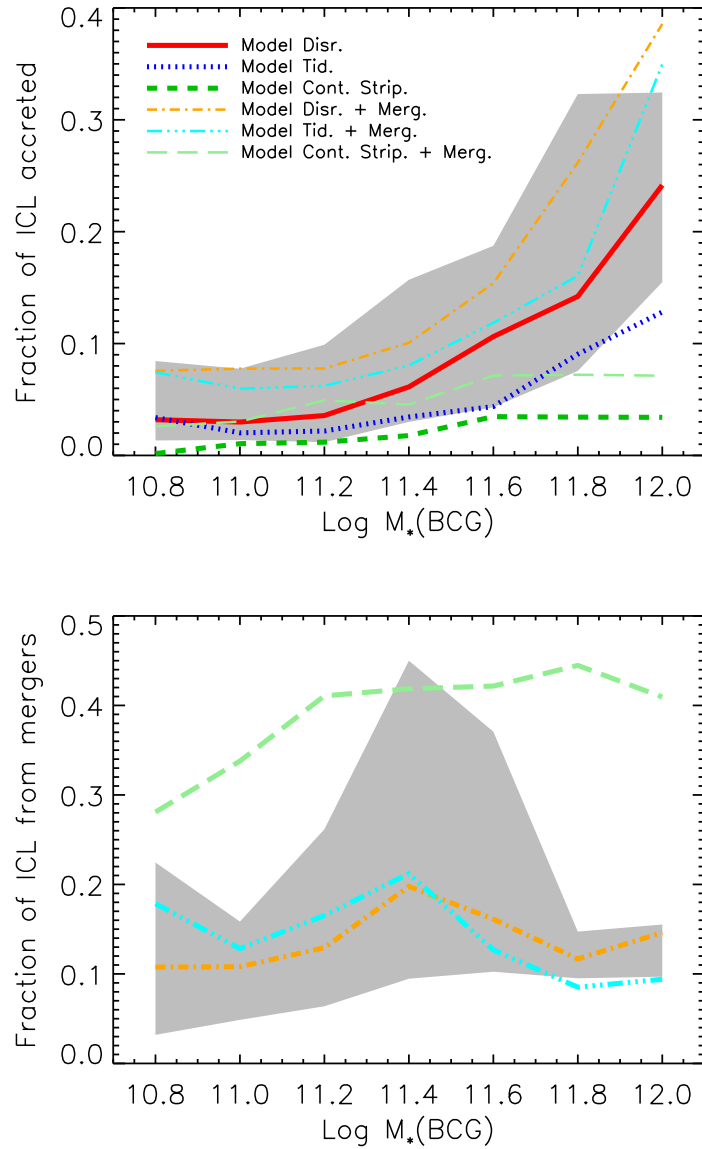


Figure 5.7: Top panel: fraction of accreted ICL as a function of the BCG stellar mass. Bottom panel: fraction of ICL contributed by the merger channel as a function of the BCG stellar mass. The grey shaded region shows the 20th and 80th percentiles of the distribution measured for model Disr. The other models exhibit similar dispersions.

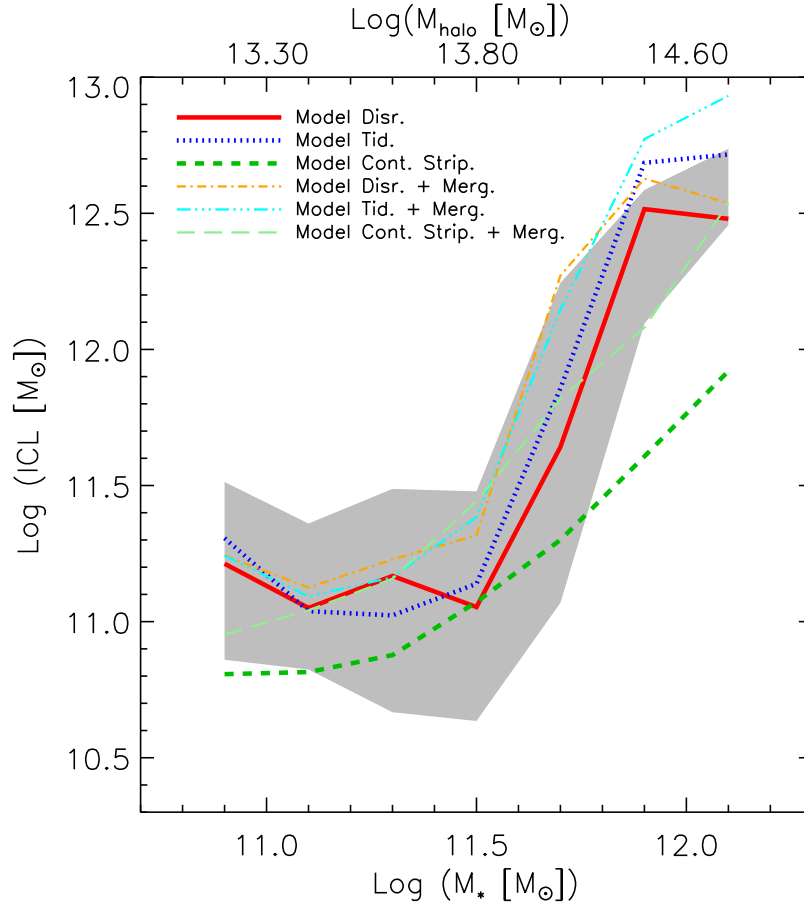


Figure 5.8: Stellar mass in the ICL component as a function of the BCGs stellar mass. Lines of different style and colour correspond to different models, as indicated in the legend. The grey shaded region shows the 20th and 80th percentiles of the distribution obtained for model Disr.

of Figure 5.7, and have been stored using the three prescriptions used in this study with the merger channel on. We find that in models Disr. and Tid. the merger channel contributes to ~ 15 per cent of the total ICL. For model Cont. Strip., the contribution from mergers is significantly larger, ranging from ~ 30 per cent for the least massive BCGs in our sample, to ~ 40 per cent for the most massive ones.

5.6 ICL and BCG properties

We now focus on the relation between the ICL and the main properties of BCGs, such as stellar mass and luminosity, and analyse how these are affected by the inclusion of our prescriptions for the formation of the ICL.

In Figure 5.8 we show the relation between the mass in the ICL component and the stellar mass of the BCG. As expected, more massive BCGs reside in haloes that host a more conspicuous ICL component. For models Disr. and Tid., the correlation is strong for BCGs more massive than $\sim 3 \times 10^{11} M_{\odot}$, while it is very weak for less massive central galaxies. Model Cont. Strip. predicts a weaker correlation over the mass range explored, and a significantly lower mass in the ICL component with respect to the other two models when the merger channel is off.

Figure 5.9 shows the luminosity of the BCG in the K-band as predicted by our models as a function of the halo mass. Model predictions are compared with observational measurements by Lin & Mohr (2004) and Popesso et al. (2007a). It is worth recalling that our model luminosities are ‘total’ luminosities, that are difficult to measure observationally: Popesso et al. (2007a) use SDSS ‘model magnitudes’, while Lin & Mohr (2004) use elliptical aperture magnitudes corresponding to a surface brightness of $\mu_K = 20 \text{ mag/arcsec}^2$, and include an extra correction of 0.2 mag to get their ‘total magnitudes’. Our reference model is in very good agreement with both sets of observational data. Models Disr. and Tid. predict slightly lower luminosities than our reference model, as a consequence of the reduced accretion of stellar mass from satellites (either because part of these are destroyed - model Disr., or because they are stripped - model Tid.). Model Cont. Strip. predicts luminosities of central galaxies brighter than those measured by Popesso et al., on the cluster mass scale. This is due to the fact that, as mentioned earlier, merger times are shorter in this model, which increases the stellar mass and the luminosity of the BCGs by accretion of (massive) satellites.

Surprisingly, we find that also in models Disr. and Tid. a small fraction of the BCGs are brighter (more massive) than in the reference model. Naively, we do not expect this to be possible as the only effect of our prescriptions should be that of reducing the stellar mass of satellite galaxies by stripping or disruption. In Figure 5.10, we show the ratio between the BCG stellar mass in the reference model and the corresponding stellar mass in model Disr., as a function of the former quantity. The Figure shows that the majority of the BCGs are more massive in the reference model, but about 23 per cent of the BCGs in our sample are actually *more* massive when we switch on our prescription for the disruption of satellite galaxies. If we additionally switch on the merger channel for the formation of the ICL, the fraction of BCGs that are more massive in model Disr. than in the reference model reduces to about 10 per cent. Model Tid. behaves in a similar way (the corresponding fractions are 28 and 9 per cent, respectively). Model Cont. Strip., as also evident from Figure 5.9 behaves differently. In this model, about half (42 per cent) of the BCGs are more massive than in the reference model, with this fraction reducing to about 26 per cent when the merger channel is switched on. While in model Disr. (and Tid.) the effect seems to be limited to the less massive BCGs (those with stellar mass lower than $\sim 10^{11.5} M_{\odot}$), in model Cont. Strip. this happens for BCGs of any mass.

In order to understand this finding, we have analysed the evolution of the stellar mass,

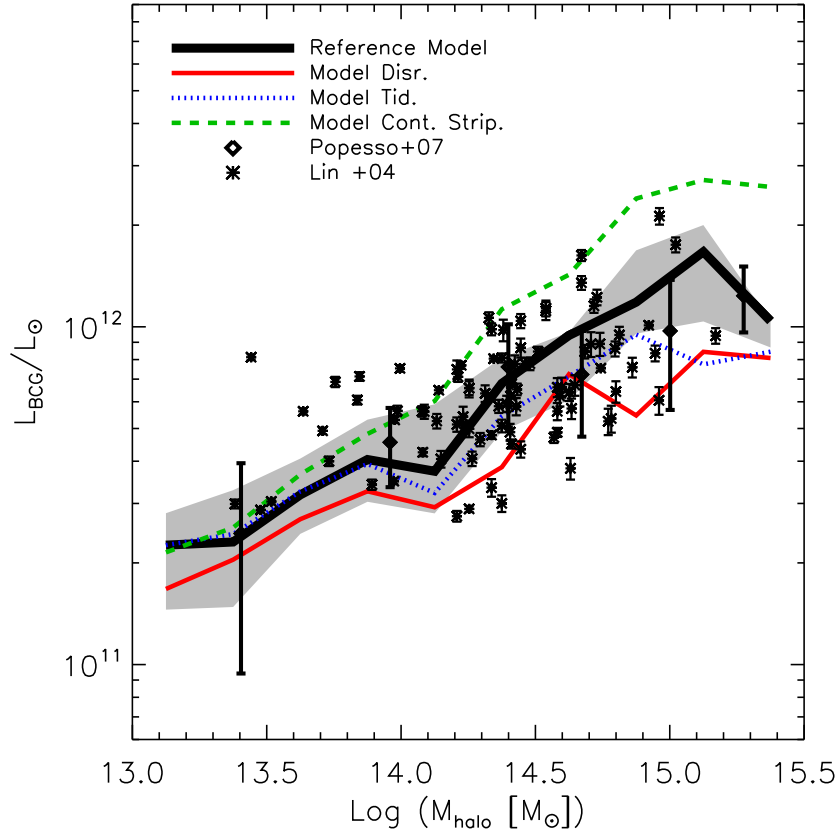


Figure 5.9: Relation between the BCG luminosity in K-band and the cluster mass (M_{200}). Black stars with error bars show the observational measurements by Lin & Mohr (2004), while black diamonds with error bars are observational measurements by Popesso et al. (2007a). The thick black solid line shows predictions from our reference model (DLB07), while thinner lines of different style show predictions from the models including our different prescriptions for the formation of the ICL. The grey shaded region shows the 20th and 80th percentiles of the distribution obtained for the reference model. Our other models have comparable scatter.

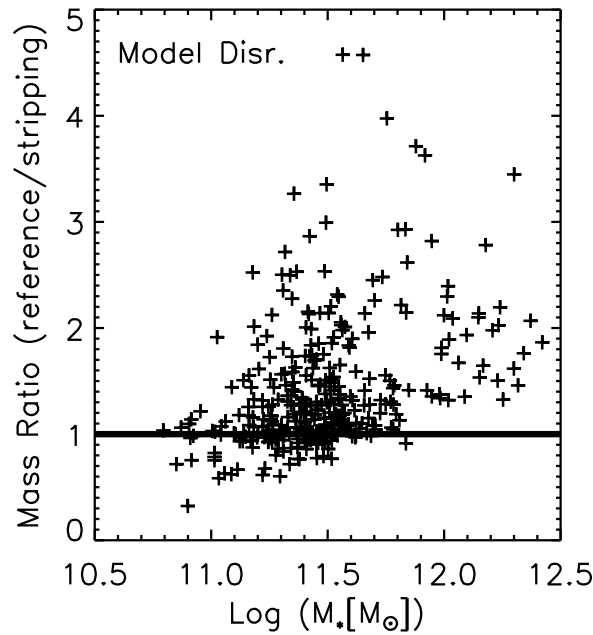


Figure 5.10: Ratio between the stellar mass of BCGs in the reference model and the corresponding value in model Disr., as a function of the stellar mass in the reference model, at $z = 0$.

mass gained through mergers, and cooling rate for a number of the BCGs that are more massive in model Disr. than in the reference model. We have found that in all cases, the reason for the increased mass of the BCGs can be traced back to a more efficient cooling rate. In order to illustrate this, we show in Figure 5.11 a representative example. The top panel shows the amount of hot gas available for cooling onto the main progenitor of the BCG, up to $z \sim 3$, while the bottom panel shows the corresponding metallicity. Results are shown for the reference model, and for our models Disr. and Cont. Strip. (model Tid. behaves similarly to the reference model). For this particular BCG, the evolution of both the hot gas content and that of its metallicity in model Disr. follow very closely the evolution in the reference model. At $z \sim 1.5$, the metallicity of the hot gas in model Disr. becomes higher than in the reference model, and this causes a significant increase in the cooling rate. In turn, the more efficient cooling determines an increase in the star formation, and therefore of the final BCG stellar mass. The behaviour is different in model Cont. Strip. where the metallicity of the hot gas actually falls below the corresponding value in the reference model. As we have explained earlier, for this particular model we have used a different implementation of the merger times which introduces a net decrease in the merger time of satellite galaxies. This more rapid merger rates causes about half of the BCGs to be more massive in model Cont. Strip. than in the reference model.

The difference in the hot gas metallicity of the BCG between model Disr. and Cont.

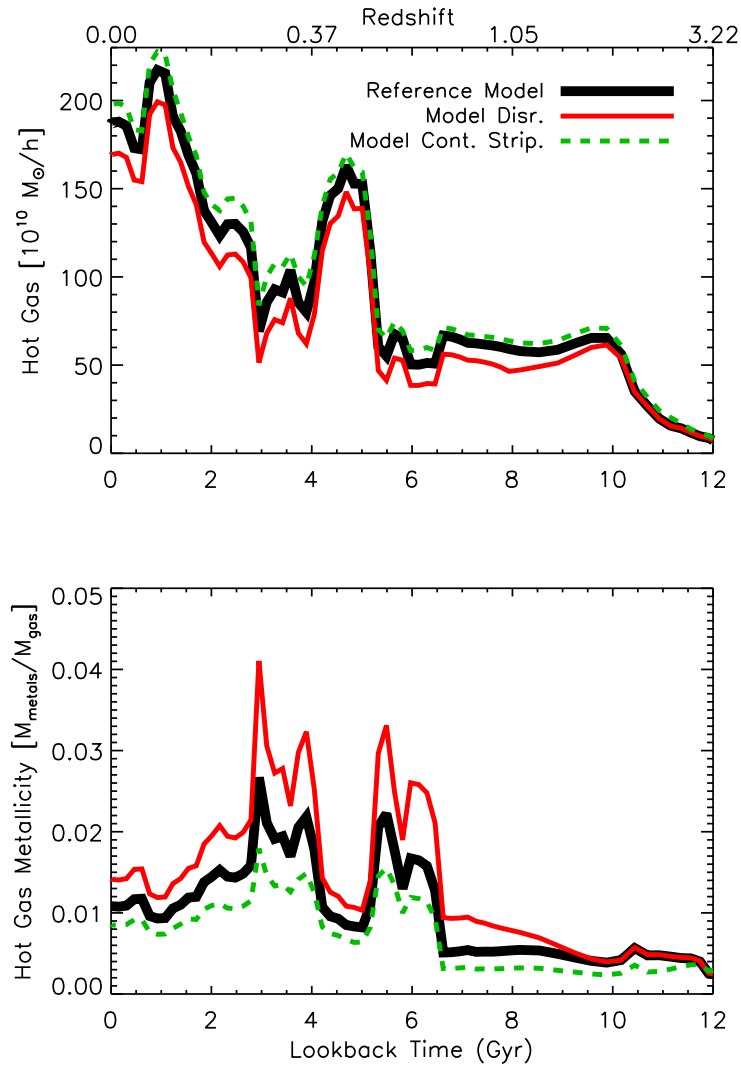


Figure 5.11: Top panel: Mass in the hot component available at each redshift, for a BCG that is found to be more massive in model Disr. (and less massive in model Cont. Strip.) than in the reference model. Bottom panel: hot gas metallicity at each redshift. Results are shown for different models, as indicated in the legend.

Strip. is due to a different metal content of the gas accreted from satellite galaxies. We recall that when a satellite galaxy is destroyed (or stripped), its stellar mass goes to the ICL while its gaseous content, including the corresponding metals, go to the hot gas component associated with the central galaxy. In model Cont. Strip., stripping is a continuous process that starts as soon as a galaxy becomes a satellite. In addition, in this model the formation of the ICL component starts earlier than in the other models, as shown in Figure 5.6. In this case, the gas that is removed from satellites tends to dilute the metallicity of the hot gas component. In model Disr. (as well as in model Tid.), the formation of the ICL starts a bit later, and satellite galaxies are more massive than in model Cont. Strip. (and therefore also more metal rich - see Figure 5.5), so that their disruption tends on average to increase the metal content of the hot gas component.

5.7 ICL metallicity

From the observational viewpoint, little is known about the stellar populations of the ICL component. Using I-band HST data, Durrell et al. (2002) compared the brightness of Virgo ICL red giant branch (RGB) stars to that of RGB stars in a metal-poor dwarf galaxies, and estimated an age for the ICL population older than ~ 2 Gyr, and a relatively high metallicity ($-0.8 \lesssim [\text{Fe}/\text{H}] \lesssim -0.2$). Williams et al. (2007) use HST observations of a single intra-cluster field in the Virgo Cluster and find that the field is dominated by low-metallicity stars ($[\text{M}/\text{H}] \lesssim -1.$) with ages older than ~ 10 Gyr. However, they find that the field contains stars of the full range of metallicities probed ($-2.3 \leq [\text{M}/\text{H}] \leq 0.0$), with the metal-poor stars exhibiting more spatial structure than metal-rich stars, suggesting that the intra-cluster population is not well mixed. Using long-slit spectra and measuring the equivalent width of Lick indices, Coccato et al. (2011) find that most of the stars in the dynamically hot halo of NGN3311 (the BCG in the Hydra I cluster) are old and metal-poor ($[\text{Z}/\text{H}] \sim -0.35$).

In this section, we present predictions of our models concerning in particular the metallicity of the ICL component. We recall that our model adopts an instantaneous recycling approximation for chemical enrichment. In particular, we assume that a constant yield of heavy elements is produced per solar mass of gas converted into stars, and that all metals are instantaneously returned to the cold phase. Metals are then exchanged between the different phases proportionally to the mass flows. When a satellite galaxy is stripped of some fraction of its stars (or destroyed), a proportional fraction (or all) of the metals are also moved from the satellite stars into the ICL.

The left panel of Figure 5.12 shows the median metallicity of the ICL component, as a function of halo mass, for our different prescriptions. The grey shaded region shows

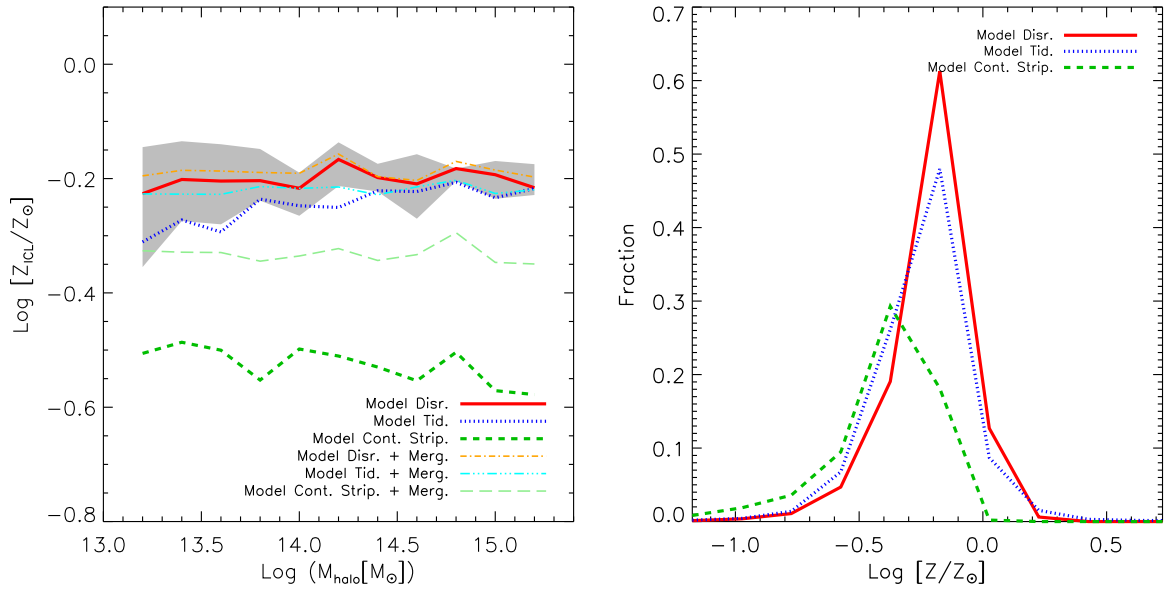


Figure 5.12: Left panel: mean metallicity of the ICL component as a function of halo mass. Predictions from different models are shown using lines of different style and colour. The shaded grey region shows the 20th and 80th percentiles of the distribution obtained for model Disr. Right panel: average distribution of the metallicities of the stars in the ICL component for all haloes in our sample.

the 20th and 80th percentiles of the distribution found for model Disr. (the other models exhibit similar dispersions). In our models, the ICL metallicity does not vary significantly as a function of the halo mass. Assuming $Z_{\odot} = 0.02$, the average metallicity of the ICL in models Disr. and Tid. is $\sim 0.63Z_{\odot}$, while for model Cont. Strip. the ICL metallicity is significantly lower ($\sim 0.32 - 0.50Z_{\odot}$). This is a consequence of the fact that the galaxies contributing to the ICL are on average less massive (and more metal-poor) than those that contribute to the ICL in models Disr. and Tid. (see Figure 5.5). In the right panel of Figure 5.12, we show the average metallicity distribution of stars in the ICL component for all haloes in our sample. As a consequence of the results shown in Figure 5.5, model Cont. Strip. predicts a distribution shifted towards lower metallicities, with a peak at $\sim 0.4Z_{\odot}$. Models Disr. and Tid. predict distributions that are less broad and peaked at higher metallicities.

Our model results are therefore qualitatively consistent with observational measurements by Williams et al. (2007), with most of the stars in the ICL having sub-solar metallicity but covering a relatively wide range.

Figure 5.13 shows the BCG metallicity predicted by the different models used in our study, as a function of the halo mass. The figure shows that all models predict very similar metallicities for the BCGs, of about $0.74Z_{\odot}$. Predictions are close to those of the reference model (thick solid black line). On average, stellar stripping slightly increases the BCG

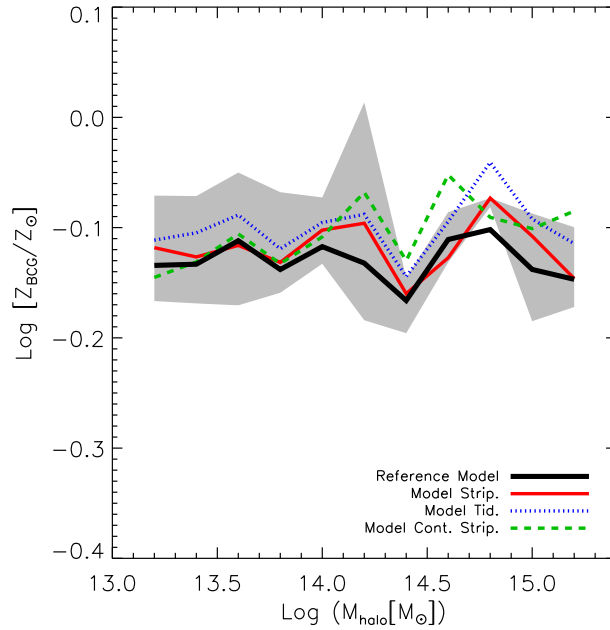


Figure 5.13: BCG stellar metallicity as a function of halo mass. Lines of different style and colour correspond to the different prescriptions used in our study, as indicated in the legend. The thick solid black line shows predictions from our reference model.

metallicity, particularly in model Tid. This happens because the most massive galaxies receive less low-metallicity stars from satellite galaxies whose masses (and metal contents) are reduced because of stellar stripping.

Our results confirm findings by De Lucia & Borgani (2012) who show that the model mass-metallicity relation is offset low with respect to the observational measurements at the massive end. In particular, the observed BCG metallicities (similar to those of the most massive galaxies) are expected to be at least 0.2-0.3 dex larger (von der Linden et al., 2007; Loubser et al., 2009). Figure 5.13 shows that the inclusion of a model for the formation of the ICL component does not significantly improve this disagreement. More in general, we find that our modelling of the formation of the ICL component does not significantly affect the predicted mass-metallicity relation. This is in apparent contrast with findings by Henriques & Thomas (2010) who claim that the introduction of satellite disruption is sufficient to bring the stellar metallicities of the most massive galaxies in agreement with the observational data. We note that Henriques & Thomas (2010) use the same reference model adopted in our study and employ a Monte Carlo Markov Chain parameter estimation technique to constrain the model with the K-band luminosity function, the B-V colours, and the black hole-bulge mass relation. The ‘best fit’ model found by Henriques & Thomas (2010) includes a model for tidal stripping of the satellite galaxies, but also adopts different parameters with respect to the reference model, in particular for the supernovae feedback

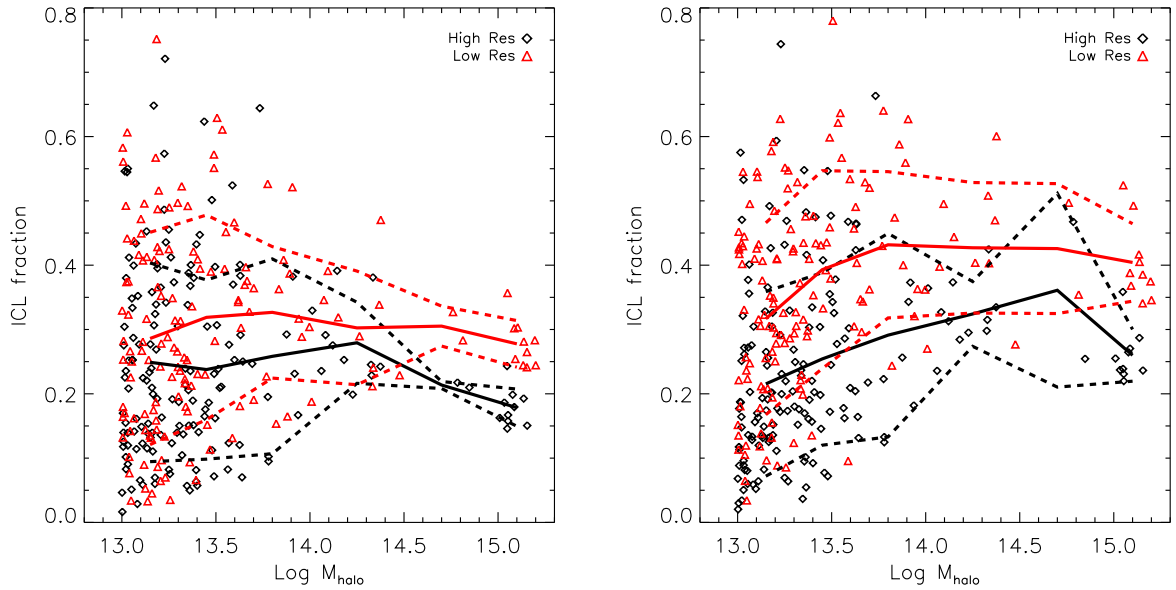


Figure 5.14: Left Panel: ICL fraction predicted by the Disruption model as a function of halo mass, for haloes in the high resolution set used in this paper (black lines and symbols), and the corresponding low-resolution version (red lines and symbols). Dashed lines show the one sigma dispersion, while solid line correspond to the mean. Right Panel: same as the left panel, but for Tidal Radius model.

and gas recycling process (see their Table 2). We therefore argue that, as discussed also in De Lucia & Borgani (2012), that stellar stripping cannot provide alone the solution to the problem highlighted above, and that modifications of the star formation and feedback processes are required.

5.8 Numerical Convergence

In the left panel of Figure 5.14 we show the ICL fraction as a function of cluster mass, as predicted by the Disruption model applied to two sets of simulations: a set with high-resolution (the one we used in the paper), and the corresponding low-resolution set where the same initial conditions were used for each halo but the particle mass adopted is one order of magnitude larger. The ICL fraction appears to be systematically higher in the low-resolution set over all the halo mass range considered, with the difference being more significant on cluster scale. This is due to the fact that, decreasing the resolution, a larger fraction of satellite galaxies are classified as Type 2 and are subject to our stripping model. The effect is weaker in low-mass haloes that have a lower number of satellites galaxies.

We carried out the same convergence test also for Tidal Radius model, and show the corresponding results in the right panel of Figure 5.14. The ICL fraction is higher in the low-resolution set than in the high resolution set, by about 40 per cent. Due to the constraint given by equation 5.5, events of stripping of Type 1 satellites are extremely rare in this model, and their contribution to the ICL fraction is lower than 1 per cent over all the halo mass range considered. This means that Type 2 galaxies are the main contributors to the total amount of ICL. The larger fraction of these galaxies in the low-resolution set causes the increase of the ICL fraction, also on group scale, where the increase seems to be more important than it is in Disruption model.

5.9 Discussion and conclusions

In this work, we build upon the semi-analytic model presented in Section 3.4 to describe the generation of intra-cluster light (ICL). We include different implementations for modelling the formation of the diffuse ICL. In particular, we consider: (i) a model that assumes the stellar component of satellite galaxies can be affected only after their parent dark matter substructures are stripped below the resolution limit of the simulation (Disruption model); (ii) a model that accounts for stellar stripping also from satellites sitting in distinct dark matter subhaloes, and based on a simple estimate of the tidal radius (Tidal Radius model); and (iii) a model based on a fitting formula derived from a suite of numerical simulations aimed to study the evolution of a disk galaxy within the global tidal field of a group environment (Villalobos et al., 2012, Continuous Stripping model). In addition, we have also considered the relaxation processes acting during galaxy-galaxy mergers by simply assuming that 20 per cent of the stellar mass of the merging satellite gets unbound and ends-up in the ICL component associated with the remnant galaxy. In our implementations, the bulk of the ICL is produced through tidal stripping and disruption of the satellite galaxies, with the merger channel contributing only for a minor fraction.

The reference model we have used is known to over-predict the abundance of galaxies with mass below $\sim 10^{10} M_{\odot}$ (Fontanot et al., 2009; Guo et al., 2011). The inclusion of a model for stellar stripping of satellite galaxies alleviates this problem, but does not solve it. In a recent work, Budzynski et al. (2012) use a catalogue of groups and clusters from SDSS DR7 in the redshift range $0.15 \leq z \leq 0.4$ and compare the galaxy number density profiles with predictions from the same reference model used in our study. They show that the model follows very well the observational measurements but in the very central regions (within $\sim 0.2R_{500}$), where the predicted profile is steeper than observational measurements. The inclusion of stellar stripping would improve the agreement with data in this region where the tidal field is stronger and galaxies are more likely to be stripped. However, the same comparison with the data by Lin et al. (2004) would lead to an opposite conclusion. This suggests that the uncertainty on the density profiles in the inner region is probably

too large to put strong constraints on stripping models.

As we discuss below, we find that the dominant contribution to the ICL formation comes from stripping and/or disruption of massive satellites so that the excess of intermediate to low-mass galaxies does not affect significantly our results. In our Cont. Strip. model, we use a different prescription for merger times with respect to that employed in the reference model and in the other two models considered (see Section 5.2.3). As a consequence, merger times are on average shorter than in the other models which result in an under-prediction of massive satellites. We note that recent work by Villalobos et al. (2013) has pointed out that the dynamical friction formula used in our Continuous Stripping model (Boylan-Kolchin et al. (2008)) under-estimate merger times at higher redshift. Implementing their proposed modification would make merger times longer in this model, making results more similar to the other two models. We have explicitly tested (by adding a fudge factor that increases again the merger times so as to bring the predicted mass function in agreement with observations) that this does not affect significantly the results presented in this work.

A number of recent studies have focused on the formation of the ICL, using both hydrodynamical numerical simulations (e.g. Murante et al., 2007; Puchwein et al., 2010; Rudick et al., 2006), and analytic models based on subhalo infall and evolution (e.g. Purcell et al., 2007; Watson et al., 2012). Less work on the subject has been carried out using semi-analytic models of galaxy formation, but for basic predictions in terms of how the fraction of ICL depends on the parent halo mass (Monaco et al., 2006; Somerville et al., 2008; Guo et al., 2011).

Our models predict an ICL fraction that varies between ~ 20 and ~ 40 per cent (depending on the particular implementation adopted), with no significant trend as a function of the parent halo mass. Results are in qualitative agreement with observational data, in particular on the cluster mass scale. We note, however, that the ICL fractions predicted by our models depend on the resolution of the simulations: for a set of simulations that use a particle mass one order of magnitude larger than that adopted in the high resolution runs used in our study, the predicted ICL fractions increase by 30-40 per cent. We stress that both the data and the model predictions exhibit a relatively large halo-to-halo scatter. On the cluster mass scale, we find that the scatter is largely due to a variety of mass accretion histories at fixed halo mass, as argued by Purcell et al. (2007): objects that formed earlier (that were also more concentrated) had more time to strip stars from their satellite galaxies or accumulate ICL through accretion of smaller systems. On group scale, where the predicted scatter is very large, we do not find any clear correlation between ICL fraction and halo concentration or formation time. We show that, on these scales, large part of the scatter is driven by individual accretion events of massive satellites. The (albeit weak) correlation between the ICL fraction and concentration on the cluster mass scale can be tested observationally, e.g. by measuring the ICL fraction and concentration for system lying in a relatively narrow halo mass range.

Our models predict that the ICL forms very late, below redshift $z \sim 1$, in agreement with previous analysis based on hydrodynamical numerical simulations (e.g. Murante et al., 2007). About 5 to 25 per cent of the diffuse light has been accreted during the hierarchical growth of dark matter haloes, i.e. it is associated with new galaxies falling onto the haloes during their assembly history. In addition, we find that the bulk of the ICL is produced by the most massive satellite galaxies, $M \sim 10^{10-11} M_{\odot}$, in agreement with recent findings based on N-body simulations (Martel et al., 2012) and analytic models (Purcell et al., 2007). Low-mass galaxies ($M_* < 10^9 M_{\odot}$) contribute very little to the ICL in terms of mass, although they dominate in terms of number. This is a natural consequence of dynamical friction triggering the generation of the ICL: the most massive satellites approach the inner cluster regions faster than their less massive counterparts. Close to the cluster centre, tidal forces are stronger, increasing the stripping efficiency. In contrast, small satellites spend most of their time in the outer regions where tidal stripping is weaker.

Since most of the ICL is produced by tidal stripping of massive satellites, this component is found to have a metallicity that is similar to that of these galaxies. Our model predictions are in qualitative agreement with observations, with most of the stars in the diffuse component having on average sub-solar metallicities (but covering a relatively large range). We also find that the mean metallicity of the ICL is approximately constant as a function of halo mass, and exhibit a relatively small halo-to-halo scatter. In contrast, Purcell et al. (2008) predict a weak increase of the ICL metallicity with increasing halo mass, over the same halo mass range considered in our study. Finally, we show that the inclusion of a model for tidal stripping of satellite galaxies does not significantly affect the predicted mass-metallicity relation, and only slightly increases the metallicity of the most massive galaxies. For all models, these galaxies have stellar metallicities significantly lower than observed (see also De Lucia & Borgani 2012). Future and more detailed observations focused e.g. on age and metallicity of the ICL component will help constraining our models and understanding the physical mechanisms driving the formation of this important stellar component.

Chapter 6

Galaxy Population in Proto-Clusters

In this chapter we investigate the galaxy population in simulated proto-cluster regions. We select the most massive clusters at redshift $z = 0$ in our set of simulations, and follow their main progenitors back in time. At each redshift of interest, $1 \lesssim z \lesssim 3$, we collect all progenitors of $z = 0$ galaxies within the virial radius of each cluster. We analyse, at different redshifts, the proto-cluster region corresponding to the most massive cluster at redshift zero. We then perform a statistical study comprising the full sample of proto-clusters, to characterize the typical proto-cluster region at high redshift. We probe the galaxy population in proto-clusters by analysing the evolution of the stellar mass functions of the passive and active populations, their relative fractions as a function of distance from the central galaxy and their stellar mass, and the number of interlopers (defined as those objects that are not progenitors of galaxies in clusters at $z = 0$) as a function of redshift and stellar mass. We conclude that proto-clusters are very extended objects comprising a active galaxy population that evolves in time giving rise to the passive population, and with properties more similar to those of field rather than cluster galaxies.

6.1 Introduction

As discussed in Section 2.4, galaxy clusters host a population of galaxies typically dominated by red colours and elliptical shapes. These galaxies are no longer star forming and evolve passively. In less dense regions of the Universe, such as field environments, the galaxy population is instead dominated by blue galaxies with spiral and irregular shapes, that are actively star forming (Dressler 1980; Postman & Geller 1984; Gómez et al. 2003; Kauffmann et al. 2004; Balogh et al. 2004; Weinmann et al. 2006; van den Bosch et al. 2008; Weinmann et al. 2010; von der Linden et al. 2010). The red early-type galaxies in clusters populate a tight linear sequence in the colour-magnitude diagram known as the red-sequence. The scatter of the red sequence is small (Bower et al. 1992; Stanford et al. 1998) and, as well as the slope, it does not show any evolution with redshift (Gladders

et al. 1998; Blakeslee et al. 2003). The traditional interpretation of these observations is that the stellar populations of elliptical galaxies should form during an epoch of intense star formation at high redshift (Hatch et al. 2011a, and references therein), $z \gtrsim 2$, the epoch at which clusters start to form.

Proto-clusters are the progenitors of galaxy clusters. These objects have high masses that suggest they can evolve in cluster-sized structures, have started to collapse but are not yet virialized. They represent the densest regions of the early Universe, and the galaxies they contain are thought to be progenitors of present day galaxies. Recently, Chiang et al. (2013) have performed a systematic study of cluster formation utilizing the Millennium Simulations to track the evolution of dark matter and galaxies in ~ 3000 clusters from high redshift to the present time, characterizing the growth in size and mass of proto-cluster regions. They have shown that the progenitor regions of galaxy clusters with mass larger than $\sim 10^{14} h^{-1} M_{\odot}$ can already be identified at least up to $z \sim 5$. Moreover, they have derived the probability that a structure having a given galaxy overdensity is a proto-cluster, finding that the higher the observed galaxy overdensity, the higher the probability that a structure is a genuine proto-cluster (see their Figure 8 and Table 4).

Studying these objects at high redshift is useful for improving our knowledge of galaxy formation and evolution, particularly the role of the environment. Proto-clusters are then interesting laboratories for studying the earliest properties of galaxies that belong to the first galaxy clusters in the Universe, and investigating the conditions in the epoch of their birth.

The main goal of this study goes in this direction. We select massive clusters at redshift $z = 0$ from the set of simulations presented in Section 4.2, and follow the progenitors of the galaxies they contain within their virial radius R_{200} . The regions occupied by progenitors of redshift zero galaxies define, by construction, our sample of proto-cluster regions at each redshift (as we explain in Section 6.2). We stress, however, that this definition is different to that usually used observationally. We make use of this sample to characterize the typical proto-cluster region, that is larger than the virialised cluster region at $z \sim 2 - 3$. We start by analysing a case study, i.e. the proto-cluster that corresponds to the most massive cluster, and then compute some important quantities such as typical size and number of interlopers through a statistical analysis of the full sample. Our second goal is to investigate the galaxy population in such proto-clusters by looking at the evolution of the stellar mass functions separately for passive (quiescent) and active (star forming) galaxies, their relative abundances at different times, and the progenitors that build-up the red galaxy population in clusters, from $z \sim 3$ to $z \sim 1$.

The chapter is structured as follows: in Section 6.2 we present our catalogue of proto-cluster regions. Our case study is discussed in Section 6.3, and we use the full sample to statistically characterize the typical proto-cluster region in Section 6.4. In Section 6.5 we address the problem of interlopers (defined as those objects that are not progenitors of galaxies in cluster at $z = 0$) by analysing mock observations of proto-clusters. In Section 6.6

we follow the evolution of the proto-cluster galaxy population. We then compare prediction of the total star formation rate in proto-clusters with observations in Section 6.7, and finally discuss the main conclusions in Section 6.8.

6.2 The Set of Simulated Proto-Clusters

We make use of the merger-trees extracted from the set of simulations presented in Section 4.2 to construct a mock catalogue of proto-cluster regions. More in detail, we run the semi-analytic model (including the prescriptions for stellar stripping presented in Chapter 5) to generate galaxy-trees, i.e catalogues where each galaxy is followed back in time and all the information about all its progenitors is stored. We select 27 high-density regions at redshift $z = 0$, which correspond to the regions occupied by the 27 most massive clusters, i.e. the main central object of each simulation. We then select all galaxies within the virial radius R_{200} of the cluster, and for each of them, we follow its tree by considering all progenitors with stellar mass larger than $2 \cdot 10^8 M_{\odot}$, that roughly corresponds to the resolution limit in stellar mass. At each redshift, we consider the region occupied by all progenitors of $z = 0$ galaxies as the proto-cluster region, i.e. the boundaries of the proto-cluster regions are given by the distribution of progenitors they contain. We end-up with 27 proto-cluster regions selected around clusters at redshift $z = 0$, of which 5 have mass (at $z = 0$) $\sim 10^{14} M_{\odot}$, 9 with mass $\sim 7 - 8 \cdot 10^{14} M_{\odot}$ and the other 13 with mass $\sim 10^{15} M_{\odot}$. For the analysis that follows, unless otherwise stated, we will consider comoving coordinates.

6.3 A Case Study

As discussed in Section 6.1, it is not trivial to define (in observations) a region in the sky that contains all the objects belonging to the proto-cluster. We start addressing this point by analysing a case study, given by our proto-cluster region corresponding to the most massive cluster at redshift $z = 0$, with mass $\sim 10^{15} h^{-1} M_{\odot}$. In Figure 6.1 we show the x-y projection of progenitor positions at four redshifts, $z = 0.60, 1.00, 1.61, 3.02$. We also split galaxies in star forming and passive according to their specific star formation rate (SSFR), assuming that active galaxies are those having $\log \text{SSFR} > -11$, and between satellites and centrals. We use the same definition of passive galaxies adopted by Weinmann et al. (2010), who use the reference model (De Lucia & Blaizot 2007). They show that the cut chosen corresponds roughly to the location of the minimum in the bimodal distribution of SSFR in both the model and observations. The black circle in each panel indicates the virial radius of the halo that contains the central galaxy (CG, hereafter), identified by following the main

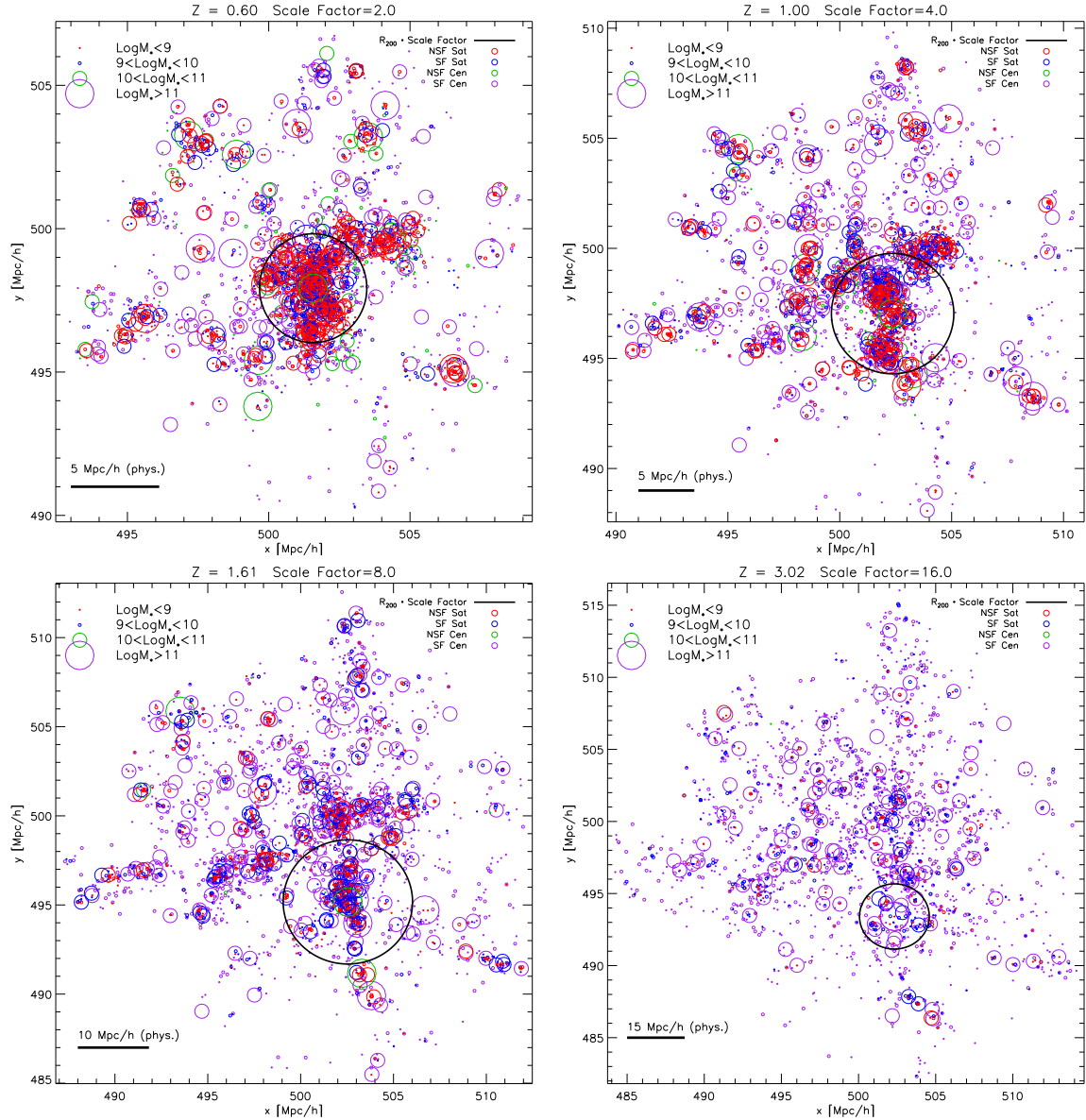


Figure 6.1: X-Y positions of progenitors of galaxies in the largest cluster, at different redshifts. Red and green circles represent passive galaxies, satellites and centrals respectively. Blue and purple circles represent star forming galaxies, satellites and centrals respectively. Black circles represent the virial radius of the halo that contains the central galaxy, multiplied by the factor called "Scale Factor" in the legend. The dimension of each circle is proportional to the stellar mass of the galaxy it represents, that we have split in four bins: $\log M_* > 9$, $9 < \log M_* < 10$, $10 < \log M_* < 11$, and $\log M_* > 11$.

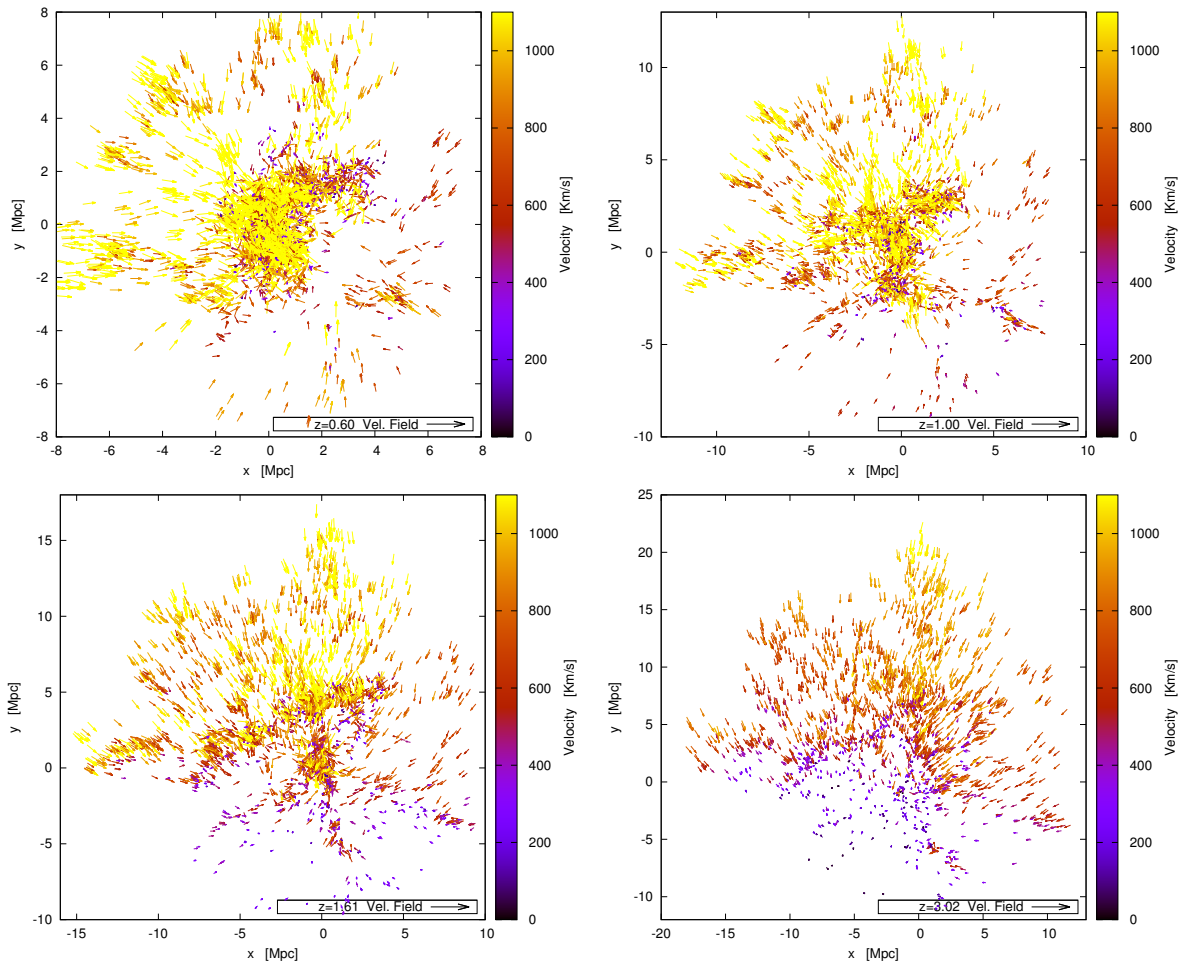


Figure 6.2: Velocity field of progenitors of galaxies in the largest cluster, at different redshifts. Positions and velocities have been normalized to the position and velocity of the main progenitor of the central galaxy found to be the BCG at redshift $z = 0$. Arrows indicate the direction of the motion while the modulus is shown by colours (see vertical header).

progenitor of the final cluster. The radius of the black circle is multiplied by the factor called "Scale Factor" in the legend, introduced in order to give an idea of how large the proto-cluster region is, when compared with the region occupied by the satellites orbiting around the CG, and how the proportion increases at increasing redshift. The virial radius R_{200} of the CG's halo is equal to 0.95, 0.68, 0.44, $0.14 h^{-1} Mpc$ at $z = 0.60, 1.00, 1.61, 3.02$, respectively.

Progenitors become redder and tend to cluster nearby the CG at decreasing redshift. This is a consequence of the fact that the CG traces also the centre of the potential. The CG grows by a factor four in stellar mass between $z \sim 3$ and $z \sim 1$, and does not grow much more by the present time. During its growth, the CG seems not to be surrounded by many galaxies with stellar mass comparable with its mass (about one half or more).

Clearly, the number of progenitors within the proto-cluster region changes as time proceeds. We select all galaxies within R_{200} , $2 \cdot R_{200}$, $5 \cdot R_{200}$ and $10 \cdot R_{200}$ (with R_{200} the virial radius of the CG halo at each time) and found that the fraction of progenitors within those regions increases with decreasing redshift. Only 10 per cent of progenitors are located within R_{200} at $z = 0.6$, and the percentage becomes negligible at higher redshifts. If we consider twice the virial radius we find that the fraction of progenitors is negligible down to $z = 1.61$, almost 10 per cent at redshift $z = 1$, while about one fourth is located within $2 \cdot R_{200}$ at redshift $z = 0.6$. These percentages rapidly increase by taking larger regions around the CG. If we consider $10 \cdot R_{200}$, basically all progenitors stay within this region at $z = 0.6$, only 12 per cent at $z = 1.61$ and negligible fractions at higher redshifts. Similar numbers are inferred by considering the total star formation rate and total stellar mass instead of the number of progenitors. Within $10 \cdot R_{200}$ of the CG halo we find the total star formation rate and stellar mass of the proto-cluster region at $z = 0.6$. The star formation rate within $10 \cdot R_{200}$ becomes negligible at $z = 2.16$, while the stellar mass becomes negligible at $z = 3.02$, with respect to total star formation rate of the whole proto-cluster region. Qualitatively speaking, star formation proceeds quickly at higher redshift and in progenitors that are not part of the region considered ($10 \cdot R_{200}$).

As discussed above, passive galaxies tend to occupy the densest regions, close to the CG, and this effect increases with decreasing redshift. We have binned the proto-cluster region in 10 bins, from the centre to $20 \cdot R_{200}$ and calculated the fraction of active and passive galaxies in each bin. Galaxies in dense environments are redder (Kauffmann et al. 2004; van den Bosch et al. 2008; von der Linden et al. 2010). The expected trend is an increasing fraction of passive galaxies as we approach the CG, that traces the densest part of the proto-cluster region. The results of our analysis do confirm this expectation. This is a consequence of the increasing fraction of satellite galaxies towards the centre. In our model, satellites typically become passive in relatively short times after their accretion. To quantify: at redshift $z < 1$, the fraction of passive galaxies is negligible beyond $10 \cdot R_{200}$, and rapidly increases reaching about 70 per cent within $2 \cdot R_{200}$; at redshift $z > 2$, the percentage is constant over all the radial range considered, and approximatively 30-40 per cent; between $z \sim 2$ and $z \sim 1$ ($\sim 2.5 Gyr$), the fraction of passive galaxies start to increase

both with time and location in the proto-cluster region. We will come back to this point in Section 6.6 where we better characterize the redshift range of this transition.

In Figure 6.2, we show maps of velocity field at different redshifts. The header on the right side of each panel shows the velocity modulus, while arrows indicate the direction of the motion. Positions and velocities have been normalized to the CG position and velocity at each redshift. At high redshifts these objects have, on average, low velocities (with respect to the CG), which indeed tend to increase towards $z = 0$, and when they get closer to CG. This happens because they feel very little the CG halo potential at higher redshift, since it is weak and they are on average more distant. Approaching CG, they start to feel more intensely the potential and their velocity increases. This picture explains also why we find different velocity dispersions of passive and active galaxies. In fact, by measuring the velocity dispersion of active and passive galaxies located in the first physical Mpc from the CG at each redshift, we find that the dispersion of active galaxies is always larger than that of passive galaxies up to $z \sim 1.6$, while passive galaxies have a higher dispersion at higher redshift. As said above, passive galaxies tend to occupy the densest regions, while active galaxies are, on average, accreted recently, and have experienced dynamical friction for a shorter time and less intensively. At high redshift, the velocity dispersion of active galaxies decreases because in 1 Mpc we are sampling galaxies less bound to the CG (basically central galaxies), while passive galaxies are still located internally. In agreement with observations (e.g., Venemans et al. 2007) we find an increasing velocity dispersion of the proto-cluster galaxy population with cosmic time.

The proto-cluster region connected to the most massive cluster at $z = 0$ of our sample is very extended, $\sim 20 h^{-1} Mpc$, and hosts mainly a active galaxy population that dominates at increasing redshift. In the next section we make a statistical analysis of our set of proto-cluster regions, with the aim to better characterize the typical proto-cluster region by addressing the same points discussed in this section.

6.4 Statistical Analysis of Proto-Cluster Regions

The case study analysed in the last section pointed-out that proto-clusters are extended objects and their size clearly depends on the particular redshift at which they are observed. In this section we focus on the characterization of the typical size of proto-cluster regions by looking at the fraction of progenitors in regions of fixed comoving size, the star formation rate and stellar mass within the box. The number of objects we have (27) allows us to obtain a statistically significant object-to-object scatter. As pointed out in Section 6.2, these objects evolve in clusters of different mass at $z = 0$. Since the results described below do not depend on the mass of the cluster, we will average results for the full sample of proto-clusters.

In Figure 6.3 we plot the ratio between the number of progenitors contained in cubic

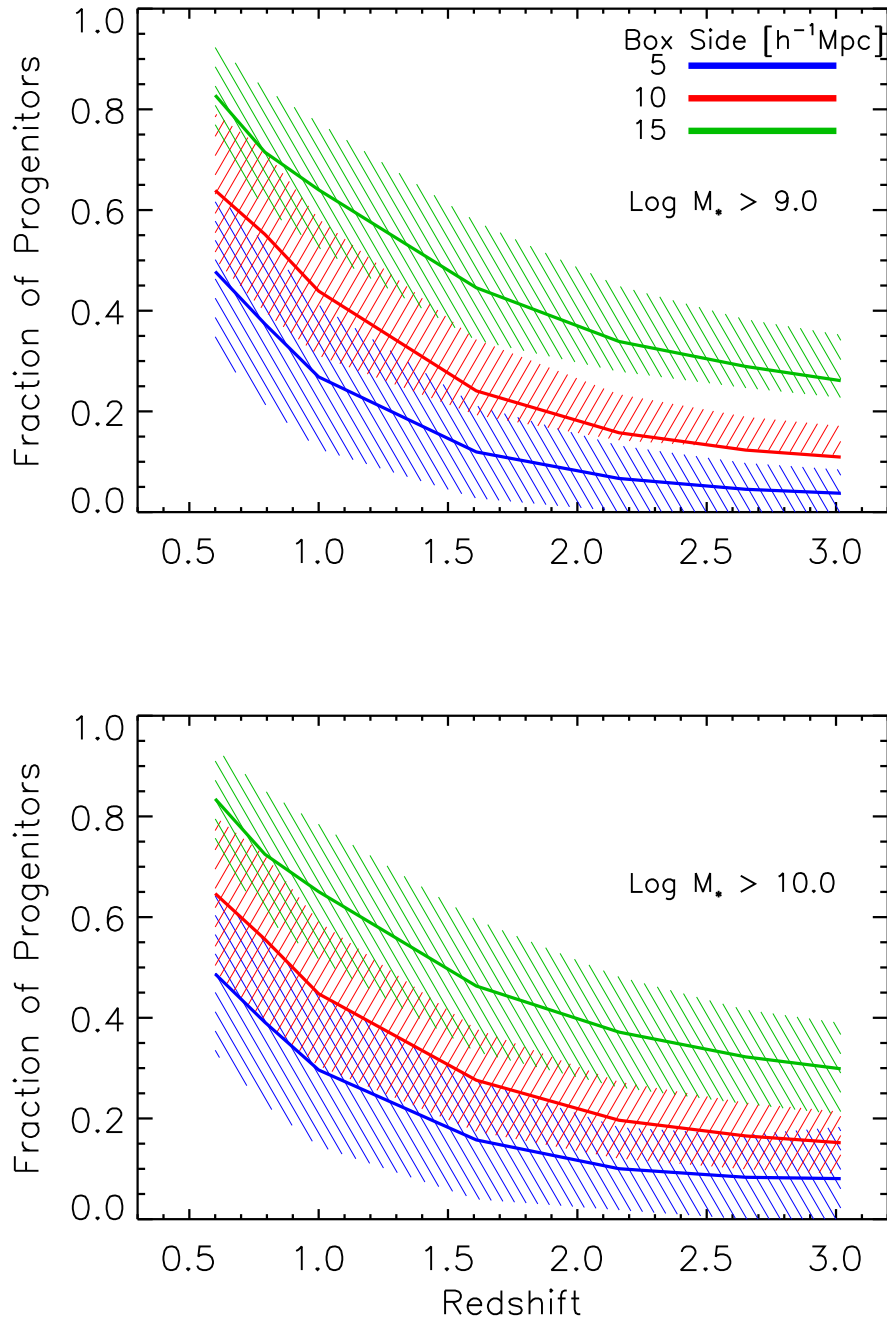


Figure 6.3: Top panel: ratio between the number of progenitors contained in cubic boxes of different sizes ($5, 10, 15 h^{-1}Mpc$) centred around the CG at each redshift, and the total number of progenitors in the proto-cluster region with stellar mass above $10^9 M_\odot$, as a function of redshift. Solid lines represent the mean, while dashed areas represent the 1sigma scatter of the distributions. Bottom panel: same as the top panel, but for progenitors with mass above $10^{10} M_\odot$.

boxes of different sizes ($5, 10, 15 h^{-1} Mpc$) centred around the CG at each redshift, and the total number of progenitors in the proto-cluster region with stellar mass above the adopted mass threshold ($10^9 M_{\odot}$ and $10^{10} M_{\odot}$ in the top and bottom panel, respectively) as a function of the redshift at which the proto-cluster regions are located. Solid lines represent the mean fractions derived over all the objects, while shaded areas of different colours represent the 1sigma scatter of the distributions. The plots show that the fraction does not depend on the adopted threshold, regardless the size of the box. Proto-clusters are often found around high- z radio galaxies (see Section 2.4) at redshift higher than $z \sim 1.5$, considering an area of few Mpc^2 (typically less than $2 \times 2 Mpc$ physical) around the radio galaxy. At this redshift we find that the fraction of progenitors goes from 0.1 to about zero if computed within a box of $5 h^{-1} Mpc$ (blue solid line and dashed area), and from 0.5 to 0.25 if computed within a box of $15 h^{-1} Mpc$ (green solid line and dashed area). This means that at most only about 50 per cent of progenitors can be detected within relatively large apertures such as the largest among ours. Smaller apertures contain large fractions of progenitors only at lower redshifts, below $z \sim 0.8$. Hatch et al. (2009) study the stellar mass assembly of MRC 1138-262, also known as the Spiderweb Galaxy, a massive radio galaxy in a proto-cluster at $z = 2.2$. They identify the galaxy population that lies at the same redshift and within a projected distance of $150 kpc$ from the radio galaxy. They fit stellar population models to the photometry of 19 protocluster galaxies that they find, and look at the stellar mass distribution and ongoing star formation. These authors find that satellites with mass in the range $10^8 - 10^{11} M_{\odot}$ contribute between 10 and 50 per cent of the stellar mass of the system, and, by means of analytic approximations, predict that most of these satellites will merge with the central radio galaxy before $z = 0$, thus increasing its mass by up to a factor 2. We test this prediction with our proto-clusters, at the same redshift, by restricting the analysis to the first physical $150 kpc$. We find that, on average, 95 per cent of these satellites will merge with the central object by $z = 0$ and, on average, they contribute up to 55 per cent to its mass, thus in agreement with the prediction by Hatch et al.

We have also investigated the ratio between the stellar mass in progenitors within the box and the total stellar mass of the proto-cluster regions, as a function of redshift. As the previous case, the fraction is not sensitive to the particular threshold in stellar mass chosen. It increases at increasing box size and decreases at increasing redshift. Percentages are very similar to those reported above. At redshift higher than $z \sim 1.5$, the box with the largest aperture ($15 h^{-1} Mpc$) contains from about 30 (at $z \sim 3$) to 50 (at $z \sim 1.5$) per cent of the total stellar mass of the proto-cluster regions. The smallest box ($5 h^{-1} Mpc$) does not reach 20 per cent at every redshift of interest. We have repeated the analysis by investigating the ratio between the total star formation rate of progenitors within the box and the total star formation rate of the entire proto-cluster region, as a function of redshift. Again, the behaviour is similar to those discussed above for the number of progenitors and their total stellar mass. Percentages are almost the same in the redshift range of interest, while tend to be slightly lower below redshift $z \sim 0.8$, in the case of total star formation rate.

This analysis points out that proto-cluster regions, which are destined to become massive (with mass of the order of $[5 - 10] \cdot 10^{14} M_{\odot}$) clusters of galaxies at redshift $z = 0$, are very extended objects. In the redshift range explored, and of interest for this topic, very wide boxes centred around the most massive galaxy are needed in order to take a significant sample of progenitors. The percentage of progenitors within the box, as well as the stellar mass and star formation rate, are particularly sensitive to the size of the box and the redshift at which the object is located. In the next section, we will select proto-cluster regions by considering as a proto-cluster the region around the most massive galaxy and all the galaxies within boxes of fixed sizes. This is closer to the observational approach, since these regions may now contain *interlopers*, i.e. galaxies that are not progenitors. We then re-address the question considered in this section, studying what is the number of actual progenitors as a function of redshift and size of the box.

6.5 Interlopers in Observed-like Proto-Cluster Regions

Real proto-cluster regions are often found around luminous galaxies at high redshifts and the sample of galaxies might contain interlopers. Observationally speaking, it is not possible to know which, among all galaxies in the sample, are actual progenitors and which are not. In this section we want to characterize proto-cluster regions by selecting them as observers do, and probe the typical fraction of interlopers. We will consider interlopers all those objects in the sample that are not progenitors of galaxies located within $2 \cdot R_{200}$ of the cluster at $z = 0$.

As done in Section 6.2, we select the main central object of each simulation, and walking the main branch of the tree, we take the main progenitor at each redshift of interest. To build-up *observed-like* proto-cluster regions, we select all galaxies within a cubic box of $15 h^{-1} Mpc$ size for haloes more massive than $\sim 7 \cdot 10^{14} M_{\odot}$ at $z = 0$ (22), and $7 h^{-1} Mpc$ for less massive haloes (5), having stellar mass larger than the threshold adopted in Section 6.2. These apertures have been chosen in order to avoid (at every redshift) low-resolution regions of the simulations.

In Figure 6.4 we plot the fraction of actual progenitors in our proto-cluster regions within cubic boxes of different sizes ($5 h^{-1} Mpc$ (27 regions), 10 and $15 h^{-1} Mpc$ (22 regions corresponding to the 22 most massive clusters at $z = 0$)), as a function of their stellar mass, and at redshift $z = 1.00, 1.61, 2.16, 3.02$. Solid lines represent the mean fraction, while dashed areas represent the 1sigma scatter. This scatter appears to be more significant at increasing redshift, irrespective of the size of the box and the stellar mass range. The plot shows that the fraction of actual progenitors is almost constant, and between 0.8 and 0.9, up to stellar masses of about $10^{11} M_{\odot}$ at $z = 1$, and weakly increases with stellar mass at higher redshifts. Above $M_* \sim 10^{11} M_{\odot}$, the fraction drops at every redshift because of the increasing fraction of centrals, that tend to be more massive than satellite galaxies. Hence,

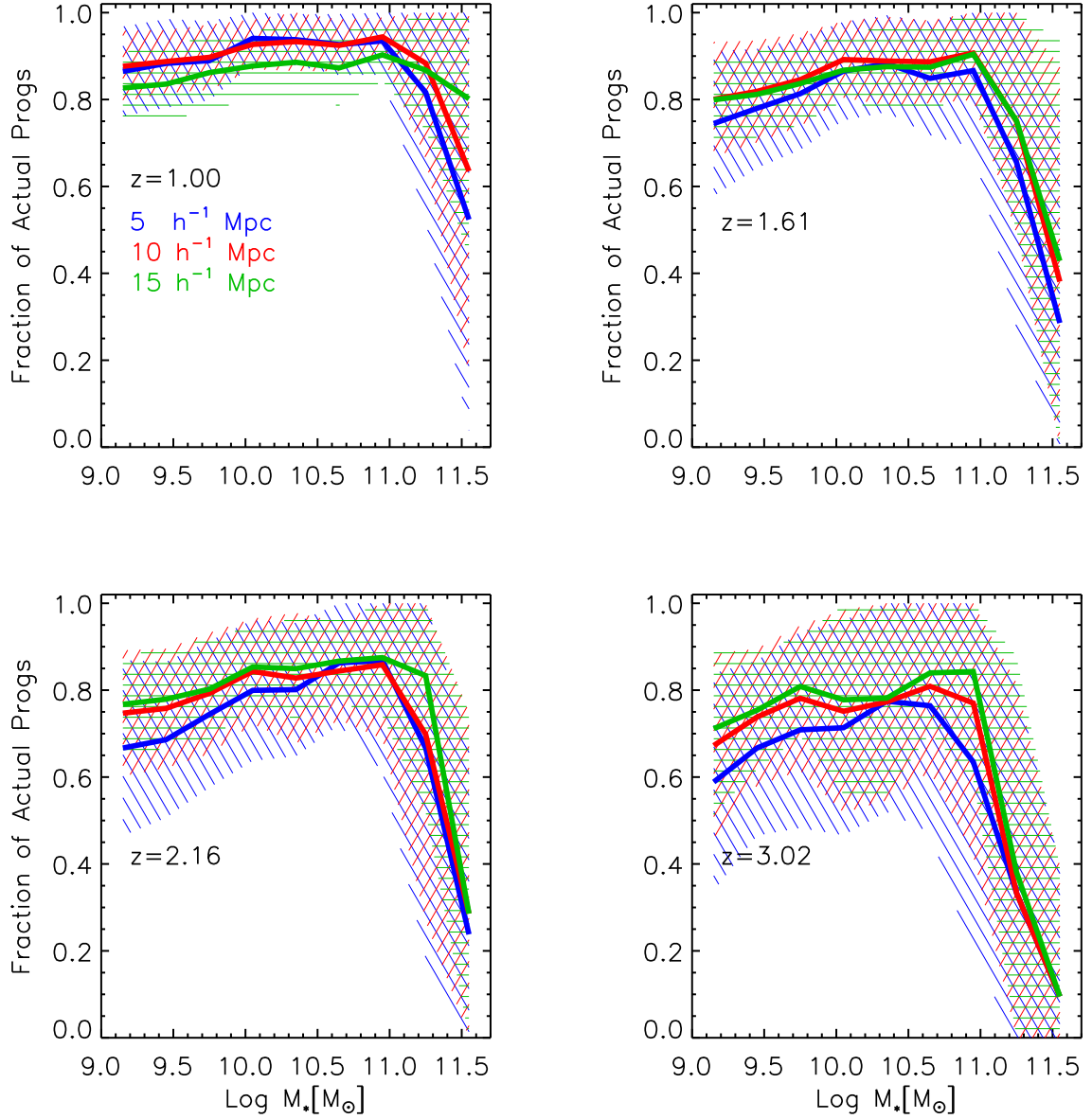


Figure 6.4: Fraction of actual progenitors in observed-like proto-cluster regions within cubic boxes of different sizes as indicated in the legend, as a function of stellar mass and at different redshift (panels). Solid lines represent the mean, while dashed areas represent the 1σ scatter of the distributions.

the fraction of interlopers predicted by our model depends weakly on the galaxy stellar mass and on the redshift at which proto-cluster regions are located, and does not strongly depend on the size of the box. We find that about 30 per cent of galaxies with mass smaller than $\sim 10^{10} M_{\odot}$, and about 20 per cent of galaxies with larger stellar mass, are interlopers at $z \sim 3$. Slightly smaller fractions are found at lower redshifts, and when considering progenitors of galaxies within R_{200} (instead of $2 \cdot R_{200}$) at redshift zero.

It is virtually impossible to distinguish between interlopers and actual progenitors by looking at properties such as colour, star formation rate, stellar mass and distance from the centre of the proto-cluster region. We have addressed this issue with the purpose to find features able to characterize possible differences among these two populations. Distributions of colour, star formation rate, as well as stellar mass or location in the proto-cluster regions, appear to be almost the same for interlopers and actual progenitors.

6.6 Galaxy Population in Proto-Clusters

Proto-clusters enclose a population of star forming galaxies (see, e.g., Kurk et al. 2004), but also passive galaxies could exist in high- z systems, as recently found in a $z \sim 2$ cluster (Gobat et al. 2011). In fact, these galaxies are difficult to observe and spectroscopically confirm at $z \gtrsim 2$ (Hatch et al. 2011b). The $H\alpha$ luminosity function in proto-clusters has shape similar to that of the field. Hatch et al. (2011b) have recently found that its normalisation is a factor about 13 higher than that of the field. Moreover, galaxies in high density environments at redshift $z \gtrsim 2$ appear to have redder colours and higher stellar masses than galaxies in the field (Hatch et al. 2011b; Koyama et al. 2013). In this section we want to investigate the galaxy population in our proto-cluster regions and see how it evolves. For this purpose, we split our sample of galaxies in active and passive galaxies, according to the definition used in Section 6.3, i.e. by defining as active galaxies those that have $\log \text{SSFR} > -11$.

In Figure 6.5 we plot the galaxy stellar mass functions within a box of $7 h^{-1} \text{Mpc}$ size centred around the CG of each proto-cluster region, for active galaxies (top panel), and for passive galaxies (bottom panel), at redshift $z = 1.00$ (blue), $z = 1.61$ (red), $z = 2.65$ (green), and $z = 3.02$ (cyan). Solid lines represent the mean value derived by averaging the 27 regions, and dashed areas represent 1sigma scatters. The figure shows that active and passive galaxies evolve differently. The number density of passive galaxies increases very rapidly between $z = 3.02$ and $z = 1.00$, and, given the scatter, this increase seems not to depend on stellar mass. The knee moves to higher masses continuously, and the difference in number density between $z \sim 3$ and $z \sim 1$ is ~ 1.5 dex at stellar masses around $10^{10.5} M_{\odot}$, i.e. a factor ~ 30 higher at redshift $z = 1.00$. A rather different evolution is shown by the stellar mass function of active galaxies (top panel of Figure 6.5). For galaxies with stellar mass smaller than $\sim 10^{11.2} M_{\odot}$, the number density increases at increasing redshift, and the difference between $z = 3$ and $z = 1$ is $0.4 - 0.5$ dex, about a factor 3 higher at redshift

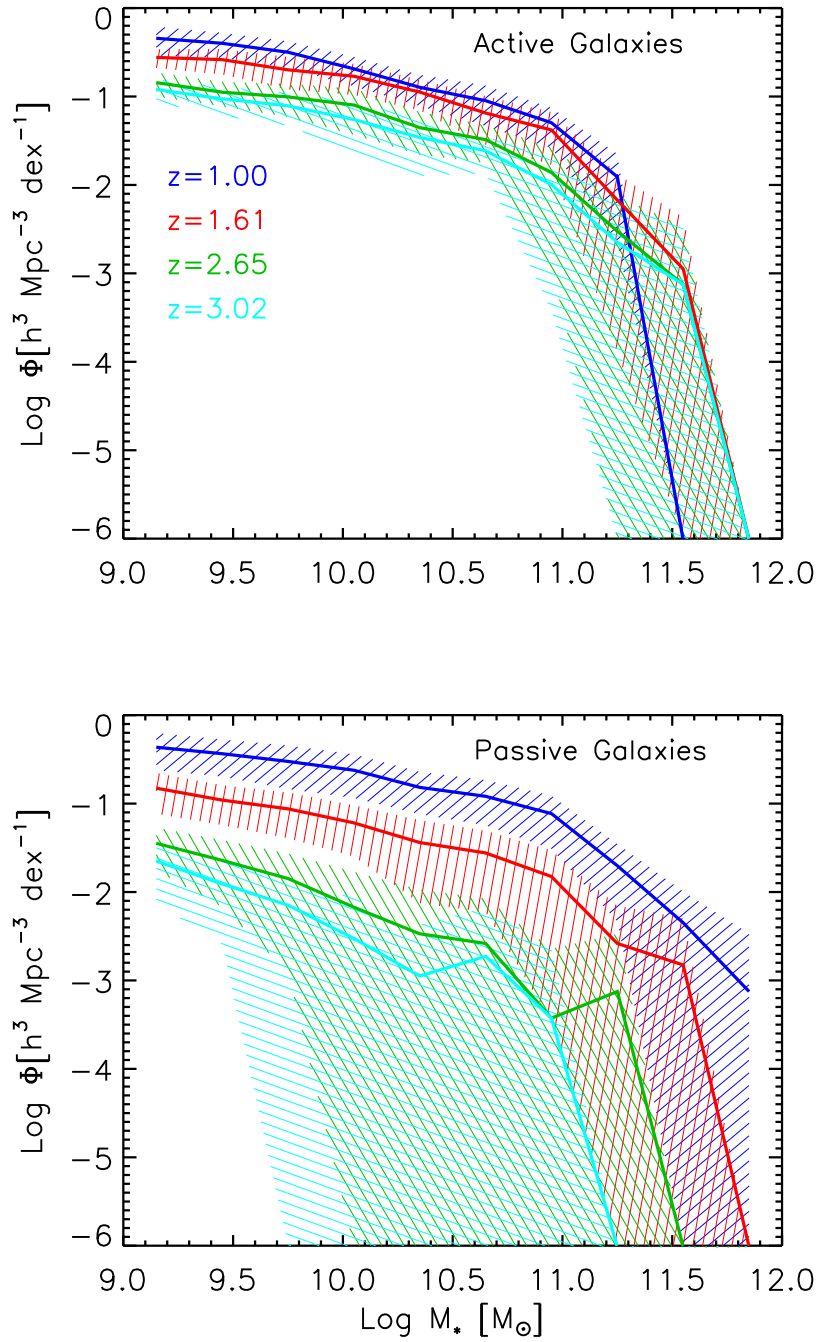


Figure 6.5: Galaxy stellar mass functions within boxes of $7h^{-1}\text{Mpc}$ sizes centred around the CG, for active galaxies (top panel), and passive galaxies (bottom panel), at different redshifts (different colours). Solid lines represent the mean value calculated by averaging 27 proto-cluster regions, and dashed areas represent the 1sigma scatter of the distributions.

$z = 1$. At the very massive end, for galaxies with stellar mass larger than $\sim 10^{11.2} M_{\odot}$, the stellar mass function drops at lower stellar mass as the redshift decreases. An evolution in number density is clear in the last $\sim 2\text{Gyr}$ between $z = 1.61$ and $z = 1.00$. Since these are star forming galaxies whose stellar mass increases with time through the ongoing star formation, this drop in number density is due to a rapid and sudden process that transforms massive active galaxies in passive galaxies.

It must be noted that the trends shown in Figure 6.5 do not change by considering larger boxes around the CG, except the normalisation of the stellar mass functions due to the enlarged volume. A similar trend has been observed by Ilbert et al. (2013), who construct a large and deep sample of 220,000 galaxies selected using the new UltraVISTA DR1 data release up to $z \sim 4$. The author find a mass-dependent evolution of the global and star forming populations in the field, with the low-mass end of the mass functions evolving more rapidly than the high-mass end, while the number density of quiescent galaxies increases over the entire mass range from $z \sim 3$ to $z \sim 1$.¹ They argue that if the stellar mass functions of blue and red galaxies have the same slope, the process which quenches galaxies acts with the same efficiency up to the characteristic stellar mass M^* . In the field, the quenching of intermediate stellar mass galaxies (up to $M_* \sim 10^{10.7-10.9} M_{\odot}$) is consistent with an environment driven quenching, that acts with the same efficiency regardless the mass of galaxies. Above that threshold in stellar mass, quenching is more efficient and rapidly builds up the red galaxy population.

As shown in Figure 6.5, passive galaxies start to dominate the population of massive objects below redshift $z = 1.61$, while active galaxies dominate over all the range of stellar mass at higher redshifts. On average, galaxies become passive with decreasing redshift as they tend to preferentially reside within denser regions, infalling towards the centre of the potential. The fraction of passive galaxies is expected to increase with decreasing redshift (since galaxies consume their cold gas with time), and should be linked to the fraction of satellites (the gas is stripped when galaxies become satellites). In Figure 6.6 we show the fraction of passive galaxies (top panel), and the fraction of satellites (bottom panel), as a function of redshift at which our proto-cluster regions are located, for galaxies with stellar mass larger than $10^9 M_{\odot}$ lying in boxes with different size (different colours). Both fractions increase at decreasing redshift, even though the fraction of passive galaxies is smaller than the fraction of satellites at high redshift, and increases faster towards lower redshift. These fractions depend on the size of the box, and the scatter shown by satellites is larger at higher redshift. Both the fraction of passive galaxies and that of satellites decrease with increasing size of the box because larger boxes capture more active galaxies, preferentially located at larger distances from the CG with respect to passive galaxies. This is confirmed by Figure 6.7, where we show the fraction of active and passive galaxies as a

¹It must be noted, however, that the massive-end of the stellar mass function is very sensitive to the error estimates of the stellar mass (see, e.g. Marchesini et al. 2009, but also discussion in Fontanot et al. 2009).

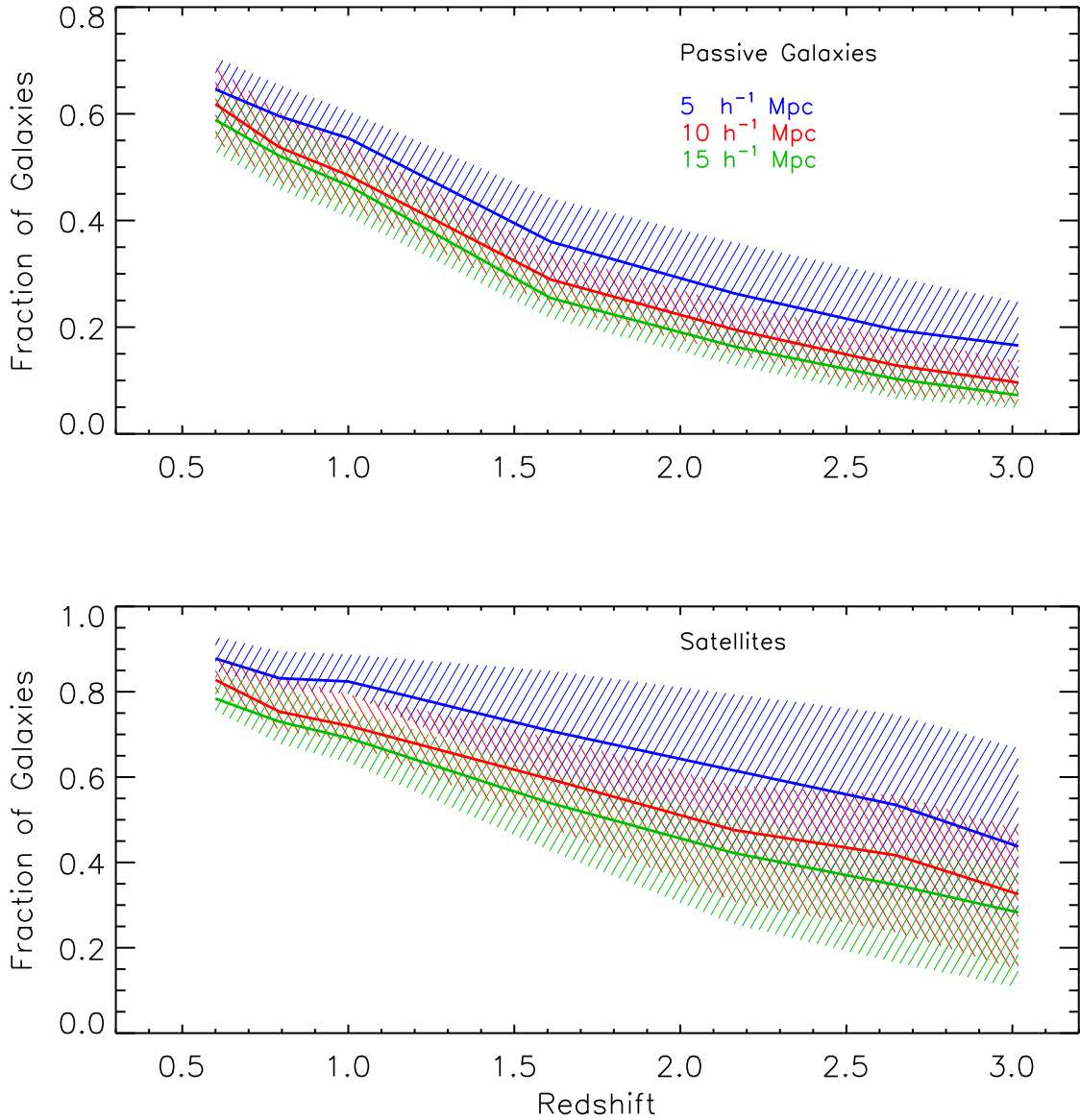


Figure 6.6: Fraction of passive galaxies (top panel) and satellites (bottom panel) within boxes of different sizes (different colours) centred around the CG. Solid lines represent the mean value calculated by averaging among 27 proto-cluster regions, and dashed areas represent the 1σ scatter of the distributions. The threshold in stellar mass is $M_* = 10^9 M_\odot$, but the trends shown do not depend on the particular threshold chosen.

function of the distance from the CG at four redshifts (different panels). Dashed regions represent the 1sigma scatter. At high redshift, ~ 2.6 , the active fraction is higher than the passive fraction over all the range plotted on the x-axis, and the scatter is relatively large. As redshift decreases, the scatter gets smaller and the two fractions are approximately the same at redshift $z \sim 1.6$ in the very inner regions of our proto-clusters, where the fraction of passive galaxies overtakes the fraction of active galaxies during the following $\sim 2 \text{ Gyr}$. The fraction of active galaxies that we find at high redshift is consistent with recent results by Hatch et al. (2011a) concerning the fraction of blue galaxies. They find that 77 ± 10 per cent of galaxies in a sample of proto-clusters at $2.2 < z < 2.6$ are blue. This estimate should be considered as an upper limit given the intrinsic difficulty to observe low-mass red galaxies at high redshifts.

At lower redshift, the fraction of passive galaxies increases and dominates the cluster galaxy population within the virial radius (see, e.g., Weinmann et al. 2010). Where are the progenitors of passive galaxies in cluster located in the proto-cluster region? We addressed this point by selecting passive galaxies belonging to our 27 clusters and located within their virial radius R_{200} , and finding the position of their progenitors at higher redshifts in the proto-cluster regions. We have also split the sample of progenitors in active and passive at the redshift of interest. We find no clear difference between the two distributions at any redshift, meaning that progenitors of passive galaxies at $z = 0$ distribute similarly in the proto-cluster region, irrespective of their colour. In Figure 6.8 we investigate the distribution in stellar mass of the sample of galaxies described above, splitting them in passive (red histograms), and active (blue histograms) progenitors at the redshift of interest (different panels). The distributions of active and passive progenitors are different at high redshift, being active progenitors preferentially more massive than the passive ones. However, a Kolmogorov-Smirnov (KS) test has been used to investigate whether the pair of distributions (at each redshift) match. The KS test applied to the distributions at $z = 1.00$, $z = 1.61$, $z = 2.16$ and $z = 2.65$ gives the probabilities 0.99, 0.99, 0.93 and 0.92, respectively, that the distributions of passive and active progenitors are the same. The offset weakens towards lower redshift and vanishes at redshift $z = 1$. Therefore, progenitors of passive galaxies at redshift zero approach the innermost regions of proto-clusters to assemble their descendants irrespective of the colour. As redshift decreases, these progenitors tend to be closer to virial region of the cluster at $z = 0$. Among these progenitors, those that are more massive and active will build up the most massive passive present-day galaxies. The progenitors of massive passive galaxies in clusters at redshift $z = 0$ are typically active galaxies in proto-clusters, consistent with the evolution of the mass functions discussed above. In order to demonstrate it, in Figure 6.9 we plot the fraction of passive (red lines) and active (blue lines) progenitors of passive galaxies at redshift $z = 0$ as a function of their mass at the redshift of interest (different panels). Solid lines represent the mean value calculated by averaging our 27 proto-cluster regions, and dashed areas represent the 1sigma scatter. The figure shows that the fraction of active progenitors is almost constant with mass and

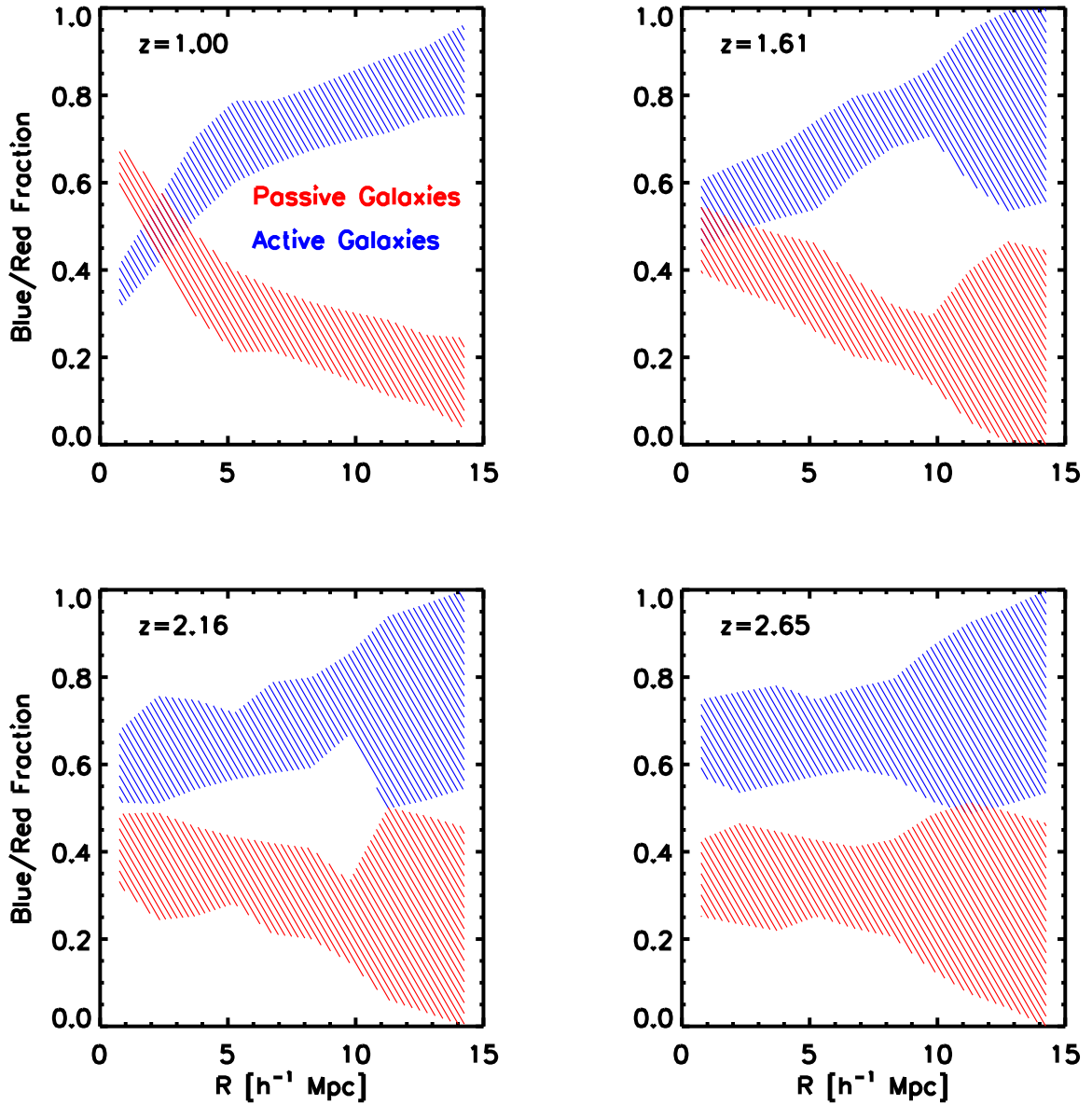


Figure 6.7: Fraction of active/passive galaxies as a function of their distance from the CG, at redshift $z = 1.00, 1.61, 2.16, 2.65$ (different panels). The threshold in stellar mass is $M_* = 10^9 M_\odot$. Dashed areas represent the 1-sigma scatter of the distributions.

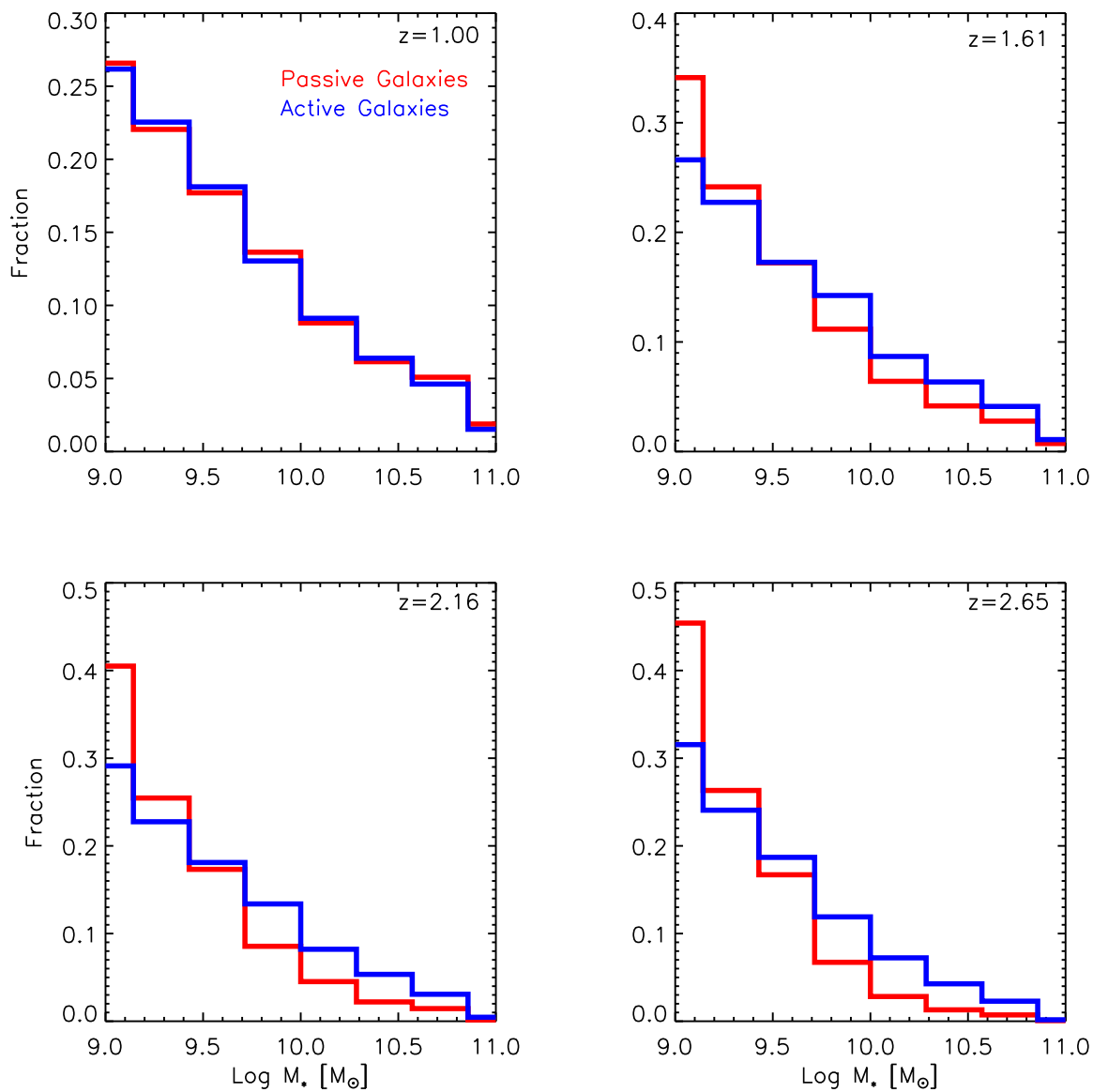


Figure 6.8: Mass distributions of passive and active progenitors of passive galaxies at redshift $z = 0$ within the virial radius R_{200} of the final cluster, at different redshift (different panels).

always larger than the fraction of passive progenitors at redshift higher than $z = 1$, and it decreases at decreasing redshift. This means that the population of passive galaxies in clusters comes mainly from the population of active galaxies in proto-clusters, that accounts for 80 to almost 100 per cent of the entire population of galaxies at $z = 2.65$, and from 80 to 90 per cent at $z \sim 2.2$.

6.7 Star Formation Rate in Proto-Clusters

Proto-clusters are regions of strong star formation activity (Pentericci et al. 2001; Miley et al. 2006; Overzier et al. 2008; Hatch et al. 2008, 2011b; Tanaka et al. 2011; Hayashi et al. 2012). Tanaka et al. (2011) report the discovery of a significant excess, about a factor 5 with respect to the field, of candidate $H\alpha$ emitters in the proto-cluster associated with the radio galaxy 4C 23.56 at $z = 2.48$. Combined with mid-infrared photometric data, they conclude that active star formation must be occurring in the proto-cluster region around the radio galaxy, and that should be comparable with the general field. Hatch et al. (2011b), who investigate the proto-clusters surrounding MRC 1138-262, at $z \sim 2.2$, and 4C + 10.48, at $z \sim 2.35$, find a total star formation rate within the central $1.5 Mpc$ of about $5000 M_{\odot}/yr$ for the former, and about 3000 for the latter, much higher than the typical star formation rate in local galaxy clusters (Koyama et al. 2010; Wetzel et al. 2012, and references therein). Hayashi et al. (2012), however, find smaller total star formation rates in three clumps (two of which with areas larger than $4.5 Mpc^2$) around the radio galaxy USS 1558-003 at redshift $z = 2.53$. In the central region $50 \times 40 kpc$ of MRC 1138-262, Miley et al. (2006) find a total star formation rate $\gtrsim 100 M_{\odot}/yr$, in good agreement with the total star formation rate, $130 \pm 13 M_{\odot}/yr$, that Hatch et al. (2008) find in the central region $65 \times 65 kpc$ of the same object, and with the total star formation rate, $302 M_{\odot}/yr$, that Hatch et al. (2011b) find in the central region, $100 \times 100 kpc$, of 4C + 10.48.

In Figure 6.10 we show the total star formation rate of galaxies in our proto-cluster regions within an area of size plotted on the x-axis, at different redshifts (different colours). Solid lines represent the mean value, while dashed areas represent the 1sigma scatter of the distributions. The total star formation rate of galaxies within a given area of our proto-cluster regions is a decreasing function of redshift, in agreement with Tanaka et al. (2011), who suggest that the star formation activity gets stronger at increasing redshift. We compare our result with the above mentioned observational data by Hatch et al. (2008) and Hatch et al. (2009) (black triangles) that have to be compared with the green line, by Hatch et al. (2011b) (black diamond), and Hayashi et al. 2012 that should lie between the green and magenta lines. These studies (but Hatch et al. 2009) use a Salpeter IMF (Salpeter 1955), while our model (and Hatch et al. 2009) uses a Chabrier initial mass function (Chabrier 2003). Following Longhetti & Saracco (2009), we have corrected star formation rates of

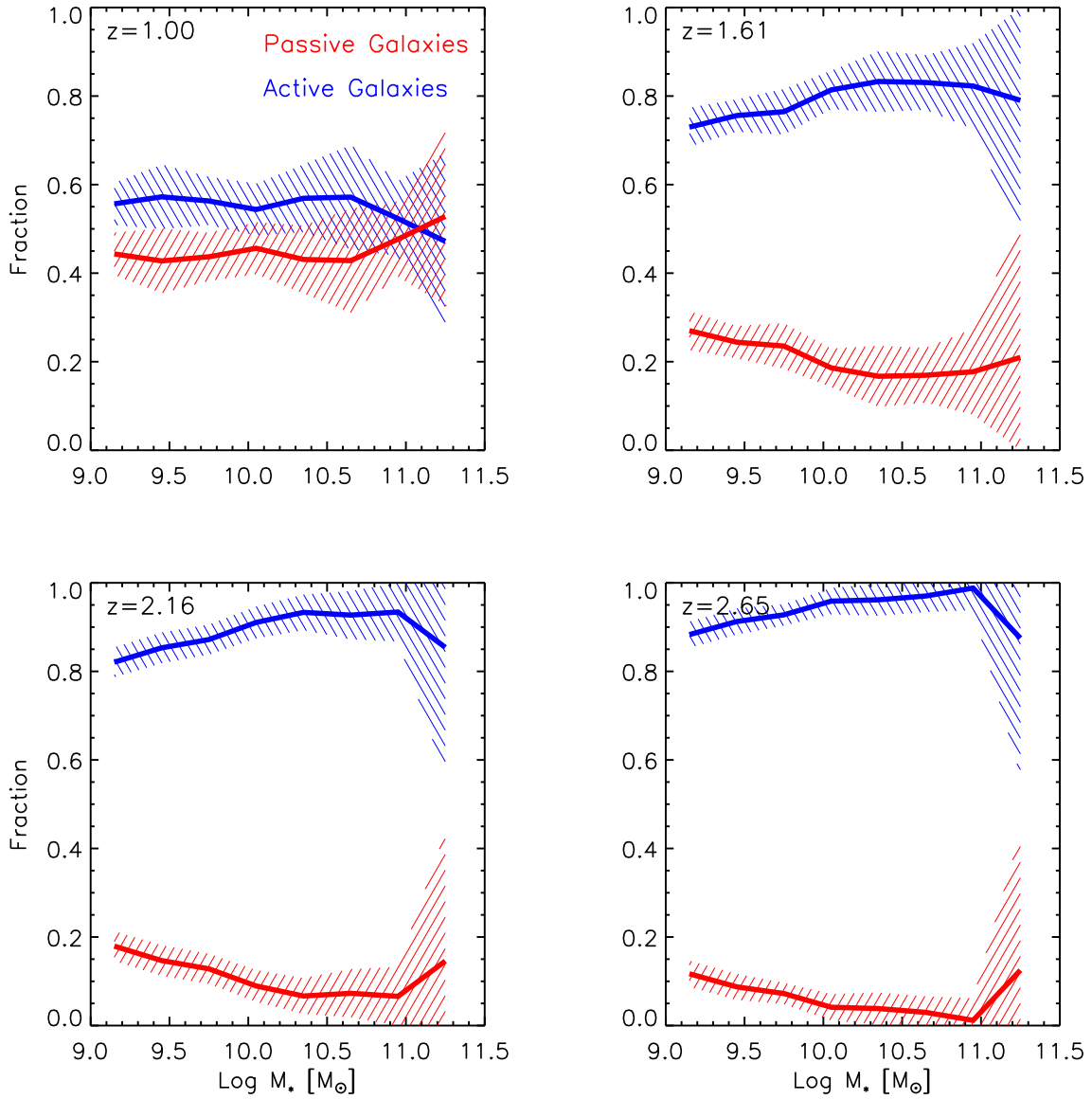


Figure 6.9: Fraction of passive and active progenitors of passive galaxies at redshift $z = 0$ within the virial radius R_{200} , as a function of their stellar mass at the redshift of interest (different panels). Solid lines represent the mean value calculated by averaging 27 proto-cluster regions, and dashed areas represent the 1-sigma scatter of the distributions.

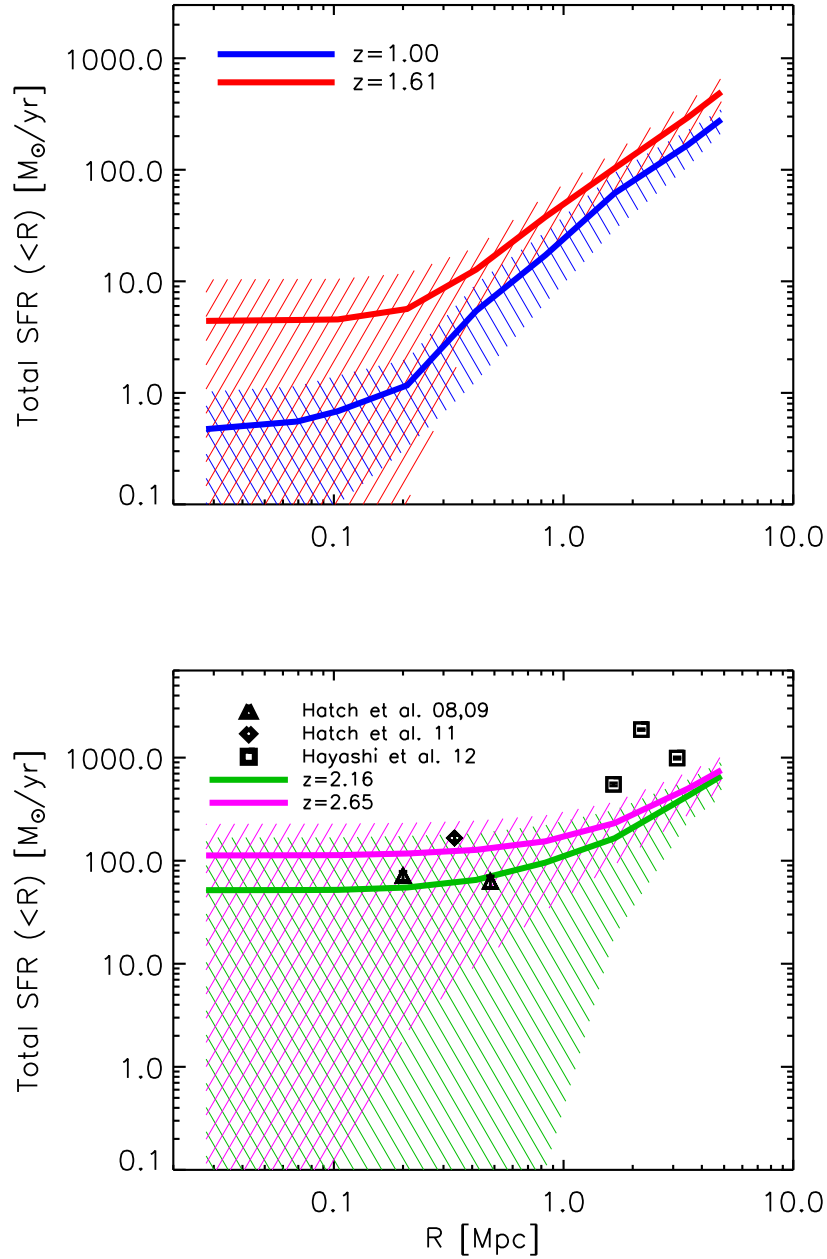


Figure 6.10: Total star formation rate of galaxies in the proto-cluster regions as a function of the projected distance from the centre, at different redshifts (different colours). Solid lines represent the mean value calculated by averaging 27 proto-cluster regions, and dashed areas represent the 1sigma scatter of the distributions. Black triangles and diamond represent the observational data by Hatch et al. (2008, 2009), and Hatch et al. (2011b), respectively, and black squares represent observational measurements by Hayashi et al. (2012).

these studies by means of the relation

$$M_{Cha}(z) = 0.55 \cdot M_{Sal}(z).$$

These star formation rates are dust-uncorrected. Assuming a minimum of dust extinction, especially in the inner regions, they move up to the upper limits of our predictions, or even beyond. Hence, despite the large object-to-object scatter especially at high redshift and in the inner regions, our model predicts star formation rates that are likely too low with respect observational data.

6.8 Conclusions

We have analysed a sample of 27 proto-cluster regions extracted from a set of high-resolution simulations, that become massive clusters, with $M \sim 10^{15} M_{\odot}$, at $z = 0$. These regions have been built by considering all progenitors of $z = 0$ galaxies within the virial radius R_{200} of the clusters into which these objects will evolve. Our analysis shows that proto-clusters are very extended objects. In fact, we find that at most 50 per cent of progenitors are located within a box of $15 h^{-1} Mpc$ size centred on the central galaxy of the proto-cluster, at redshift higher than ~ 1.5 . The percentage decreases drastically in smaller boxes, to at most 20 per cent for $5 h^{-1} Mpc$ apertures. This demonstrates that one has to consider fairly large regions, having comoving sizes larger than $15 Mpc$, in order to trace the distribution of a large fraction of the progenitors of the galaxies belonging to local clusters.

We find that the number of interlopers, i.e. those galaxies that are not progenitors of any cluster galaxy at $z = 0$, is weakly dependent on the galaxy stellar mass and redshift, and does not strongly depend on the size of the box. On average, we find that about 30 per cent of galaxies with stellar mass smaller than $\sim 10^{10} M_{\odot}$, and about 20 per cent of galaxies with larger stellar masses, are interlopers in proto-cluster regions at $z \sim 3$. Slightly smaller fractions are found at lower redshift and/or considering only progenitors of galaxies within the virial radius (instead of $2 \cdot R_{200}$).

Galaxies in proto-clusters are actively star forming, more intensively at increasing redshift. Nevertheless, if we consider a minimum dust correction, our model predicts proto-cluster regions that are slightly less star forming than those observed, and tend to be even less star forming than observed if we take into account larger apertures ($\gtrsim 1 Mpc$).

The population of active galaxies, those that have a specific star formation rate larger than $10^{-11} M_{\odot}/yr$, is the dominant one at redshift higher than ~ 1.5 . In fact, we find that at $z \gtrsim 2$ active galaxies constitute almost 80 per cent of the entire population and the percentage is weakly dependent on the size of the box. This fraction increases along with the fraction of centrals, suggesting that these two populations are linked. At fixed redshift, the fraction of active galaxies increases at increasing distance from the central galaxy, and equals the fraction of passive galaxies only in the first $2 Mpc$, at redshift $z \sim 1.6$.

We have studied the evolution with redshift of the stellar mass function, separately for active and passive galaxies in our proto-clusters, within a box of $7 h^{-1} Mpc$ size. The two populations evolve differently, and similar to their counterparts in the field. The stellar mass functions of passive galaxies at different redshift show that massive galaxies evolve as fast as less massive galaxies: the number density of passive galaxies increases at every stellar mass, with a difference of a factor about 30 between redshift $z \sim 3$ and $z = 1$. The number density of active galaxies increases of a factor 0.4-0.5 dex between $z \sim 3$ and $z = 1$ for galaxies with stellar mass up to $10^{11.2} M_{\odot}$; in the very massive-end, the stellar mass function drops at lower stellar mass as the redshift decreases. Our results are in agreement with recent observational data by Ilbert et al. (2013), in the field. We have investigated the progenitors of passive galaxies at redshift $z = 0$ and found that a large fraction of them are active at $z \gtrsim 1.6$ regardless their mass, and active progenitors are also preferentially more massive than the passive ones. This means that the progenitors of passive galaxies in clusters were typically active galaxies in proto-clusters, and the most massive passive galaxies in clusters are built-up from the most massive and active galaxies in proto-clusters, in agreement with the trend shown by the evolution of the stellar mass functions.

Chapter 7

Conclusions and Future Prospects

The aim of my Thesis was to explore the physical properties of the galaxy population in clusters and proto-clusters. A large number of physical processes play an important role in the formation and evolution of galaxies: cooling, that allows the condensation of gas at the centre of dark matter haloes; star formation, that converts cold gas in stars; feedback from Active Galactic Nuclei (AGN), that prevents the gas in the central regions of haloes from "over-cooling"; feedback from Supernovae, that liberates energy in the surrounding, mixing the gas and enriching it with heavy metals. Galaxy clusters are special environments in which additional important processes take place, and play an important role in the evolution of the cluster galaxy population. Galaxy merging, harassments, tidal interactions, ram pressure stripping and strangulation are all processes acting in dense environments such as clusters of galaxies.

In this Thesis, I have taken advantage of a *state of the art*-semi-analytic model of galaxy formation and of a set of 27 high-resolution dark matter only simulations: the semi-analytic model is based on physically motivated and observationally constrained prescriptions for the physical processes mentioned above and makes use of merger-trees extracted from the simulations to generate mock catalogues of galaxies.

In a first step, I have utilised this set of simulations to carry out a statistical study of dark matter substructures. In the framework of modern theories of galaxy formation, these are considered the birth-sites of luminous galaxies. Therefore, the analysis of subhaloes, and in particular of their mass and spatial distributions, merger and mass accretion histories, provides important information about the expected properties of galaxies in the framework of hierarchical galaxy formation models.

I have studied the amount and distribution of dark matter substructures within dark matter haloes in Chapter 4, focusing mainly on the measured properties of subhaloes as a function of the mass and physical properties of their parent haloes, and redshift. I have shown that the fraction of halo mass in substructures increases with increasing mass: it is of the order of 5 per cent for haloes with $M_{200} \sim 10^{13} M_{\odot}$ and of the order of 10 per cent

for the most massive haloes in the sample, with $M_{200} \sim 10^{15} M_{\odot}$. There is, however, a very large halo-to-halo scatter that can be explained only in part by a range of halo physical properties, e.g. concentration. At given halo mass, less concentrated haloes contain significantly larger fractions of mass in substructures because of the reduced strength of tidal disruption. Most of the substructure mass is located at the outskirts of the parent haloes, in relatively few massive subhaloes. This mass segregation appears to become stronger at increasing redshift, and should induce a more significant mass segregation of the galaxy population at different cosmic epochs. When haloes are accreted onto larger structures, their mass is significantly reduced by tidal stripping. Haloes that are more massive at the time of accretion (these should host more luminous galaxies) are brought closer to the centre on shorter time-scales by dynamical friction, and therefore suffer of a more significant stripping. The halo merger rate depends strongly on the environment with substructures in more massive haloes suffering more important mergers than their counterparts residing in less massive systems. This should translate into a different morphological mix for haloes of different mass.

In a second part of the Thesis, I have described the implementation of physical processes responsible for the generation of the Intra-Cluster Light (ICL) in the available semi-analytic model, that, in its original form, does not account for them. The inclusion of these physical processes, which describe stellar stripping, was expected to improve model predictions. I have taken advantage of this upgrade of the model in Chapter 5 to investigate the origin of the ICL and to understand how the main properties of galaxies change with respect to a model that does not include these additional prescriptions. I have assumed that the ICL forms by (a) stellar stripping of satellite galaxies and (b) relaxation processes that take place during galaxy mergers. I have shown that the fraction of ICL in groups and clusters predicted by these models ranges between 10 and 40 per cent, with a large halo-to-halo scatter and no halo mass dependence. I have demonstrated, however, that the predicted ICL fractions depend on the resolution: for a set of simulations with particle mass one order of magnitude larger than that adopted in the high resolution runs used for the analysis, I have found that the predicted ICL fractions are 30-40 per cent larger than those found in the high resolution runs. On cluster scale, large part of the scatter is due to a range of dynamical histories, while on smaller scale it is driven by individual accretion events and stripping of very massive satellites, $M_* \gtrsim 10^{10.5} M_{\odot}$, that we find to be the major contributors to the ICL. The ICL in the models forms very late (below $z \sim 1$), and a fraction varying between 5 and 25 per cent of it has been accreted during the hierarchical growth of haloes. In agreement with recent observational measurements, the ICL is found to be made of stars covering a relatively large range of metallicity, with the bulk of them having sub-solar metallicity.

In the last part of the Thesis, the updated model is used to investigate the properties of the galaxy population in proto-cluster regions. These regions have been built by considering all progenitors of those galaxies that at $z = 0$ are found within the virial radius

R_{200} of the clusters. The analysis performed in Chapter 6 has shown that proto-clusters are very extended objects. In fact, 50 per cent of progenitors are located within a region of $15 h^{-1} Mpc$ size centred on the central galaxy of the proto-cluster region, at redshift higher than ~ 1.5 . The percentage rapidly decreases by considering smaller regions, with only 20 per cent of such progenitors found within a box of 5 comoving $h^{-1} Mpc$ on a side. I have investigated the galaxy population in proto-clusters, first looking at the contamination given by interlopers (defined as those objects that are not progenitors of galaxies in clusters at $z = 0$), then focusing on the main properties of progenitors. I have found that the number of interlopers is weakly dependent on the galaxy stellar mass and redshift, and does not strongly depend on the size of the box. On average, about 30 per cent of galaxies with stellar mass smaller than $\sim 10^{10} M_{\odot}$, and about 20 per cent of galaxies with larger stellar masses, are interlopers in proto-cluster regions at $z \sim 3$. Slightly smaller fractions are found at lower redshift and/or considering only progenitors of galaxies within the virial radius (instead of $2 \cdot R_{200}$). Galaxies in proto-clusters appear to be actively star forming, more intensely at increasing redshift. The model predicts proto-cluster regions that are slightly less star forming than those observed if we consider a minimum dust correction, and tend to be even less star forming than observed if we take into account larger apertures (larger than $\sim 1 Mpc$). The population of blue galaxies is the dominant one at redshift higher than ~ 1.5 , accounting for almost 80 per cent of the entire population. At fixed redshift, the fraction of blue galaxies also increases at increasing distance from the central galaxy. Blue and red galaxies evolve differently and similar to their counterparts in the field (as suggested by recent observational data by Ilbert et al. 2013), as shown by the analysis of their stellar mass function. The stellar mass functions of red galaxies at different redshift show that massive galaxies evolve as fast as less massive galaxies: the number density of red galaxies increases at every stellar mass. The number density of blue galaxies, instead, increases of a factor 0.4-0.5 dex between $z \sim 3$ and $z = 1$ for galaxies with stellar mass up to $10^{11.2} M_{\odot}$; in the very massive-end, the stellar mass function drops at lower stellar mass as the redshift decreases.

Despite the success of the semi-analytic model used in this Thesis in reproducing a number of observational results, several directions should be followed in order to improve the description of galaxy formation. The implementation of processes such as stellar stripping brings model prediction into better agreement with some observations such as the stellar mass function (in addition to the generation of the diffuse light not described before). These processes take into account the mutual interactions between satellite galaxies and the cluster in which they reside, thereby allowing stars to unbind and form a diffuse component. An interesting prospect arises from the analysis of the properties of this diffuse component, especially its metallicity. Most of the diffuse component is produced by tidal stripping of massive satellites, and this diffuse component has a metallicity similar

to that of these galaxies. Predictions of the model are qualitatively in agreement with observations, with most of the stars in the diffuse component having sub-solar metallicities. The inclusion in the model of specific prescriptions for tidal stripping have not affected the predicted mass-metallicity relation, and only slightly increases the metallicity of the most massive galaxies. For all models, these galaxies have stellar metallicities significantly lower than observed. Future and more detailed observations focused e.g. on age and metallicity of the diffuse component will help constraining the models of stellar stripping used in this Thesis and understanding the physical mechanisms that drive the formation of this intra-cluster light.

The analysis presented in Chapter 6 has shown that the galaxy population in proto-clusters is similar to that of the general field. The blue galaxy population at high redshift evolves so as to build up the red galaxy population in clusters. Another interesting direction of investigation would be that of providing detailed comparisons between model predictions and observational measurements of specific properties of galaxies in proto-clusters. In fact, the model has some limits in reproducing the properties of galaxies, especially those of satellites as they experience dense environments. For example, one particular limit is given by the simplistic description of the gas stripping currently adopted. Such detailed comparisons, that might concern the gas content and star formation rate of high-redshift galaxies, can help to understand, and then to better describe in the model, those processes responsible more for galaxy evolution rather than for galaxy formation. These might be processes that involve gas stripping, such as ram pressure, or there might simply be the need of more sophisticated implementations of processes already modelled, such as feedback or star formation. This need comes out from the fact that the model underpredicts the observed star formation rate at high redshift.

This Thesis has demonstrated that theoretical models aimed at describing galaxy formation and evolution requires more and more detailed and complex modelling of the most important processes at play. More detailed semi-analytic models, as well as numerical simulations, are needed in order to interpret the large amount of observational data of properties of galaxies, in different environments and at different epochs, that will be provided in the next future by new telescopes and missions (e.g., the James Webb Space Telescope (JWST), the Square Kilometre Array (SKA) and Euclid). Thanks to a constant link between model predictions and observational evidence, these models can provide a better description of galaxy properties, allowing us to do a step forward in the comprehension of galaxy formation.

Appendix A

Basics of Cosmology

Linear Evolution of Density Perturbations

An important cornerstone of structure formation is given by the theory that describes the gravitational instability. This theory, also known as Jean's theory, was first thought to explain the formation of planets and stars. Then, it was conveniently revised and used in cosmology. Jeans (see Coles & Lucchin 2002) proved that small perturbations of a homogeneous isotropic fluid can grow with time if its pressure is negligible compared to its self gravity.

Let us consider an ideal, self-gravitating and pressureless fluid that dominates the matter content of an expanding Universe. In principle, this assumption is valid if we deal with the evolution of dark matter perturbations or with structures larger than the characteristic baryonic Jeans scale¹.

If \bar{x} is the comoving coordinate and $a(t)$ the cosmic expansion factor, $\bar{r} = a(t)\bar{x}$ provides the proper coordinate. Consequently, the total velocity of a fluid element is given by $\bar{v} = \dot{\bar{r}} = \dot{a}\bar{x} + \bar{u}$, where $\dot{a}\bar{x}$ and $\bar{u} = a(t)\dot{\bar{x}}$ are the Hubble flow and the peculiar velocities, respectively. Under these assumptions, the Newtonian treatment of the evolution of density perturbations is described by the continuity, the Euler, and the Poisson equations:

$$\frac{\partial \delta}{\partial t} + \nabla \cdot [(1 + \delta)\bar{u}] = 0 \quad (\text{A.1})$$

$$\frac{\partial \bar{u}}{\partial t} + 2H(t)\bar{u} + (\bar{u} \cdot \nabla)\bar{u} = -\frac{\nabla \phi}{a^2} \quad (\text{A.2})$$

$$\nabla^2 \phi = 4\pi G \bar{\rho} a^2 \delta, \quad (\text{A.3})$$

¹The Jeans length, the characteristic length scale for the self-gravity of the gas, is defined as $\lambda_J = \sqrt{\frac{15k_B T}{4\pi G \mu \rho_{gas}}}$, with k_B the Boltzmann constant, T the gas temperature, G the Newton's constant, μ the mean molecular weight and ρ_{gas} the mass density of the gas.

where $\delta = (\rho - \rho_b)/\rho_b$ is the perturbation of the density with respect to the background density ρ_b , ∇ is the gradient taken with respect to \bar{x} , $\phi(\bar{x})$ is the perturbation of the gravitational potential, and $H(t) = \dot{a}/a = E(t)H_0$ is the time-dependent Hubble parameter, where

$$E(z) \equiv \frac{H(t)}{H_0} = [(1+z)^3\Omega_m + (1+z)^2\Omega_k + \Omega_\Lambda]^{1/2} \quad (\text{A.4})$$

is connected to the different density parameters as provided by non-relativistic matter, Ω_m , curvature, $\Omega_k = 1 - \Omega_m - \Omega_\Lambda$, and cosmological constant, Ω_Λ .

If we consider small density fluctuations ($\delta \ll 1$), all the non-linear terms with respect to δ and \bar{u} can be ignored and, therefore, the above equations can be written as

$$\frac{\partial^2 \delta}{\partial t^2} + 2H(t) \frac{\partial \delta}{\partial t} = 4\pi G \bar{\rho} \delta. \quad (\text{A.5})$$

Equation A.5 is the fundamental equation of the linear theory of gravitational collapse. The term $2H(t) \frac{\partial \delta}{\partial t}$ represents the cosmic expansion that contrasts the exponential growth of the gravitational instability. Since equation A.5 is a second order differential equation in time t , its solution can be written as

$$\delta(\bar{x}, t) = \delta_+(\bar{x}, t_i) D_+(t) + \delta_-(\bar{x}, t_i) D_-(t), \quad (\text{A.6})$$

where $D_+(t)$ and $D_-(t)$ are, respectively, the growing and decaying modes of the density perturbation, and $\delta_+(\bar{x}, t_i)$ and $\delta_-(\bar{x}, t_i)$ the corresponding spatial distribution of the primordial matter field. These density growing modes depend on the particular background cosmology such that, in different Friedmann–Lemaître–Robertson–Walker (FLRW) universes, structures will grow in a different way. For a Λ CDM cosmology, the exact expression for the growing mode of perturbations is given by (see, e.g., Peebles 1993)

$$D_+(z) = \frac{5}{2} \Omega_m E(z) \int_z^\infty \frac{1+z'}{E(z')^3} dz'. \quad (\text{A.7})$$

In the case of a flat matter-dominated Einstein–de–Sitter Universe ($\Omega_m = 1$, $\Omega_\Lambda = 0$), given that $H(t) = 2/(3t)$, $D_+(t) = (t/t_i)^{2/3} \propto a(t)$ and $D_-(t) = (t/t_i)^{-1}$. In this particular case, one can demonstrate that cosmic expansion and gravitational instability proceed at the same rate.

This linear approximation can be applied after recombination, while $\delta \ll 1$, to describe the evolution of fluctuations in the density field on an initial mass scale $M \gtrsim M_J(z_{rec}) \sim 10^5 M_\odot$. The linear theory cannot be applied to the study of the growth of structures in a strong non-linear regime, where typical fluctuations reach overdensities with $\delta \gg 1$. In this case, non-linear models or numerical simulations are required to solve the evolution.

Spherical Collapse Model

The spherical collapse is an example of exact analytical solution of non-linear evolution, that holds for a specific geometry of collapse. To describe the spherical collapse model, we can start thinking that the evolution of a spherical density perturbation is identical to the evolution of the Universe with a matter density equal to the density of the halo. With a spherical perturbation, Gauss' Law states that we can ignore the matter outside the sphere, and that the mass interior is constant. The equation of motion

$$\frac{d^2r}{dt^2} = -\frac{GM}{r^2} \quad (\text{A.8})$$

can be integrated once to obtain the conservation of energy

$$\dot{r}^2 = 2\frac{GM}{r} + C. \quad (\text{A.9})$$

For a matter-dominated universe, the relation between the proper radius of the sphere and time is given by

$$r = A(1 - \cos \theta) \quad (\text{A.10})$$

and

$$t = B(\theta - \cos \theta) \quad (\text{A.11})$$

where A and B are two constants linked together by means of $A^3 = GMB^2$, $C = -A^2/B^2$ and $\theta = [0, 2\pi]$ is a parametric time variable. This is a cycloid, and since $C < 0$, the system is bound (the kinetic energy is smaller than the potential one). This is identical to the solution for the evolution of the scale factor in a closed Universe. Expanding the relation for r and t to the leading order in θ , we get $r(t)$ for small t :

$$r \simeq \frac{A}{2} \left(\frac{6t}{B}\right)^{2/3} \left[1 - \frac{1}{20} \left(\frac{6t}{B}\right)^{2/3}\right], \quad (\text{A.12})$$

and we can approximate the density perturbation within the sphere as

$$\delta \simeq \frac{3}{20} \left(\frac{6t}{B}\right)^{2/3} \quad (\text{A.13})$$

that agrees with what we get from the linear theory: at early times the sphere expands with the $a \propto t^{2/3}$ Hubble flow and the density perturbations grow proportional to a . Following Peacock (1999), we can now see how the linear theory breaks down as the perturbation evolves. Comparing only with linear theory for an $\Omega = 1$ background, we see the three interesting epoch in the final stage of the evolution of the perturbation.

The first epoch is called *turnround*. The spherical perturbation detaches from the general expansion of the Universe and reaches a maximum radius at $\theta = \pi$, $t = \pi B$. At this point, the true density enhancement with respect to the background is just

$$\left[\left(\frac{A}{2} \right) \left(\frac{6t}{B} \right)^{2/3} \right]^3 r^{-3} = \frac{9\pi^2}{16} \simeq 5.55,$$

while the extrapolation of the linear theory gives

$$\delta_{lin} = \left(\frac{3}{20} \right) (6\pi)^{2/3} \simeq 1.06.$$

The second interesting epoch is called *collapse*. If only gravity operates, then the sphere will collapse to a singularity at $\theta = 2\pi$, and this occurs when

$$\delta_{lin} = \left(\frac{3}{20} \right) (12\pi)^{2/3} \simeq 1.69.$$

The third epoch is the *virialization*. The collapse will never occurs because during the collapse, the dissipative physics intervenes converting the kinetic energy of collapse in random motions. If we consider the time at which the sphere has collapsed by a factor 2 from maximum expansion, at this point the link between its kinetic energy K and its potential energy V is given by the virial theorem, i.e.

$$V = -2K.$$

This is usually taken as the endpoint of gravitational collapse, and occurs at $\theta = 3\pi/2$ where the corresponding density enhancement is $(9\pi + 6)^2/8 \simeq 147$. Other authors, instead, prefer to assume that the virialized size is reached only at collapse, where the contrast becomes

$$(6\pi)^2/2 \simeq 178.$$

Bibliography

- Abadi, M.G., Navarro, J.F., & Steinmetz, M., 2006. *MNRAS*, 365:747
- Abell, G.O., 1958. *ApJS*, 3:211
- Abell, G.O., Corwin, Jr., H.G., & Olowin, R.P., 1989. *ApJS*, 70:1
- Aguerri, J.A.L., Sánchez-Janssen, R., & Muñoz-Tuñón, C., 2007. *A&A*, 471:17
- Allen, S.W., Evrard, A.E., & Mantz, A.B., 2011. *A&A Annual Rev.*, 49:409
- Almgren, A.S., Beckner, V.E., Bell, J.B., Day, M.S., Howell, L.H., Joggerst, C.C., Lijewski, M.J., Nonaka, A., Singer, M., & Zingale, M., 2010. *ApJ*, 715:1221
- Andreon, S. & Etti, S., 1999. *ApJ*, 516:647
- Andreon, S., Lobo, C., & Iovino, A., 2004. *MNRAS*, 349:889
- Andreon, S., Quintana, H., Tajer, M., Galaz, G., & Surdej, J., 2006. *MNRAS*, 365:915
- Arnaboldi, M., Ventimiglia, G., Iodice, E., Gerhard, O., & Coccato, L., 2012. *A&A*, 545:A37
- Bahcall, N.A., McKay, T.A., Annis, J., Kim, R.S.J., Dong, F., Hansen, S., Goto, T., Gunn, J.E., Miller, C., Nichol, R.C., Postman, M., Schneider, D., Schroeder, J., Voges, W., Brinkmann, J., & Fukugita, M., 2003. *ApJS*, 148:243
- Bahcall, N.A. & Soneira, R.M., 1983. *ApJ*, 270:20
- Baldry, I.K., Balogh, M.L., Bower, R.G., Glazebrook, K., Nichol, R.C., Bamford, S.P., & Budavari, T., 2006. *MNRAS*, 373:469
- Balogh, M.L., Baldry, I.K., Nichol, R., Miller, C., Bower, R., & Glazebrook, K., 2004. *ApJ*, 615:L101
- Balogh, M.L., Schade, D., Morris, S.L., Yee, H.K.C., Carlberg, R.G., & Ellingson, E., 1998. *ApJ*, 504:L75

- Bamford, S.P., Nichol, R.C., Baldry, I.K., Land, K., Lintott, C.J., Schawinski, K., Slosar, A., Szalay, A.S., Thomas, D., Torki, M., Andreescu, D., Edmondson, E.M., Miller, C.J., Murray, P., Raddick, M.J., & Vandenberg, J., 2009. *MNRAS*, 393:1324
- Barnes, J. & Hut, P., 1986. *Nature*, 324:446
- Barnes, J.E., 1992. *ApJ*, 393:484
- Barnes, J.E. & Hernquist, L., 1992. *A&A Annual Rev.*, 30:705
- Baugh, C.M., 2006. *Reports on Progress in Physics*, 69:3101
- Baum, W.A., 1959. *PAPS*, 71:106
- Behroozi, P.S., Conroy, C., & Wechsler, R.H., 2010. *ApJ*, 717:379
- Bell, E.F., Wolf, C., Meisenheimer, K., Rix, H.W., Borch, A., Dye, S., Kleinheinrich, M., Wisotzki, L., & McIntosh, D.H., 2004. *ApJ*, 608:752
- Benson, A.J., 2005. *MNRAS*, 358:551
- Berlind, A.A., Weinberg, D.H., Benson, A.J., Baugh, C.M., Cole, S., Davé, R., Frenk, C.S., Jenkins, A., Katz, N., & Lacey, C.G., 2003. *ApJ*, 593:1
- Binney, J. & Tremaine, S., 2008. *Galactic Dynamics: Second Edition*. Princeton University Press
- Biviano, A., 2000. In *Constructing the Universe with Clusters of Galaxies*
- Blakeslee, J.P., Anderson, K.R., Meurer, G.R., Benítez, N., & Magee, D., 2003. In H.E. Payne, R.I. Jedrzejewski, & R.N. Hook, editors, *Astronomical Data Analysis Software and Systems XII, Astronomical Society of the Pacific Conference Series*, vol. 295, page 257
- Blanton, M.R., Eisenstein, D., Hogg, D.W., Schlegel, D.J., & Brinkmann, J., 2005. *ApJ*, 629:143
- Böhringer, H., Schuecker, P., Guzzo, L., Collins, C.A., Voges, W., Schindler, S., Neumann, D.M., Cruddace, R.G., De Grandi, S., Chincarini, G., Edge, A.C., MacGillivray, H.T., & Shaver, P., 2001. *A&A*, 369:826
- Böhringer, H. & Werner, N., 2010. *A&A Rev.*, 18:127
- Bonafede, A., Dolag, K., Stasyszyn, F., Murante, G., & Borgani, S., 2011. ArXiv e-prints
- Bond, J.R., Cole, S., Efstathiou, G., & Kaiser, N., 1991. *ApJ*, 379:440
- Borgani, S., Moscardini, L., Plionis, M., Gorski, K.M., Holtzman, J., Klypin, A., Primack, J.R., Smith, C.C., & Stompor, R., 1997. *NewA*, 1:321

- Borgani, S., Rosati, P., Tozzi, P., Stanford, S.A., Eisenhardt, P.R., Lidman, C., Holden, B., Della Ceca, R., Norman, C., & Squires, G., 2001. *ApJ*, 561:13
- Bower, R.G., Lucey, J.R., & Ellis, R.S., 1992. *MNRAS*, 254:601
- Boylan-Kolchin, M., Ma, C.P., & Quataert, E., 2008. *MNRAS*, 383:93
- Brodwin, M., Gonzalez, A.H., Stanford, S.A., Plagge, T., Marrone, D.P., Carlstrom, J.E., Dey, A., Eisenhardt, P.R., Fedeli, C., Gettings, D., Jannuzi, B.T., Joy, M., Leitch, E.M., Mancone, C., Snyder, G.F., Stern, D., & Zeimann, G., 2012. *ApJ*, 753:162
- Bruzual, G. & Charlot, S., 2003. *MNRAS*, 344:1000
- Bryan, G.L. & Norman, M.L., 1997. *ArXiv Astrophysics e-prints*
- Bryan, G.L. & Norman, M.L., 1998. *ApJ*, 495:80
- Budzynski, J.M., Kuposov, S.E., McCarthy, I.G., McGee, S.L., & Belokurov, V., 2012. *MNRAS*, 423:104
- Bullock, J.S., Kolatt, T.S., Sigad, Y., Somerville, R.S., Kravtsov, A.V., Klypin, A.A., Primack, J.R., & Dekel, A., 2001. *MNRAS*, 321:559
- Bullock, J.S., Wechsler, R.H., & Somerville, R.S., 2002. *MNRAS*, 329:246
- Butcher, H. & Oemler, Jr., A., 1978. *ApJ*, 219:18
- Butcher, H. & Oemler, Jr., A., 1984. *ApJ*, 285:426
- Calcáneo-Roldán, C., Moore, B., Bland-Hawthorn, J., Malin, D., & Sadler, E.M., 2000. *MNRAS*, 314:324
- Cappellari, M., Bacon, R., Bureau, M., Damen, M.C., Davies, R.L., de Zeeuw, P.T., Emmen, E., Falcón-Barroso, J., Krajnović, D., Kuntschner, H., McDermid, R.M., Peletier, R.F., Sarzi, M., van den Bosch, R.C.E., & van de Ven, G., 2006. *MNRAS*, 366:1126
- Carlstrom, J.E., Holder, G.P., & Reese, E.D., 2002. *A&A Annual Rev.*, 40:643
- Chabrier, G., 2003. *PAPS*, 115:763
- Chiang, Y.K., Overzier, R., & Gebhardt, K., 2013. *ApJ*, 779:127
- Cocato, L., Gerhard, O., Arnaboldi, M., & Ventimiglia, G., 2011. *A&A*, 533:A138
- Cole, S., Norberg, P., Baugh, C.M., Frenk, C.S., Bland-Hawthorn, J., Bridges, T., Cannon, R., Colless, M., Collins, C., Couch, W., Cross, N., Dalton, G., De Propris, R., Driver, S.P., Efstathiou, G., Ellis, R.S., Glazebrook, K., Jackson, C., Lahav, O., Lewis, I., Lumsden, S., Maddox, S., Madgwick, D., Peacock, J.A., Peterson, B.A., Sutherland, W., & Taylor, K., 2001. *MNRAS*, 326:255

- Coles, P. & Lucchin, F., 2002. *Cosmology: The Origin and Evolution of Cosmic Structure, Second Edition*
- Colless, M., Dalton, G., Maddox, S., Sutherland, W., Norberg, P., Cole, S., Bland-Hawthorn, J., Bridges, T., Cannon, R., Collins, C., Couch, W., Cross, N., Deeley, K., De Propriis, R., Driver, S.P., Efstathiou, G., Ellis, R.S., Frenk, C.S., Glazebrook, K., Jackson, C., Lahav, O., Lewis, I., Lumsden, S., Madgwick, D., Peacock, J.A., Peterson, B.A., Price, I., Seaborne, M., & Taylor, K., 2001. MNRAS, 328:1039
- Collister, A.A. & Lahav, O., 2005. MNRAS, 361:415
- Compostella, M., Cantalupo, S., & Porciani, C., 2013. MNRAS, 435:3169
- Conroy, C., Wechsler, R.H., & Kravtsov, A.V., 2006. ApJ, 647:201
- Conroy, C., Wechsler, R.H., & Kravtsov, A.V., 2007. ApJ, 668:826
- Contini, E., De Lucia, G., & Borgani, S., 2012. MNRAS, 420:2978
- Contini, E., De Lucia, G., Villalobos, Á., & Borgani, S., 2014. MNRAS, 437:3787
- Cooke, J., Barton, E.J., Bullock, J.S., Stewart, K.R., & Wolfe, A.M., 2008. ApJ, 681:L57
- Couchman, H.M.P. & Rees, M.J., 1986. MNRAS, 221:53
- Cox, T.J., Jonsson, P., Primack, J.R., & Somerville, R.S., 2006. MNRAS, 373:1013
- Croton, D.J., Springel, V., White, S.D.M., De Lucia, G., Frenk, C.S., Gao, L., Jenkins, A., Kauffmann, G., Navarro, J.F., & Yoshida, N., 2006. MNRAS, 365:11
- Crowl, H.H., Kenney, J.D.P., van Gorkom, J.H., & Vollmer, B., 2005. AJ, 130:65
- De Lucia, G., 2009. In G. Giobbi, A. Tornambe, G. Raimondo, M. Limongi, L.A. Antonelli, N. Menci, & E. Brocato, editors, *American Institute of Physics Conference Series, American Institute of Physics Conference Series*, vol. 1111, pages 3–10
- De Lucia, G. & Blaizot, J., 2007. MNRAS, 375:2
- De Lucia, G. & Borgani, S., 2012. MNRAS, 426:L61
- De Lucia, G., Boylan-Kolchin, M., Benson, A.J., Fontanot, F., & Monaco, P., 2010. MNRAS, 406:1533
- De Lucia, G., Kauffmann, G., Springel, V., White, S.D.M., Lanzoni, B., Stoehr, F., Tormen, G., & Yoshida, N., 2004a. MNRAS, 348:333
- De Lucia, G., Kauffmann, G., & White, S.D.M., 2004b. MNRAS, 349:1101

- De Lucia, G., Poggianti, B.M., Aragón-Salamanca, A., Clowe, D., Halliday, C., Jablonka, P., Milvang-Jensen, B., Pelló, R., Poirier, S., Rudnick, G., Saglia, R., Simard, L., & White, S.D.M., 2004c. *ApJ*, 610:L77
- De Lucia, G., Springel, V., White, S.D.M., Croton, D., & Kauffmann, G., 2006. *MNRAS*, 366:499
- De Propris, R., Phillipps, S., & Bremer, M.N., 2013. *MNRAS*, 434:3469
- De Propris, R., Stanford, S.A., Eisenhardt, P.R., & Dickinson, M., 2003. *ApJ*, 598:20
- De Propris, R., Stanford, S.A., Eisenhardt, P.R., Holden, B.P., & Rosati, P., 2007. *AJ*, 133:2209
- Diemand, J., Madau, P., & Moore, B., 2005. *MNRAS*, 364:367
- Dolag, K., Murante, G., & Borgani, S., 2010. *MNRAS*, 405:1544
- Doroshkevich, A.G., Zel'dovich, Y.B., & Novikov, I.D., 1967. *Soviet Astronomy*, 11:233
- Dressler, A., 1980. *ApJ*, 236:351
- Duc, P.A., Poggianti, B.M., Fadda, D., Elbaz, D., Flores, H., Chanical, P., Franceschini, A., Moorwood, A., & Cesarsky, C., 2002. *A&A*, 382:60
- Durrell, P.R., Ciardullo, R., Feldmeier, J.J., Jacoby, G.H., & Sigurdsson, S., 2002. *ApJ*, 570:119
- Efstathiou, G., 1992. *MNRAS*, 256:43P
- Eisenhardt, P.R.M., Brodwin, M., Gonzalez, A.H., Stanford, S.A., Stern, D., Barmby, P., Brown, M.J.I., Dawson, K., Dey, A., Doi, M., Galametz, A., Jannuzi, B.T., Kochanek, C.S., Meyers, J., Morokuma, T., & Moustakas, L.A., 2008. *ApJ*, 684:905
- Eisenstein, D.J., Zehavi, I., Hogg, D.W., Scoccimarro, R., Blanton, M.R., Nichol, R.C., Scranton, R., Seo, H.J., Tegmark, M., Zheng, Z., Anderson, S.F., Annis, J., Bahcall, N., Brinkmann, J., Burles, S., Castander, F.J., Connolly, A., Csabai, I., Doi, M., Fukugita, M., Frieman, J.A., Glazebrook, K., Gunn, J.E., Hendry, J.S., Hennessy, G., Ivezić, Z., Kent, S., Knapp, G.R., Lin, H., Loh, Y.S., Lupton, R.H., Margon, B., McKay, T.A., Meiksin, A., Munn, J.A., Pope, A., Richmond, M.W., Schlegel, D., Schneider, D.P., Shimasaku, K., Stoughton, C., Strauss, M.A., SubbaRao, M., Szalay, A.S., Szapudi, I., Tucker, D.L., Yanny, B., & York, D.G., 2005. *ApJ*, 633:560
- Ellingson, E., Lin, H., Yee, H.K.C., & Carlberg, R.G., 2001. *ApJ*, 547:609
- Evrard, A.E., 1997. *MNRAS*, 292:289
- Fabian, A.C., 1991. *MNRAS*, 253:29P

- Fabjan, D., Borgani, S., Rasia, E., Bonafede, A., Dolag, K., Murante, G., & Tornatore, L., 2011. ArXiv e-prints
- Fan, X., Strauss, M.A., Becker, R.H., White, R.L., Gunn, J.E., Knapp, G.R., Richards, G.T., Schneider, D.P., Brinkmann, J., & Fukugita, M., 2006. *AJ*, 132:117
- Fasano, G., Marmo, C., Varela, J., D'Onofrio, M., Poggianti, B.M., Moles, M., Pignatelli, E., Bettoni, D., Kjærgaard, P., Rizzi, L., Couch, W.J., & Dressler, A., 2006. *A&A*, 445:805
- Feldmeier, J.J., Ciardullo, R., Jacoby, G.H., & Durrell, P.R., 2004. *ApJ*, 615:196
- Font, A.S., Bower, R.G., McCarthy, I.G., Benson, A.J., Frenk, C.S., Helly, J.C., Lacey, C.G., Baugh, C.M., & Cole, S., 2008. *MNRAS*, 389:1619
- Font, A.S., Johnston, K.V., Bullock, J.S., & Robertson, B.E., 2006. *ApJ*, 638:585
- Fontanot, F., De Lucia, G., Monaco, P., Somerville, R.S., & Santini, P., 2009. *MNRAS*, 397:1776
- Gao, L., De Lucia, G., White, S.D.M., & Jenkins, A., 2004a. *MNRAS*, 352:L1
- Gao, L., Frenk, C.S., Boylan-Kolchin, M., Jenkins, A., Springel, V., & White, S.D.M., 2011. *MNRAS*, 410:2309
- Gao, L., White, S.D.M., Jenkins, A., Stoehr, F., & Springel, V., 2004b. *MNRAS*, 355:819
- Gettings, D.P., Gonzalez, A.H., Stanford, S.A., Eisenhardt, P.R.M., Brodwin, M., Mancone, C., Stern, D., Zeimann, G.R., Masci, F.J., Papovich, C., Tanaka, I., & Wright, E.L., 2012. *ApJ*, 759:L23
- Ghigna, S., Moore, B., Governato, F., Lake, G., Quinn, T., & Stadel, J., 1998. *MNRAS*, 300:146
- Ghigna, S., Moore, B., Governato, F., Lake, G., Quinn, T., & Stadel, J., 2000. *ApJ*, 544:616
- Gingold, R.A. & Monaghan, J.J., 1977. *MNRAS*, 181:375
- Giocoli, C., Tormen, G., & Sheth, R.K., 2012. *MNRAS*, 422:185
- Gladders, M.D., Lopez-Cruz, O., Yee, H.K.C., & Kodama, T., 1998. *ApJ*, 501:571
- Gladders, M.D. & Yee, H.K.C., 2005. *ApJS*, 157:1
- Gnedin, N.Y., 2000. *ApJ*, 542:535
- Gobat, R., Daddi, E., Onodera, M., Finoguenov, A., Renzini, A., Arimoto, N., Bouwens, R., Brusa, M., Chary, R.R., Cimatti, A., Dickinson, M., Kong, X., & Mignoli, M., 2011. *A&A*, 526:A133

- Gómez, P.L., Nichol, R.C., Miller, C.J., Balogh, M.L., Goto, T., Zabludoff, A.I., Romer, A.K., Bernardi, M., Sheth, R., Hopkins, A.M., Castander, F.J., Connolly, A.J., Schneider, D.P., Brinkmann, J., Lamb, D.Q., SubbaRao, M., & York, D.G., 2003. *ApJ*, 584:210
- Gonzalez, A.H., Zabludoff, A.I., & Zaritsky, D., 2005. *ApJ*, 618:195
- Gonzalez, A.H., Zaritsky, D., & Zabludoff, A.I., 2007. *ApJ*, 666:147
- Goto, T., Okamura, S., Yagi, M., Sheth, R.K., Bahcall, N.A., Zabel, S.A., Crouch, M.S., Sekiguchi, M., Annis, J., Bernardi, M., Chong, S.S., Gómez, P.L., Hansen, S., Kim, R.S.J., Knudson, A., McKay, T.A., & Miller, C.J., 2003. *PAPJ*, 55:739
- Gott, III, J.R., Gunn, J.E., Schramm, D.N., & Tinsley, B.M., 1974. *ApJ*, 194:543
- Gregg, M.D. & West, M.J., 1998. *Nature*, 396:549
- Guennou, L., Adami, C., Ulmer, M.P., Lebrun, V., Durret, F., Johnston, D., Ilbert, O., Clowe, D., Gavazzi, R., Murphy, K., Schrabback, T., Allam, S., Annis, J., Basa, S., Benoist, C., Biviano, A., Cappi, A., Kubo, J.M., Marshall, P., Mazure, A., Rostagni, F., Russeil, D., & Slezak, E., 2010. *A&A*, 523:A21
- Gunn, J.E. & Gott, III, J.R., 1972. *ApJ*, 176:1
- Guo, Q., White, S., Boylan-Kolchin, M., De Lucia, G., Kauffmann, G., Lemson, G., Li, C., Springel, V., & Weinmann, S., 2011. *MNRAS*, 413:101
- Guo, Q., White, S., Li, C., & Boylan-Kolchin, M., 2010. *MNRAS*, 404:1111
- Haines, C.P., Smith, G.P., Egami, E., Ellis, R.S., Moran, S.M., Sanderson, A.J.R., Merluzzi, P., Busarello, G., & Smith, R.J., 2009. *ApJ*, 704:126
- Hao, J., McKay, T.A., Koester, B.P., Rykoff, E.S., Roza, E., Annis, J., Wechsler, R.H., Evrard, A., Siegel, S.R., Becker, M., Busha, M., Gerdes, D., Johnston, D.E., & Sheldon, E., 2010. *ApJS*, 191:254
- Hatch, N.A., De Breuck, C., Galametz, A., Miley, G.K., Overzier, R.A., Röttgering, H.J.A., Doherty, M., Kodama, T., Kurk, J.D., Seymour, N., Venemans, B.P., Vernet, J., & Zirm, A.W., 2011a. *MNRAS*, 410:1537
- Hatch, N.A., Kurk, J.D., Pentericci, L., Venemans, B.P., Kuiper, E., Miley, G.K., & Röttgering, H.J.A., 2011b. *MNRAS*, 415:2993
- Hatch, N.A., Overzier, R.A., Kurk, J.D., Miley, G.K., Röttgering, H.J.A., & Zirm, A.W., 2009. *MNRAS*, 395:114

- Hatch, N.A., Overzier, R.A., Röttgering, H.J.A., Kurk, J.D., & Miley, G.K., 2008. *MNRAS*, 383:931
- Hayashi, M., Kodama, T., Tadaki, K.i., Koyama, Y., & Tanaka, I., 2012. *ApJ*, 757:15
- Henriques, B.M.B. & Thomas, P.A., 2010. *MNRAS*, 403:768
- Hernquist, L., 1989. *Nature*, 340:687
- Herschel, W., 1785. *Royal Society of London Philosophical Transactions Series I*, 75:213
- Hoessel, J.G., Gunn, J.E., & Thuan, T.X., 1980. *ApJ*, 241:486
- Hogg, D.W., Blanton, M.R., Brinchmann, J., Eisenstein, D.J., Schlegel, D.J., Gunn, J.E., McKay, T.A., Rix, H.W., Bahcall, N.A., Brinkmann, J., & Meiksin, A., 2004. *ApJ*, 601:L29
- Hogg, D.W., Blanton, M.R., Eisenstein, D.J., Gunn, J.E., Schlegel, D.J., Zehavi, I., Bahcall, N.A., Brinkmann, J., Csabai, I., Schneider, D.P., Weinberg, D.H., & York, D.G., 2003. *ApJ*, 585:L5
- Holden, B.P., Stanford, S.A., Squires, G.K., Rosati, P., Tozzi, P., Eisenhardt, P., & Spinrad, H., 2002. *AJ*, 124:33
- Hou, A., Parker, L.C., Wilman, D.J., McGee, S.L., Harris, W.E., Connelly, J.L., Balogh, M.L., Mulchaey, J.S., & Bower, R.G., 2012. *MNRAS*, 421:3594
- Ilbert, O., McCracken, H.J., Le Fèvre, O., Capak, P., Dunlop, J., Karim, A., Renzini, M.A., Caputi, K., Boissier, S., Arnouts, S., Aussel, H., Comparat, J., Guo, Q., Hudelot, P., Kartaltepe, J., Kneib, J.P., Krogager, J.K., Le Flo'c'h, E., Lilly, S., Mellier, Y., Milvang-Jensen, B., Moutard, T., Onodera, M., Richard, J., Salvato, M., Sanders, D.B., Scoville, N., Silverman, J.D., Taniguchi, Y., Tasca, L., Thomas, R., Toft, S., Tresse, L., Vergani, D., Wolk, M., & Zirm, A., 2013. *A&A*, 556:A55
- Into, T. & Portinari, L., 2013. *MNRAS*, 430:2715
- Inutsuka, S.I., 2002. *Journal of Computational Physics*, 179:238
- Ishiyama, T., Fukushige, T., & Makino, J., 2009. *ApJ*, 696:2115
- Jarrett, T.H., Chester, T., Cutri, R., Schneider, S., Skrutskie, M., & Huchra, J.P., 2000. *AJ*, 119:2498
- Jiang, C.Y., Jing, Y.P., Faltenbacher, A., Lin, W.P., & Li, C., 2008. *ApJ*, 675:1095
- Jing, Y.P., Mo, H.J., & Boerner, G., 1998. *ApJ*, 494:1
- Kauffmann, G., 1995. *MNRAS*, 274:153

- Kauffmann, G., 1996. MNRAS, 281:487
- Kauffmann, G. & Haehnelt, M., 2000. MNRAS, 311:576
- Kauffmann, G., Heckman, T.M., White, S.D.M., Charlot, S., Tremonti, C., Peng, E.W., Seibert, M., Brinkmann, J., Nichol, R.C., SubbaRao, M., & York, D., 2003. MNRAS, 341:54
- Kauffmann, G., White, S.D.M., Heckman, T.M., Ménard, B., Brinchmann, J., Charlot, S., Tremonti, C., & Brinkmann, J., 2004. MNRAS, 353:713
- Kennicutt, Jr., R.C., 1998. ApJ, 498:541
- Klypin, A., Gottlöber, S., Kravtsov, A.V., & Khokhlov, A.M., 1999. ApJ, 516:530
- Klypin, A.A. & Shandarin, S.F., 1983. MNRAS, 204:891
- Knebe, A., Knollmann, S.R., Muldrew, S.I., Pearce, F.R., Aragon-Calvo, M.A., Ascasibar, Y., Behroozi, P.S., Ceverino, D., Colombi, S., Diemand, J., Dolag, K., Falck, B.L., Fasel, P., Gardner, J., Gottlöber, S., Hsu, C.H., Iannuzzi, F., Klypin, A., Lukić, Z., Maciejewski, M., McBride, C., Neyrinck, M.C., Planelles, S., Potter, D., Quilis, V., Rasera, Y., Read, J.I., Ricker, P.M., Roy, F., Springel, V., Stadel, J., Stinson, G., Sutter, P.M., Turchaninov, V., Tweed, D., Yepes, G., & Zemp, M., 2011. MNRAS, 415:2293
- Kodama, T. & Arimoto, N., 1997. A&A, 320:41
- Kodama, T., Arimoto, N., Barger, A.J., & Arag'on-Salamanca, A., 1998. A&A, 334:99
- Kodama, T., Yamada, T., Akiyama, M., Aoki, K., Doi, M., Furusawa, H., Fuse, T., Imanishi, M., Ishida, C., Iye, M., Kajisawa, M., Karoji, H., Kobayashi, N., Komiyama, Y., Kosugi, G., Maeda, Y., Miyazaki, S., Mizumoto, Y., Morokuma, T., Nakata, F., Noumaru, J., Ogasawara, R., Ouchi, M., Sasaki, T., Sekiguchi, K., Shimasaku, K., Simpson, C., Takata, T., Tanaka, I., Ueda, Y., Yasuda, N., & Yoshida, M., 2004. MNRAS, 350:1005
- Koester, B.P., McKay, T.A., Annis, J., Wechsler, R.H., Evrard, A., Bleem, L., Becker, M., Johnston, D., Sheldon, E., Nichol, R., Miller, C., Scranton, R., Bahcall, N., Barentine, J., Brewington, H., Brinkmann, J., Harvanek, M., Kleinman, S., Krzesinski, J., Long, D., Nitta, A., Schneider, D.P., Sneddin, S., Voges, W., & York, D., 2007. ApJ, 660:239
- Komatsu, E., Dunkley, J., Nolta, M.R., Bennett, C.L., Gold, B., Hinshaw, G., Jarosik, N., Larson, D., Limon, M., Page, L., Spergel, D.N., Halpern, M., Hill, R.S., Kogut, A., Meyer, S.S., Tucker, G.S., Weiland, J.L., Wollack, E., & Wright, E.L., 2009. ApJS, 180:330
- Komatsu, E., Smith, K.M., Dunkley, J., Bennett, C.L., Gold, B., & Hinshaw, 2011. ApJS, 192:18

- Kowalski, M., Rubin, D., Aldering, G., Agostinho, R.J., Amadon, A., Amanullah, R., Baland, C., Barbary, K., Blanc, G., Challis, P.J., Conley, A., Connolly, N.V., Covarrubias, R., Dawson, K.S., Deustua, S.E., Ellis, R., Fabbro, S., Fadeyev, V., Fan, X., Farris, B., Folatelli, G., Frye, B.L., Garavini, G., Gates, E.L., Germany, L., Goldhaber, G., Goldman, B., Goobar, A., Groom, D.E., Haissinski, J., Hardin, D., Hook, I., Kent, S., Kim, A.G., Knop, R.A., Lidman, C., Linder, E.V., Mendez, J., Meyers, J., Miller, G.J., Moniez, M., Mourão, A.M., Newberg, H., Nobili, S., Nugent, P.E., Pain, R., Perdureau, O., Perlmutter, S., Phillips, M.M., Prasad, V., Quimby, R., Regnault, N., Rich, J., Rubenstein, E.P., Ruiz-Lapuente, P., Santos, F.D., Schaefer, B.E., Schommer, R.A., Smith, R.C., Soderberg, A.M., Spadafora, A.L., Strolger, L.G., Strovink, M., Suntzeff, N.B., Suzuki, N., Thomas, R.C., Walton, N.A., Wang, L., Wood-Vasey, W.M., Yun, J.L., & Supernova Cosmology Project, 2008. *ApJ*, 686:749
- Koyama, Y., Kodama, T., Shimasaku, K., Hayashi, M., Okamura, S., Tanaka, I., & Tokoku, C., 2010. *MNRAS*, 403:1611
- Koyama, Y., Kodama, T., Tadaki, K.i., Hayashi, M., Tanaka, M., Smail, I., Tanaka, I., & Kurk, J., 2013. *MNRAS*, 428:1551
- Kravtsov, A.V., Berlind, A.A., Wechsler, R.H., Klypin, A.A., Gottlöber, S., Allgood, B., & Primack, J.R., 2004a. *ApJ*, 609:35
- Kravtsov, A.V. & Borgani, S., 2012. *A&A Annual Rev.*, 50:353
- Kravtsov, A.V., Gnedin, O.Y., & Klypin, A.A., 2004b. *ApJ*, 609:482
- Kuiper, E., Hatch, N.A., Miley, G.K., Nesvadba, N.P.H., Röttgering, H.J.A., Kurk, J.D., Lehnert, M.D., Overzier, R.A., Pentericci, L., Schaye, J., & Venemans, B.P., 2011. *MNRAS*, 415:2245
- Kurk, J.D., Pentericci, L., Overzier, R.A., Röttgering, H.J.A., & Miley, G.K., 2004. *A&A*, 428:817
- Lacey, C. & Cole, S., 1993. *MNRAS*, 262:627
- Lacey, C. & Cole, S., 1994. *MNRAS*, 271:676
- Lagos, C.d.P., Lacey, C.G., & Baugh, C.M., 2013. *MNRAS*, 436:1787
- Larson, R.B., Tinsley, B.M., & Caldwell, C.N., 1980. *ApJ*, 237:692
- Lee, K.S., Giavalisco, M., Gnedin, O.Y., Somerville, R.S., Ferguson, H.C., Dickinson, M., & Ouchi, M., 2006. *ApJ*, 642:63
- Lerchster, M., Seitz, S., Brimiouille, F., Fassbender, R., Rovilos, M., Böhringer, H., Pierini, D., Kilbinger, M., Finoguenov, A., Quintana, H., & Bender, R., 2011. *MNRAS*, 411:2667

- Lewis, I., Balogh, M., De Propriis, R., Couch, W., Bower, R., Offer, A., Bland-Hawthorn, J., Baldry, I.K., Baugh, C., Bridges, T., Cannon, R., Cole, S., Colless, M., Collins, C., Cross, N., Dalton, G., Driver, S.P., Efstathiou, G., Ellis, R.S., Frenk, C.S., Glazebrook, K., Hawkins, E., Jackson, C., Lahav, O., Lumsden, S., Maddox, S., Madgwick, D., Norberg, P., Peacock, J.A., Percival, W., Peterson, B.A., Sutherland, W., & Taylor, K., 2002. *MNRAS*, 334:673
- Lidman, C., Rosati, P., Tanaka, M., Strazzullo, V., Demarco, R., Mullis, C., Ageorges, N., Kissler-Patig, M., Petr-Gotzens, M.G., & Selman, F., 2008. *A&A*, 489:981
- Lin, Y.T. & Mohr, J.J., 2004. *ApJ*, 617:879
- Lin, Y.T., Mohr, J.J., & Stanford, S.A., 2004. *ApJ*, 610:745
- Liu, L., Yang, X., Mo, H.J., van den Bosch, F.C., & Springel, V., 2010. *ApJ*, 712:734
- Loh, Y.S., Ellingson, E., Yee, H.K.C., Gilbank, D.G., Gladders, M.D., & Barrientos, L.F., 2008. *ApJ*, 680:214
- Longhetti, M. & Saracco, P., 2009. *MNRAS*, 394:774
- Loubser, S.I., Sánchez-Blázquez, P., Sansom, A.E., & Soechting, I.K., 2009. *MNRAS*, 398:133
- Lucy, L.B., 1977. *AJ*, 82:1013
- Mahajan, S. & Raychaudhury, S., 2009. *MNRAS*, 400:687
- Mancone, C.L., Baker, T., Gonzalez, A.H., Ashby, M.L.N., Stanford, S.A., Brodwin, M., Eisenhardt, P.R.M., Snyder, G., Stern, D., & Wright, E.L., 2012. *ApJ*, 761:141
- Mancone, C.L., Gonzalez, A.H., Brodwin, M., Stanford, S.A., Eisenhardt, P.R.M., Stern, D., & Jones, C., 2010. *ApJ*, 720:284
- Marchesini, D., van Dokkum, P.G., Förster Schreiber, N.M., Franx, M., Labbé, I., & Wuyts, S., 2009. *ApJ*, 701:1765
- Margoniner, V.E., de Carvalho, R.R., Gal, R.R., & Djorgovski, S.G., 2001. *ApJ*, 548:L143
- Marín, F.A., Blake, C., Poole, G.B., McBride, C.K., Brough, S., Colless, M., Contreras, C., Couch, W., Croton, D.J., Croom, S., Davis, T., Drinkwater, M.J., Forster, K., Gilbank, D., Gladders, M., Glazebrook, K., Jelliffe, B., Jurek, R.J., Li, I.h., Madore, B., Martin, D.C., Pimblet, K., Pracy, M., Sharp, R., Wisnioski, E., Woods, D., Wyder, T.K., & Yee, H.K.C., 2013. *MNRAS*, 432:2654
- Martel, H., Barai, P., & Brito, W., 2012. *ApJ*, 757:48
- Martin, C.L., 1999. *ApJ*, 513:156

- Matthews, T.A., Morgan, W.W., & Schmidt, M., 1964. *ApJ*, 140:35
- McGee, S.L. & Balogh, M.L., 2010. *MNRAS*, 403:L79
- McGreer, I.D., Mesinger, A., & Fan, X., 2011. *MNRAS*, 415:3237
- McLure, R.J., Kukula, M.J., Dunlop, J.S., Baum, S.A., O'Dea, C.P., & Hughes, D.H., 1999. *MNRAS*, 308:377
- Mei, S., Holden, B.P., Blakeslee, J.P., Ford, H.C., Franx, M., Homeier, N.L., Illingworth, G.D., Jee, M.J., Overzier, R., Postman, M., Rosati, P., Van der Wel, A., & Bartlett, J.G., 2009. *ApJ*, 690:42
- Merlin, E., Buonomo, U., Grassi, T., Piovan, L., & Chiosi, C., 2010. *A&A*, 513:A36
- Messier, C., 1784. *Connaissance des temps*. Tech. rep.
- Metevier, A.J., Romer, A.K., & Ulmer, M.P., 2000. *AJ*, 119:1090
- Mihos, J.C., 2004. *Clusters of Galaxies: Probes of Cosmological Structure and Galaxy Evolution*, page 277
- Mihos, J.C. & Hernquist, L., 1994. *ApJ*, 437:611
- Miley, G. & De Breuck, C., 2008. *A&A Rev.*, 15:67
- Miley, G.K., Overzier, R.A., Tsvetanov, Z.I., Bouwens, R.J., Benítez, N., Blakeslee, J.P., Ford, H.C., Illingworth, G.D., Postman, M., Rosati, P., Clampin, M., Hartig, G.F., Zirm, A.W., Röttgering, H.J.A., Venemans, B.P., Ardila, D.R., Bartko, F., Broadhurst, T.J., Brown, R.A., Burrows, C.J., Cheng, E.S., Cross, N.J.G., De Breuck, C., Feldman, P.D., Franx, M., Golimowski, D.A., Gronwall, C., Infante, L., Martel, A.R., Menanteau, F., Meurer, G.R., Sirianni, M., Kimble, R.A., Krist, J.E., Sparks, W.B., Tran, H.D., White, R.L., & Zheng, W., 2004. *Nature*, 427:47
- Miley, G.K., Overzier, R.A., Zirm, A.W., Ford, H.C., Kurk, J., Pentericci, L., Blakeslee, J.P., Franx, M., Illingworth, G.D., Postman, M., Rosati, P., Röttgering, H.J.A., Venemans, B.P., & Helder, E., 2006. *ApJ*, 650:L29
- Mo, H., van den Bosch, F.C., & White, S., 2010. *Galaxy Formation and Evolution*
- Mo, H.J., Mao, S., & White, S.D.M., 1998. *MNRAS*, 295:319
- Monaco, P., Fontanot, F., & Taffoni, G., 2007. *MNRAS*, 375:1189
- Monaco, P., Murante, G., Borgani, S., & Fontanot, F., 2006. *ApJ*, 652:L89

- Moore, B., Ghigna, S., Governato, F., Lake, G., Quinn, T., Stadel, J., & Tozzi, P., 1999. *ApJ*, 524:L19
- Moore, B., Katz, N., Lake, G., Dressler, A., & Oemler, A., 1996. *Nature*, 379:613
- Moore, B., Lake, G., & Katz, N., 1998. *ApJ*, 495:139
- Moster, B.P., Somerville, R.S., Maulbetsch, C., van den Bosch, F.C., Macciò, A.V., Naab, T., & Oser, L., 2010. *ApJ*, 710:903
- Murante, G., Arnaboldi, M., Gerhard, O., Borgani, S., Cheng, L.M., Diaferio, A., Dolag, K., Moscardini, L., Tormen, G., Tornatore, L., & Tozzi, P., 2004. *ApJ*, 607:L83
- Murante, G., Borgani, S., Brunino, R., & Cha, S.H., 2011. ArXiv e-prints
- Murante, G., Giovalli, M., Gerhard, O., Arnaboldi, M., Borgani, S., & Dolag, K., 2007. *MNRAS*, 377:2
- Nagai, D. & Kravtsov, A.V., 2005. *ApJ*, 618:557
- Navarro, J.F., Frenk, C.S., & White, S.D.M., 1996. *ApJ*, 462:563
- Neto, A.F., Gao, L., Bett, P., Cole, S., Navarro, J.F., Frenk, C.S., White, S.D.M., Springel, V., & Jenkins, A., 2007. *MNRAS*, 381:1450
- Oemler, Jr., A., Dressler, A., Gladders, M.G., Rigby, J.R., Bai, L., Kelson, D., Villanueva, E., Fritz, J., Rieke, G., Poggianti, B.M., & Vulcani, B., 2013. *ApJ*, 770:61
- Okamoto, T., Gao, L., & Theuns, T., 2008. *MNRAS*, 390:920
- Overzier, R.A., Bouwens, R.J., Cross, N.J.G., Venemans, B.P., Miley, G.K., Zirm, A.W., Benítez, N., Blakeslee, J.P., Coe, D., Demarco, R., Ford, H.C., Homeier, N.L., Illingworth, G.D., Kurk, J.D., Martel, A.R., Mei, S., Oliveira, I., Röttgering, H.J.A., Tsvetanov, Z.I., & Zheng, W., 2008. *ApJ*, 673:143
- Padmanabhan, T., 1996. *Cosmology and Astrophysics through Problems*
- Peacock, J.A., 1999. *Cosmological Physics*
- Peebles, P.J.E., 1993. *Principles of Physical Cosmology*
- Pentericci, L., McCarthy, P.J., Röttgering, H.J.A., Miley, G.K., van Breugel, W.J.M., & Fosbury, R., 2001. *ApJS*, 135:63
- Pentericci, L., Roettgering, H.J.A., Miley, G.K., Carilli, C.L., & McCarthy, P., 1997. *A&A*, 326:580

- Penzias, A.A. & Wilson, R.W., 1965. *ApJ*, 142:419
- Percival, W.J., Cole, S., Eisenstein, D.J., Nichol, R.C., Peacock, J.A., Pope, A.C., & Szalay, A.S., 2007. *MNRAS*, 381:1053
- Perlmutter, S., Aldering, G., Goldhaber, G., Knop, R.A., Nugent, P., Castro, P.G., Deustua, S., Fabbro, S., Goobar, A., Groom, D.E., Hook, I.M., Kim, A.G., Kim, M.Y., Lee, J.C., Nunes, N.J., Pain, R., Pennypacker, C.R., Quimby, R., Lidman, C., Ellis, R.S., Irwin, M., McMahon, R.G., Ruiz-Lapuente, P., Walton, N., Schaefer, B., Boyle, B.J., Filippenko, A.V., Matheson, T., Fruchter, A.S., Panagia, N., Newberg, H.J.M., Couch, W.J., & Supernova Cosmology Project, 1999. *ApJ*, 517:565
- Phleps, S., Peacock, J.A., Meisenheimer, K., & Wolf, C., 2006. *A&A*, 457:145
- Poggianti, B.M., De Lucia, G., Varela, J., Aragon-Salamanca, A., Finn, R., Desai, V., von der Linden, A., & White, S.D.M., 2010. *MNRAS*, 405:995
- Poggianti, B.M., Desai, V., Finn, R., Bamford, S., De Lucia, G., Varela, J., Aragón-Salamanca, A., Halliday, C., Noll, S., Saglia, R., Zaritsky, D., Best, P., Clowe, D., Milvang-Jensen, B., Jablonka, P., Pelló, R., Rudnick, G., Simard, L., von der Linden, A., & White, S., 2008. *ApJ*, 684:888
- Poggianti, B.M., Fasano, G., Bettoni, D., Cava, A., Dressler, A., Vanzella, E., Varela, J., Couch, W.J., D'Onofrio, M., Fritz, J., Kjaergaard, P., Moles, M., & Valentinuzzi, T., 2009. *ApJ*, 697:L137
- Poggianti, B.M., von der Linden, A., De Lucia, G., Desai, V., Simard, L., Halliday, C., Aragón-Salamanca, A., Bower, R., Varela, J., Best, P., Clowe, D.I., Dalcanton, J., Jablonka, P., Milvang-Jensen, B., Pello, R., Rudnick, G., Saglia, R., White, S.D.M., & Zaritsky, D., 2006. *ApJ*, 642:188
- Popesso, P., Biviano, A., Böhringer, H., & Romaniello, M., 2007a. *A&A*, 464:451
- Popesso, P., Biviano, A., Romaniello, M., & Böhringer, H., 2007b. *A&A*, 461:411
- Postman, M., Coe, D., Benítez, N., Bradley, L., Broadhurst, T., Donahue, M., Ford, H., Graur, O., Graves, G., Jouvel, S., Koekemoer, A., Lemze, D., Medezinski, E., Molino, A., Moustakas, L., Ogaz, S., Riess, A., Rodney, S., Rosati, P., Umetsu, K., Zheng, W., Zitrin, A., Bartelmann, M., Bouwens, R., Czakon, N., Golwala, S., Host, O., Infante, L., Jha, S., Jimenez-Teja, Y., Kelson, D., Lahav, O., Lazkoz, R., Maoz, D., McCully, C., Melchior, P., Meneghetti, M., Merten, J., Moustakas, J., Nonino, M., Patel, B., Regös, E., Sayers, J., Seitz, S., & Van der Wel, A., 2012. *ApJS*, 199:25
- Postman, M. & Geller, M.J., 1984. *ApJ*, 281:95

- Power, C., Knebe, A., & Knollmann, S.R., 2012. *MNRAS*, 419:1576
- Press, W.H. & Schechter, P., 1974. *ApJ*, 187:425
- Price, D.J., 2008. *Journal of Computational Physics*, 227:10040
- Puchwein, E., Baldi, M., & Springel, V., 2013. *ArXiv e-prints*
- Puchwein, E., Springel, V., Sijacki, D., & Dolag, K., 2010. *MNRAS*, 406:936
- Pujol, A., Gaztanaga, E., Giocoli, C., Knebe, A., Pearce, F.R., Skibba, R.A., Ascasibar, Y., Behroozi, P., Elahi, P., Han, J., Lux, H., Muldrew, S.I., Neyrinck, M., Onions, J., Potter, D., & Tweed, D., 2013. *ArXiv e-prints*
- Purcell, C.W., Bullock, J.S., & Zentner, A.R., 2007. *ApJ*, 666:20
- Purcell, C.W., Bullock, J.S., & Zentner, A.R., 2008. *MNRAS*, 391:550
- Read, J.I., Pontzen, A.P., & Viel, M., 2006. *MNRAS*, 371:885
- Romer, A.K., Viana, P.T.P., Liddle, A.R., & Mann, R.G., 2001. *ApJ*, 547:594
- Roos, N. & Norman, C.A., 1979. *A&A*, 76:75
- Rudick, C.S., Mihos, J.C., & McBride, C., 2006. *ApJ*, 648:936
- Rudick, C.S., Mihos, J.C., & McBride, C.K., 2011. *ApJ*, 732:48
- Saitoh, T.R., Daisaka, H., Kokubo, E., Makino, J., Okamoto, T., Tomisaka, K., Wada, K., & Yoshida, N., 2009. *PAPJ*, 61:481
- Salpeter, E.E., 1955. *ApJ*, 121:161
- Saro, A., De Lucia, G., Borgani, S., & Dolag, K., 2010. *MNRAS*, 406:729
- Scannapieco, C., Wadepuhl, M., Parry, O.H., Navarro, J.F., Jenkins, A., Springel, V., Teyssier, R., Carlson, E., Couchman, H.M.P., Crain, R.A., Dalla Vecchia, C., Frenk, C.S., Kobayashi, C., Monaco, P., Murante, G., Okamoto, T., Quinn, T., Schaye, J., Stinson, G.S., Theuns, T., Wadsley, J., White, S.D.M., & Woods, R., 2012. *MNRAS*, 423:1726
- Schmidt, M., 1959. *ApJ*, 129:243
- Schuecker, P., Böhringer, H., Collins, C.A., & Guzzo, L., 2003. *A&A*, 398:867
- Shao, L., Kauffmann, G., Li, C., Wang, J., & Heckman, T.M., 2013. *MNRAS*, 436:3451
- Shapley, H., 1936. *Harvard College Observatory Bulletin*, 903:17
- Shlosman, I., 2012. *ArXiv e-prints*

- Simha, V., Weinberg, D.H., Davé, R., Fardal, M., Katz, N., & Oppenheimer, B.D., 2012. *MNRAS*, 423:3458
- Skibba, R.A. & Sheth, R.K., 2009. *MNRAS*, 392:1080
- Smail, I., Edge, A.C., Ellis, R.S., & Blandford, R.D., 1998. *MNRAS*, 293:124
- Somerville, R.S., Hopkins, P.F., Cox, T.J., Robertson, B.E., & Hernquist, L., 2008. *MNRAS*, 391:481
- Somerville, R.S., Primack, J.R., & Faber, S.M., 2001. *MNRAS*, 320:504
- Sommer-Larsen, J., 2006. *MNRAS*, 369:958
- Spergel, D.N., Verde, L., Peiris, H.V., Komatsu, E., Nolta, M.R., Bennett, C.L., Halpern, M., Hinshaw, G., Jarosik, N., Kogut, A., Limon, M., Meyer, S.S., Page, L., Tucker, G.S., Weiland, J.L., Wollack, E., & Wright, E.L., 2003. *ApJS*, 148:175
- Springel, V., 2010a. *MNRAS*, 401:791
- Springel, V., 2010b. *A&A Annual Rev.*, 48:391
- Springel, V. & Hernquist, L., 2005. *ApJ*, 622:L9
- Springel, V., White, S.D.M., Jenkins, A., Frenk, C.S., Yoshida, N., Gao, L., Navarro, J., Thacker, R., Croton, D., Helly, J., Peacock, J.A., Cole, S., Thomas, P., Couchman, H., Evrard, A., Colberg, J., & Pearce, F., 2005. *Nature*, 435:629
- Springel, V., White, S.D.M., Tormen, G., & Kauffmann, G., 2001a. *MNRAS*, 328:726
- Springel, V., Yoshida, N., & White, S.D.M., 2001b. *NewA*, 6:79
- Stanford, S.A., Eisenhardt, P.R., & Dickinson, M., 1998. *ApJ*, 492:461
- Stoehr, F., White, S.D.M., Springel, V., Tormen, G., & Yoshida, N., 2003. *MNRAS*, 345:1313
- Stone, J.M., Gardiner, T.A., Teuben, P., Hawley, J.F., & Simon, J.B., 2008. *ApJS*, 178:137
- Stott, J.P., Pimblett, K.A., Edge, A.C., Smith, G.P., & Wardlow, J.L., 2009. *MNRAS*, 394:2098
- Strateva, I., Ivezić, Ž., Knapp, G.R., Narayanan, V.K., Strauss, M.A., Gunn, J.E., Lupton, R.H., Schlegel, D., Bahcall, N.A., Brinkmann, J., Brunner, R.J., Budavári, T., Csabai, I., Castander, F.J., Doi, M., Fukugita, M., Győry, Z., Hamabe, M., Hennessy, G., Ichikawa, T., Kunszt, P.Z., Lamb, D.Q., McKay, T.A., Okamura, S., Racusin, J., Sekiguchi, M., Schneider, D.P., Shimasaku, K., & York, D., 2001. *AJ*, 122:1861
- Strazzullo, V., Gobat, R., Daddi, E., Onodera, M., Carollo, M., Dickinson, M., Renzini, A., Arimoto, N., Cimatti, A., Finoguenov, A., & Chary, R.R., 2013. *ApJ*, 772:118

- Strazzullo, V., Rosati, P., Pannella, M., Gobat, R., Santos, J.S., Nonino, M., Demarco, R., Lidman, C., Tanaka, M., Mullis, C.R., Nuñez, C., Rettura, A., Jee, M.J., Böhringer, H., Bender, R., Bouwens, R.J., Dawson, K., Fassbender, R., Franx, M., Perlmutter, S., & Postman, M., 2010. *A&A*, 524:A17
- Sunyaev, R.A. & Zeldovich, Y.B., 1972. *Comments on Astrophysics and Space Physics*, 4:173
- Sutherland, R.S. & Dopita, M.A., 1993. *ApJS*, 88:253
- Szabo, T., Pierpaoli, E., Dong, F., Pipino, A., & Gunn, J., 2011. *ApJ*, 736:21
- Takey, A., Schwobe, A., & Lamer, G., 2013. *A&A*, 558:A75
- Tanaka, I., Breuck, C.D., Kurk, J.D., Taniguchi, Y., Kodama, T., Matsuda, Y., Packham, C., Zirm, A., Kajisawa, M., Ichikawa, T., Seymour, N., Stern, D., Stockton, A., Venemans, B.P., & Vernet, J., 2011. *PAPJ*, 63:415
- Teyssier, R., 2002. *A&A*, 385:337
- Tikhonov, A.V. & Klypin, A., 2009. *MNRAS*, 395:1915
- Toledo, I., Melnick, J., Selman, F., Quintana, H., Giraud, E., & Zelaya, P., 2011. *MNRAS*, 414:602
- Toomre, A. & Toomre, J., 1972. *ApJ*, 178:623
- Tormen, G., Bouchet, F.R., & White, S.D.M., 1997. *MNRAS*, 286:865
- Toshikawa, J., Kashikawa, N., Ota, K., Morokuma, T., Shibuya, T., Hayashi, M., Nagao, T., Jiang, L., Malkan, M.A., Egami, E., Shimasaku, K., Motohara, K., & Ishizaki, Y., 2012. *ApJ*, 750:137
- Tran, K.V.H., van Dokkum, P., Illingworth, G.D., Kelson, D., Gonzalez, A., & Franx, M., 2005. *ApJ*, 619:134
- Trentham, N. & Mobasher, B., 1998. *MNRAS*, 293:53
- Trujillo-Gomez, S., Klypin, A., Primack, J., & Romanowsky, A.J., 2011. *ApJ*, 742:16
- Tully, R.B. & Fisher, J.R., 1977. *A&A*, 54:661
- Urquhart, S.A., Willis, J.P., Hoekstra, H., & Pierre, M., 2010. *MNRAS*, 406:368
- Vale, A. & Ostriker, J.P., 2006. *MNRAS*, 371:1173
- van den Bergh, S., 2000. *The Galaxies of the Local Group*. Cambridge

- van den Bosch, F.C., Aquino, D., Yang, X., Mo, H.J., Pasquali, A., McIntosh, D.H., Weinmann, S.M., & Kang, X., 2008. MNRAS, 387:79
- van den Bosch, F.C., Tormen, G., & Giocoli, C., 2005. MNRAS, 359:1029
- van den Bosch, F.C., Yang, X., Mo, H.J., Weinmann, S.M., Macciò, A.V., More, S., Cacciato, M., Skibba, R., & Kang, X., 2007. MNRAS, 376:841
- van der Wel, A., 2008. ApJ, 675:L13
- van der Wel, A., Bell, E.F., Holden, B.P., Skibba, R.A., & Rix, H.W., 2010. ApJ, 714:1779
- van der Wel, A., Holden, B.P., Franx, M., Illingworth, G.D., Postman, M.P., Kelson, D.D., Labbé, I., Wuyts, S., Blakeslee, J.P., & Ford, H.C., 2007. ApJ, 670:206
- van Dokkum, P.G., Franx, M., Fabricant, D., Kelson, D.D., & Illingworth, G.D., 1999. ApJ, 520:L95
- Venemans, B.P., Röttgering, H.J.A., Miley, G.K., van Breugel, W.J.M., de Breuck, C., Kurk, J.D., Pentericci, L., Stanford, S.A., Overzier, R.A., Croft, S., & Ford, H., 2007. A&A, 461:823
- Villalobos, Á., De Lucia, G., Borgani, S., & Murante, G., 2012. ArXiv e-prints
- Villalobos, Á., De Lucia, G., Weinmann, S., Borgani, S., & Murante, G., 2013. ArXiv e-prints
- von der Linden, A., Best, P.N., Kauffmann, G., & White, S.D.M., 2007. MNRAS, 379:867
- von der Linden, A., Wild, V., Kauffmann, G., White, S.D.M., & Weinmann, S., 2010. MNRAS, 404:1231
- Wadsley, J.W., Stadel, J., & Quinn, T., 2004. NewA, 9:137
- Wang, J., De Lucia, G., Kitzbichler, M.G., & White, S.D.M., 2008. MNRAS, 384:1301
- Wang, L., Li, C., Kauffmann, G., & De Lucia, G., 2006. MNRAS, 371:537
- Warnick, K., Knebe, A., & Power, C., 2008. MNRAS, 385:1859
- Watson, D.F., Berlind, A.A., & Zentner, A.R., 2012. ArXiv e-prints
- Weinberg, D.H., Mortonson, M.J., Eisenstein, D.J., Hirata, C., Riess, A.G., & Rozo, E., 2012. ArXiv e-prints
- Weinberg, S., 1993. *The first three minutes : a modern view of the origin of the universe*
- Weinmann, S.M., Kauffmann, G., von der Linden, A., & De Lucia, G., 2010. MNRAS, 406:2249

- Weinmann, S.M., Lisker, T., Guo, Q., Meyer, H.T., & Janz, J., 2011. *MNRAS*, 416:1197
- Weinmann, S.M., van den Bosch, F.C., Yang, X., & Mo, H.J., 2006. *MNRAS*, 366:2
- Wetzel, A.R., Tinker, J.L., & Conroy, C., 2012. *MNRAS*, 424:232
- White, S.D.M., Clowe, D.I., Simard, L., Rudnick, G., De Lucia, G., Aragón-Salamanca, A., Bender, R., Best, P., Bremer, M., Charlot, S., Dalcanton, J., Dantel, M., Desai, V., Fort, B., Halliday, C., Jablonka, P., Kauffmann, G., Mellier, Y., Milvang-Jensen, B., Pelló, R., Poggianti, B., Poirier, S., Rottgering, H., Saglia, R., Schneider, P., & Zaritsky, D., 2005. *A&A*, 444:365
- White, S.D.M., Navarro, J.F., Evrard, A.E., & Frenk, C.S., 1993. *Nature*, 366:429
- White, S.D.M. & Rees, M.J., 1978. *MNRAS*, 183:341
- Williams, B.F., Ciardullo, R., Durrell, P.R., Vinciguerra, M., Feldmeier, J.J., Jacoby, G.H., Sigurdsson, S., von Hippel, T., Ferguson, H.C., Tanvir, N.R., Arnaboldi, M., Gerhard, O., Aguerri, J.A.L., & Freeman, K., 2007. *ApJ*, 656:756
- Willman, B., Governato, F., Wadsley, J., & Quinn, T., 2004. *MNRAS*, 355:159
- Wilson, G., Muzzin, A., Yee, H.K.C., Lacy, M., Surace, J., Gilbank, D., Blindert, K., Hoekstra, H., Majumdar, S., Demarco, R., Gardner, J.P., Gladders, M.D., & Lonsdale, C., 2009. *ApJ*, 698:1943
- Yee, H.K.C., Ellingson, E., & Carlberg, R.G., 1996. *ApJS*, 102:269
- Yee, H.K.C., Gladders, M.D., Gilbank, D.G., Majumdar, S., Hoekstra, H., & Ellingson, E., 2007. In N. Metcalfe & T. Shanks, editors, *Cosmic Frontiers, Astronomical Society of the Pacific Conference Series*, vol. 379, page 103
- Young, J.S., Kenney, J.D., Tacconi, L., Claussen, M.J., Huang, Y.L., Tacconi-Garman, L., Xie, S., & Schloerb, F.P., 1986. *ApJ*, 311:L17
- Zhang, W., Howell, L., Almgren, A., Burrows, A., & Bell, J., 2011. *ApJS*, 196:20
- Zheng, Z., 2004. *ApJ*, 610:61
- Zheng, Z., Berlind, A.A., Weinberg, D.H., Benson, A.J., Baugh, C.M., Cole, S., Davé, R., Frenk, C.S., Katz, N., & Lacey, C.G., 2005. *ApJ*, 633:791
- Zibetti, S., 2008. In J.I. Davies & M.J. Disney, editors, *IAU Symposium, IAU Symposium*, vol. 244, pages 176–185
- Zibetti, S., White, S.D.M., Schneider, D.P., & Brinkmann, J., 2005. *MNRAS*, 358:949

Zirm, A.W., Overzier, R.A., Miley, G.K., Blakeslee, J.P., Clampin, M., De Breuck, C., Demarco, R., Ford, H.C., Hartig, G.F., Homeier, N., Illingworth, G.D., Martel, A.R., Röttgering, H.J.A., Venemans, B., Ardila, D.R., Bartko, F., Benítez, N., Bouwens, R.J., Bradley, L.D., Broadhurst, T.J., Brown, R.A., Burrows, C.J., Cheng, E.S., Cross, N.J.G., Feldman, P.D., Franx, M., Golimowski, D.A., Goto, T., Gronwall, C., Holden, B., Infante, L., Kimble, R.A., Krist, J.E., Lesser, M.P., Mei, S., Menanteau, F., Meurer, G.R., Motta, V., Postman, M., Rosati, P., Sirianni, M., Sparks, W.B., Tran, H.D., Tsvetanov, Z.I., White, R.L., & Zheng, W., 2005. *ApJ*, 630:68

Zwicky, F., 1933. *Helvetica Physica Acta*, 6:110

Zwicky, F., 1937. *ApJ*, 86:217

Zwicky, F., 1952. *PAPS*, 64:242